Studies of the fragmentation process in hadronic decays of Z boson

Smirnova, Oxana

1996

Studies of the Fragmentation Process in Hadronic Decays of Z^0 Boson

Thesis submitted for the degree of
Doctor of Philosophy in Physics
by

Oxana Smirnova

DEPARTMENT OF PHYSICS, LUND UNIVERSITY
LUND, 1996

ISBN 91-628-2183-0
LUNFD6/(NFFL–7127)1996

Studies of the Fragmentation Process in Hadronic Decays of Z^0 Boson

By due permission of the faculty of mathematics and natural science at the Lund University to be publicly discussed at the lecture hall B at the department of Physics, October 17, 1996, at 10:15 a.m. for the degree of Doctor of Philosophy

by

Oxana Smirnova

Department of Particle Physics
Lund University
Professorsgatan 1
S-223 63 Lund
Sweden

This thesis is based on following papers, included as Appendices A to E:

A "The Performance of the DELPHI Hadron Calorimeter at LEP", IEEE Trans. on Nucl. Science **NS-43** (1996) No.3.

B "The Cathode Read-out of the DELPHI Hadron Calorimeter", IEEE Trans. on Nucl. Science **NS-42** (1995) No.4.

C "On the determination of the longitudinal component of the fragmentation function of the process $e^+e^- \to h + X$ from DELPHI data", DELPHI Note 95-11 Phys 472 (1995).

D "Measurement of the Quark and Gluon Fragmentation Functions in Z^0 Hadronic Decays", to be submitted to Zeit. Phys. **C**.

E "Transverse Mass Dependence of Bose-Einstein Correlation Radii in e^+e^- Annihilation at the LEP Energies", in Proceedings of 7th International Workshop on Multiparticle Production 'Correlations and Fluctuations', Nijmegen, The Netherlands, June 30 – July 6, 1996.

Contents

Abstract

This thesis is based on the work that was done during 1992–1996 at the DELPHI detector at LEP. Its main parts are outlined below.

The brief Introduction gives an overview of the science of Particle Physics, its development and contemporary status.

The first chapter represents an introduction to the DELPHI detector at LEP, describing the main features of the LEP machine and the DELPHI detector as means to obtain an important information for the analysis.

The second chapter is devoted to description of the development of one of the components of the DELPHI detector: the hadron calorimeter and its cathode readout system in particular.

The third chapter describes the wide possibilities of QCD analysis using the information about hadronic decays of the Z^0 boson produced in e^+e^- annihilation. The main goal of this work was to extract different components of the charged hadron cross section and to derive the gluon fragmentation function.

In the fourth chapter results of the studies of two-particles correlations in hadronic Z^0 decays are presented. The analysis of directional and transverse mass dependences of the Bose-Einstein correlations is performed.

... if [the universe] is divisible through and through, there is no 'one' and therefore no 'many' either, but the Whole is void; while to maintain that it is divisible at some points, but not at others, looks like an arbitrary fiction. For up to what limits is it divisible? And for what reason is part of the Whole indivisible, i.e. a plenum, and part divided?

"On Generation and Corruption"
by Aristotle

Introduction

The idea of discovering the basic building blocks of the matter powers scientific researches through millennia. In the year 400 B. C., ancient Greek philosopher Democritus proclaimed that "in reality, there are atoms and space". By atoms he meant smallest indivisible particles. Couple of millennia later chemists learned out that the matter is built up of molecules, and those molecules are built up of something they called atoms. At about the same time, physicists were studying electricity, magnetism and optics. In 1897 A. D., the English physicist J. J. Thomson discovered in cathode rays experiment the electron, which become the first elementary particle to be found. Hence the year 1897 can be regarded as the birth date of the science of Particle Physics. Existence of electrons proved that atoms are not indivisible, although they are the smallest units into which matter can be divided without the release of electrically charged particles. The discovery of electron triggered investigations of the atomic structure. While all the classical mechanical models failed, in 1913, the Danish physicist Niels Bohr introduced quantum theory to account for the structure of atoms. Presuming the hydrogen atom model, in which negatively charged electrons orbits a positively charged nucleus, he asserted that electron can occupy discrete energy orbits. Later, in mid-1920s, the theory of quantum mechanics was developed with the introduction of the uncertainty principle by the German scientist Werner Heizenberg. In 1924-1925 the subdivision of elementary particles into fermions (after Italian physicist Enrico Fermi) and bosons (after Indian mathematician and physicist Satyendra Nath Bose) was developed. In quantum field theory, fermions have antisymmetric wave functions, like electrons, and bosons have symmetric wave functions, like photons.

Theoretical and experimental studies in atomic and nuclear physics progressed rapidly, and by the 1940s proton and neutron were known as building parts of nuclei, muon and positron also were discovered, increasing the number of known elementary particles and improving the knowledge of the structure of matter. It was known that the nuclear fission can release a great amount of thermal energy, as well as gamma rays and neutrons. And it was clear that the further studies of elementary particles need experimental installations which force particles to interact at very high energies. In 1932 the British physicists John Douglas Cockcroft and E. T. S. Walton first observed the disintegration of a nucleus by artificially accelerated particles. Thereafter, the importance of accelerators in basic research became comparable to that of microscopes and telescopes. The rapid advance in the science of accelerating particles to high energies occurred since 1945, when two physicists, American Edwin Mattison McMillan and Russian Vladimir Iosifovich Veksler, independently described the principle of phase stability, which made possible the construction of magnetic-resonance accelerators, called synchrotrons. By the same time, the Quantum Electrodynamics (QED) as a quantum theory of the interactions of charged

name	acts on:	carrier	range	strength	examples	
					stable systems	induced reaction
Gravity	all particles	proposed graviton	long; $F \propto 1/r^2$	$\sim 10^{-39}$	solar system	object falling
Weak force	fermions	bosons $W^{\pm}, Z^0$	$< 10^{-17} m$	10^{-5}	none	beta decay
Electro-magnetism	particles with electric charge	photon,γ	long; $F \propto 1/r^2$	1/137	atoms, rocks	chemical reactions
Strong force	quarks, q, and gluons, g	gluons,g	$10^{-15} m$	1	hadrons, nuclei	nuclear reactions

Table 0.1: *The four basic forces of nature.*

particles, became fully developed.

Simultaneous development in both experiment and theory led to enormous progress in high energy physics, or particle physics. Elementary particles were discovered in abundance, and classified to gamma-quanta, leptons, mesons and barions. Throughout the 1960s theoretical physicists, trying to account for the ever-growing number of subatomic particles observed in experiments, considered the possibility that protons and neutrons were composed of smaller units of matter. In 1961 two physicists, Murray Gell-Mann of the United States and Yuval Ne'eman of Israel, proposed a particle classification scheme called the Eightfold Way, based on the mathematical symmetry group SU(3), that described strongly interacting particles in terms of building blocks. Later, these blocks were called quarks. In 1970s, the Quantum Chromodynamics (QCD) was developed as the theory of strong interaction between quarks, introducing gluons as quanta of the strong field.

Discovery of intermediate vector bosons, W and Z, in 1983 at the European Laboratory for Particle Physics (CERN) in Geneva, Switzerland, provided a strong support to the electroweak theory, developed during 1960s independently by Sheldon Glashow, Abdus Salam, and Steven Weinberg. It was constructed as a gauge-invariant theory of the weak force, of which physicists were aware since 1930s, also including the electromagnetic force. Thus the picture of the modern understanding of the forces which drive the Universe (see Table 0.1) became almost complete. Gravitation is by far the weakest known force in nature and thus plays no role in determining the internal properties of everyday matter. Proposed by the relativistic gravitation theory gravity waves and quanta of the gravitational field, gravitons, are not discovered yet.

The combination of the electroweak theory and QCD, called the Standard Model, proved to be a highly successful framework. The Standard Model operates with two families of fermions: leptons and quarks, that build up matter and interact by means of bosons: γ, W, Z and g. Elementary particles are subdivided into three generations, see Fig. 0.1. Leptons are electron e, muon μ, tau-lepton τ, their respective neutrinos ν_e, ν_μ and ν_τ, and their antiparticles. Quarks are of six different "flavours" : up, down, charm, strange, top and bottom. The modern Standard Model does not explain, why there are

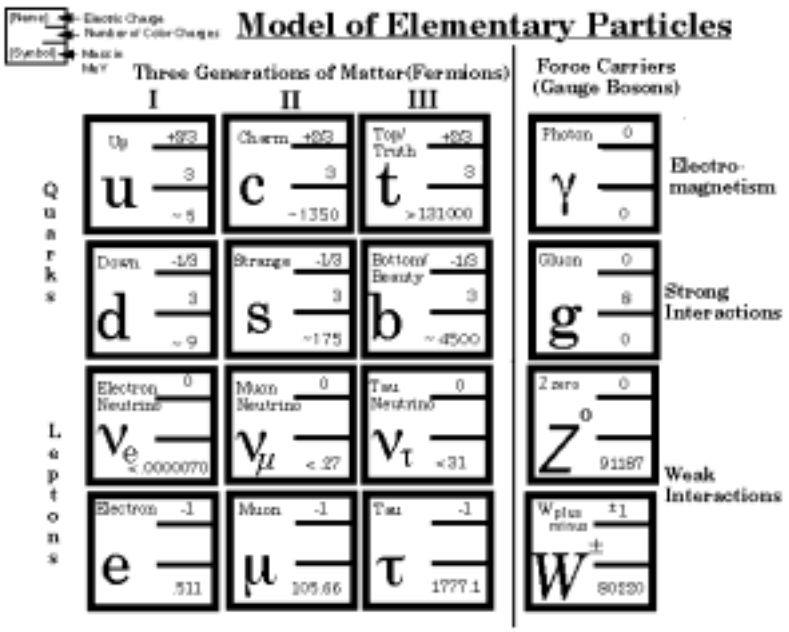

Figure 0.1: *Elementary particles in the Standard Model. Each particle has a corresponding antiparticle of the opposite charge.*

three generation of leptons and quarks, neither does it predict their masses. However, recent experiments confirmed existence of all six quarks and three generations. The heaviest quark, the top quark, was discovered in 1995 at the Fermi National Accelerator Laboratory in Brookhaven, USA.

Current researches in particle physics are focused on the Higgs particle, the particle associated with the mechanism that allows the symmetry of the electroweak force to be broken, or hidden, at low energies and that requires the W and Z bosons to have mass. Researchers know that the Higgs particle must have spin 0, but that is virtually all that can be definitely predicted. Theory provides a poor guide as to the particle's mass or even the number of different varieties of Higgs particles involved.

At the time being, scientists can admit that the knowledge of the laws of nature is by far not complete. Profound theoretical and experimental investigations yet have to be done, new theories have to be written, new accelerators have to be built.

In 1989, the largest contemporary accelerator, the LEP collider, began operation in CERN. Four detectors devoted to the electron-positron annihilation experiments were installed at the collider ring. The author of this thesis got a grand opportunity to contribute to the construction, operation and data analysis of one of them, the DELPHI. The result of this activity during the years 1992–1996 is summarised in the dissertation.

Chapter 1

The DELPHI Detector at LEP

Modern science of particle physics is heavily based on high energy accelerators, which produce wide range of elementary particles for consecutive studies. For precision analysis, electron-positron colliders are factories which provide scientists with sufficient statistical material of high purity. The biggest contemporary accelerator of this kind has been built in the European Particle Physics Laboratory, CERN. Four different detectors have been constructed to collect data on electron-positron collisions: ALEPH, DELPHI, L3 and OPAL. This work will be concentrated on the DELPHI detector at LEP.

1.1 The LEP Collider

The CERN Large Electron Positron (LEP) collider [1] is a 26.67 km circumference e^+e^- storage ring (see Fig. 1.1) which was designed to operate in an energy range of 20 GeV to 50 GeV per beam at the first stage and up to 90 GeV at the second stage. The basic feature of the LEP design is a large accelerating ring circumference in which the machine is installed in stages corresponding to the new physics events that are predicted by the unified theory of weak and electromagnetic interactions. The first such event is the Z^0 boson at an energy of $\simeq 90$ GeV. Since these bosons can be produced singly, the LEP machine energy is about 50 GeV per beam, giving 100 GeV in the centre of mass. The next predicted event is the production of pairs of the charged intermediate boson (W^+W^-) at an energy of about 180 GeV which requires LEP energies of about 90 GeV per beam. This increased energy at the second stage is obtained by installing additional superconducting accelerating cavities. Another advantage of the LEP Project is to use the PS and SPS machines as the injectors for LEP.

1.1.1 The LEP collider design

The LEP Main Ring 26.67 km tunnel is complemented with four experimental caverns, 18 pits, 3 km of secondary tunnel, and some 60 chambers and alcoves. The plane of the tunnel is inclined by 1.4% to ensure that all underground caverns and the main part of the tunnel would be located in solid rock while, at the same time, limiting the maximum depth of the shafts to less than 150 m.

The electromagnetic guide field system of LEP consists of dipoles, quadrupoles, sextupoles, horizontal and vertical dipole correctors, rotated quadrupoles, and finally electrostatic dipole deflectors. Magnets are combined in "standard cells" in the following order: a defocusing quadrupole, a vertical orbit corrector, a group of six bending dipoles, a focusing sextupole, a focusing quadrupole, a horizontal orbit corrector, a second group of six bending dipoles, and finally a defocusing sextupole. The length of a standard cell is 79.11 m.

Each experimental collision point in LEP is surrounded by a large solenoidal magnet used for particle separation. The bunches of each beam must be tightly focused to very small dimensions in the centre of these detectors in order to increase the luminosity or particle production rate. This is accomplished by a set of superconducting quadrupoles with very strong field gradients that focus the transverse beam dimensions to about 10 μm and 250 μm in the vertical and horizontal planes respectively. The solenoidal detector magnets produce another effect, however: they cause the horizontal oscillations to be "coupled" into the vertical plane; if this were uncompensated it would greatly increase the vertical beam size and cause a reduction in the luminosity. For this reason, rotated quadrupoles are installed around each solenoid to compensate this magnetic coupling. These quadrupoles are similar to conventional quadrupoles but rotated about their axis by 45°.

The radio-frequency acceleration system consists of 120 accelerating copper cavities fed with 16 MW of continuous power at 352 MHz. Each cavity consists of a low-loss storage cavity coupled to a five-cell accelerating cavity in such a way that the electromagnetic power continuously oscillates between the two sets of cavities. The coupling is arranged so that the power is at its peak in the acceleration cavities at the instant of the passage of the beam bunches. In this way, the bunches receive the maximum possible accelerating gradient, but the power loss due to heating of the copper cavity walls is greatly reduced since the electromagnetic power spends half of its time in the very-low-loss storage cavities.

The LEP beam-instrumentation system is used to observe the position, shape, or other relevant properties (such as polarisation or electrical current) of the beam. The beam electrical current is measured in LEP as in other accelerators by current transformers placed around the vacuum chamber. In order to position the beam accurately in the middle of the vacuum aperture, it is essential to measure the transverse beam positions at many azimuthal locations on the circumference. In the case of LEP it is measured by 504 monitors fairly evenly distributed around the circumference. Since charged particles, being bent in a circular trajectory, radiate photons, the beams can be "seen" by measuring this flux in the ultraviolet (UV) frequency range. Four UV monitors are used in LEP to measure the transverse dimensions of both beams at two different locations. The synchrotron radiation results in another problem: background originating from the high-energy spectrum of the photon emissions. In order to reduce this background, collimators are installed around each experimental point. Each of these collimators consists of remotely movable jaws of tungsten and copper, which can intercept and absorb the high-energy photons. Since these collimators can be placed very close to the beam, they were designed to accommodate, inside each horizontal jaw, a mini-calorimeter consisting of tungsten absorbers and silicon detectors. These mini-calorimeters are used to measure the relative luminosity in each experimental point by counting the number of Bhabha

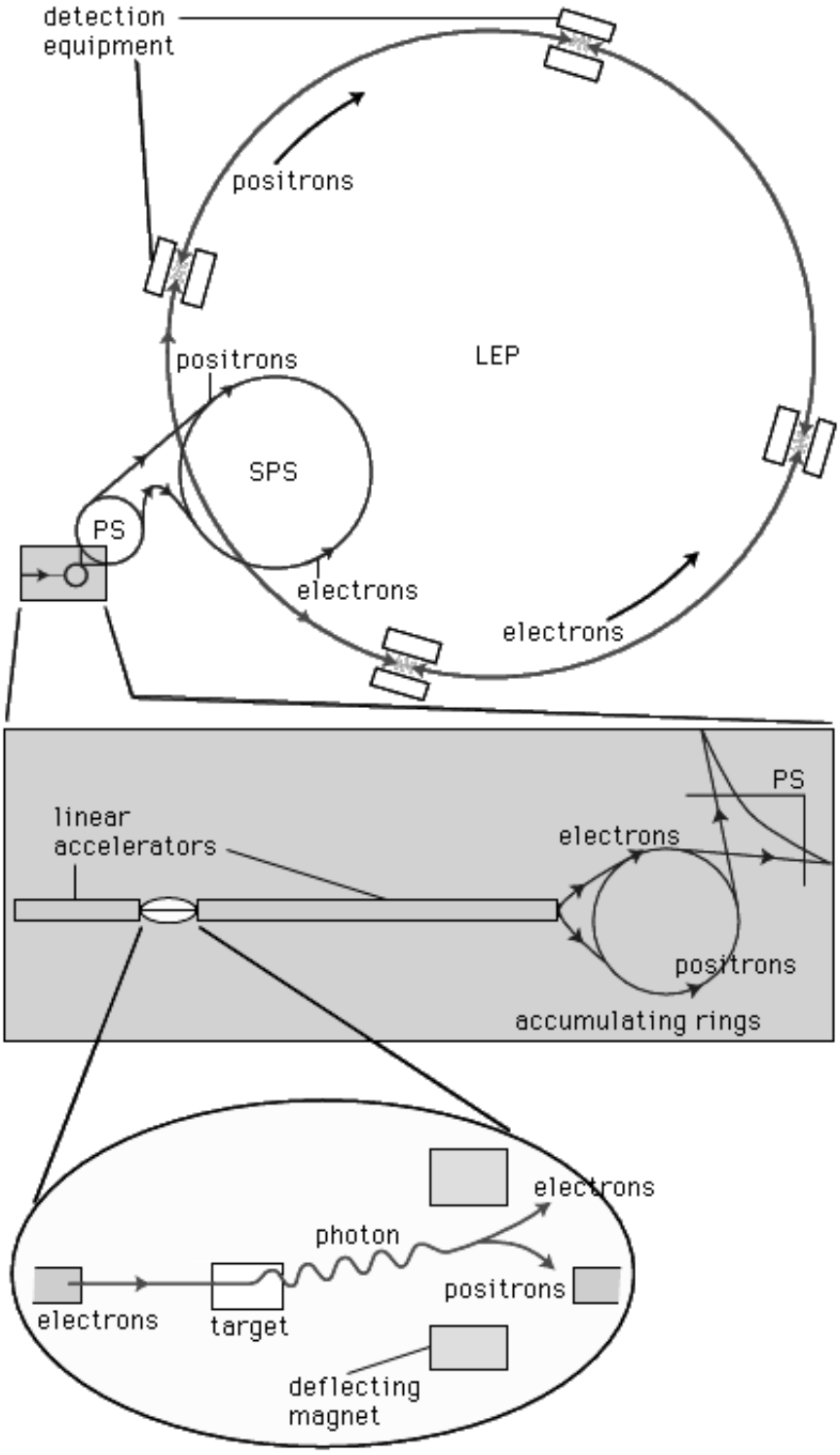

Figure 1.1: *Scheme of the CERN accelerator complex*

events at very small angles to the beam trajectory. In addition, other collimators are located far from all the experiments: these define the LEP aperture and remove any beam halo that might otherwise end up in one of the detectors. The system of collimators has proved invaluable in LEP and has resulted in low background conditions in the detectors practically from the first physics run.

Under certain circumstances it is essential that the beams of electrons and positrons do not collide. In LEP this has been achieved by equipping each of the eight possible collision points with four electrostatic separators, each of which is 4 m long and produces a vertical electric field of 2.5 MV/m between the plates, which are separated by 11 cm. This produces a separation between the bunches of electrons and positrons of more than 40 standard deviations of the vertical beam size. The separators are powered in all eight possible collision points during injection, accumulation, and energy ramping. Some time before physics data taking starts the separators in the experimental points are switched off to allow collisions.

The duration of a typical operation to fill LEP with particles for a physics run is 12 hours. During this time each of the 10^{12} particles in the beams will have traversed the complete 26.67 km of the LEP vacuum chamber about 500 million times. In order to minimise particle losses due to collisions with residual gas molecules, the whole vacuum chamber must be pumped down to very low pressures. The achieved static pressure for LEP is 8×10^{-12} $Torr$ whereas in the presence of beam the pressure rises to about 10^{-9} $Torr$. For reasons of reliability the 26.67 km of the LEP vacuum system is subdivided into smaller "vacuum sectors" with a maximum length of 474 m. There are two independent pumping systems for each of these sectors: a rough system, which provides pressures down to the 10^{-4}–10^{-5} $Torr$ range; and the second system needed to provide and maintain ultrahigh vacuum.

The LEP storage ring is the last accelerator in a chain of five (see Fig. 1.1), each of which handles the same electrons and positrons generated on every pulse by the electron gun and the positron converter. The LEP injectors consist of two linear accelerators of 200 MeV and 600 MeV followed by a 600 MeV Electron-Positron Accumulator (EPA), which injects into the CERN Proton Synchrotron (PS) operating as a 3.5 GeV e^+e^- synchrotron. The PS then injects into the CERN Super Proton Synchrotron (SPS), which operates as a 20 GeV electron-positron injector for LEP. The PS allows acceleration of electrons and positrons from 600 MeV to 3.5 GeV. The SPS accepts electrons and positrons from the PS at 3.5 GeV, accelerates them to 20.0 GeV, and finally transfers them to the LEP collider.

LEP obtained its first circulating beam on 14 July 1989 and performed collisions one month later, on 13 August 1989. Since then, operation has been a mixture of physics data taking around the Z^0 energy (45.6 GeV) and machine studies aimed at performance improvement, beam energy calibrations, and future upgrades. This first phase (LEP1) provides excellent data for studies of the Z^0 properties due to the high luminosity achieved (up to 24×10^{30} $cm^{-2}s^{-1}$) and high cross section of the Z^0 boson production.

For the second phase (LEP2) the collider has to operate at an energy of about 90 GeV with an expected luminosity $\approx 7 \times 10^{31}$ $cm^{-2}s^{-1}$ to produce pairs of W bosons.

1.2 The DELPHI Detector

DELPHI (DEtector with Lepton, Photon and Hadron Identification) is a general purpose detector for e^+e^- physics at LEP on and above the Z^0, offering three-dimensional information on curvature and energy deposition with fine spatial granularity as well as identification of leptons and hadrons over most of the solid angle. It has been operating since 1989. Comprehensive review of the performance of the DELPHI could be found elsewhere ([2,3]). Here only the short description will be given.

The DELPHI detector is installed in a cavern 100 m below ground. The general layout is shown in Fig. 1.3. It consists of a cylindrical section (the barrel), covered with two end-caps.

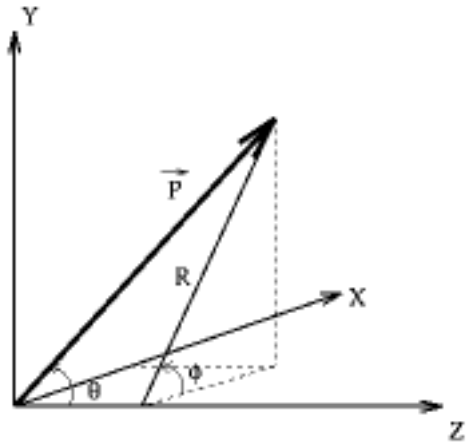

Figure 1.2: *The DELPHI coordinates.*

In the following description, the standard DELPHI coordinate system will be used (see Fig. 1.2), with the z axis along the electron direction, the x axis points towards the centre of LEP, and the y axis points to zenith. The polar angle to the z axis is called $\theta : 0 < \theta < \pi$ and the azimuthal angle in the plane perpendicular to the z axis is called $\phi : 0 < \phi < 2\pi$.

A superconducting solenoid provides a 1.23 T solenoidal field of high uniformity parallel to the z axis in the volume containing barrel tracking detectors. Tracking relies on the Vertex Detector (VD), the Inner Detector (ID), the Time Projection Chamber (TPC), the Outer Detector (OD) and forward drift chambers (FCA and FCB). Electromagnetic showers are measured in the barrel with high granularity by the High Density Projection Chamber (HPC) in the barrel region and in the end-caps by the Forward Electromagnetic Calorimeter (FEMC). The smaller polar angles, essential for detecting electrons and positrons from two-photon processes and for luminosity measurements, were covered until 1994 by the Small Angle Tagger (SAT) and the Very Small Angle Tagger (VSAT). Later SAT was replaced with the Small angle TIle Calorimeter (STIC). In addition, scintillator systems are implemented in the barrel and forward regions for triggering purposes and in order to achieve complete hermeticity for high energy photon detection.

The iron return yoke of the magnet is instrumented with limited streamer mode detectors to create the HAdron Calorimeter (HAC) which serves also as filter for muons, which are identified in two drift chamber layers. In 1994 a layer of Surrounding Muon Chambers (SMC) was installed outside the end-caps to fill the gap between the barrel and forward regions.

Charged particle identification is provided mainly by liquid and gas Ring Imaging Cherenkov Counters (RICH) both in barrel and forward regions.

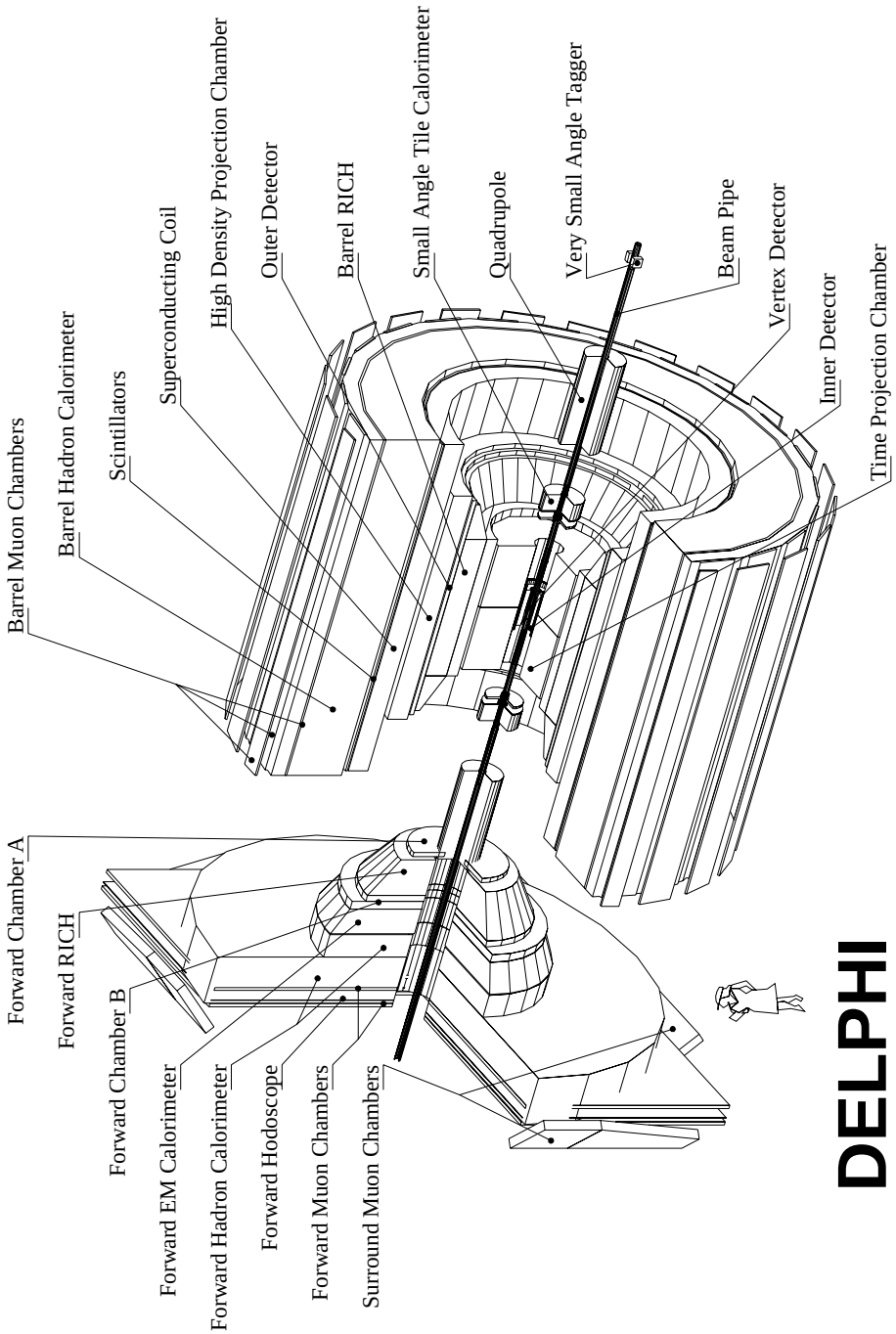

Figure 1.3: *The DELPHI detector layout*

1.2.1 Performance of the DELPHI detector

Tracking system

The tracking system consists of different sub-detectors which cover different space regions, have different performance and aims.

The **Vertex Detector** (VD) consists of three coaxial cylindrical layers of silicon strip detectors at average radii of 6.3, 9.0 and 10.9 cm. Each layer covers the full azimuthal angle in 24 sectors with overlaps between adjacent sectors. There are 4 detectors along the beam direction in each sector. For polar angles of $44^\circ \leq \theta \leq 136^\circ$, a particle crosses all three layers of the VD. At the start of 1994, the closer (w.r.t. beam pipe) and outer layers were equipped with double-sided silicon detectors, having strips orthogonal to each other on opposite sides of the detector wafer, giving measurements also in the z direction. The single hit precision of the VD is estimated to 7.6 μm for one layer in $R\phi$ plane and down to 9 μm along the z coordinate.

The **Inner Detector** (ID) consists of two main parts. The inner drift chamber of the ID has a jet-chamber geometry with 24 azimuthal sectors, each providing up to 24 $R\phi$ points per track between radii of 12 and 23 cm. Up to the beginning of 1995, for polar angles in the range $23^\circ \leq \theta \leq 157^\circ$, a track crossed a volume of the detector sensed by a minimum of 10 wires (now the polar angle acceptance changed to $15^\circ \leq \theta \leq 165^\circ$). Surrounding the jet-chamber, there were 5 cylindrical multi-wire proportional chambers (MWPC) layers with sense wires spaced by about 8 mm (192 wires per layer) and with circular cathode strips giving Rz information. The polar angle coverage was $30^\circ \leq \theta \leq 150^\circ$. In 1995 they were replaced with 5 cylindrical layers of straw tube detectors (192 tubes per layer) measuring $R\phi$ and having the same functionality. The polar angle acceptance increased to $15^\circ \leq \theta \leq 165^\circ$. For the old configuration (with which all the data used in this work have been taken), single wire precision of the parameters of the local track element are $\sigma(R\phi) = 50$ μm and $\sigma(\phi) = 1.5$ $mrad$. The two track resolution is about 1 mm. The z precision from a single MWPC layer for an isolated track varies from 0.5 to 1 mm depending on θ.

The **Time Projection Chamber** (TPC) consists of two end-plates, each of which is divided into 6 azimuthal sectors, each with 192 sense wires and 16 circular pad rows with constant spacing. The detector thus provides up to 16 space points per particle trajectory at radii of 40 to 110 cm between polar angles of $39^\circ \leq \theta \leq 141^\circ$. At least three pad rows are crossed down to polar angles of $20^\circ \leq \theta \leq 160^\circ$. The single point precision is 250 μm in the $R\phi$ plane and 880 μm in the Rz plane. The two-point resolution is about 1 cm in both directions. Distortions currently limit the precision on the track elements to about 150 μm in $R\phi$ and about 600 μm in z.

The **Outer Detector** (OD) consists of 5 layers of drift tubes, operated in the limited streamer mode, located between radii of 197 and 206 cm. Successive layers are staggered and adjacent modules of the 24 azimuthal sectors overlap, giving full azimuthal coverage. Three layers are equipped to read the z coordinate by timing the signals at the ends of the anode wires. The active length of the detector corresponds to polar angles of $42^\circ \leq \theta \leq 138^\circ$. The single point precision is $\sigma(R\phi) = 110$ μm, the precision in the z coordinate is $\sigma(z) = 3.5$ cm.

The **Forward Chamber A** (FCA) consists of three modules. They are mounted on

each end of the TPC at a distance from the interaction point of about 160 cm in $|z|$. A module consists of 2 staggered planes of drift tubes, operated in the limited streamer mode. There is a rotation of 120° between the wire orientations of the modules. The chamber covers polar angles of $11° \leq \theta \leq 32°$ and $148° \leq \theta \leq 169°$. The reconstructed track elements have precisions of $\sigma(x) = 290\ \mu m$, $\sigma(y) = 240\ \mu m$, $\sigma(\theta) = 8.5\ mrad$, and $\sigma(\phi)$ averaged over θ is 24 $mrad$.

The **Forward Chamber B** (FCB) is a drift chamber at an average distance of $|z| = 275\ cm$ from the interaction point. The chamber consists of 12 readout planes, coordinates in each of three directions rotated by 120° being defined by 4 planes. The sensitive area of the chamber corresponds to polar angles of $11° \leq \theta \leq 36°$ and $144° \leq \theta \leq 169°$. The precisions achieved on the parameters of the reconstructed track elements are $\sigma(x, y) = 150\ \mu m$, $\sigma(\theta) = 3.5\ mrad$ and $\sigma(\phi) = 4.0/\sin\theta\ mrad$.

The momentum precision of the tracking system in the barrel region, measured in $Z \rightarrow \mu^+\mu^-$ events, is

$$\sigma(1/p) = 0.57 \times 10^{-3}\ (GeV/c)^{-1}\ . \tag{1.1}$$

For the forward region the momentum precision is

$$\sigma(1/p) = 1.31 \times 10^{-3}\ (GeV/c)^{-1}\ . \tag{1.2}$$

Electromagnetic Calorimetry

The electromagnetic calorimetry system of DELPHI is composed of a barrel calorimeter, the HPC, a forward calorimeter, the FEMC, and two very forward calorimeters, the STIC and the VSAT. The latter two are used mainly for luminosity measurement. There is no gap in angular coverage between the FEMC and the STIC. Supplementary photon taggers have been installed to cover the gap between the HPC and FEMC at $\theta \simeq 40°$ and the 90° and ϕ cracks in the HPC coverage (i.e. between the HPC modules) not already covered by the TOF, thus establishing complete hermeticity.

The **High Density Projection Chamber** (HPC) consists of 144 modules arranged in 6 rings inside the magnetic field. Each ring consists of 24 modules coaxially arranged around the beam axis with an inner radius of 208 cm and an outer radius of 260 cm. Each HPC module is a small TPC with layers of high density material in the gas volume. These layers are made from lead wires which serve not only as converter material, but provide the drift field as well. The total converter thickness is $18\ X_0/\sin\theta$. In each module there are 128 pads arranged in 9 rows. In the first row, nearest to the beam-spot, the pads are 2 cm wide, increasing to 8 cm wide in the last row. The reference point spatial resolutions achieved using electrons from $Z \rightarrow e^+e^-$ events are (for 45 GeV electrons) $\sigma(z) = 0.13\ cm$ in the innermost rings (smallest $|z|$), 0.22 cm in the middle rings and 0.31 cm in the outer rings. This corresponds to a nearly constant θ resolution of 0.6 $mrad$ for 45 GeV electrons. The apparent ϕ resolution for electrons is 3.1 $mrad$. The energy resolution obtained for 45 GeV electrons is about 6.5%. The linearity of the HPC energy response is monitored using neutral pions reconstructed with high precision from one photon converted before the TPC and one photon reconstructed in the HPC . The relative precision on the measured energy can be parametrized as $\sigma(E)/E = [0.043^2 + 0.32^2/E]^{1/2}$ (E in GeV) and the angular precisions for high energy photons are $\pm 1.7\ mrad$ in the azimuthal angle ϕ and $\pm 1.0\ mrad$ in the polar angle θ.

The **Forward Electromagnetic Calorimeter** (FEMC) consists of two arrays of 4532 Cherenkov lead glass blocks; the front faces are placed at $|z| = 284\ cm$, covering the polar angles $8^\circ < \theta < 35^\circ$ and $145^\circ < \theta < 172^\circ$. The blocks are truncated pyramids with inner (outer) face dimensions of 5.0×5.0 (5.6×5.6) cm^2 and depth of 40 cm, corresponding to 20 radiation lengthes. The energy resolution for Bhabha electrons used in calibration is 4.8%. The relative precision on the measured energy can be parametrized as $\sigma(E)/E = [(0.03 + 0.12/\sqrt{E})^2 + (0.11/E)^2]^{1/2}$ where E is in GeV. For neutral showers of energy larger than 2 GeV, the average precision on the reconstructed hit position in x and y projected to $|z| = 284\ cm$ is about 0.5 cm.

The **Very Small Angle Tagger** (VSAT) consists of four rectangular modules placed symmetrically at $z = \pm 7.7\ m$ around the elliptic beam pipe and fixed to the support of the superconducting quadrupoles. Each VSAT module contains 12 tungsten absorbers interspaced with 12 silicon planes for energy measurement. The dimension of the calorimeters are 3 cm along x, 5 cm along y and 24 radiation length (about 10 cm) along z directions. The angular acceptance of the detector is between 5 and 7 $mrad$ in polar angle and about 50° in azimuth. The energy resolution for Bhabha events is 5%.

The **Small Angle Tagger** (SAT) was functioning until 1994. It consisted of a pair of calorimeters which surrounded the beam pipe at $\pm 2300\ mm$ from the interaction point, a set of precise acceptance masks located in front of one of the calorimeters and a 2-plane silicone track detector located in front of the calorimeter which is opposite the masks. The calorimeter, covering polar angles from 43 to 135 $mrad$, consisted of alternating layers of lead sheets (0.9 mm thick) and plastic scintillating fibres ($\varnothing = 1\ mm$), aligned parallel to the beam. The tracker was installed in front of the calorimeter and consisted of 2 planes of large area silicon detectors at $z = 2030$, 2160 and 2300 mm with inner radius of 99.5 mm. The sensitive region extended from 43.3 to 120.3 $mrad$. The planes were composed of 3 rings of 300 μm thick silicon-strip detectors with 39 radial strips per detector. Each detector covered a 5° azimuthal sector.

In 1994 the SAT was replaced by the **Small angle Tile Calorimeter** (STIC). The STIC is a sampling lead-scintillator calorimeter formed by two cylindrical detectors placed on either side of the DELPHI interaction region at a distance of 2200 mm, and covers a wider angular region between 29 and 185 $mrad$ in θ (from 65 to 420 mm in radius). The total length of the detector is 27 radiation lengthes. Each STIC arm is divided into 10 rings and 16 sectors, giving an $R\phi$ segmentation of 3 $cm \times 22.5^\circ$. At 45.6 GeV the energy resolution is $\sigma_E/E = 2.7\%$.

Hadron Calorimeter

The **Hadron Calorimeter** (HAC) is a sampling gas detector installed in the return yoke of the DELPHI superconducting solenoid. It is described separately in the Chapter 2.

Trigger

The DELPHI trigger system is composed of four successive levels (T1, T2, T3 and T4) of increasing selectivity. The first two trigger levels (T1 and T2) are synchronous with respect to the Beam Cross Over (BCO) signal. T1 is a loose preliminary trigger while T2 triggers the acquisition of the data collected by the front-end electronics. With a typical

bunch crossing interval of 11 μs, the T1 decision being taken 3.5 μs and T2 – 39 μs after the BCO. The dead-time introduced is then typically 3%, with 2% due to T1 and 1% to T2 for a typical readout time of 3 ms per event. The inputs to T1 are supplied by individual detectors, namely by the fast tracking detectors (ID, OD, FCA and FCB), by the scintillator arrays in the barrel region (Time Of Flight, TOF) and in the end-caps (Forward HOdoscope, HOF), by the scintillators embedded in the HPC, by the FEMC and by the MUB. In T2 these are complemented by signals from the TPC, HPC and MUF and combinations of signals from different sub-detectors are used.

T3 and T4 are software filters performed asynchronously with respect to the BCO. T3 halves the background passing T2 by applying the same logic as T2 but using more detailed information. It was implemented with the aim of maintaining the data logging rate below 2 Hz. T4 was implemented to reject about half of the background events remaining after T3.

Chapter 2

HAC Cathode Read-out

2.1 DELPHI Hadron Calorimeter

The DELPHI Hadron Calorimeter (see Appendix A) is an instrument to measure the energy of hadrons and hadronic jets. It was also expected to be able to distinguish muons from pions. The HAC is installed in the return yoke of the DELPHI superconducting solenoid. It is made of the barrel section covering polar angles between 42.6°–137.4°, and two end-caps between polar angles of 11.2°–48.5° and 131.5°–168.8° (see Fig. 2.1). The whole Hadron Calorimeter thus covers the solid angle of $11.2° < \theta < 168.8°$. The barrel is constructed of 24 sectors, with 20 layers of limited streamer mode detectors (Iarocci tubes) inserted into 18 mm slots between the 50 mm iron plates in each sector. The modularity of the end-caps is similar to the barrel, with a sampling depth of 19 layers. The detectors are wire chambers which consist of a plastic cathode forming 8 cells of 9×9 mm^2 with one anode wire in each. The inner surface of the cathode cells is coated with a poorly conductive graphite varnish. The 80 μm anode wires are made of copper-beryllium.

The calorimeter contains more than 19 000 limited streamer tubes (8 cm in width, and varying in length between 40 to 410 cm). They operate stably with relatively low i-butane content: Ar/CO_2/i-butane 10%/60%/30%. The limited streamer tubes are mounted on copper clad readout boards which are segmented into pads each covering a fixed angular region of $\Delta\phi = 3.75°$ and $\Delta\theta = 2.96°$. In the barrel part, five pads in the radial direction, called a tower (see Fig. 2.2), are read out together by the same electronic channel. In part (about 20%) of the end-cap, a tower is formed by seven pads, in the rest by four pads. The charge in each tower is integrated during 2 μs and afterwards digitised by an 8-bit ADC.

Muons produced in $Z \rightarrow \mu^+\mu^-$ decays are used for calibration. They have only 2% contamination from the $\tau^+\tau^-$ channel and give a clean sample of penetrating particles. Hadronic showers are also used to set the energy scale. The calibration for hadronic showers is checked using pions from single-prong τ decays that penetrate the electromagnetic calorimeter. In the barrel region ($52° < \theta < 128°$) the energy precision in the hadron calorimeter is found to be

$$\sigma(E)/E = \sqrt{0.21^2 + 1.12^2/E}$$

(with E expressed in GeV). The fixed term in this expression is due to the material

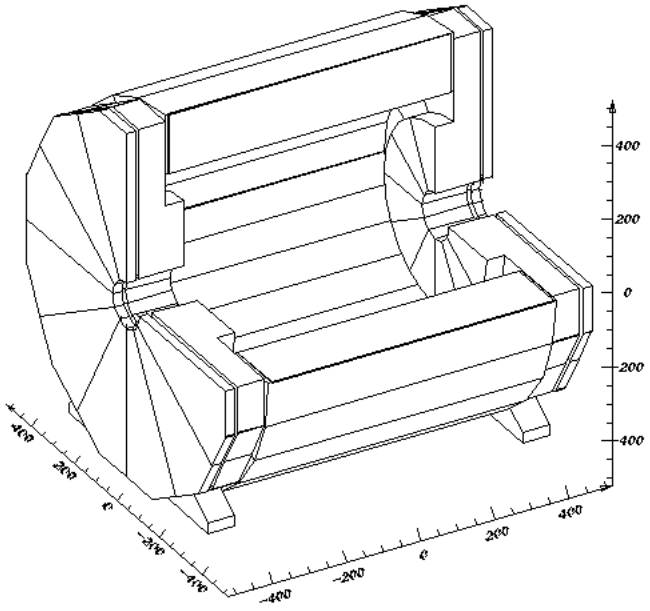

Figure 2.1: *DELPHI Hadron Calorimeter*

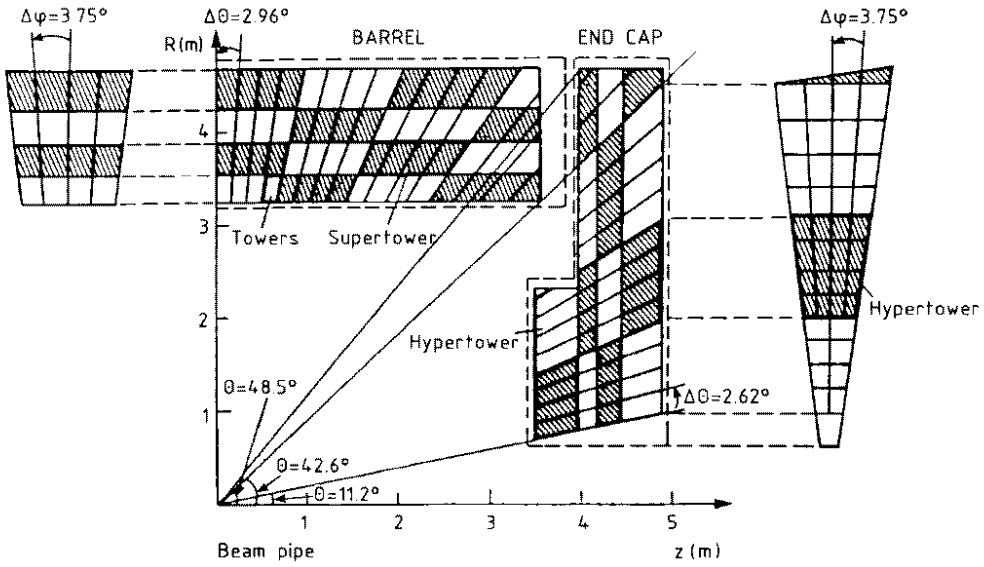

Figure 2.2: *Tower structure of readout for the hadron calorimeter*

located before the hadron calorimeter.

Before 1994 only the pads were read out, as described above. Recently it has been found possible to use streamer tubes cathodes as strips, providing thus better granularity and tracking abilities, by reading out the cathode signals of individual tubes. The simultaneous anode readout will be ready by the start of the LEP2 operation. It will involve not the single tube signal read-out, but the whole plane. It will provide fast signal which can be included in a trigger.

2.2 Cathode Read-out

The new cathode read-out system (Appendix B) is independent of the pad readout and improves the granularity in ϕ by a factor of 3 and in R by a factor of 5. It leads also to an improved energy resolution, better muon identification, a better pion/muon separation, improved detection of neutral long-lived particles, enhanced discrimination between neighboring showers and more precise hadron energy measurement. An example of the K_L^0 candidate seen in cathode read-out is shown in Fig. 2.7.

Due to the high resistivity of the cathode, the shape and the amplitude of the pulse is not really informative, thus only a 'yes/no' information being extracted.

2.2.1 Geometry

Hadron Calorimeter consists of four basic components: EA (*End-cap A*), BA (*Barrel A*), BC (*Barrel C*) and EC (*End-cap C*). With respect to the DELPHI coordinate system, EA and BA have the positive z coordinate ($90^\circ < \theta < 180^\circ$), while BC and EC – negative ($0^\circ < \theta < 90^\circ$).

Each of the components of the Hadron Calorimeter (EA, BA, BC and EC), consists of 24 modules (thus there are total of 96 modules). Further the following numbering conventions for modules will be used :

N°_{module}				
EA	BA	BC	EC	Location
1	25	60	84	$0^\circ < \varphi < 15^\circ$
2	26	59	83	$15^\circ < \varphi < 30^\circ$
3	27	58	82	$30^\circ < \varphi < 45^\circ$
4	28	57	81	$45^\circ < \varphi < 60^\circ$
5	29	56	80	$60^\circ < \varphi < 75^\circ$
6	30	55	79	$75^\circ < \varphi < 90^\circ$
7	31	54	78	$90^\circ < \varphi < 105^\circ$
8	32	53	77	$105^\circ < \varphi < 120^\circ$
9	33	52	76	$120^\circ < \varphi < 135^\circ$
10	34	51	75	$135^\circ < \varphi < 150^\circ$
11	35	50	74	$150^\circ < \varphi < 165^\circ$
12	36	49	73	$165^\circ < \varphi < 180^\circ$
13	37	72	96	$180^\circ < \varphi < 195^\circ$
14	38	71	95	$195^\circ < \varphi < 210^\circ$

15	39	70	94	$210° < \varphi < 225°$
16	40	69	93	$225° < \varphi < 240°$
17	41	68	92	$240° < \varphi < 255°$
18	42	67	91	$255° < \varphi < 270°$
19	43	66	90	$270° < \varphi < 285°$
20	44	65	89	$285° < \varphi < 300°$
21	45	64	88	$300° < \varphi < 315°$
22	46	63	87	$315° < \varphi < 330°$
23	47	62	86	$330° < \varphi < 345°$
24	48	61	85	$345° < \varphi < 360°$

Thus the angular size of a module is about $\approx 15°$.

In what follows, only the barrel part of the HAC will be considered. In the barrel each module is built of 20 planes of limited streamer mode tubes (planes are interlaced with iron layers, between planes $N°$ 18 and 19 there is a gap for muon chambers). Number of tubes in a plane varies form 9 in the first plane (closest to the beam axis) up to 13 in the very last plane :

plane $N°$	1	2	3	4	5	6	7	8	9	10	11	12	13	14	15	16	17	18	19	20
number of tubes	9	9	9	10	10	10	10	10	11	11	11	11	12	12	12	12	12	12	13	13

In total one module of the barrel part of HAC amounts 219 tubes.

Since all tubes are of the same width ($\approx 8.5\ cm$), gaps between them are inevitable. Each plane contains one gap of different size. Tubes are arranged in such a way that the probability of a track crossing more than one gap is as low as possible. The length of tubes is different and varies about the value of 350 cm in the barrel part, whereas edges of tubes adjoining end-caps have coordinates of $z = \pm 352.9\ cm$. In the middle part of the detector (i.e. $z \approx 0\ cm$), in the barrel side "A" edges of tubes in odd planes have coordinates $z \approx 0\ cm$, whilst in even planes – $z \approx 10\ cm$, in order to prevent dead spaces in the middle part of the detector (see Fig. 2.3).

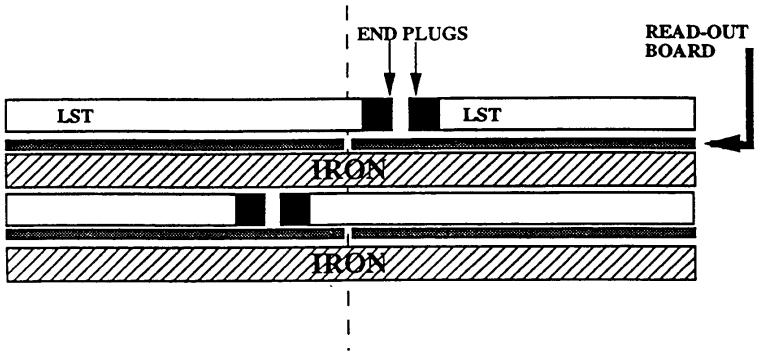

Figure 2.3: *Layout of Limited Streamer mode Tubes (LST) in the middle part of the DELPHI detector*

	Crate	Modules			
		$N°1$	$N°2$	$N°3$	$N°4$
BA	1	30	29	28	27
	2	26	25	48	47
	3	46	45	44	43
	4	42	41	40	39
	5	38	37	36	35
	6	34	33	32	31
BC	7	55	56	57	58
	8	59	60	61	62
	9	63	64	65	66
	10	67	68	69	70
	11	71	72	49	50
	12	51	52	53	54

Table 2.2: *Crate numbering scheme.*

2.2.2 Data acquisition

The signal being read out from each tube cathode. Due to the high cathode resistivity, this signal bears only "yes/no" information. Thus it is only one bit per tube that gives the comprehensive event picture.

Signals from each modules being read out by means of four Input Cards (IC) (see Fig. 2.4) : first card reads and transfers information from planes $1 \div 6$, second – $7 \div 11$, third – $12 \div 15$ and fourth – $16 \div 20$. Every IC transmits 64 bits of information, total of $4 \times 64 = 256$: more then enough for 219 tubes.

Every four modules are joined to one crate. By the time of writing, crates were numbered only in the barrel part – six crates for each BA and BC. Inside a crate modules have the local numeration scheme from 1 to 4. Correspondence between the local and global numerations is shown in the Table 2.2.

Information from each IC arrives in two Input Pages (IP). IP's are separated in time and each contains 32 bits. This information being received by the four ports of Octopus input/output fastbus card [5] in 8 bits per port. Empty IP's (those without "yes" bits) are suppressed, thus number of IP's transmitted from one module is usually less than eight ($8 = 4$ IC $\times$ 2 pages). Every crate finishes the transmission with control and status words.

Thus the decoding procedure have the following steps :

1. Split data words sample into 4 groups according to Octopus's port number.

2. It is known that data being transmitted in order with number of crate increasing ($1 \div 12$), inside a crate – with number of module increasing ($1 \div 4$, see also Tab. 2.2), and inside a module – with number of IC increasing ($1 \div 4$). They are split in four parts since there are four input ports. Thus it's necessary to regroup data in words of $4 \times 8 = 32$ bits. Meanwhile it should be taken into account that the highest bit comes to a port first, and of all ports the one with lowest number gets the

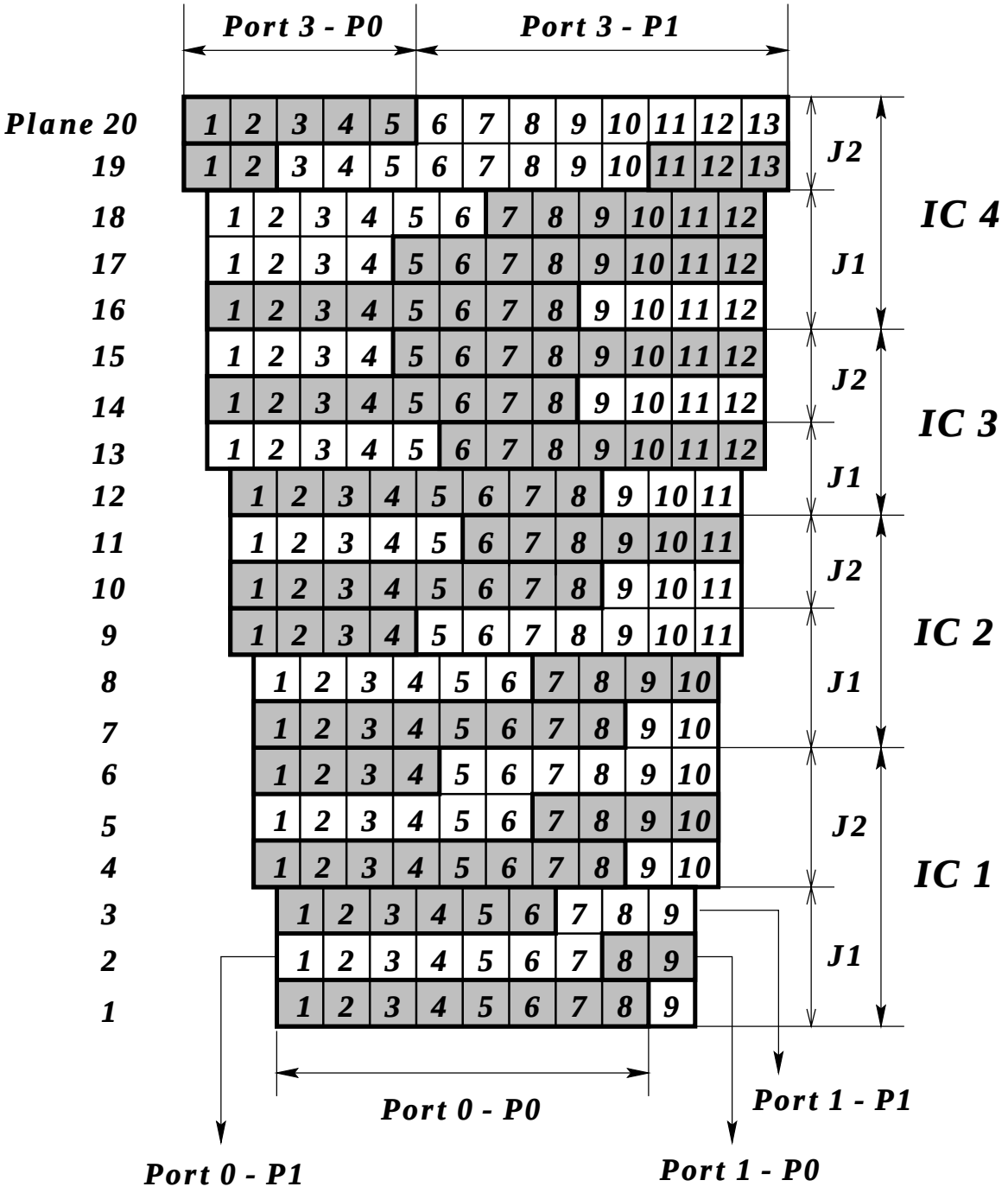

Figure 2.4: *One module information read-out scheme*

information first. Therefore in order to reconstruct the first IP of information, one should construct a 32-bit word according to the following scheme : lowest 8 bits are highest 8 bits from the port N° 1, next 8 bits – highest from the port N° 2 and so on. To reconstruct the second IP one should combine in the same order lowest 8 bits from each port.

3. The obtained array of 32-bit words (each of them represents one IP, or half of IC) is split by control and status words to groups by number of crates. Per each crate there are two control words which contain, for example, crate number information (it is written explicitly in four lowest bits of both words), and also one 64-bit status word, split in two 32-bit parts. Thus the next step of decoding is to find out such groups of control words and to define a crate number and status information. Status information is written in 32 bits of the status word and consists of one bit per IP : 2 IP$\times$4 IC$\times$4 modules = 32. Those of status bits switched to "yes" position point out IP's with non-zero information (otherwise IP is suppressed and no information being received from it).

4. For the final decoding stage the table showing the correspondence between a tube number and a bit in an IP is needed. In other words, it is a table of $32 \times 8 = 256$ entries (some of them are empty, for there are only 219 tubes per module). As a result one can obtain a comprehensive picture of hit in an event tubes : module position, plane position and the position of a tube in a plane.

2.2.3 Preliminary analysis

It is possible to get an important information about the detector performance already on the decoding stage. The simplest but the most important one is the information about tubes occupancy. Filling the histogram with counts in every tube in every layer (Fig. 2.5), one can get a plot which allows to monitor switched-off, malfunctioning or noisy tubes. White rectangles at Fig. 2.5 show switched-off tubes and planes, while black rectangles indicate noisy tubes. Occupancy plot can serve as the first check of the reliability of the decoding procedure, since positions of switched off planes can also be defined with other monitoring methods and a match can be made. Moreover, knowledge of tubes occupancy is very important during the electronics threshold tuning.

Another important information is the efficiency of streamer tubes. For every track the minimal number of traversed planes is known (the last hit layer), and the ratio of hit tubes number to this maximal possible number gives the estimation of internal efficiency of the detector. The most interesting figure is dependence of such an efficiency on the polar angle θ of a track (it could be defined using the general hadron calorimeter information). Since for tracks with $\theta \simeq 90^\circ$ the drift time of a signal is considerably big (the signal being read out from the opposite edges), and also because there are significant gaps in that angular zone, one must expect quite a strong decrease in efficiency for such a values of θ (see Fig. 2.6).

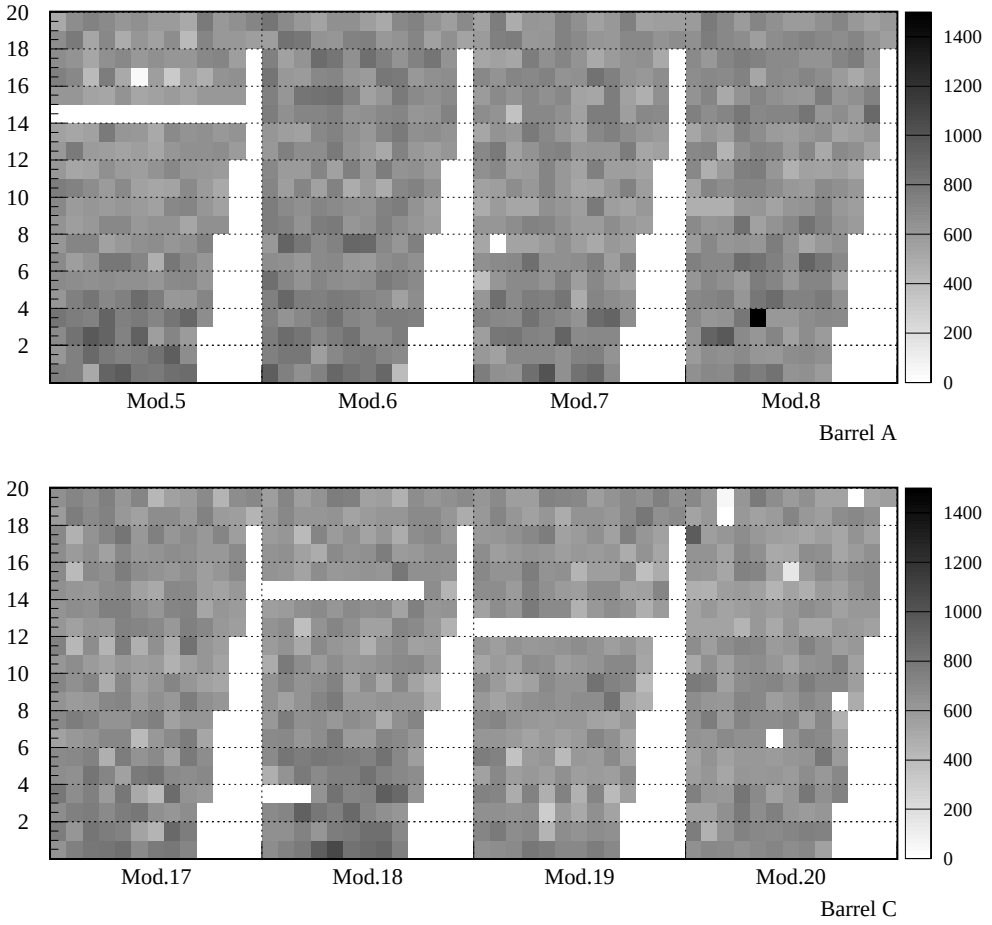

Figure 2.5: *Tubes occupation chart. For each module, integrated number of hits in every tube is shown.*

2.2.4 Results presentation

As it was noted before, using the detector database it is possible to define coordinates of every hit in an event streamer tube. For considerably good definition of a coordinate it is enough to know the space coordinates of the module, the radii of every plane, number of tubes per plane and also the gaps (dead zones) positions. The simplicity of the presentation stems mainly from the two-dimensional picture of the Cathode Read-out event with two coordinates being radius R of a plane and azimuthal angle of a tube ϕ. The natural way is to plot the picture in those polar coordinates. Such a possibility exists in almost every graphical package, including HIGZ [6] and its realisation in PAW [7]. Using the PAW, first pictures of the Cathode Read-out events were plotted, see for example Fig. 2.7.

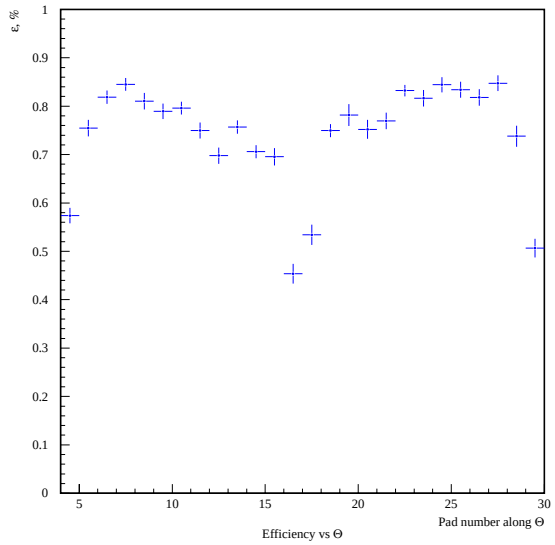

Figure 2.6: *Efficiency as function of the HAC pad number (along θ)*

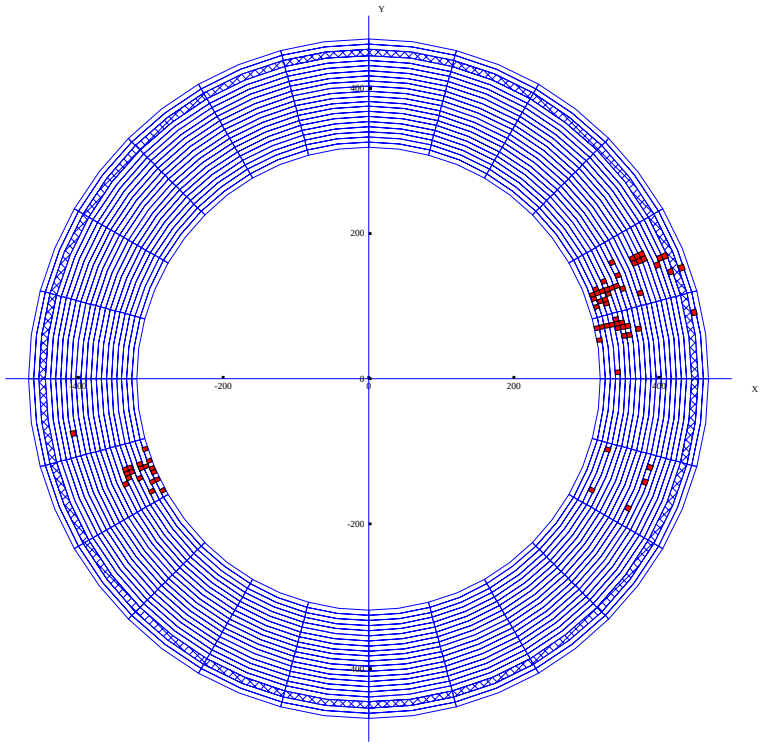

Figure 2.7: *Example of a K_L^0 candidate decay seen in Cathode Read-out of the DELPHI Hadron Calorimeter.*

Chapter 3

QCD and Hadronic Z^0-Decays

The modern understanding of the structure of matter is heavily based on the high energy physics experimental results. After observing in the late 1960's scaling in deep inelastic electron scattering experiments at SLAC, the idea of strong interacting partons arose. Further, processes like e^+e^- annihilation into hadrons and inclusive high $p_\perp$ hadron production in hadron-hadron collisions confirmed early phenomenological parton models [8].

The partons matched very well with the simultaneously developed theory of quarks, which are the building blocks of mesons and baryons. With introduction of the concept of colour as an additional quark quantum number, analogical to an electric charge in electromagnetic interactions, in 1970s the theory of Quantum Chromodynamics (QCD) was formulated in analogy to Quantum Electrodynamics (QED) as a gauge theory which describes strong interactions between quarks via exchange of massless bosons, the gluons. Since the colour charge is assigned to every quark, gluons must themselves be coloured; they are in fact bicoloured objects. For three different colours there are eight different gluons instead of a single photon in QED. Since the gluons themselves carry a colour charge, they can directly interact with other gluons.

The theory of QCD considers three basic vertices (see Fig. 3.1) : a quark-gluon vertex (a), a three-gluon vertex (b) and a four-gluon vertex (c). While the quark-gluon coupling is similar to an electron-photon coupling in QED, three- and four-gluon couplings are

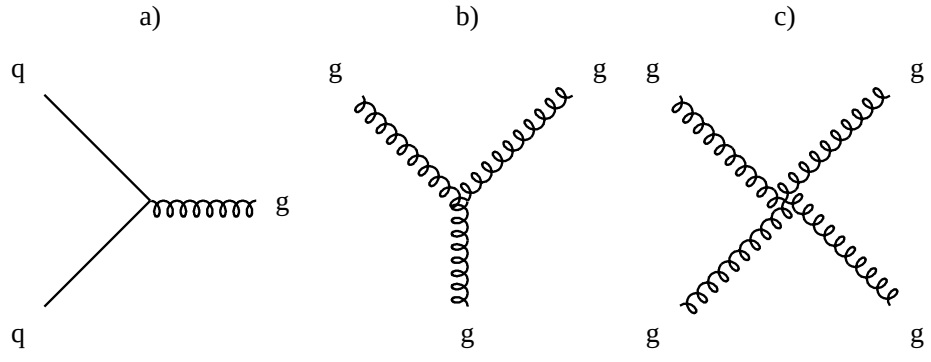

Figure 3.1: *Fundamental QCD couplings: a) quark-(antiquark-)gluon vertex, b) three-gluon vertex, c) four-gluon vertex.*

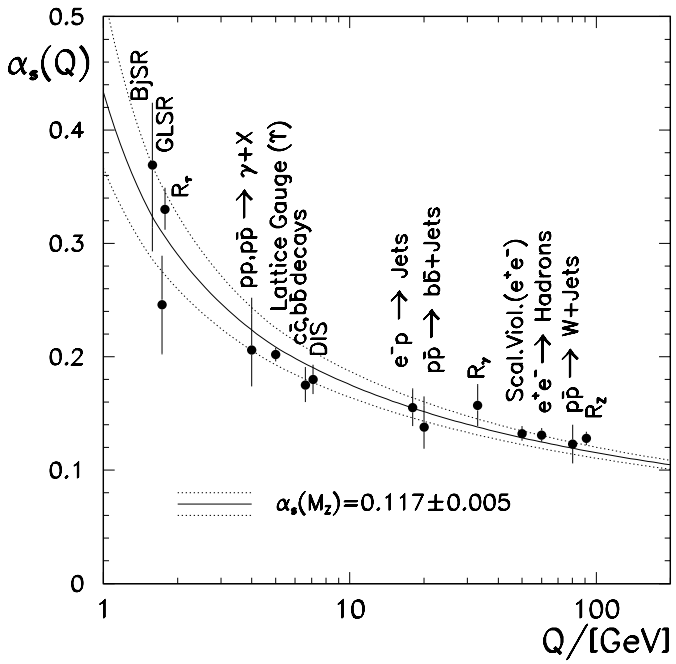

Figure 3.2: *Different α_s measurements compared to the QCD prediction based on the averaged value of $\alpha_s(M_Z) = 0.117 \pm 0.005$.*

specific for QCD and reflect its non-Abelian structure. Analogously to QED, all these couplings are described with the coupling constant of the strong interaction, α_s. More precisely, α_s is not a constant, but depends on the energy transfer scale, Q^2, being called therefore the "running constant". Taking into account only fundamental couplings, the running of α_s can be expressed by the formula :

$$\alpha_s(Q) = \frac{12\pi}{(33 - 2n_f)ln(Q^2/\Lambda^2)} \ , \tag{3.1}$$

were n_f is the number of quark flavours, involved in the interaction, and Λ is the QCD scale, which sets a boundary between the quasi-free partons and hadrons. At short distances, or large Q^2, the strong coupling constant is sufficiently small to treat quarks and gluons as almost free particles. This is known as the "asymptotic freedom" behaviour. At large distances, or at $Q^2 \rightarrow 0$, α_s diverges, which is the consequence of the anti-screening of the bare QCD charges, produced by the vacuum polarisation effects. In the framework of QCD, this is the reason why quarks can not be observed as free particles, but always have to confine inside hadrons. The running of the $\alpha_s(Q)$ is illustrated in Fig. 3.2 by comparing measurements of the strong coupling constant at different energies.

In high energy processes involving a large momentum transfer, one can factorise the process in two basic stages. First stage involves only hard interactions and is calculable using *perturbative* QCD [9]. Second stage includes quark confinement and requires detailed nonperturbative information as to how hadrons are built out of quarks and gluons. The parts of hard processes involving nonperturbative physics are not energy dependent and can be used in one process after having been measured in another one.

The aim of perturbative QCD is to describe quantitatively the structure of multipartonic systems produced by QCD cascades in order to gain a knowledge about confinement from comparing the calculable characteristics on quark-gluon level with measurable quantities of final hadronic states in hard processes.

Electron-positron annihilation at high energy is the simplest and most fundamental deep inelastic process. The Z^0 boson produced in e^+e^- annihilation is not only an ideal laboratory to study electroweak interactions, but it also permits precision measurements of strong interactions by studying QCD corrections to the well defined initial state of a Z^0 decaying into a quark-antiquark pair. Perturbative QCD predicts corrections which evolve as $1/ln(Q)$ whereas non-perturbative effects are expected to scale with $1/Q$. Thus the LEP centre-of-mass energy of 91.2 GeV allows indeed precise tests of perturbative QCD. Moreover, e^+e^- annihilation is a "clean" process in the sense that leptons (rather than hadrons, which are complex structures made of partons) appear in the initial state. This makes it easier to interpret the data both from experimental and theoretical points of view. The initial state is perfectly known, and there are a number of quantities which do not depend on details of formation of the final state hadrons. These quantities, e.g. the total cross section or various jet related correlations, can be calculated in QCD as a function of a single parameter Λ. Because of this, the various QCD tests at electron-positron colliders can be regarded as experiments for the determination of α_s.

However, tests of QCD are connected with certain complications. In QED, the interactions are so weak that the perturbation theory is almost always reliable. Fields in this theory are at the same time observable particles, like leptons. QCD, on the contrary, is the theory of invisible partons, which exist in the real world only as the components of hadrons. That means that the direct observations of subjects of the theory is impossible. Moreover, perturbative methods can only be applied in the region, where the asymptotic freedom can be reached. Therefore, the hadronic final state can not be accurately predicted by perturbative QCD. Distributions in infrared safe variables can be calculated as a power expansion in the strong coupling constant, but for every particular case a different appropriate technique must be applied to avoid possible divergence. Another complication is that in many cases it is impossible to calculate physical quantities in the necessary order of the perturbative expansion, required to meet experimental accuracy. Power expansions in strong coupling constant are often known only to leading orders, which presumes that contribution from higher order terms is negligible. However, this is not always true, which means that the experimental data, that contain contributions of all orders, might not be adequately described by the theory.

3.1 Parton Fragmentation Phenomenology

The basic scenario of a hadronic Z^0 decay is depicted on Fig. 3.3. The common approach is to divide the whole process into four stages:

1. On the first stage, electron and positron annihilate to a virtual photon γ^* or Z^0 boson. Electron or positron can emit a photon before the annihilation (so called initial state radiation), thus reducing effective centre-of-mass energy Q and producing a virtual photon or an off-shell Z^0 boson in the annihilation. The resulting virtual

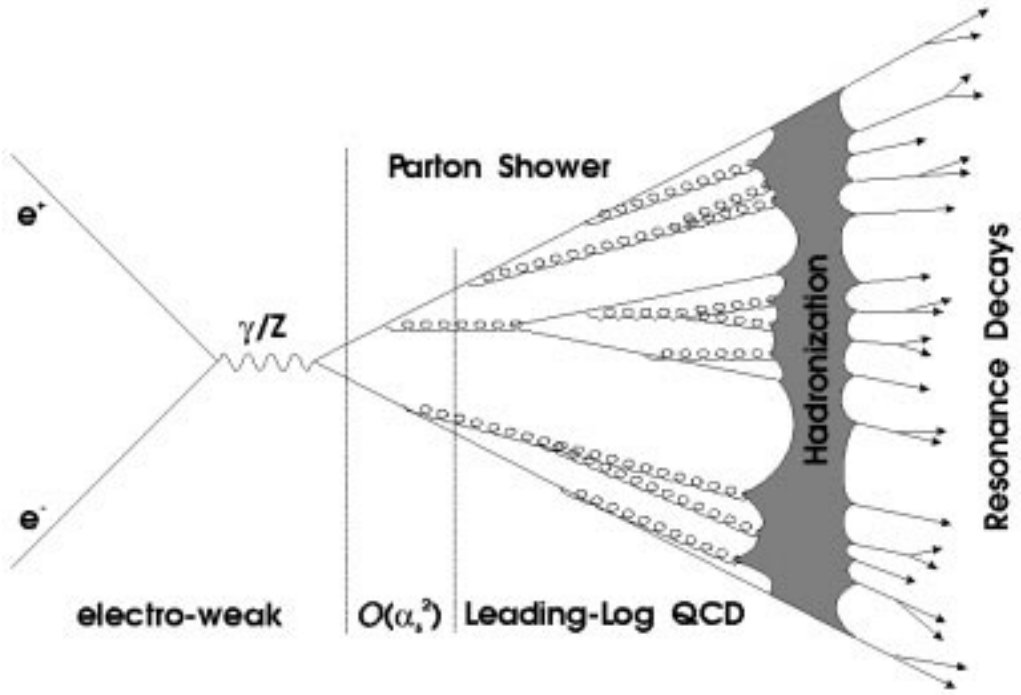

Figure 3.3: *Scheme of the e^+e^- annihilation process.*

boson produces primary quark-antiquark pair: $e^+e^- \rightarrow q\overline{q}$. This stage is described by the electroweak theory.

2. On the second stage, the primary partons radiates gluons, which can decay in quarks or gluons themselves, producing thus multi-parton cascades or showers. To describe this phase, the perturbation theory must be used. Period of shower development is characterised by scales t such that $Q^2 > t > t_0$. The showering cutoff scale, t_0, should be much greater than the QCD scale Λ^2 and should satisfy the requirement that a perturbative description of this stage remains appropriate down to this scale.

3. During the third stage, partons with virtual mass-squares of the order of t_0 do fragment in observable hadrons. This process is not perturbatively calculable, therefore phenomenological models are used to describe this phase. As long as this stage of the process involves only small momentum transfers, presumably of a magnitude set by the QCD scale $\Lambda \sim 250\ MeV$, the power corrections to observed quantities are expected to be determined by the two earlier stages of shower development.

4. On the last stage, nonstable resonances do decay in observable particles. This is where detectors being applied to register all possible particles and to reconstruct the primary process.

3.1.1 Parton Showers

The second stage of the Z^0 hadronic decay, namely, the development of the partonic cascade, can in principle be described consistently in the framework of the perturbative QCD.

However, full matrix element calculations become very complicated when it comes to high parton multiplicities. Therefore, the probabilistic *parton shower* approach is a convenient way to describe the evolution of the event. Within this approach, the evolution from two initial quarks to the higher parton multiplicities is described as consecutive branchings of the kinds $q \to qg$, $g \to gg$ and $g \to q\overline{q}$. Calculations of respective probabilities are usually performed in the Leading Logarithms Approximation (LLA), where only the leading terms in the perturbative expansion are kept. Higher order terms are usually taken into account as corrections, but mostly they are neglected, which proved so far to be a good approximation. The probability $\mathcal{P}_{a\to bc}$ that the branching of a kind $a \to bc$ will occur during a small change of the evolution parameter $t = ln(Q^2_{evol}/\Lambda^2)$ (Q^2_{evol} is the evolution scale) is given by the DGLAP [1] evolution equations [10] :

$$\frac{d\mathcal{P}_{a\to bc}}{dt} = \int dz \frac{\alpha_s(Q)}{2\pi} P_{a\to bc} \ , \tag{3.2}$$

where $P_{a\to bc}$ are the splitting kernels (assuming that the particle b takes fraction z of the four-momentum of a) :

$$\begin{aligned} P_{q\to qg} &= C_F \frac{1+z^2}{1-z} \ , \\ P_{g\to gg} &= N_C \frac{(1-z(1-z))^2}{z(1-z)} \ , \qquad (3.3) \\ P_{g\to q\overline{q}} &= T_R(z^2+(1-z)^2) \ , \end{aligned}$$

(3.4)

where $N_C = 3$ is the number of colours, colour factor $C_F = (N_C^2 - 1)/2N_C = 4/3$ and $T_R = n_f/2$ with n_f being the effective number of quark flavours. The actual probability that a branching took place, is the multiplication of Eq. (3.2) and the probability that the branching has not already happened,

$$\mathcal{P}_{no}(t_{max}, t) = exp\left(- \int_t^{t_{max}} dt' \frac{d\mathcal{P}_{a\to bc}}{dt'} \right) \ , \tag{3.5}$$

where t_{max} is the maximal allowed value of the evolution parameter t for parton a. Every parton produced in such a branching is allowed to branch in turn, unless the t is below certain t_{min} value.

Theoretical studies of corrections beyond LLA provide important contributions to phenomenological models. The most significant effects come from intrajet and interjet coherence [9] phenomenons.

Intrajet coherence manifests itself in the effect of the angular ordering of soft gluons emission. Presumably, the soft gluon in the reaction like $q_0 \to qg$ has such a big transverse wavelength, that it can not distinguish, whether it was emitted by the original quark q_0, or by the qg system. This implies the restriction on the emission angle of the gluons,

[1] DGLAP stands for Dokshitzer-Gribov-Lipatov-Altarelli-Parisi

emitted by the qg system in such a way, that these angles decrease in every consecutive branching. This leads to non-isotropic angular emission probabilities.

Interjet coherence deals with the angular structure of soft particle flows when three or more energetic partons are involved in a hard process. Here the particle angular distributions depend on the geometry and colour topology of the whole jet ensemble. It also implies requirement of proper azimuthal angles of branchings to be properly distributed. It is also one of the reasons why the jet definition at high energies is to great extent artificial.

Shower algorithms are implemented in many particle generators [11], and differ mainly in the interpretation of the evolution variables and scales, methods of inclusion of the angular ordering and other higher order effects and corrections.

3.1.2 Fragmentation and Particle Generators

The fragmentation process is so far a weak chain in the theory of QCD. It is not calculable in its framework (see Section 3.1), thus only phenomenological models can be used to reproduce the experimental data and possibly to predict as much as possible properties. As was mentioned above, existing particle generators do not differ strongly in the part of the partonic cascade development, but they are significantly different when it comes to the fragmentation models.

During the last decade, four distinguishable approaches arose. One is the hypothesis of *local parton-hadron duality* (LPHD) [9], which presumes that spectra of final state hadrons follow those of partons before hadronization, differing in some parameters, like normalization. This allows to use perturbative calculations for the partonic level to predict hadronic shapes. However, LPHD does not provide prescriptions for every fragmentation aspects, although it proved to be useful for some observables.

Other approaches, embedded in particle generators, are all of iterative and probabilistic nature, being based on few kinds of branchings, during each of them energy and momentum is shared between the products according to a given probability. Different flavour production is also based on the probabilities, since there are no QCD recipes for this matter. Here a short overview of the *independent fragmentation* and the *cluster fragmentation* models will be given, while the *string fragmentation* model will be described in more details, since it proved to be the most suitable for the LEP1 energies.

The independent fragmentation model (implemented, for example, in the COJETS [12] generator) is the simplest scheme for generating hadron distributions from those of partons. Each hadron is supposed to be produced independently. For each fragmenting quark, the counterpart is taken from a quark-antiquark pair, which is produced out of the vacuum. This procedure creates a meson with certain energy fraction z of the fragmenting quark. The leftover quark is allowed to fragment in the same way, until remaining energy comes to a predefined cutoff. Energy fraction z is distributed according to what is known as a *fragmentation function*. For gluon fragmentation, gluons are first split into a quark-antiquark pair, and then fragmentation continues in a standard way. Relative transverse momenta of the created $q\overline{q}$ pairs are given a Gaussian distribution. The width of this distribution is the parameter of the independent fragmentation model, along with ratios of quark flavours creation and vector to pseudoscalar meson production. Hence, the

model has very few parameters, which is rather suitable, and it gives a satisfactory description of features of two-jet and three-jet final states in electron-positron annihilation at lower than LEP1 energies. However, the independent fragmentation scenario needs many corrections, which arise from the presumption that the fragmenting parton always remains on mass shell. Also, it needs special procedure to neutralise the residual colour and flavour of the leftover parton. Yet another problem appears for the case of the very close jets : since each of them fragments independently, there will be no interference even between two absolutely collinear jets.

The cluster model, embedded in the popular HERWIG [13] generator, is based on the phenomenon of the preconfinement of colour, which is the property of the parton showering process. This implies that the pairs of colour-connected neighbouring partons have asymptotically Q^2-independent universal mass distribution, that falls rapidly at high masses. Therefore, it is straightforward to develop a cluster hadronization model, in which the perturbative phase of the jet development comes to the number of colour-singlet clusters, that decay into the observed hadrons. The simplest way to form such clusters is through non-perturbative splitting of gluons into quark-antiquark pairs. The mass distribution of clusters formed through such a splitting is also universal, and its form is determined by the QCD scale Λ, the parton shower cutoff and by the gluon-splitting mechanism. For the cutoff values of about 1 GeV^2, clusters can be treated as superpositions of meson resonances. Each such cluster usually is allowed to decay isotropically into a pair of hadrons. The angular distribution in e^+e^- three-jet events is successfully described, provided soft gluon coherence is taken into account on the level of the parton shower development by implementing the angular ordering of successive branchings.

The string model [14], implemented in the JETSET [15] generator of the e^+e^- annihilation events, is based on the lattice QCD studies, that suggest that the three-gluon coupling forces the colour flux lines, stretched between quark and antiquark, not to spread out as for the case of the electromagnetic field, but to be constrained to a comparatively thin tube-like region. Transverse dimensions of a tube are of typical hadronic sizes, about 1 fm. The colour field assumed to be uniform between two back-to-back quarks, in the sense that the amount of energy per length unit, κ, is constant, and also there are no concentrations of energy, transverse momentum or angular momentum along the field. This is a *linear confinement* picture, i.e., the energy stored in the colour field between a charge and an anticharge increases linearly with the separation between charges. The most suitable way of describing this linear confinement, is to use the dynamics of a massless relativistic string with κ being a string constant. Experimental measurements give the value of $\kappa \approx 1\ GeV/fm \approx 0.2\ GeV^2$.

As the quark and antiquark move apart, the potential energy in the string increases, leading to string breakups, which produce new quark-antiquark pair. The system consequently splits into two new strings, and if invariant mass of any is large enough, further breaks may occur. The process of string-breakings stops when only hadrons (mesons, for that matter) on their mass shell remain.

The important feature of the Lund string model is the mechanism of the quark-antiquark pairs creations at the string break-ups. In order to generate such pairs, the model invokes the idea of quantum mechanical tunneling. In terms of the transverse mass

$m_T = \sqrt{m^2 + p_T^2}$ of the produced quark, the probability of the pair to appear is given by

$$exp\left(-\frac{\pi m_T^2}{\kappa}\right) = exp\left(-\frac{\pi m^2}{\kappa}\right) exp\left(-\frac{\pi p_T^2}{\kappa}\right) \ . \tag{3.6}$$

The factorization of the p_T and m terms leads to the flavour-independent Gaussian spectrum for the transverse momentum of produced quark-antiquark pairs. Since quark and antiquark are produced with the opposite transverse momenta, the transverse excitations are locally compensated. The transverse mass of the final state hadron is made up out of p_T's of contributing quarks.

The formula (3.6) also implies a suppression of heavy quarks production. However, the suppression of the strangeness production is a free parameter of this model. Another free parameter is the ratio of pseudoscalar and vector mesons, to which neighbouring quarks and antiquarks are combined.

Gluon emission in the $q\overline{q}$ event is described as a kink on the string : the string is stretched between quark and antiquark via the gluon, thus the latter has two string pieces attached. The details become more complicated, but no new fragmentation parameters have to be introduced.

There are no special requirements on where to start the description of a string breaking. A fragmentation process described in terms of starting at the $\overline{q}$ end of the system and fragmenting towards the q should be equivalent to that described other way around. This constrains the allowed shape of fragmentation functions to the form of

$$f(z) \propto \frac{1}{z}(1-z)^a exp(-bm_T^2/z) \ , \tag{3.7}$$

where z is the fraction of the total light cone momentum, $E + p_L$, taken by a hadron. Parameters a and b are free and can be tuned to the experimental data.

An area which is not very well described by the string model is the baryon production. It can be described with the similar tunneling mechanism, allowing diquark-antidiquark pairs production at the string breaks. In this process, baryon and antibaryon ought to be produced close to each other, and share at least two quark flavours. Another mechanism is so-called "popcorn" production of quark-antiquark pairs, where the additional possibility of meson production between a baryon and antibaryon exists.

The Lund string model agrees very well with most of the LEP results, thus making JETSET the basic particle generator used by the LEP experiments, DELPHI in particular. However, this model has far too many free parameters, allowing, on the one hand, a fine tuning of the generator, but limiting, on the other hand, the predictive capacity of the model.

3.2 Fragmentation Functions

Studies of the processes with one hadron observed in the final state (so called inclusive processes) provide data for QCD tests. A schematic view of the inclusive one-hadron e^+e^- annihilation is shown on Fig. 3.4. Measuring properties of every single outgoing hadron, such as fractional momentum or azimuthal angle, one can obtain differential

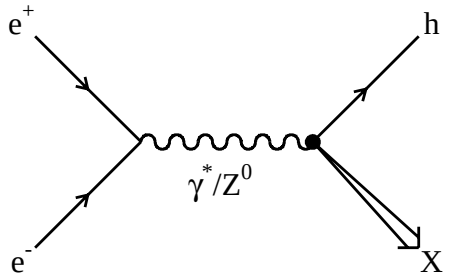

Figure 3.4: *Scheme of the inclusive hadroproduction in e^+e^- annihilation process. Properties of a hadron h are measured independently on remaining particles.*

cross sections of the process, which are strictly connected to the fragmentation functions. Fragmentation functions do reflect the processes of quarks confinement into hadrons. The formalism used to derive these functions is analogous to that used to describe the quark distribution inside hadrons, or structure functions.

In the simplest case, Z^0 boson decays to quark q and antiquark $\overline{q}$. Both q and $\overline{q}$ materialise in two back-to-back jets of hadrons, which can be registered by a detector. Measuring the fractional momentum of every hadron h, $x_p = p_h/p_q$, where p_h is the momentum of a hadron and p_q is the momentum of the quark, which can be replaced in the case of electron-positron colliders, like LEP, by the energy of the electron beam, E_{beam}, one can write down the corresponding differential cross section as

$$\frac{d\sigma^h}{dx_p} = \sum_q \sigma^q \left[D_q^h(x_p) + D_{\overline{q}}^h(x_p) \right] \ . \tag{3.8}$$

Here σ^h is the cross section of the inclusive hadroproduction process $e^+e^- \to hX$, σ^q is the cross section of the process $e^+e^- \to q\overline{q}$, and $D^h_{q(\overline{q})}(x_p)$ are fragmentation functions, which describe the transition of the quark, q, or antiquark, $\overline{q}$, to hadron in the same way that the structure functions describe how the hadron is built up of partons. They represent the probability that the hadron h is found in the quark (antiquark) jet carrying a fraction x_p of its momentum. The summation goes over all possible quark flavours. The physical meaning of the fragmentation functions implies

$$\sum_h \int_0^1 dx_p x_p D_q^h(x_p) = 1 \ , \tag{3.9}$$

which stems basically from the energy conservation law. Important feature of the fragmentation function is, that the integration of their sum gives the average multiplicity $\langle n_h \rangle$ of hadrons of type h:

$$\sum_q \int_{x_{p,min}}^1 \left[D_q^h(x_p) + D_{\overline{q}}^h(x_p) \right] dz = \langle n_h \rangle \ . \tag{3.10}$$

The total hadronic cross section is connected to the well-known cross section of the

reaction $e^+e^- \to \mu^+\mu^-$:

$$\sigma_{tot} = \sum_q \sigma^q = \sum_q 3e_q^2\sigma_0 \ , \tag{3.11}$$

where e_q is the fractional charge of a quark and σ_0 is the point-like cross section for $e^+e^- \to \mu^+\mu^-$,

$$\sigma_0 = \frac{4\pi\alpha_s^2}{3Q^2} \ . \tag{3.12}$$

The factor 3 in eq. (3.11) is from colour and the index q runs over the various flavors of quarks. The ratio of the differential cross section (3.8) and the total hadronic cross section, σ_{tot}, is an important function which is predicted to scale within the naive parton model :

$$F^h(x_p) = \frac{1}{\sigma_{tot}}\frac{d\sigma^h}{dx_p} = \frac{\sum\limits_q e_q^2\left[D_q^h(x_p) + D_{\bar{q}}^h(x_p)\right]}{\sum\limits_q e_q^2} \ . \tag{3.13}$$

Experimentally, the sum of $F(x_p) = \sum\limits_h F^h(x_p)$ over all hadrons is measured. Fragmentation functions $F(x_p, Q)$ for charged only hadrons measured by the TASSO [16] ($Q = 14\ GeV, 22\ GeV, 35\ GeV, 44\ GeV$) and the DELPHI ($Q = 91\ GeV$) experiments are shown on Fig. 3.5. Equation (3.13) suggests that, in spite of both σ_{tot} and $d\sigma^h/dx_p$ being dependent on the annihilation energy Q, their ratio, $F^h(x_p)$, is independent on Q. The scaling of fragmentation functions, however, is not perfect, as can be seen from Fig. 3.5. Gluon emission from quark or antiquark introduces *scaling violation*, making $F(x_p)$ dependent on Q^2 in such way, that $F(x_p, Q)$ increases at small x_p with increasing values of Q, but decreases at $x_p \approx 1$. Production of heavy quarks also contributes to scaling violation in the region of $x_p \lesssim 0.2$.

From the point of view of perturbative QCD calculations, radiation of gluons introduces corrections at higher orders of the strong coupling constant, α_s (Fig. 3.6 shows several examples of processes, contributing to QCD calculations at different orders of α_s). The phenomenon of scaling violation is predictable in the framework of perturbative QCD, and this is one of the main successes of the theory. The evolution of fragmentation functions is described by the DGLAP evolution equations [10] with the α_s being the parameter. Thus studies of the scaling violation can be regarded as experiments of extracting the value of the strong coupling constant, usually to the order of $\mathcal{O}(\alpha_s^2)$.

QCD predicts scaling violation in fragmentation functions of all partons, quarks and gluons. To test these predictions, a special technique which allows to distinguish between quark and gluon fragmentation functions, has been developed. In QCD calculations, it is convenient to split fragmentation functions into orthogonal components. In the paper [17], the definition of fragmentation functions in terms of the transverse and longitudinal cross sections in one-hadron inclusive electron-positron annihilation has been introduced. This definition is particularly convenient because it automatically preserves the energy-momentum sum rule for fragmentation functions. For the e^+e^- annihilation into an off-shell virtual boson of a spin 1, with unpolarised beams, the inclusive hadronic cross

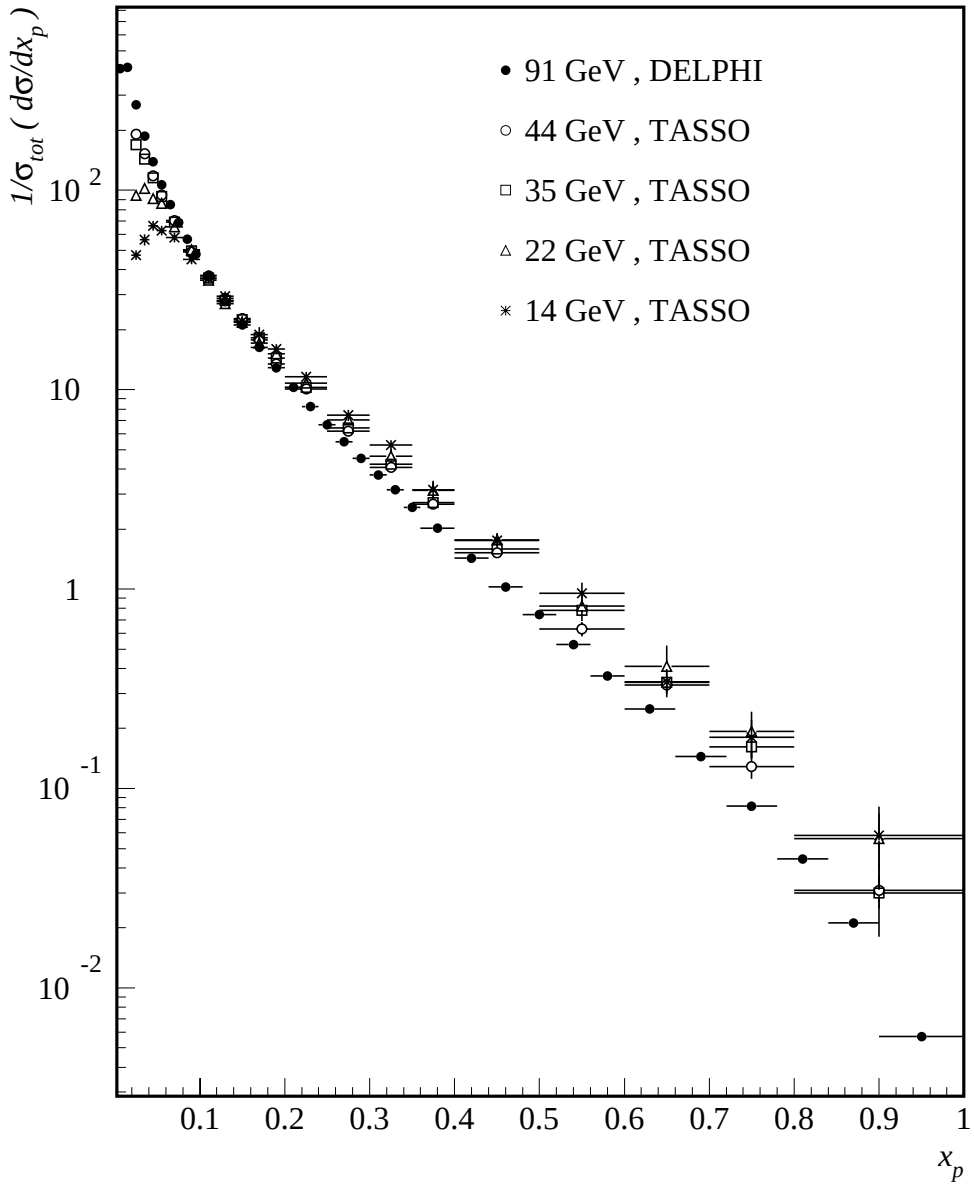

Figure 3.5: *Normalized differential charged hadrons cross sections as measured by the TASSO and DELPHI experiments at different center-of-mass energies.*

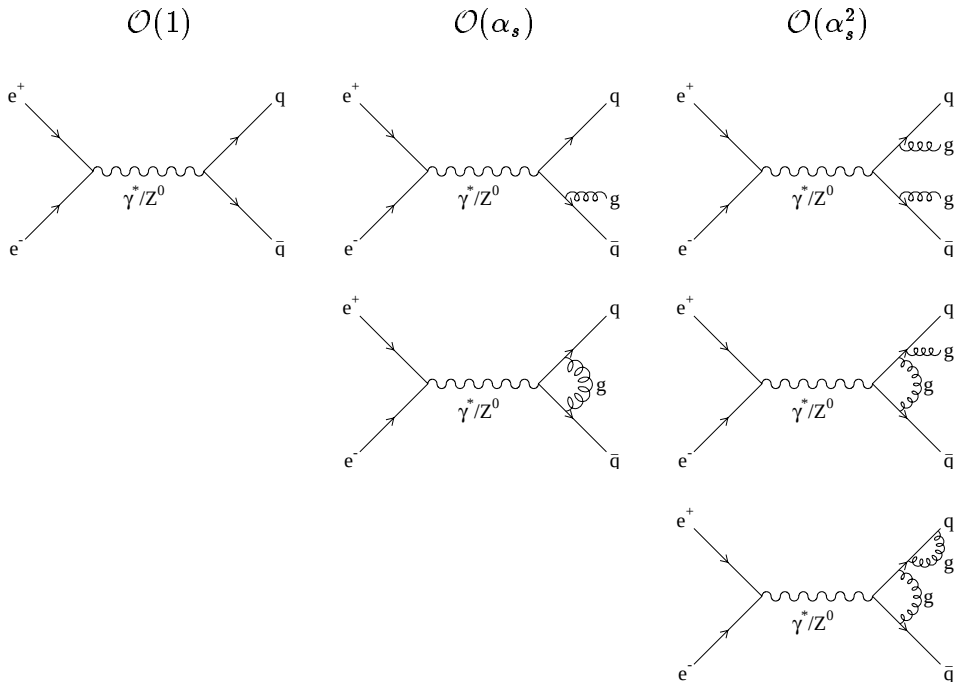

Figure 3.6: *Feynman diagrams representing processes at different orders of the strong coupling constant, α_s.*

section in angle and energy can be written as

$$\frac{d^2\sigma^h}{dx_p\, d\cos\theta} = \frac{3}{8}(1+\cos^2\theta)\frac{d\sigma_T^h}{dx_p} + \frac{3}{4}\sin^2\theta\frac{d\sigma_L^h}{dx_p}\ , \tag{3.14}$$

where θ is the angle of the outgoing hadron h with respect to the beam axis, and $d\sigma_T^h/dx_p$, $d\sigma_L^h/dx_p$ are the transverse and longitudinal components of the differential cross section, respectively. Evidently, after integration over the full angular range, one obtains

$$\frac{d\sigma^h}{dx_p} = \frac{d\sigma_T^h}{dx_p} + \frac{d\sigma_L^h}{dx_p}\ . \tag{3.15}$$

In the naive parton model ($\alpha_s \to 0$), the longitudinal component of the differential cross section equals to zero,

$$\frac{d\sigma_L^h}{dx_p} = 0 \quad \text{and} \quad \frac{d\sigma_T^h}{dx_p} = 3\sigma_0 \sum_q e_q^2 \left[D_q^h(x_p) + D_{\bar{q}}^h(x_p)\right]\ . \tag{3.16}$$

Proceeding beyond the zeroth order in α_s, corrections of order $\mathcal{O}(\alpha_s)$ give rise to nonzero contributions to $d\sigma_L^h/dx_p$ (see [17, 18]):

$$\frac{d\sigma_L^h}{dx_p} = 3\sigma_0\frac{\alpha_s C_F}{2\pi}\int_{x_p}^1 \frac{dz}{z}\left\{\sum_q e_q^2\left[D_q^h\left(\frac{x_p}{z}\right) + D_{\bar{q}}^h\left(\frac{x_p}{z}\right)\right] + \sum_q e_q^2 D_g^h\left(\frac{x_p}{z}\right)\frac{4(1-z)}{z}\right\}. \tag{3.17}$$

Being proportional to α_s, the longitudinal component $d\sigma_L^h/dx_p$ is connected by definition to the scaling violation effects, which are the main subject of QCD studies.

In formula (3.17), D_g^h appears to describe the gluon fragmentation function, since corrections of order $\mathcal{O}(\alpha_s)$ arise with gluon emission (see Tab. 3.6). From now on gluon fragmentation function enters, analogously with quark and antiquark fragmentation functions, into equations like (3.8), (3.10) and (3.13). The knowledge of the longitudinal component of the differential cross section gives therefore a possibility to extract the gluon fragmentation function, and the transverse component can be considered as a quark fragmentation function.

More generally, expression (3.17) can be written for all components of the fragmentation function as

$$\frac{d\sigma_P^h}{dx_p} = \sum_i \int_{x_p}^1 \frac{dz}{z} C_{P,i}(z,\alpha_s) D_i^h \left(\frac{x_p}{z}\right) \ , \tag{3.18}$$

where $P = T, L$; the sum on i runs over all types of partons (quarks, antiquarks and gluons), and $C_{P,i}$ are coefficient functions calculable in perturbative theory (they enter eq. (3.17) explicitly). This equation, together with eq. (3.9) implies that the corresponding contributions to the total cross section are

$$\sigma_P \equiv \frac{1}{2}\sum_h \int_0^1 dx_p \, x_p \frac{d\sigma_P^h}{dx_p} = \frac{1}{2}\sum_h \int_0^1 dz \, z C_{P,i}(z,\alpha_s) \ . \tag{3.19}$$

Important consequence of eq. (3.17) and eq. (3.19) is the fact that the integrated longitudinal cross section can be given as:

$$\frac{1}{2}\sum_h \int_0^1 dx_p \, x_p \frac{d\sigma_L^h}{dx_p} = \frac{\alpha_s}{\pi} 3\sigma_0 \sum_q e_q^2 \ , \tag{3.20}$$

while, on the other hand, the total cross section of the electron-positron annihilation into hadrons is well-defined in the massless theory and is given by [17]

$$\sigma_{tot} = 3\sigma_0 \sum_q e_q^2 \left(1 + \frac{\alpha_s}{\pi}\right) \ . \tag{3.21}$$

Hence the whole correction to σ_{tot} in order $\mathcal{O}(\alpha_s)$ can be ascribed to the longitudinal component of the differential cross section. Performing $\mathcal{O}(\alpha_s)$ calculations, the value of the strong coupling constant can be estimated to this order using the transverse and longitudinal components of the charged hadron cross section as [21]

$$\alpha_s = \pi \frac{\sigma_L}{\sigma_T} \ . \tag{3.22}$$

At high center-of-mass energies corrections in high orders α_s become significant, therefore analysis of the longitudinal component of the differential inclusive hadron cross section provides important precision test of QCD. A number of collaborations [19,20] performed

studies of this subject at energies, lower than Z^0 peak, and it was shown that the longitudinal component of the differential cross section is non-zero in the region of $x_p \lesssim 0.2$ and vanishes at big x_p. It was also shown [20] that the contribution of the $d\sigma_L/dx_p$ increases with Q of the e^+e^- annihilation increasing. The present work is aimed at studies of the $d\sigma_L/dx_p$ and corresponding QCD tests at the LEP energies, using the DELPHI experiment data.

3.3 Experimental tests of QCD

In order to extract longitudinal and transverse contribution to the differential cross sections experimentally, the formula (3.14) has to be rewritten, taking into account also the asymmetric contribution, normalising by the total hadronic cross section and making summation over all hadrons, as follows:

$$\frac{1}{\sigma_{tot}}\frac{d^2\sigma}{dx_p\, d\cos\theta} = \frac{3}{8}(1+\cos^2\theta)\frac{1}{\sigma_{tot}}\frac{d\sigma_T}{dx_p} + \frac{3}{4}\sin^2\theta\frac{1}{\sigma_{tot}}\frac{d\sigma_L}{dx_p} + \frac{3}{4}\cos\theta\frac{1}{\sigma_{tot}}\frac{d\sigma_A}{dx_p}\ . \qquad (3.23)$$

Following reference [21], transverse and longitudinal components of the fragmentation function are defined as

$$F_T \equiv \frac{1}{\sigma_{tot}}\frac{d\sigma_T}{dx_p}\ ,\ F_L \equiv \frac{1}{\sigma_{tot}}\frac{d\sigma_L}{dx_p}\ ,\ F_A \equiv \frac{1}{\sigma_{tot}}\frac{d\sigma_A}{dx_p}\ . \qquad (3.24)$$

There are different ways of extracting components of the fragmentation function from the measured double-differential hadronic cross section, as stems from eq. (3.23) :

(I) In the case of low statistics, the most acceptable method is to rewrite eq. (3.23), neglecting the asymmetric contribution, in the form

$$\frac{1}{\sigma_{tot}}\frac{d^2\sigma}{dx_p\, d\cos\theta} \sim 1 + A\cos^2\theta\ , \qquad (3.25)$$

where A is defined as follows:

$$A = \frac{F_T - 2F_L}{F_T + 2F_L}\ . \qquad (3.26)$$

Fit of the experimentally obtained distributions to the formula (3.25) with A being a free parameter was performed by the TASSO collaboration [20] at the center-of-mass energies of 14, 22, 35 and 44 GeV, and by the DELPHI experiment (see Appendix C) at $Q = 91.2$ GeV.

(II) Another method is to fit the experimental distribution directly to the form (3.23), treating F_T, F_L and F_A as free parameters. This analysis was done by the OPAL [23] and ALEPH [24] collaborations at LEP.

(III) For the case of high statistics and in order to estimate statistical errors on extracted components of fragmentation functions properly, the weighting method has to be

used. It bases on the fact of the orthogonality of the F_T, F_L and F_A. This means that every component enters the differential cross section with an appropriate weighting functions [21] :

$$F_P = \int_{-v}^{+v} W_P(\cos\theta, v) \left[\frac{1}{\sigma_{tot}} \frac{d^2\sigma}{dx_p\, d\cos\theta} \right] d\cos\theta \ , \tag{3.27}$$

where $P = T, L$ or A and weighting functions W_P are :

$$\begin{aligned} W_T(\cos\theta, v) &= [5\cos^2\theta(3 - v^2) - v^2(5 - 3v^2)]/2v^5 \ , \\ W_L(\cos\theta, v) &= [v^2(5 + 3v^2) - 5\cos^2\theta(3 + v^2)]/4v^5 \ , \\ W_A(\cos\theta, v) &= 2\cos\theta/v^3 \ . \end{aligned} \tag{3.28}$$

The variable $v = \cos\theta_{max}$ delimits the cosine of the angular range used in the analysis. The necessity in introducing this delimiter is caused by the fact that the detectors do not provide the full angular range acceptance, requiring thus appropriate compensations.

Following the energy conservation, the inclusive cross section satisfies the sum rule

$$\frac{1}{2} \int dx_p\, d\cos\theta\, x_p \frac{1}{\sigma_{tot}} \frac{d^2\sigma}{dx_p\, d\cos\theta} = \sigma_{TOT} = \sigma_T + \sigma_L \ , \tag{3.29}$$

where transverse and longitudinal cross sections are

$$\sigma_P \equiv \int_0^1 x_p F_P dx_p \ \ (P = T, L) \ . \tag{3.30}$$

If all outgoing particles are taken into account, σ_{TOT} equals to one, but since for this analysis only charged hadrons are used, this number is smaller.

The asymmetric component of the differential cross section, F_A, being summed over all the hadron species, equals to zero. However, it becomes distinguishable from zero when only positive or only negative hadrons are taken into account [22]. Thus, the asymmetry fragmentation function must be defined as

$$\tilde{F}_A = \frac{1}{\sigma_{tot}} \left(\frac{d\sigma_A^{h+}}{dx_p} - \frac{d\sigma_A^{h-}}{dx_p} \right) \ , \tag{3.31}$$

where $d\sigma_A^{h+}/dx_p \equiv F_A^+$ and $d\sigma_A^{h-}/dx_p \equiv F_A^-$, are the asymmetric components of the fragmentation function for positively and negatively charged hadrons, respectively.

An important quantity which can be calculated using fragmentation functions, is the average hadron multiplicity, in this case for charged hadrons only. It is given by the formula (see also eq. (3.10) :

$$\langle n_{ch} \rangle = \int dx_p \frac{1}{\sigma_{tot}} \frac{d\sigma}{dx_p} = \int (F_T + F_L) dx_p \ . \tag{3.32}$$

Knowledge of components of the fragmentation function gives the possibility to extract the gluon fragmentation function, D_g. Using next-to-leading order calculations, the longitudinal fragmentation function can be written as [17,18,21] :

$$F_L(x_p) = \frac{\alpha_s}{2\pi} C_F \int_{x_p}^{1} \frac{F_T(z)}{z} dz + \frac{2\alpha_s}{\pi} C_F \int_{x_p}^{1} \left(\frac{z}{x_p} - 1 \right) D_g(z) \frac{dz}{z} + \mathcal{O}(\alpha_s^2) \ . \tag{3.33}$$

The term $\mathcal{O}(\alpha_s^2)$ is not yet known and is assumed to be negligible. Various approaches could be used to solve this equation and to find out D_g. Omission of $\mathcal{O}(\alpha_s^2)$ suggests the formal solution which assumes *a priori* knowledge of the strong coupling constant, α_s, to the leading order, i.e., α_s^{LO}. Also it requires functions F_T and F_L to be defined with a very good precision. In practice, there are ambiguities in both cases. Experimental definitions of α_s at the Z^0 peak normally include contributions of higher orders, thus a special recalculation to the lower order must be used. Expression (3.22) can be used to estimate α_s^{LO} too, but as discussed in Appendix D, it is rather strong approximation. Also, even the high statistics, collected by the DELPHI experiment, can not provide the definition of the longitudinal fragmentation function precise enough in the whole x_p range. Therefore, the most convenient is the method suggested by OPAL [23] and ALEPH [24], where the gluon fragmentation function is parametrized in a way, similar to a standard fragmentation function parametrization. The F_L can be fitted then according to the formula (3.33).

The gluon fragmentation function $D_g(x_p)$ can be parametrized by the form [23,24]

$$D_g(x_p) = P_1 \cdot x_p^{P_2} (1 - x_p)^{P_3} e^{-P_4 \ln^2 x_p} \ , \tag{3.34}$$

where the P_i are free parameters of the fitting procedure. Exponential term is motivated by the Modified Leading Log Approximation [9], otherwise this parametrization is similar to that of eq. (3.7).

The strong coupling constant, α_s^{LO}, can be treated as yet another free parameter of the fit. Thus, this analysis can give results both on the behaviour of the gluon fragmentation function D_g and on the value of α_s^{LO}.

Assuming that the gluon fragmentation function does not depend on the quark flavour and neglecting corrections due to the heavy quark production, it is possible to estimate the $\mathcal{O}(\alpha_s^2)$ corrections to the eq. (3.33) by studying events with the different flavour contents, since it is known that the quark fragmentation functions are different for light and heavy quarks. This, however, is a superfine analysis which needs more data than was available during this analysis, therefore it is still the task for future studies.

Fragmentation function method can be used also for the charge asymmetry measurements [22]. The forward-backward asymmetry of the fermion pair production is connected to the electroweak parameter $\sin^2 \theta_W$ (θ_W is known as the weak mixing angle, or the Weinberg angle). Measurements of this asymmetry usually are performed either by the heavy flavour tagging, or by the charge asymmetry analysis. The latter is normally made using the jet charge definition procedures, which to big extent rely on the Monte Carlo simulations, being thus model-dependent.

Fragmentation function method can not so far provide direct measurements of the $\sin^2\theta_W$, but it is much less model dependent. The only assumption used in this approach is the existence of the valence dominance of the fragmentation functions at large values of x_p, in other words, at very large x_p one observes only hadrons, containing a primary quark. For instance, the π^+ can come only from a u or $\overline{d}$ quark, thus one can write [22] :

$$\frac{\tilde{F}_A^\pi(x_p)}{F_T^\pi(x_p)+F_L^\pi(x_p)} = \left(\frac{2v_e a_e}{a_e^2+v_e^2}\right)\frac{2a_u+v_u-2a_d v_d}{(a_u^2+v_u^2)+(a_d^2+v_d^2)}\ , \tag{3.35}$$

where a_f and v_f are axial and vector couplings of the fermions to the Z^0 boson respectively, defined as

$$v_f = I_3^f - 2e_f\sin^2\theta_W\ ,\quad a_f = I_3^f \tag{3.36}$$

with e_f the charge and I_3^f the third component of the weak isospin. Knowing this ratio, it is possible, in principle, to estimate the $\sin^2\theta_W$ value, although it requires the appropriate choice of the x_p, since the statistics at high x_p is particularly poor.

Analogously to the expression (3.35), expressions for other hadrons, like kaons or protons, can be written down. Obviously, the ratio $R = \tilde{F}_A/(F_T+F_L)$ will be different for different hadrons. Taking the average value of $\sin^2\theta_W = 0.23$, one can obtain [22] $R^\pi = -0.0375$ for pions and $R^p = 0.1373$ for protons. Therefore, it is of certain interest to test the behaviour of R for different hadrons.

3.3.1 Data samples

Data used in this analysis were collected by the DELPHI detector (see Section 1.2) in 1992–1993 running period at the centre-of-mass energies $Q = 91.2\ GeV$. Information collected by the detector was analysed by the DELANA [25], which is the main software for event processing, for raw data decoding, pattern recognition, track reconstruction and event tagging. The main output stream of this package is the post-processing data sets, called DST [26] for Data Summary Tapes. Physics analysis of the data from DST is performed with the help of the PHDST [27] input–output package.

Only charged particles in hadronic events were used. Tracks were taken into account if their impact parameter was below 5 cm in the transverse plane and below 10 cm along the beam axis, measured track length was above 50 cm, momentum between 0.1 GeV/c and 50 GeV/c and polar angle between 11° and 169°.

Hadronic events were then selected by requiring that they contain at least 5 charged particles with momenta above 0.2 GeV/c, the total energy of all charged particles exceeded 15 GeV (assuming the $\pi^\pm$ mass for particles), having at least 3 GeV in each hemisphere with respect to the sphericity axis, which polar angle was between 26° and 154°. The momentum imbalance was restricted to 20 GeV/c. About one million hadronic events were selected according to these criteriae.

For each track, its fractional momentum, x_p, and cosine of the azimuthal angle, $\cos\theta$, where measured. All particles assumed to be pions, unless specified explicitly. Typical double-differential distribution of charged hadrons in x_p and $\cos\theta$ is shown in Fig. 3.7.

The double-differential cross section suggests that the data must be split into bins both on x_p and $\cos\theta$ variables. In order to provide satisfactory statistics for analysis in

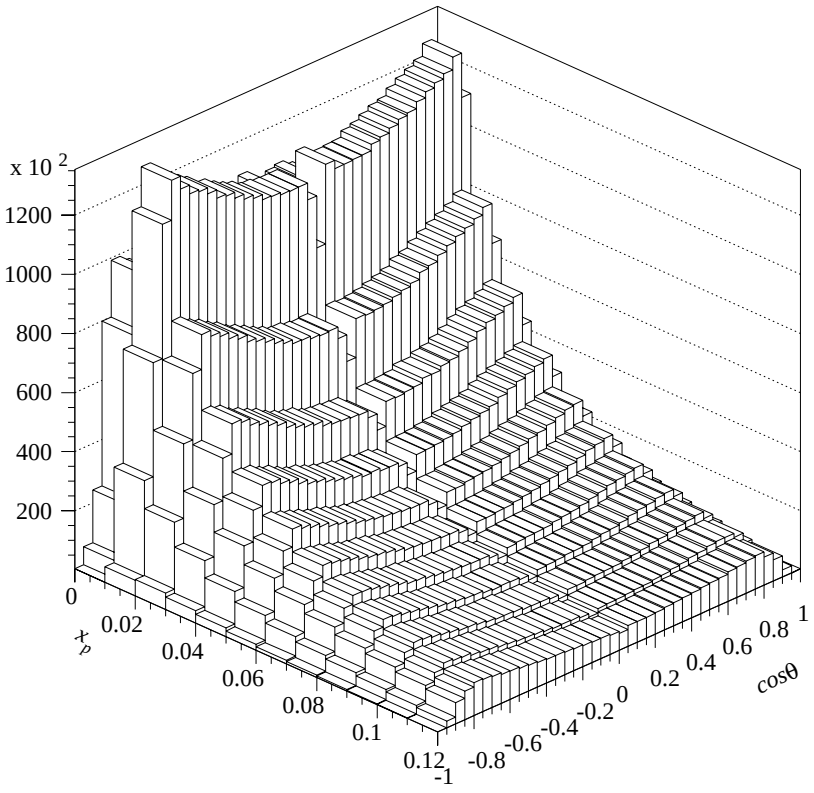

Figure 3.7: *Experimental charged hadrons distribution in x_p and* $\cos\theta$.

every bin, the range of $-1 < \cos\theta < 1$ was split in 40 equidistant bins, and the fractional momentum range of $0 < x_p < 1$ was split in 22 non-equidistant bins, having more frequent bining at $x_p < 0.2$ because of abundance of comparatively soft hadrons in the spectrum.

To correct raw data for the detector acceptance and efficiency, for the kinematical cuts and for the initial state radiation, the correction factor

$$C(x_p, \cos\theta) = \frac{f(x_p, \cos\theta)_{true}}{f(x_p, \cos\theta)_{reconstructed}} \tag{3.37}$$

for different bins of x_p were calculated. They are shown in Fig. 3.8 as a function of $\cos\theta$. The values of $C(x_p, \cos\theta)$ were obtained by analysing events generated with the JETSET 7.3 PS program [15] with parameters taken from the DELPHI tuning [29]. Here $f(x_p, \cos\theta)_{true}$ is the distribution obtained from the final state hadrons in generated events, and $f(x_p, \cos\theta)_{reconstructed}$ represents the same distribution after applying the DELPHI detector simulation [28], charged particle track reconstruction and hadronic event selection criteria.

Correction factors are not only a step in the physics analysis, but also reflect an important experimental philosophy. Since the aim of the whole experiment is to detect products of the electron–positron annihilation reaction, the detecting facilities must provide experimentalists with the most precise information on every possible particle.

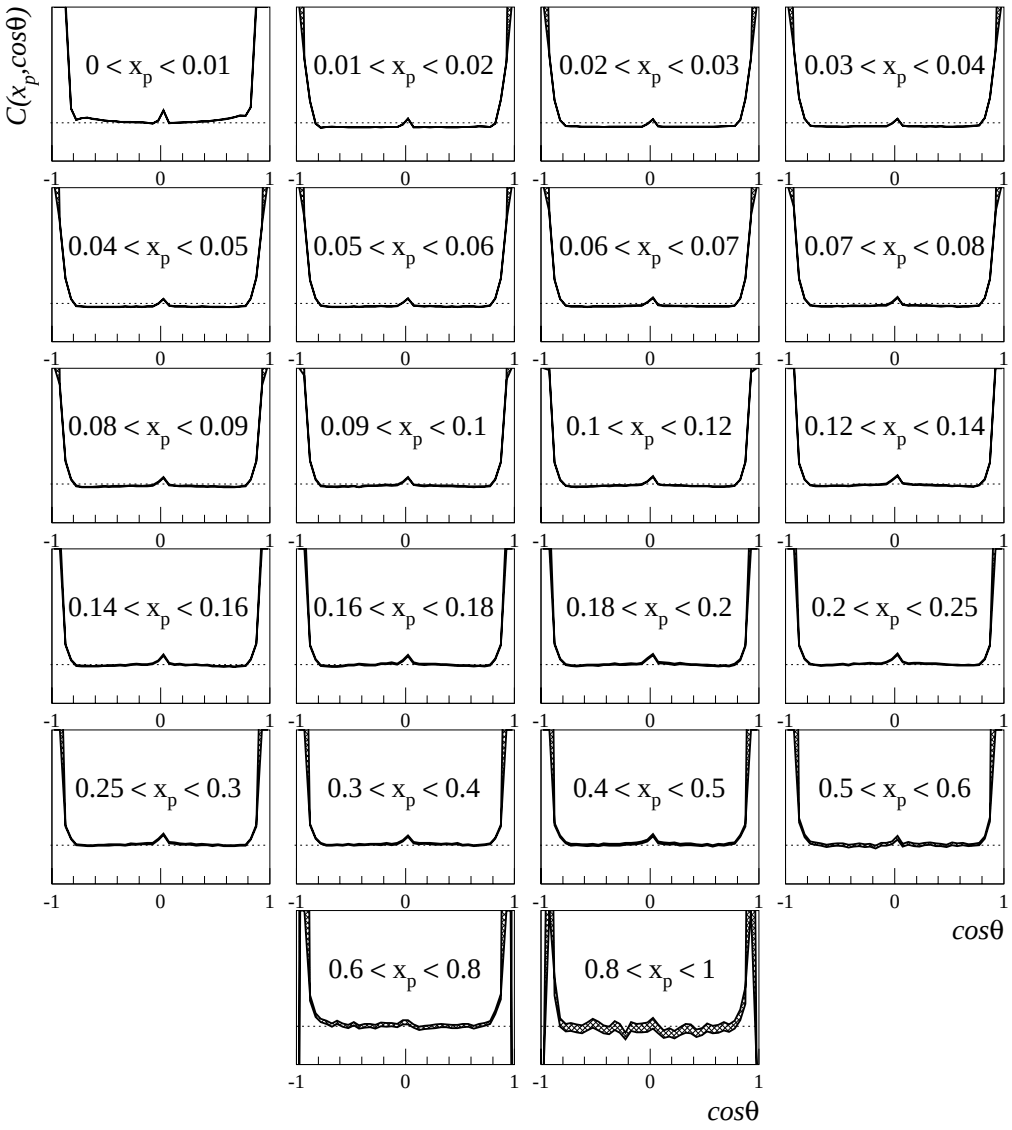

Figure 3.8: *Correction factors for the double differential charged hadron distributions. Dashed line indicates the unit.*

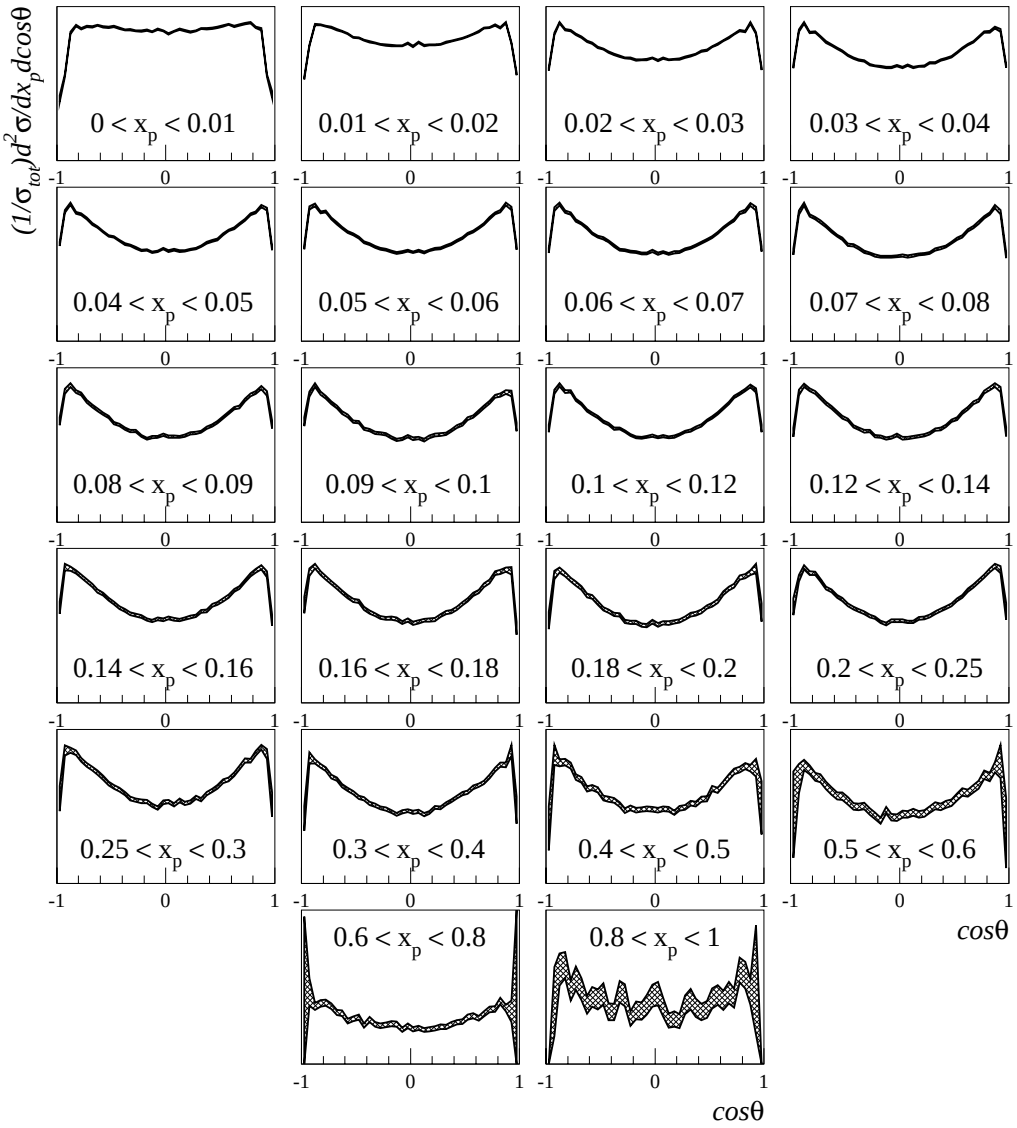

Figure 3.9: *Corrected double differential charged hadron distributions (showed to the scale).*

The whole analysis can be done only under assumption that the detector caught all the produced particles and did not induce fake tracks. Since such an ideal detector can not possibly exist, the knowledge of the effects, introduced by both hardware and software, is of great importance. To evolve this knowledge, the complete detector simulation package is needed, which is the DELSIM [28] for the DELPHI experiment. On the input of this package, any kind of Monte Carlo generated events must be directed. To test the capabilities of the detector, it does not really matter, which generator should it be. As long as correction factors for any distribution are independent of a chosen variable and equal to unity, one can conclude that detector performs satisfactory. However, it is important to have on input generated events as similar to the real events as possible, in order to be able to estimate backgrounds and corrections for every particular distribution, both inclusive and exclusive. The JETSET generator provides not only a very reliable model, but it has also a big number of parameters, which can be tuned to the experimental results. It reduces the predictive power of the model, but, on the other hand, makes the correction procedure more flexible. Even in this case, correction factors generally do not equal to unity in all the range of any variable. The consequence of this fact is that one is allowed to perform the analysis only in the range, were corrections are linear, or almost linear, and to avoid regions were correction factors change rapidly. For the case of Fig. 3.8, it is clear that any analysis can be done only in the region of $-0.8 < \cos\theta < 0.8$ (which is defined in this case by the geometry of the detector, see Section 1.2). Extension of the analysis to the region of $-0.9 < \cos\theta < 0.9$ is also allowed, but one has to be aware of the systematic uncertainties, introduced by such a choice.

Knowing that the correction factors are close to unity in almost the full angular range, one can take into account all the inefficiencies and backgrounds simply by multiplying experimental distributions by corresponding correction factors. The result, which is the input for the further analysis, can be seen at Fig. 3.9.

For the analysis of asymmetry, double-differential hadronic cross sections were built separately for negative and positive hadrons. Correction factors were calculated also independently for both negative and positive hadrons sub-samples, taking thus into account possible non-equivalent detecting of particles of opposite charges.

Quark flavour tagging

In e^+e^- annihilation at the Z^0 energy, five flavours of quarks can be produced, leading to basically different hadronic events, assuming that different quarks do have different fragmentation functions. Apparently, for the light quarks (u, d, s), this difference is negligible and experimentally indistinguishable. Events originated by heavy quarks, especially $Z^0 \to b\bar{b}$ events, can be separated using various techniques. One approach is to use leptons, produced at high transverse momentum with respect to the closest jet, as they come from B-hadron semi-leptonic decays. The disadvantage of this method is that it requires additional lepton identification procedures and correct estimates of the background contamination. Leptons coming from charm hadrons C usually are considered as a background in $b\bar{b}$ events tagging, since there are no effective enough methods to study $c\bar{c}$ production in Z^0 decays.

Another approach, widely used last years, is the lifetime tagging [30]. Because of the

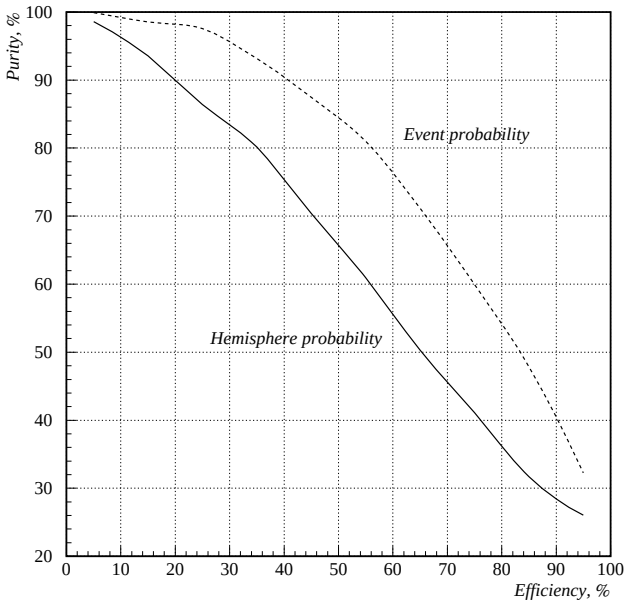

Figure 3.10: *Purity versus efficiency for the b quark events tagging, calculated with different probability cuts.*

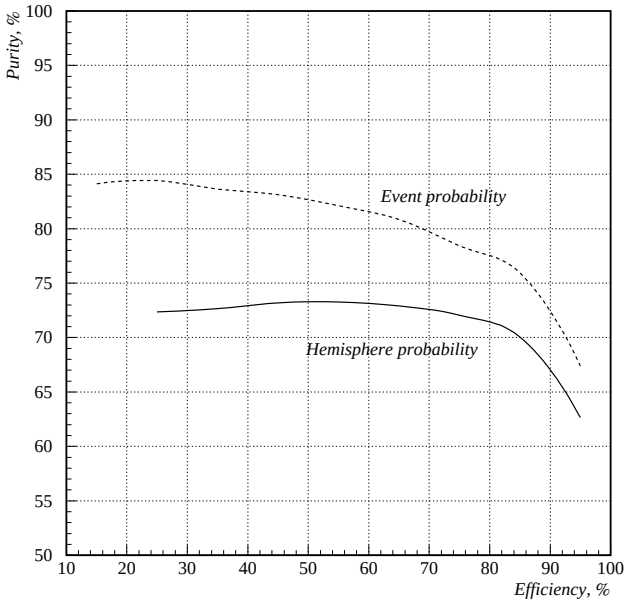

Figure 3.11: *Purity versus efficiency for the light (u, d, s) quark events tagging, calculated with different probability cuts.*

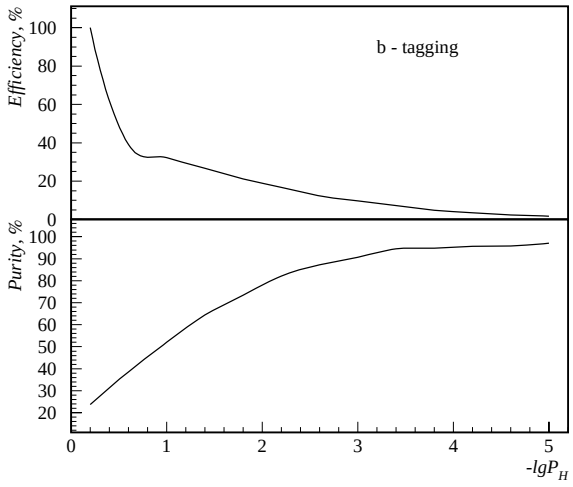

Figure 3.12: *Efficiency and purity for b quark tagging versus logarithm of inverse hemisphere probability P_H.*

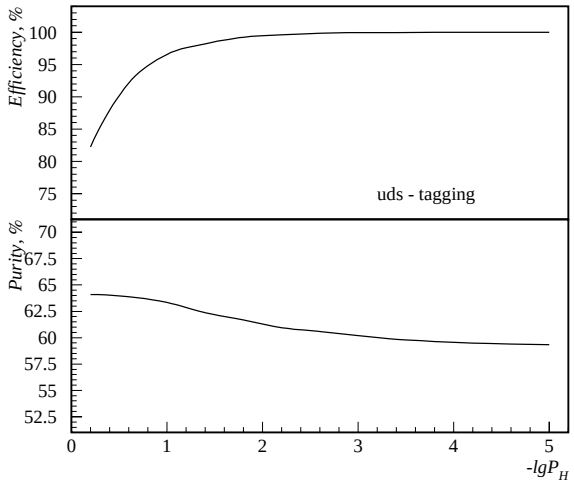

Figure 3.13: *Efficiency and purity for u, d, s quark tagging versus logarithm of inverse hemisphere probability P_H.*

comparatively big lifetime of B-hadrons ($\approx 1.58\,ps$ [31]) and high transverse momentum of their production, they can move apart from the primary vertex before decaying. Therefore, charged particles originating from B-hadrons decay have large impact parameters. This quantity can be used as the only tagging variable to separate events with b quarks. The DELPHI software includes the AABTAG [30] algorithm which performs the analysis of hadronic events and returns the probability P_N that N charged particle tracks in an event come from the primary interaction vertex. This probability is close to unit for light quark events and takes a rather small value for b quark events. Being calculated over all charged tracks in event, it gives the *event probability* P_E, and calculations over each hemisphere gives the *hemisphere probability* P_H.

Since there are no particular prescriptions for choosing one or another probability cut in order to select $Z^0 \to b\overline{b}$ events or light quark events, it is necessary to perform corresponding studies. For this analysis, they were done with the help of the JETSET generated event samples with the DELSIM detector simulation applied. Knowing the "real" flavour contents of an event and probabilities P_E and P_H, it is possible to calculate efficiency of the tagging and purity of the sample for each given probability cut.

In Fig. 3.10, purity of the tagged sample is shown as a function of the tagging efficiency for events that contain b quark. The hemisphere probability is being calculated for both hemispheres. However, due to the detector inefficiency and the fact that only charged tracks being taken into account, this probability is not necessarily equal in both hemispheres. Thus a P_H value used for flavour selection was taken for a randomly picked hemisphere to prevent possible correlations.

This plot reflects the disadvantage of the b quark lifetime tagging : to obtain a pure sample of $Z^0 \to b\overline{b}$ events, one has to sacrifice the efficiency, i.e., the resulting statistics will be insufficiently low. Thus the compromise between desired statistics and purity must

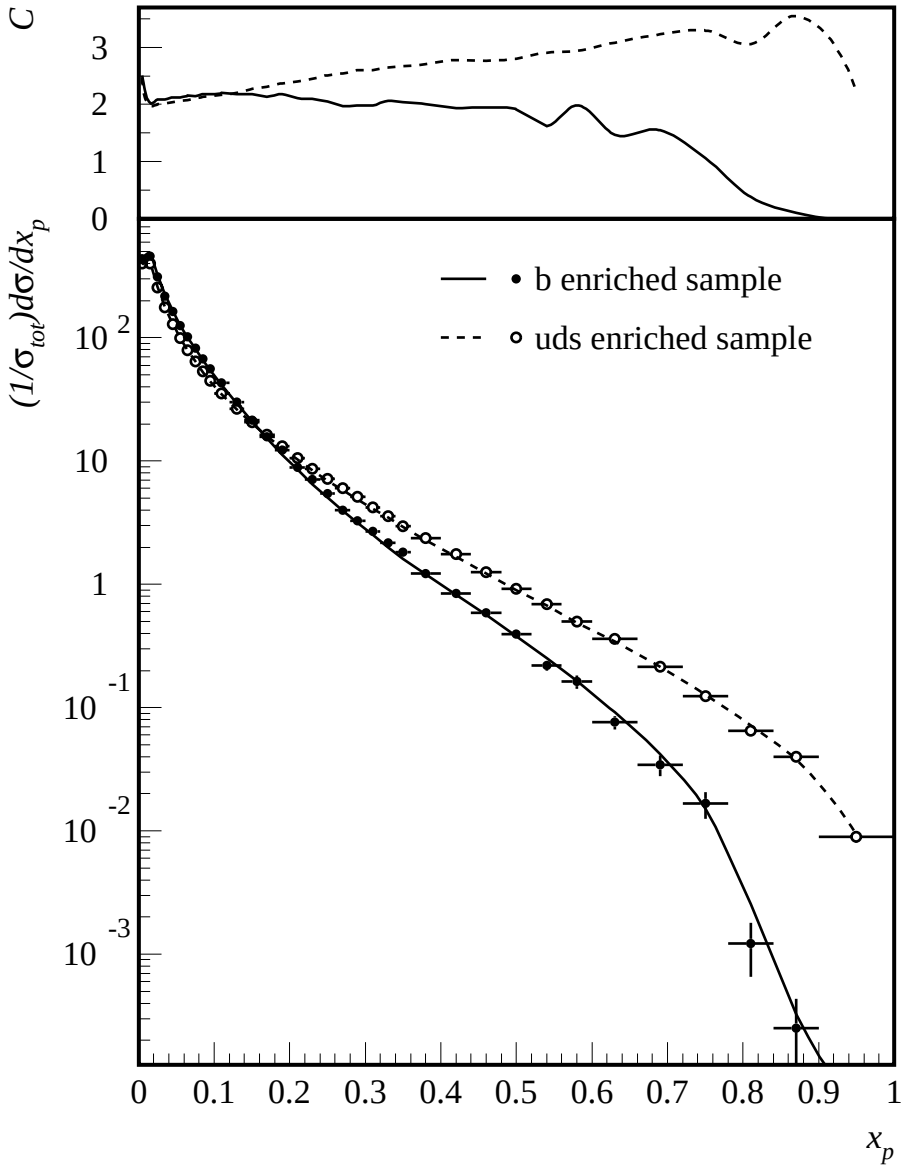

Figure 3.14: *Fragmentation functions of b quark (closed points, solid lines) and light quarks (open points, dashed lines) obtained with the help of the lifetime tagging technique. Curves show corresponding* JETSET *distributions. Correction factors are shown in inset.*

be reached for every particular kind of analysis.

The similar plot, but for light quark events, is shown in Fig. 3.11. The significantly different behaviour can be seen, namely, purity of the sample never can reach 100%. It is caused by the fact that both $Z^0 \to c\bar{c}$ and $Z^0 \to b\bar{b}$ events do contribute to the sample of high P_E or P_H probabilities.

It also can be seen, that in both b and u, d, s cases, the event tagging gives higher purities for a given efficiency. However, the hemisphere tagging is used more often in analysis, because it reduces unnecessary correlations.

Selection of appropriate cuts can be made with the help of Fig. 3.12 for b quark events and Fig. 3.13 for light quark events. For this analysis, the selection was done assuming, that a probability $P_H < 10^{-3}$ corresponds to $b\bar{b}$ events (with purity $\approx 94\%$ and efficiency $\approx 16\%$) and $P_H > 0.3$ to light quark events (purity $\approx 73\%$, efficiency $\approx 72\%$). The hemisphere tagging can be used to calculate the experimental efficiency by comparing the number of selected single hemispheres with the number of events in which both hemispheres are selected. This efficiency proved to be very close to that calculated from the simulation [30].

Samples of events, satisfying the above cuts, were used to build differential distributions in the same way as for regular hadronic events. Correction factors were calculated in the similar way, using the formula (3.37) with "true" spectra of pure generated b or u, d, s events, whereas the "reconstructed" distributions were obtained using the DELSIM detector simulation and applying the lifetime tagging procedure to the overall generated events. An example of the differential cross sections $1/\sigma_{tot} \cdot d\sigma/dx_p$ for the events of different flavour contents is shown in the Fig. 3.14. These are essentially heavy and light quarks fragmentation functions. It is clearly seen that the fragmentation function of b quark is softer than that of light quarks, i.e., it has higher values at small x_p and lower at high x_p. It agrees very well with the JETSET predictions, and can be regarded as a confirmation that the b quark has longer decay chain than light quarks, producing thus jets of higher multiplicity.

Hadron identification

Charged hadron identification in DELPHI [32,33] relies mainly on the measurements by the *Ring Imaging Cherenkov (RICH)* detector. It has been designed to provide pion, kaon and proton identification over the momentum range of particles produced in Z^0 decays.

Charged particles crossing the Cherenkov radiators with a velocity larger than the velocity of light in the same medium produce photons which are intercepted by a photon detector. The photon conversion point is determined by detecting the generated electron, called photoelectron. The photon emission angle with respect to the particle track is then reconstructed and is called *Cherenkov angle*. The number of photoelectrons associated to a particle track and their Cherenkov angles are the input information used for identifying its mass.

A mass tag is assigned to each individual particle fulfilling certain quality criteria. This tag is based on the probabilities computed for all the possible mass assignments using the RICH information.

Several algorithms [32–34] for particle identification for the DELPHI RICH detector

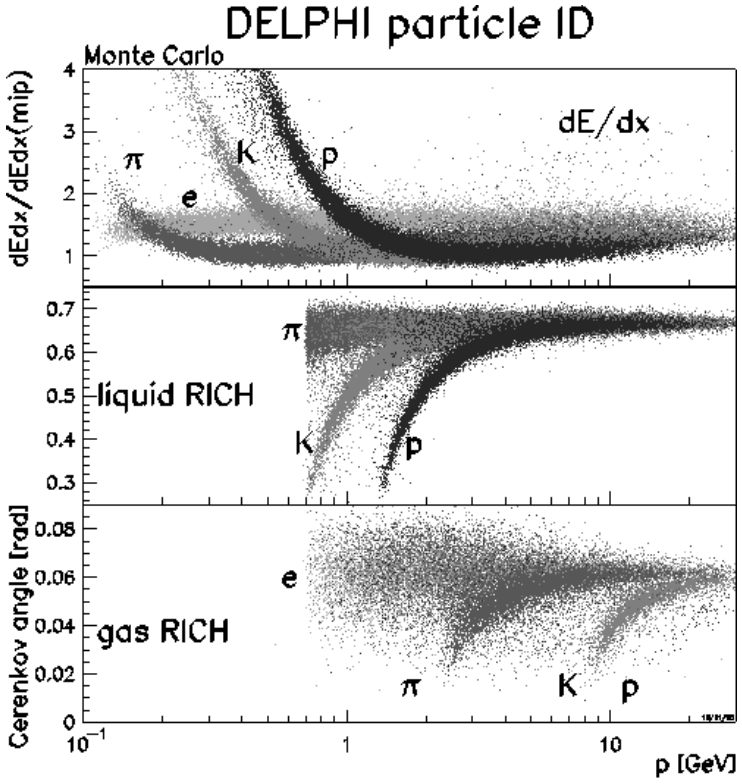

Figure 3.15: *dE/dx and RICH information for a set of simulated hadronic Z^0 decays.*

are developed to meet very different analysis requirements. The main concern of those methods is to discern between the track signal and the background in the jet environment. For this analysis, the so-called RIBMEAN [32] approach was employed, which uses a clustering algorithm to distinguish between background and signal photoelectrons. Photoelectrons are grouped into clusters which are weighted according to quality criteria, such as measurement errors or possible ambiguities between several tracks. The best cluster is retained and weights used to measure the average Cherenkov angle, its error and estimated number of photoelectrons.

However, the RICH detector does not provide satisfactory particle identification in the range of low momenta ($p < 0.7\ GeV$) particles. For soft particles identification relies on the specific ionisation energy loss per unit length (dE/dX) in the TPC. The sense wires of its proportional chambers provide up to 192 ionisation measurements per track. The total ionisation produced by a particle is proportional to its energy loss. Energy loss for a given particle in a given environment are calculable, hence correct energy loss measurements can provide an information about the particle identity. After applying certain corrections [3] and performing association of collected signals to reconstructed tracks, the TPC gives dE/dX measurements that are used for particle identification.

Comparison of the information available from dE/dX measurements and RICH versus particle momenta is shown in the Fig. 3.15. It is evident that in order to cover as much of x_p range as possible one should use combined information from dE/dX and RICH.

3.3.2 Results and discussion

Selected data samples, containing double-differential distributions $1/\sigma_{tot} \cdot d^2\sigma/dx_p\, d\cos\theta$, corrected to hardware and software inefficiencies, were used for the fragmentation functions analysis. Results of this analysis are presented in Appendices C and D.

Extraction of components of the fragmentation function

As the first approach to the analysis of components of the total fragmentation function, the method of fitting of experimental distributions to the formula (3.26) (to be refered to as "Method I", following Section 3.3) was used. Fit was done with the help of the MINUIT [35] package. Results are presented in Appendix C. As mentioned above, this method is preferable in the case of low statistics, hence it was used by the TASSO collaboration at lower energies. Performing the same analysis of the DELPHI data gives an opportunity to conclude on the centre-of-mass energy dependence of the variable A. It is shown in Appendix C, that the scaling violation behaviour can be clearly observed. The DELPHI data also provide far better statistics and allow to conclude that the longitudinal component contributes to the fragmentation function mainly in the region of $x_p \lesssim 0.2$.

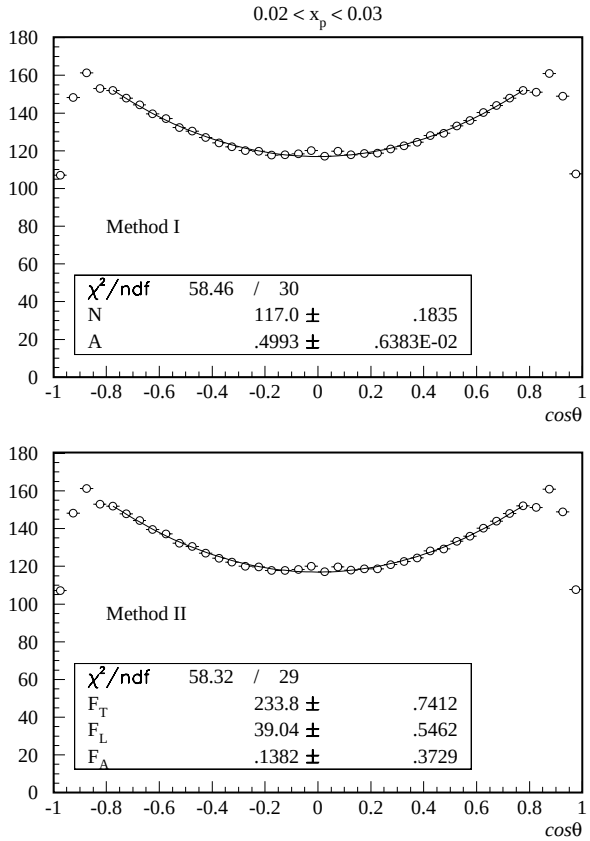

Figure 3.16: *Comparison of two fitting methods : two-parametric fit (I), upper figure, and three-parametric fit (II), bottom figure.*

Comparing equations (3.25) and (3.15), it is possible to extract F_L knowing A and the total differential charged hadron cross section :

$$F_L = \frac{1}{\sigma_{tot}} \frac{d\sigma}{dx_p} \left(\frac{1-A}{3+A} \right) \ . \tag{3.38}$$

On the other hand, fitting according to eq. (3.23) with F_T, F_L and F_A being free parameters ("Method II") directly defines the longitudinal component. An illustration of two fitting methods is given at Fig. 3.16. Comparison of results can be seen in Table 3.1. The angular range for fitting was chosen to be $|\cos\theta| < 0.8$. The general conclusion is that results of both methods are in a very good agreement, giving the same χ^2 per degree of freedom and describing the data sufficiently well. Big contribution to the χ^2 comes mainly from points around $\cos\theta \simeq 0$, which is caused by the detector geometry, namely, by the fact that the joints of different detector components are mainly situated in this region (see Section 1.2), which worsens particle registration in this zone.

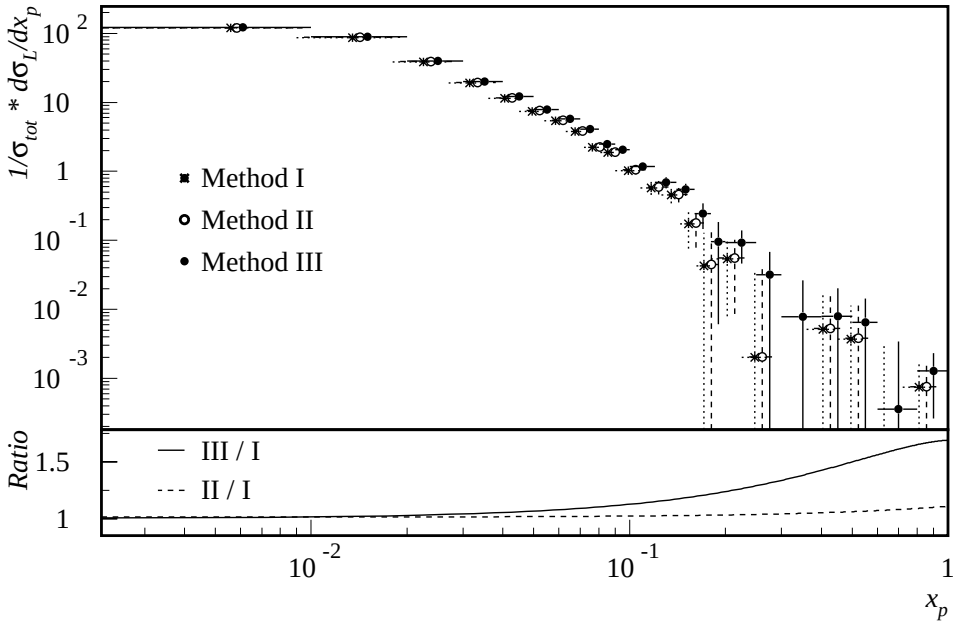

Figure 3.17: *Comparison of longitudinal components F_L obtained by different fitting methods (data points slightly shifted in x_p for better resolution). Approximate ratios of functions is shown in inset.*

A closer comparison of different methods can be seen in Fig. 3.17, where longitudinal components of the fragmentation functions are compared. While a very good agreement can be seen, there is an indication that the F_L obtained with the Method II is systematically higher that that of Method I, and the weighting method (listed under (III) in Section 3.3) gives the highest F_L values. Their approximate ratio (errors omitted) is shown in inset. The difference between two fitting methods can be explained by the fact

	Method I	Method II		Method III	
Δx_p	A	F_T	F_L	F_T	F_L
$0.00-0.01$	0.086 ± 0.005	288.722 ± 0.973	121.272 ± 0.727	287.592 ± 0.969	122.159 ± 0.725
$0.01-0.02$	0.306 ± 0.005	331.408 ± 0.910	88.012 ± 0.679	329.883 ± 0.906	89.218 ± 0.677
$0.02-0.03$	0.499 ± 0.006	233.803 ± 0.741	39.038 ± 0.546	232.758 ± 0.739	39.855 ± 0.545
$0.03-0.04$	0.630 ± 0.008	171.129 ± 0.624	19.414 ± 0.457	170.453 ± 0.623	19.952 ± 0.457
$0.04-0.05$	0.696 ± 0.010	129.791 ± 0.541	11.649 ± 0.395	129.204 ± 0.540	12.120 ± 0.395
$0.05-0.06$	0.739 ± 0.011	101.060 ± 0.476	7.594 ± 0.347	100.674 ± 0.476	7.899 ± 0.347
$0.06-0.07$	0.759 ± 0.013	80.957 ± 0.427	5.545 ± 0.311	80.643 ± 0.426	5.800 ± 0.311
$0.07-0.08$	0.792 ± 0.015	66.363 ± 0.385	3.850 ± 0.281	66.077 ± 0.385	4.078 ± 0.281
$0.08-0.09$	0.850 ± 0.017	56.008 ± 0.353	2.278 ± 0.256	55.742 ± 0.353	2.493 ± 0.257
$0.09-0.10$	0.849 ± 0.018	46.927 ± 0.324	1.909 ± 0.236	46.725 ± 0.324	2.073 ± 0.236
$0.10-0.12$	0.893 ± 0.015	37.275 ± 0.204	1.058 ± 0.148	37.113 ± 0.204	1.186 ± 0.148
$0.12-0.14$	0.918 ± 0.017	27.866 ± 0.176	0.593 ± 0.128	27.736 ± 0.176	0.697 ± 0.128
$0.14-0.16$	0.916 ± 0.020	21.217 ± 0.155	0.465 ± 0.113	21.109 ± 0.155	0.551 ± 0.113
$0.16-0.18$	0.958 ± 0.023	16.635 ± 0.137	0.177 ± 0.099	16.549 ± 0.137	0.245 ± 0.099
$0.18-0.20$	0.987 ± 0.027	13.258 ± 0.123	0.044 ± 0.089	13.196 ± 0.123	0.095 ± 0.089
$0.20-0.25$	0.976 ± 0.020	9.032 ± 0.064	0.055 ± 0.047	8.985 ± 0.064	0.093 ± 0.047
$0.25-0.30$	0.998 ± 0.027	5.431 ± 0.050	0.002 ± 0.036	5.395 ± 0.050	0.032 ± 0.036
$0.30-0.40$	1.010 ± 0.026	2.797 ± 0.025	-0.007 ± 0.018	2.779 ± 0.025	0.008 ± 0.018
$0.40-0.50$	0.982 ± 0.041	1.178 ± 0.017	0.005 ± 0.012	1.176 ± 0.017	0.008 ± 0.012
$0.50-0.60$	0.970 ± 0.061	0.508 ± 0.011	0.004 ± 0.008	0.505 ± 0.011	0.007 ± 0.008
$0.60-0.80$	0.998 ± 0.080	0.154 ± 0.004	0.000 ± 0.003	0.154 ± 0.004	0.000 ± 0.003
$0.80-1.00$	0.836 ± 0.213	0.017 ± 0.001	0.001 ± 0.001	0.017 ± 0.001	0.001 ± 0.001

Table 3.1: *Comparison of components of fragmentation function obtained by different methods.*

that the total cross section, used in eq. (3.38), is integrated over all the angular range, while A is calculated only in the limited range of $|\cos\theta| < 0.8$. All differences, however, are very well inside statistical errors. It must also be stressed that at the big values of x_p, where statistics is limited, Method I is preferable because it relies on a statistically better defined total differential cross section.

Fitting methods for the extraction of components of the fragmentation function proved to be a useful tool of the QCD analysis. However, the weighting method appears to be preferable in the case of sufficiently high statistics. One advantage of this method is that the limited angular range available for the analysis, is taken into account by the weights. Another advantage is that this method gives statistical errors defined directly from those of data, and not as evaluated parametric errors. Also, while a fit can converge to an unphysical result in the case of poorly statistically defined distribution, the weighting method always gives physically reasonable results. From Table 3.1 one can see the comparison of all three methods. The bin of $0.3 < x_p < 0.4$, in particular, shows that the F_L takes negative values for both fitting methods, which is unphysical by the definition of the fragmentation function. The weighting method gives the positive value of F_L in the same bin.

In what follows, all the analysis will be performed for the fragmentation functions, extracted with the weighting method, unless specified.

Asymmetry fragmentation function

In $e^+e^- \rightarrow Z^0 \rightarrow h + X$ events, the asymmetric component of the charged hadron differential cross section, F_A, equals to zero in the whole range of $0 < x_p < 1$ if the summation over all charged hadrons in final state is done, which is the case in eq. (3.23). In reality, however, due to inefficiency of a detector, F_A can take values different from zero. The analysis of F_A shows (see Appendix D) that this function is indeed indistinguishable from zero within statistical errors.

As was mentioned in Section 3.3, studies of asymmetry fragmentation function $\tilde{F}_A$ which takes into account charges of hadrons, can give information about the charge asymmetry and an estimation of the $\sin^2\theta_W$ within the assumption of valence dominance.

The ratio of asymmetry and total fragmentation functions for all observed charged particles is shown in Fig. 3.18. As soon as all particles were treated as pions, the formula (3.35) can be used to estimate the value of the weak mixing angle. Following the suggestion from [22], the fit in the region $x_p > 0.5$ was performed, with the only free parameter, $\sin^2\theta_W$. The result is

$$sin^2\theta_W = 0.235 \pm 0.005 \ ,$$

were error is the parametric error from the fit, reflecting the statistical uncertainty. This value is in a good agreement with those found previously by DELPHI [36]. Comparison to JETSET prediction shows that at big x_p the ratio of fragmentation functions is bigger in the model than in data, suggesting lower values of $\sin^2\theta_W$. Indeed, the weak mixing angle squared sine is one of the parameters in JETSET, and is set to be $\sin^2\theta_W = 0.23$.

The valence dominance calculations predict that ratios $\tilde{F}_A/(F_T + F_L)$ for different hadrons are different due to the different quark contents of hadrons. Therefore, it is of

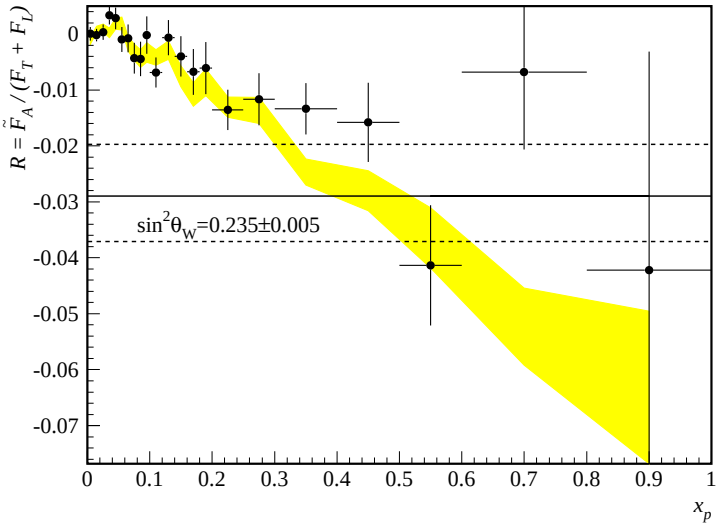

Figure 3.18: *Asymmetry fragmentation function $\tilde{F}_A(x_p)$ as measured from the charged hadrons distributions. Solid line shows the valence dominance limit at $\sin^2\theta_W = 0.235$ and dashed lines represent the error corridor. Shaded band shows the* JETSET *prediction.*

particular interest to study these ratios for identified hadrons. The problem, however, has several complications.

The main difficulty is that the hadron identification at high momentae is not very effective. As can be seen from Fig. 3.15, at $p > 20\ GeV$, it is rather difficult to distinguish between different hadrons. Not only efficiency is poor for this region, but also purity of an identified hadron sample is rather low [34]. Moreover, efficiency of particle identification in DELPHI is not uniformly distributed neither over the momentum, nor over the angular range. The result is that correction factors (3.37) become significantly higher and not uniform in different x_p intervals. They also become highly irregular at $|\cos\theta| > 0.7$.

Another difficulty is the low resulting statistics, especially for identified protons. Certain improvement can be obtained by splitting the whole range of $0 < x_p < 1$ not in 22, but in 8 bins. It is convenient to choose the last bin of $0.5 < x_p < 1$ because the valence dominance limit is presumably valid in this interval.

Figure 3.19 represents ratios $\tilde{F}_A/(F_T + F_L)$, measured for identified with the DELPHI detector hadrons. They confirm very well predictions based on the valence dominance [22]. Assuming that the fragmentation functions of the up, down and strange quarks are equal and neglecting the heavy quarks contributions, valence dominance calculations give the value of $R^p = 0.1373$ for protons [22] for $\sin^2\theta_W = 0.23$, which is in very good agreement with the experimental result.

The fragmentation functions method for charge asymmetry measurements gives so far promising results. High precision of obtained results is explained by the fact that the term in eq. (3.35) $2v_e = 4\sin^2\theta_W - 1$, so that a 10% precision in eq. (3.35) and analogous for other hadrons, implies about 1% accuracy in $\sin^2\theta_W$.

However, the present statistics does not allow one to make a clear statement about the

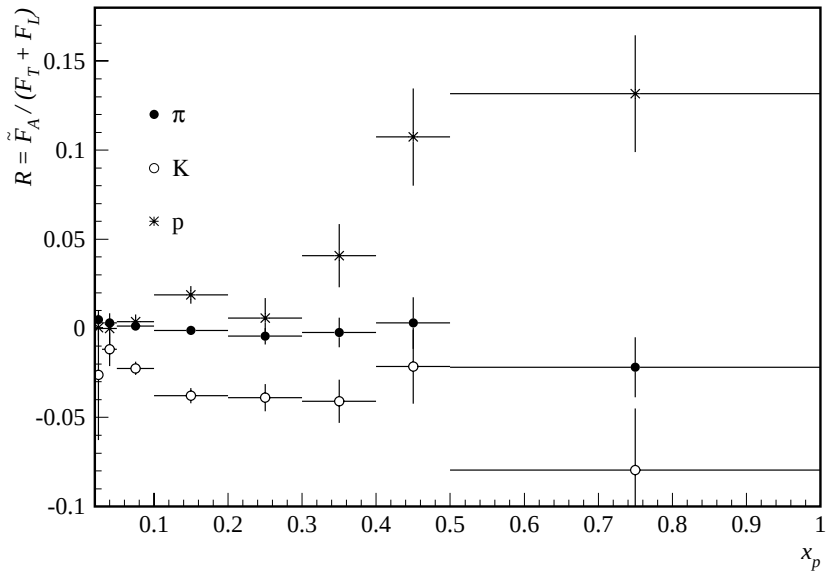

Figure 3.19: *Asymmetry fragmentation function $\tilde{F}_A(x_p)$ measured for identified hadrons.*

advantages of this method. Studies of systematic uncertainties, which may be significant, are necessary, but they are rather unreliable in the case of low statistics, especially for identified hadrons. Meanwhile, it sets the task for the future analysis, when more statistics will become available.

Strong coupling constant and charged multiplicity

To the leading order of α_s, the ratio of the transverse σ_T and longitudinal σ_L components of the total hadronic cross section is proportional to the α_s, see Section 3.2, eq. (3.22). Since all this analysis is performed to the $\mathcal{O}(\alpha_s)$ order, it is self-consistent to calculate the value of the strong coupling constant using the experimentally measured ratio σ_L/σ_T. Strictly speaking, eq. (3.22) is valid for the cross sections of all hadrons produced in electron-positron annihilation, charged and neutral. This analysis, though, relies only on charged particles measurements. The ratio of σ_L and σ_T, however, should be the same in any case.

This assumption has been checked using the JETSET generated events, where the charge of every hadron is explicitly known. Hadronic events on the generated level, without a detector simulation, allow one also to use the full angular range $-1 < \cos\theta < 1$. Applying standard weighting and fitting procedures to extract F_T and F_T and performing the integration over the x_p to obtain σ_T and σ_L as in eq. (3.30), it is possible to calculate ratio σ_L/σ_T for all hadrons and only for charged hadrons. The result for 10 millions of generated hadronic events is shown in Tab. 3.2. Comparatively high statistical errors reflect the uncertainty in x_p during the integration, since the standard splitting in 22 bins in x_p was used.

	Method II		Method III	
	Charged	All	Charged	All
σ_T	0.58 ± 0.02	0.92 ± 0.04	0.58 ± 0.02	0.92 ± 0.04
σ_L	0.034 ± 0.003	0.058 ± 0.009	0.036 ± 0.003	0.060 ± 0.009
σ_L/σ_T	0.059 ± 0.006	0.063 ± 0.010	0.061 ± 0.006	0.065 ± 0.010

Table 3.2: *Components of the total cross section extracted from the* JETSET *generated events for all hadrons and for charged hadrons only.*

From Tab. 3.2 it is clearly seen that the ratio of the longitudinal and transverse components of the total hadronic cross section remains the same for charged hadrons only. Therefore, it is consistent to use measured components of the charged hadrons cross section to extract the α_s to the leading order, i.e., α_s^{LO}

Results in Tab. 3.2 also reveal that the fitting (Method II) and weighting (Method III) give slightly different results for the longitudinal component of the cross section. Also it is important to stress that the whole available angular range was used to analyse JETSET generated events, while for real data the angular range is limited. Fig. 3.20 shows dependence of extracted from data σ_L/σ_T on the variable $v = \cos\theta$, which delimits the cosine of the angular range used in the analysis. It shows that while fitting method gives

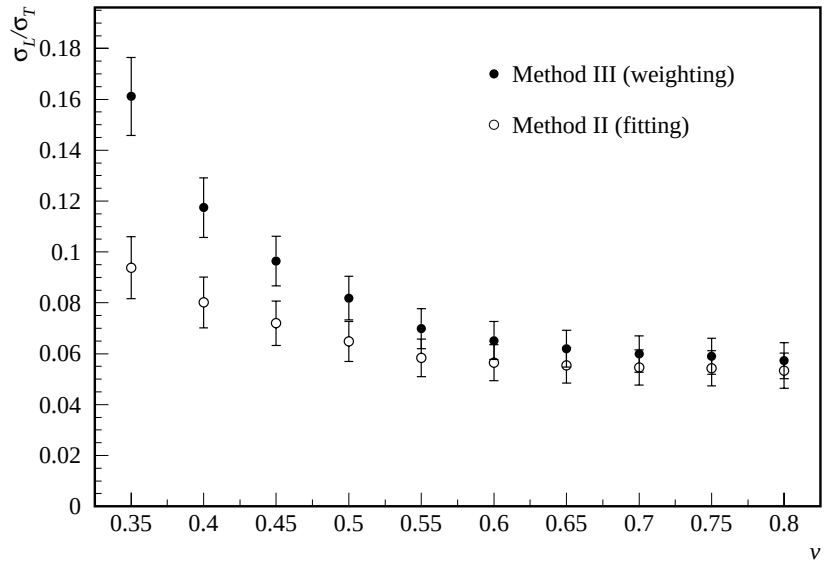

Figure 3.20: *Ratio σ_L/σ_T as extracted from the DELPHI data by different methods, versus angular range limit $v = \cos\theta$.*

systematically lower results, both methods agree well for $v = 0.8$, which corresponds to the maximal allowed angular range. Using the results obtained with the weighting

method, one can get

$$\frac{\sigma_L}{\sigma_T} = 0.057 \pm 0.007 \quad \text{and} \quad \alpha_s^{LO} = 0.180 \pm 0.022 \ .$$

The value of $\alpha_s^{LO} = 0.180$ is certainly far too high for the Z^0 mass (see Fig. 3.2), but it is consistent within used in this analysis approximations. Corrections of order $\mathcal{O}(\alpha_s^2)$ to the ratio of the cross sections on partonic level were calculated recently [37]. They show that higher order effects introduce corrections of about 25% to this ratio, which leads to the proportional decrease in the strong coupling constant.

While the total cross sections are basically first order moments of fragmentation functions, integrals of fragmentation functions are nothing but average multiplicities, see eq. (3.32). The average multiplicity of charged hadrons can be calculated directly as the integral of the normalised differential cross section $d\sigma/dx_p$. For the LEP1 energies, this gives

$$\langle n_{ch} \rangle = 21.316 \pm 0.007(stat) \pm 0.14(syst) \ ,$$

where systematic uncertainties were estimated using the systematic errors of the $d\sigma/dx_p$ [38].

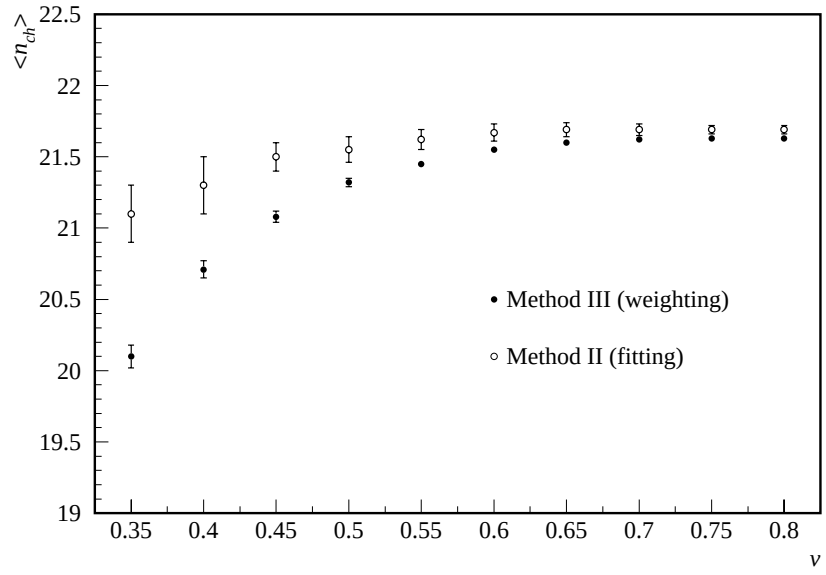

Figure 3.21: *Mean charged multiplicity $\langle n_{ch} \rangle$ as extracted from the DELPHI data by different methods, versus angular range limit $v = \cos\theta$.*

Calculation of the average multiplicity as in eq. (3.32) is a good self-consistency test of the fragmentation functions methods. For this analysis, $\langle n_{ch} \rangle$ was calculated using both fitting and weighting methods and in different angular intervals. The result is shown in Fig. 3.21. Systematic difference between the two methods is rather significant, similarly to the case of ratios σ_L/σ_T (Fig. 3.20), although now the fitting (Method II) gives higher

results. Both methods come to a satisfactory agreement for $v = 0.8$. Therefore, the mean charged multiplicity, consistent with this analysis, is

$$\langle n_{ch} \rangle = 21.631 \pm 0.009(stat) \ .$$

This value is somewhat higher than the average LEP1 value of $\langle n_{ch} \rangle = 20.92 \pm 0.24$ [39], although they are comparable, especially considering systematic uncertainties.

As can be seen from Fig. 3.21, statistical errors for the mean multiplicity are higher for the fitting method, comparing to the weighting one. The reason is that errors on transverse and longitudinal components of the fragmentation function are not exactly independent, since for both F_T and F_L statistical errors are defined by statistical deviations in the double-differential cross section, see eq. (3.23). Using the weighting procedure, it is possible to avoid effects of correlation between errors during $\langle n_{ch} \rangle$ calculation simply by adding weights W_T and W_L, while using F_T and F_L found by a fit one has to assume that their statistical errors are uncorrelated, since the correlation function is unknown. Correlation coefficients between F_T and F_L, estimated by the MINUIT package, amount to about 90%, slightly decreasing with the angular range increase, independently on the x_p interval.

Gluon fragmentation function

Equations (3.33) and (3.34) in Section 3.3 can be used to define the shape of the gluon fragmentation function D_g in assumption that the corrections of order $\mathcal{O}(\alpha_s^2)$ to the longitudinal fragmentation function F_L are negligible or can be taken into account by using the leading order value of the strong coupling constant, α_s^{LO}, in calculations.

As discussed in Section 3.3, the most affordable way of extracting D_g knowing F_T and F_L is to use the parametrization (3.34) for the gluon fragmentation function. There are generally two ways of performing the fit to the data. First is to fit F_L to the formula (3.33), using α_s^{LO} as a free parameter. Results of this method are discussed in Appendix D. Another approach is to fix α_s^{LO} to an appropriate value and to calculate the integral of D_g

$$F_g(x_p) \equiv \int_{x_p}^{1} \left(\frac{z}{x_p} - 1 \right) D_g(z) \frac{dz}{z} = \frac{\pi}{2 C_F \alpha_s^{LO}} F_L(x_p) - \frac{1}{4} \int_{x_p}^{1} \frac{F_T(z)}{z} dz \ . \qquad (3.39)$$

Fit of F_g using the parametrization (3.34) gives values of parameters P_i, hence it defines the shape of D_g. This method is more simple from the computing point of view, comparing to that discussed in Appendix D. Figure 3.22 and Table 3.3 show comparison of both approaches. In both cases fit was performed in the region $0.01 < x_p < 1.$, to avoid the region of very small x_p, where systematic uncertainties are particularly high.

The fixed value of $\alpha_s^{LO} = 0.180$ was estimated according to the expression (3.22). The quantity $\alpha_s^{LO} = 0.152 \pm 0.033$, obtained with the fit in Appendix D, is compatible with that estimation, although it is noticeably smaller. Still, compared to the average $\alpha_s(M_Z) = 0.117 \pm 0.005$ in the second order, obtained values for α_s^{LO} are significantly higher. This fact suggests that the $\mathcal{O}(\alpha_s^2)$ corrections are rather significant, which is confirmed by recent calculations [37].

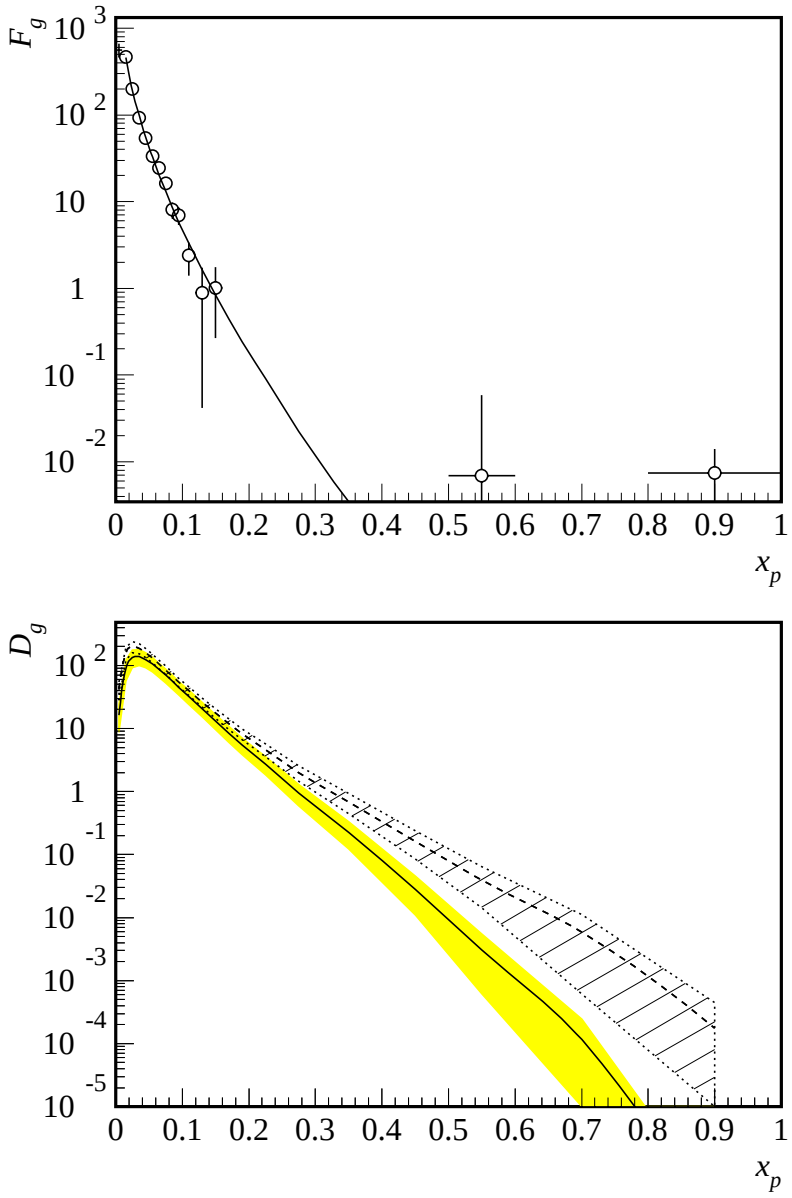

Figure 3.22: *Gluon fragmentation function D_g as obtained by the fit to the F_g, eq. (3.39). Upper figure shows F_g (open points) with the fitting function (curve). Bottom figure shows resulting D_g (solid curve, shadowed band represents errors) compared to that obtained by fitting F_L (dashed line, hatched band represents errors) with α_s treated as a free parameter.*

	$\alpha_s^{LO} = 0.180$, fixed	$\alpha_s^{LO} = 0.152 \pm 0.033$, free
P_1	0.07 ± 0.01	0.022 ± 0.002
P_2	-4.78 ± 0.03	-5.11 ± 0.03
P_3	7 ± 1	2.9 ± 0.8
P_4	0.72 ± 0.02	0.71 ± 0.01

Table 3.3: *Parameters for the D_g as in eq. (3.34). Second column corresponds to the fit of F_g with fixed α_s, third column shows results of the fit of F_L with α_s being a free parameter.*

Two approaches – fit to F_g and to F_L, – give noticeably different results, except for the parameter in the exponential term of eq. (3.34), which describes the peak at small x_p. The main reason of such discrepancies is that the choice of the parametrization is to big extent arbitrary, and parameters are correlated with each other. This fact is also reflected in big parametric errors, especially in the case of fixed α_s^{LO}.

Nevertheless, as can be seen from Fig. 3.22, the qualitative description of D_g is quite satisfactory. Both approaches show the fast decrease of D_g. In Appendix D it is shown that D_g moves below F_T already at $x_p \gtrsim 0.2$, which agrees with theory prediction and other experimental measurements, showing that gluon jets are softer than the quark ones.

Knowledge of next-to-the-leading order corrections to the F_L can help to investigate the gluon fragmentation function shape using the transverse and longitudinal components of the total fragmentation function, but for the time being these corrections are unknown for the hadronic level.

Studies of the fragmentation function components showed that they provide a powerful tool for solving various problems in particle physics. Summarised above analysis gives several examples of practical applications of QCD, confirming the validity of this theory. Being sensitive to higher orders of α_s corrections, the method of the fragmentation function components appears to be a fine probe of QCD, imposing in some cases requirements for further precision calculations within the theory to couple with experimental results. This means that the high statistics, available at LEP, indeed allows physicist to perform precision tests of the theory and in this way helps to develop it.

Chapter 4

Bose-Einstein Correlations

In the beginning of 1920s, when the quantum theory was developing intensively to describe the structure of atoms, the theory of quantum statistics became an important tool in describing ensembles of subatomic particles. Considering identical and indistinguishable particles, the theory of quantum statistics differentiates two kinds of particles, according to the way in which they may be distributed among the available wave functions associated with each energy state.

The statistics which concerns particles satisfying the exclusion principle ad hence described by antisymmetric wave functions, is called *Fermi-Dirac statistics*, and the particles are called *fermions*. In particle physics, fermions are characterised by the spin values $J = n(\hbar/2)$, where n is an odd integer. Leptons and quarks, for example, are fermions.

The second kind of statistics was first studied in 1921 by indian mathematician and physicist S.N.Bose in a paper on the statistics of photons. It concerns particles not restricted by the exclusion principle, and described by symmetric wave functions. Dirac invented the name *bosons* for such particles, and the statistics got the name of *Bose-Einstein* statistics. Bosons have an integral spin, therefore not only photons do obey the Bose-Einstein statistics, but also gluons, W and Z intermediate vector fields, and mesons.

When in 1950s, both in particle physics experiments and astronomical observations, it had been discovered that bosons emitted from the same source show the tendency to have close space-time or energy-momentum characteristics, this behaviour was ascribed to the particles obeying the Bose-Einstein statistics. The phenomenon of increasing probability for emission of identical bosons from similar regions of space and time due to the imposition of Bose symmetry, has been called *Bose-Einstein correlations*.

Presuming that only particles emitted from the same or close sources contribute to the probability enhancement of producing particles with small relative momentum, Q, it is expected that from studies of Bose-Einstein correlations one could obtain important information about the space-time extension and the coherence of sources. This approach to estimating the source size proved to be a reliable tool in astronomy, where the so-called HBT [1] effect is used to measure stellar sizes by analysing correlations between detected photons.

In particle physics, the hadron interferometry fulfils the similar task of defining the size, the shape, and the evolution in time of a microscopic source of mesons. As was

[1] HBT stands for Hanbury-Brown and Twiss, – astronomers who first reported of the effect

discussed in Chapter 3, the process of hadron production, or fragmentation, in high energy physics is less understood. It can not be described by an appropriate theory, and only phenomenological models are used so far to reproduce it. Studies of the space-time characteristics of a hadron source give an important information about the hadronization process as a whole and also provide tests of fragmentation models.

Since fragmentation models are mostly of probabilistic nature (see Section 3.1.2), it is very difficult to incorporate the Bose symmetrization into them. Thus effects of Bose-Einstein correlations are often absent in event generators, which apparently does not affect significantly their performance. However, it was shown recently [42] that in events like $e^+e^- \to W^+W^-$, where two hadron sources are produced close to each other, the Bose-Einstein effects can lead to interference between particles produced by neighbouring sources. From the experimental point of view, this will affect the observed W masses. To account to such an effect and describe it properly in event generators, the Bose-Einstein correlations have to be well understood, which requires more profound studies.

4.1 Correlation function

The Bose symmetry applies for all bosons which possibly can occupy the similar space-time region. However, in particle physics experiments it is very unlikely that more than two particles will be produced under this condition. Genuine three-particle Bose-Einstein correlations have been studied recently [40], but so far they are not in the main scope of the analysis.

Let us consider production of two identical bosons with four-momenta p_1 and p_2. Denoting $P(p_1,p_2)$ the probability density of two particles to be produced satisfying the Bose-Einstein statistics and $P(p_1)$, $P(p_2)$ – probability densities for a single particle to be produced with momentum p_1 or p_2, a correlation function C_2 of two identical bosons is defined as

$$C_2 = \frac{P(p_1,p_2)}{P(p_1)\cdot P(p_2)} \ . \tag{4.1}$$

Experimentally, $P(p_1,p_2)$ can be built as a double-differential cross section, $d^2\sigma/dp_1dp_2$, while the product $P(p_1)\cdot P(p_2)$ is not that straightforward to construct, especially in devoted heavy-ion experiments. Evidently, $P(p_1)\cdot P(p_2)$ can be regarded as a probability density of emitting two particles independently, $P_0(p_1,p_2)$, which is another double-differential cross section, implying that there is a possibility of obtaining a sample of bosons with all but Bose-Einstein correlations (usually denoted as a "reference sample").

The Bose symmetry implies that the wave function of a system of bosons is symmetric under particle exchange. In other words, if a particle A was emitted at a point r_A with momentum p_1 and another identical particle B was emitted at a point r_B with momentum p_2, then by detecting a particle with, for example, momentum p_1, it is impossible to conclude whether it was originally emitted from a point r_A or r_B. This ambiguity is reflected in the wave function of a pair of bosons, which reads

$$\Psi_{BE} = \frac{1}{\sqrt{2}}(\Psi_{1A}\Psi_{2B} + \Psi_{1B}\Psi_{2A}) \ , \tag{4.2}$$

where $\Psi_{i\alpha}$ is the wave function for a boson produced at a point r_α and registered with momentum p_i.

Describing the distribution of particle production points by a function $\rho(r)$, one can wright down the probability of finding two particles with momenta p_1 and p_2 as

$$P(p_1,p_2) = \int |\Psi_{BE}|^2 \rho(r_A)\rho(r_B) dr_A dr_B \ . \tag{4.3}$$

Obviously, the probability of independent emission $P_0(p_1,p_2)$ is given by the similar expression, replacing $|\Psi_{BE}|^2$ with $|\Psi_{ref}|^2$, where Ψ_{ref} is the wave function of a pair of particles from a reference sample, i.e., where one can distinguish between different particles, such as

$$|\Psi_{ref}|^2 = \frac{1}{2}(|\Psi_{1A}\Psi_{2B}|^2 + |\Psi_{1B}\Psi_{2A}|^2) \ . \tag{4.4}$$

Evaluation (see, for example, Ref. [41]) of eqs. (4.2), (4.4) and integration as in eq. (4.3) transforms the expression (4.1), assuming that pions can be described by the plane-wave functions, into

$$C_2 = 1 + |\tilde{\rho}(Q)|^2 \ , \tag{4.5}$$

where $\tilde{\rho}(Q)$ is the Fourier transform of $\rho(r)$ with respect to $Q = p_1 - p_2$:

$$\tilde{\rho}(Q) = \int \rho(r) e^{-(p_1-p_2)r} dr \ . \tag{4.6}$$

Considering the simplest model for a source to be a sphere of emitters distributed according to the Gaussian probability density, having a radius R,

$$\rho(r) = \frac{1}{4\pi^2 R^2} e^{-r^2/2R^2} \ , \tag{4.7}$$

the corresponding Fourier transform will take a form

$$\tilde{\rho}(Q) = e^{-Q^2R^2/2} \ . \tag{4.8}$$

This term squared is essentially the enhancement in particle production with small Q. For the two bosons with identical momenta, emitted off incoherent sources, $C_2 \overset{Q\to 0}{\longrightarrow} 2$. To account for possible effects which reduce the strength of Bose-Einstein correlations, the parameter λ is used as a factor in front of the enhancement term :

$$C_2 = 1 + \lambda e^{-Q^2R^2} \ . \tag{4.9}$$

Several interpretations of the physical meaning of λ can be given. The traditional one is that this parameter gives the fraction of pairs of identical boson which do interfere. Considering the possibility of existence of coherent sources, λ accounts for the degree of coherence, such that $\lambda = 0$ for complete coherence and $\lambda = 1$ for total incoherence. On the other hand, it could also have a meaning that the true source distribution is a sum of two or more incoherent Gaussian sources.

At $Q \to 0$, the effect of Coulomb repulsion between two identical charged bosons will lead to suppression of the probability of finding two charge-like particles with small

relative momentum. This has to be taken into account if the experiment is sensitive to this region of small Q.

Other effects, like final state interactions and resonance production, can affect the shape of the correlation function (4.1). They have to be considered specifically for every particular reaction. Meanwhile, majority of contemporary high energy physics detection equipment does not provide two-track separation sufficient for tests of correlation function at $Q \to 0$. All these complications mean that the parameters λ and R in expression (4.9) should be regarded as mostly descriptive.

4.1.1 The Longitudinal Centre-of-Mass System

In the expression (4.9), the parameter R corresponds to an average over the spatial and temporal source dimensions. To probe the actual shape of a meson source, the Bose-Einstein correlations have been studied in terms of various components of the four-momenta difference Q relative to some particular axis defined in the event.

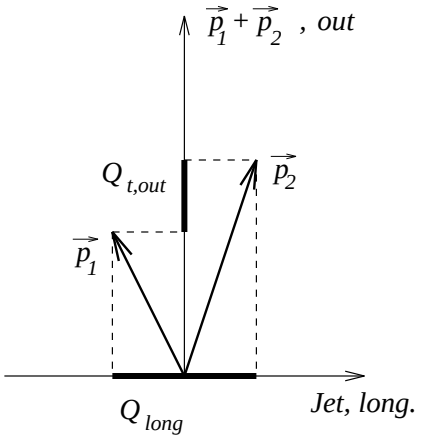

Figure 4.1: *Projection of LCMS on the (Q_{long},$Q_{t,out}$) plane.*

In this analysis, the so-called *Longitudinal Centre-of-Mass System* (LCMS) [43] has been used. The reference axis is defined as a physical axis of the process, which can be the beam direction in heavy ion collisions, or the jet direction in electron-positron annihilation. For each pair of particles, LCMS is the system in which the sum of the two particles momenta is perpendicular to the reference axis. The momentum difference of the particle pair Q is resolved into Q_{long}, parallel to the axis, $Q_{t,out}$, collinear with the pair momenta sum, and complementary $Q_{t,side}$, perpendicular to Q_{long} and $Q_{t,out}$.

Schematic picture of LCMS is shown in Fig. 4.1 in projection to (Q_{long},$Q_{t,out}$) plane. This system is particularly convenient for calculations and physical interpretations, since in LCMS the projections of the total momentum of the pair to the "longitudinal" and "side" directions are equal to zero. Also, the difference in emission times of particles couples to the energy difference between the particles only in the $Q_{t,out}$ direction [43]. This means that only $Q_{t,out}$ is sensitive to the lifetime of the source.

The two-particle correlation function C_2 can be written in the components of Q as

$$C_2 = 1 + \lambda e^{-R^2_{t,out}Q^2_{t,out} - R^2_{t,side}Q^2_{t,side} - R^2_{long}Q^2_{long}} \ . \tag{4.10}$$

Here the source is described not by a single radius R, but by the set of correlation radii $R_{t,out}$, $R_{t,side}$ and R_{long}. They reflect the geometry of a source and its dynamic characteristics. LCMS differs from the particles centre-of-mass system by the transverse boost with velocity $\beta_t = (p_{t,1} + p_{t,2})/(E_1 + E_2)$, where $p_{t,1}, E_1$ and $p_{t,2}, E_2$ are transverse momenta with respect to the reference axis and energies of two particles. Therefore, in

the centre-of-mass system, the energy difference will be related to $Q_{t,out}$ as [43]

$$\Delta E = \beta_t Q_{t,out} \ . \tag{4.11}$$

Under the assumption of a spherical shape of the source in the centre-of-mass system of a pair, correlation radii in LCMS must be related as $R_{t,side} = R_{long} = \gamma_t R_{t,out}$, where $\gamma_t = 1/\sqrt{1-\beta_t^2}$.

Further, it is useful to introduce new variable, the transverse mass of a pair of particles :

$$m_t = \frac{m_{t,1} + m_{t,2}}{2} = \frac{\sqrt{m_1^2 + p_{t,1}^2} + \sqrt{m_2^2 + p_{t,2}^2}}{2} \ , \tag{4.12}$$

where m_1 and m_2 are particle masses. Experiments in high-energy heavy-ion collisions [47,48] revealed symmetrical behaviour of the Bose-Einstein correlation function (4.10) with $R_{t,side} \simeq R_{long} \simeq R_{t,out}$. The radii were shown to have dependence on m_t of the kind $R_i \propto 1/\sqrt{m_t}$.

These experimental results need theoretical interpretation. It turned out that, in spite of being originated by the pure quantum mechanical phenomenon, such a behaviour in heavy-ion collisions can be consistently described by collective hydrodynamical behaviour [45,46]. Introducing variables, like the temperature of the freeze-out of the system T_f and the inverse gradient of four-velocity τ_0, which is close to the mean proper time at freeze-out, the longitudinal radius R_{long} can be expressed more precisely as

$$R_{long} = \sqrt{\frac{T_f}{m_t}}\tau_0 \ . \tag{4.13}$$

Within assumptions of hydrodynamical models, the radii parameters R_i represents not geometrical lengths of a system, but lengths of homogeneity of a source for an expanding hydrodynamical system [46]. For certain class of emission functions, these models give a satisfactory description of the data, proving to be useful in studies of the dynamics of a boson source and its geometrical characteristics. However, more profound studies have yet to be done to confirm or deny reliability of this approach.

4.2 Bose-Einstein correlations in e^+e^- annihilation

While collective hydrodynamic expansion so far seems to be valid for the heavy-ion experiments, it is not clear whether it fits the scenario of the electron-positron annihilation, described in Section 3.1, or not. Appendix E represents a first attempt to clarify this issue. In what follows, an extended description of the analysis method is given.

Bose-Einstein correlations between particles produced in $e^+e^- \to \gamma^*, Z^0 \to hadrons$ events were studied by numerous experiments at different center-of-mass energies [49–54]. Enhancement in the low part of Q-spectrum of the charge-like pion pairs is clearly seen in data and is well described by simple models, like (4.9). The most common correlation function parametrization for electron-positron annihilation case is

$$C_2(Q) = N\left[1 + \lambda e^{-Q^2R^2}\right](1 + \delta Q) \ , \tag{4.14}$$

where N is overall normalization, λ and R are meant to have the same meaning of the incoherence and radius parameters, as in (4.9). An additional linear term $(1+\delta Q)$ is used to describe apparent slopes in correlation function at large Q values.

Due to the low efficiency of neutral particles reconstruction in e^+e^- experiments, studies of the Bose-Einstein effect are mostly performed for charged pions, or, occasionally, for charged kaons. Therefore, all bosons to be mentioned here will be charged pions, if not specified otherwise.

In electron-positron collision, pions are produced in the hadronization of quarks and gluons directly, or in the decay of heavier objects produced in the hadronization. From the measured size of the production source, as well as from the strength of the Bose-Einstein effect, one may learn about the nature of quark and gluon hadronization.

The invariant four-momenta difference Q in e^+e^- annihilation is defined as $Q = \sqrt{-(p_1 - p_2)^2} = \sqrt{m_{\pi\pi}^2 - 4m_\pi^2}$, where $m_{\pi\pi}$ is the invariant mass of the pair of pions and m_π is the pion mass. The semi-classical model of a Gaussian source, described in Section 4.1, applies for electron-positron annihilation as well as for heavy-ion collisions, which has been proved by all studies, particularly, with a very good statistical precision by the LEP experiments [52–54].

On the other hand, QCD description of the $e^+e^- \to \gamma^*, Z^0 \to q\overline{q}$ process (see Section 3.1) suggests that pions production region is stretched between outgoing quarks, which is most successfully described within the string model, see Section 3.1.2. This model [55] implies that the pion production points are extended along the string. The extension lengths are related to the string parameters, in particular, the string tension. However, due to the one-dimensional nature of the string, there are no explicit spatial dimensions of the pion production region. The amplitude for a pair of particles produced with a given momenta ind in a given order is related to the area spanned by the string in space-time. Hence the Bose-Einstein effect arises for the pair of identical particles with the same momentum because the configuration of the state in space-time does not change under exchange of the two particles. Incoherence of the source, widely discussed in semi-classical models, appears in the string model from the sum over many different configurations with different phase.

One of the most interesting features of the string model is that the pions of the same charge cannot be produced as neighbours in fragmentation process, while neutral pions can be produced several in a row. That means that the measured, e.g., with the form (4.9) correlation length is larger for charged than for neutral bosons, and the most proper description of this length is that it measures not the total source size, but the distance between production points for which the momentum distribution can overlap. This statement is consistent with mentioned earlier experimental data, which found the radii parameters being less than 1 fm and the shape of the source being close to a sphere.

So far, the string model provides an appropriate framework in which to consider Bose-Einstein enhancement. However, the associated calculations are quite complex and time-consuming, especially when more than two particles being considered to underwent Bose symmetrization. For these reason, it is more convenient to use the simple semi-classical model in event generators, as it is implemented within the JETSET generator. In the current standard algorithm, identical particles are pulled closer together in such a way as to enhance the two-particle correlation at small Q values. Several shapes of the enhance-

ment can be used in the algorithm; in particular, for the analysis to be discussed here, the Gaussian shape of the correlation function (4.9) was used with parameters λ and R tuned to the DELPHI data [29].

As was mentioned in Section 3.1.2, gluon emission in the string fragmentation model is described as a kink on the string, which produces effectively two string pieces attached with one end to a gluon and with opposite ends to quark and antiquark. Gluon fragments to hadrons with high transverse momenta with respect to the quark or antiquark direction. This effect introduces bias in the event axis definition. Misalignment of the event axis can lead to side effects in the analysis in LCMS, therefore special selections should be done in order to reduce the gluon jet influence.

4.2.1 Data samples

The main goal of this analysis was to study the transverse mass dependence of correlation function parameters in the LCMS. To construct the correlation function (4.1) for the pions produced in $e^+e^- \rightarrow Z^0 \rightarrow hadrons$ process at the LEP1 energies, hadronic events collected by the DELPHI detector in 1991 – 1994 running period were used. Selection criteria for hadronic events are basically the same as described in the Section 3.3.1.

In order to be able to test the string model, to suppress the gluon contribution and to be able to perform the analysis in the LCMS system, only two-jet events were selected out of all hadronic events. Since at LEP1 energies gluon contribution is significant in every event, rather tight cuts were applied.

The two-jet event selection was done with the help of the LUCLUS [15] clustering algorithm (with parameter $d_{join} = 2.7$), requiring also the thrust value to be higher than 0.95 and the jet opening angle to be at least 175°. A total of about 670 000 events satisfied these criteria.

No hadron identification procedure was applied, thus every particle was assumed to have the mass of the pion.

The correlation function (4.1) of two particles in LCMS was constructed using the thrust axis of an event as a reference boost axis : within each jet, a pair of charge-like particles was boosted and rotated to LCMS, where components $Q_{t,out}$, $Q_{t,side}$ and Q_{long} of four-momenta difference were calculated. The triple-differential cross sections $d^3\sigma/dQ_{t,out}dQ_{t,side}dQ_{long}$ (the numerator in eq. (4.1)) were built in five m_t intervals, namely, $m_t < 0.25\ GeV$, $0.25\ GeV \leq m_t < 0.35\ GeV$, $0.35\ GeV \leq m_t < 0.45\ GeV$, $0.45\ GeV \leq m_t < 0.6\ GeV$ and $0.6\ GeV \leq m_t < 1.5\ GeV$.

The reference sample, which corresponds to the denominator in eq. (4.1), has to be a sample of particles which are not subject to Bose-Einstein correlations, but do obey the same kinematics as in regular e^+e^- hadronic event.

There are several recipes of preparing such a reference sample; the simplest one is to construct it using the opposite-sign particle pairs. However, the Q distribution of these pairs includes peaks due to neutral meson resonances decay products and suffers from many other dynamical effects.

Another approach is to use an event generator without Bose-Einstein effects included to build up a reference sample. In this case one must be sure that the generator describes properly the physics in the absence of Bose-Einstein symmetry. Also, the adequate de-

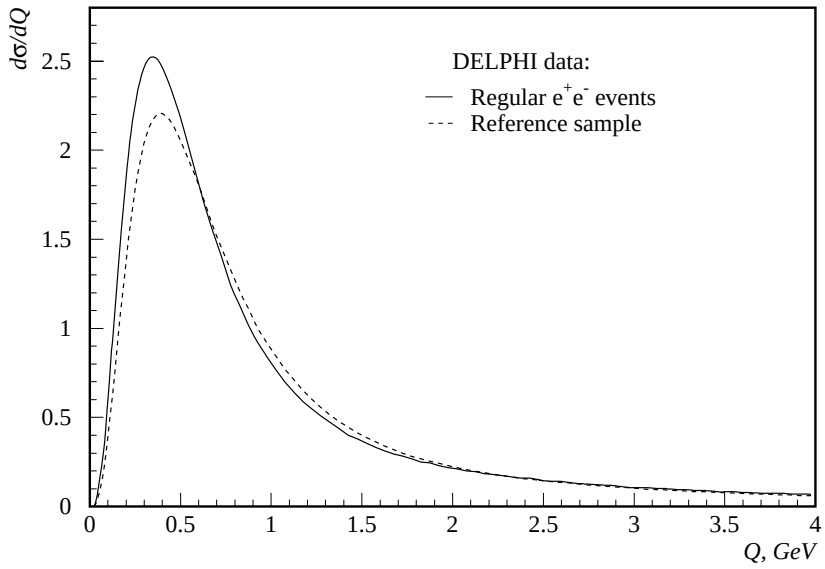

Figure 4.2: *Obtained from the DELPHI data $d\sigma/dQ$ distributions for regular e^+e^- hadronic events (solid line) and the reference sample (dashed line). Both distributions are normalised to unity for comparison.*

tector simulation has to be applied onto generated events, which makes the task more difficult considering the high probability of introduction of systematic deviations.

For these studies, the reference sample was prepared using the so-called *mixing procedure*. The idea is to combine particles from different events, assuming that the two-jet event selection criteria provide us with a row of kinematically similar events. The mixing procedure can be described in following steps :

- After the thrust axis calculation, each event has been rotated to the thrust axis coordinate system, i.e., z axis was rotated to the thrust direction.
- Tracks from each rotated event have been stored in a reference buffer. For this analysis the reference buffer consisted of 21 events to match the average charged multiplicity in e^+e^- hadronic events. Events in the buffer were continuously exchanged to prevent any regularities in particle spectra.
- The reference distributions $d^3\sigma/dQ_{t,out}dQ_{t,side}dQ_{long}$ were built using randomly picked tracks from the reference buffer. First, a random event of 21 stored was selected, then a track from this event was picked also randomly.

Since three-dimensional distributions $d^3\sigma/dQ_{t,out}dQ_{t,side}dQ_{long}$ can not possibly be plotted on a sheet of paper, the comparison of $d\sigma/dQ$ distributions for real events and for reference sample is shown at Fig. 4.2. It can be seen that there is an excess in the real events distribution over the reference sample in the region of $Q < 0.5\ GeV$, which is the manifestation of Bose-Einstein correlations.

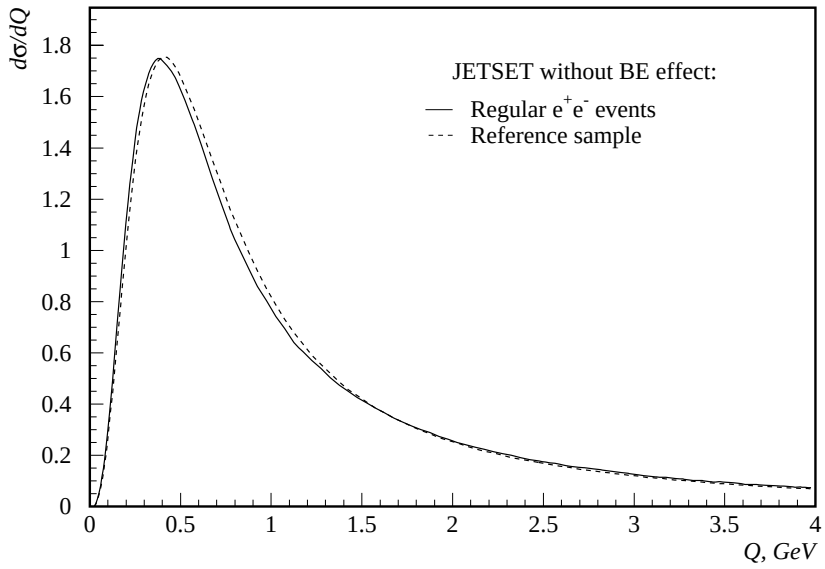

Figure 4.3: *Obtained with the help of the* JETSET *generator without Bose-Einstein effects included $d\sigma/dQ$ distributions for regular e^+e^- hadronic events (solid line) and the reference sample (dashed line). Both distributions are normalised to unity for comparison.*

However, the mixing procedure does not conserve momenta and energy, thus leading to certain side effects. Another drawback is that it changes the multiplicity of a mixed "event". Appropriate corrections can still be done with the help of a event generator without Bose-Einstein effects. Constructing Q distributions of charge-like pairs from generated events and similar distributions for generated events which underwent the mixing procedure, one obtains an adequate correction without even applying the detector simulation routines.

On Fig. 4.3, the comparison of $d\sigma/dQ$ obtained from the JETSET generated events without inclusion of Bose-Einstein effects is shown. The procedure of mixing in this case introduces some fake correlations in the region of $Q > 0.3\ GeV$, that have to be taken into account by the correction.

Consecutively, the correlation function for the pairs of pions can be expressed as

$$C_2(Q) = \frac{[N^{\pm\pm}(Q)/N^{\pm\pm}_{mix}(Q)]_{data}}{[N^{\pm\pm}(Q)/N^{\pm\pm}_{mix}(Q)]_{\text{JETSET}}} \ . \tag{4.15}$$

Here $N^{\pm\pm}(Q)$ indicates number of charge-like particles in a bin of Q variable. This formulation was used to construct the tree-dimensional correlation function $C_2(Q_{t,out}, Q_{t,side}, Q_{long})$, used in the present analysis.

For the comparison purposes, the same analysis was performed using the DELPHI tuned [29] JETSET PS generated events (Bose-Einstein effects included) with the DELSIM [28] detector simulation applied. This simulated data underwent the same event selection criteria, mixing procedures and correction, as the real data.

4.2.2 Results and discussion

Main results of the analysis of the transverse mass dependence of correlation function parameters in the LCMS are presented in Appendix E. An illustration of the correlation function behaviour in selected m_t intervals is shown at Fig. 4.4, where two-dimensional correlation function $C_2(Q_t, Q_{long})$ with $Q_t = \sqrt{Q^2_{t,out} + Q^2_{t,side}}$ is plotted for simplicity.

The enhancement in C_2 at low Q values is clearly seen, and its amplitude grows with increasing m_t, while the width of the peak narrows. This qualitative picture is confirmed by the three-dimensional fit using the parametrization

$$\begin{aligned} C_2 &= N\left[1+\lambda e^{-R^2_{t,out}Q^2_{t,out}-R^2_{t,side}Q^2_{t,side}-R^2_{long}Q^2_{long}}\right] \\ &\times \ (1+\delta_{t,side}Q_{t,side}+\delta_{t,out}Q_{t,out}+\delta_{long}Q_{long}) \end{aligned} \tag{4.16}$$

in the region of $Q_{t,out} < 1\ GeV$, $Q_{t,side} < 1\ GeV$ and $Q_{long} < 2\ GeV$ (this is to stay in statistically well populated region). Parameter λ corresponds to the amplitude of the enhancement, which is proportional to the strength of the Bose-Einstein correlations. As noted in Appendix E, value of λ grows almost linearly from 0.19 at $m_t < 0.25 GeV$ to 1.3 at $0.6\ GeV \leq m_t < 1.5\ GeV$. Meanwhile, all three radii parameters tend to decrease.

Comparison of the radii values shows that while all of them vary in the range from approximately 0.3 fm to 1 fm, their mean values are different: $\langle R_{t,out}\rangle = 0.64 \pm 0.04\ fm$, $\langle R_{t,side}\rangle = 0.30 \pm 0.02\ fm$, and $\langle R_{long}\rangle = 0.48 \pm 0.01\ fm$. This indicates that the source might not be spherical in LCMS, contrary to the heavy-ion collision studies results.

From the point of view of the string model, such a behaviour can not be immediately understood. While λ dependence on m_t can be easily explained by the fact that the resonance decay products reduce the correlation strength at low m_t values, the m_t dependences of correlation radii needs more reasoning. Also, the fact that λ exceeds the unit at high m_t values, needs more attention.

According to the definitions of LCMS (see Section 4.1.1), the radii parameter $R_{t,out}$ differs from $R_{t,side}$ only in that sense that the former is sensitive to the difference in the emission time of the particles. On the other hand, within the string model frameworks the geometrical transverse dimensions of a source must be very similar, i.e., that the transverse cross section of a source has a circular shape. That leads to a naive conclusion that $R_{t,out}$ must exceed $R_{t,side}$. While for the small m_t values this is true, at higher m_t $R_{t,out}$ drops below the $R_{t,side}$ values. An interpretation of this effect could be that the $R_{t,out}(m_t)$ dependence in LCMS for e^+e^- annihilation reflects the invariance of the transverse radius of the source in the centre-of-mass system (CMS) [56]. Indeed, taking into account eq. (4.11) and the fact that the invariant Q^2 in LCMS projections is

$$Q^2 = Q^2_{t,out} + Q^2_{t,side} + Q^2_{long} - \Delta E^2\ , \tag{4.17}$$

one can rewrite the correlation function (4.9) in CMS as

$$C_2^{CMS} = 1 + \lambda exp(-R_I^2 Q^2_{t,out}(1-\beta_t^2) - R_I^2 Q^2_{t,side} - R_I^2 Q^2_{long})\ , \tag{4.18}$$

where R_I denotes the invariant *out* radius parameter in CMS, which takes the form of

$$R_I = \gamma_t R_{t,out}\ . \tag{4.19}$$

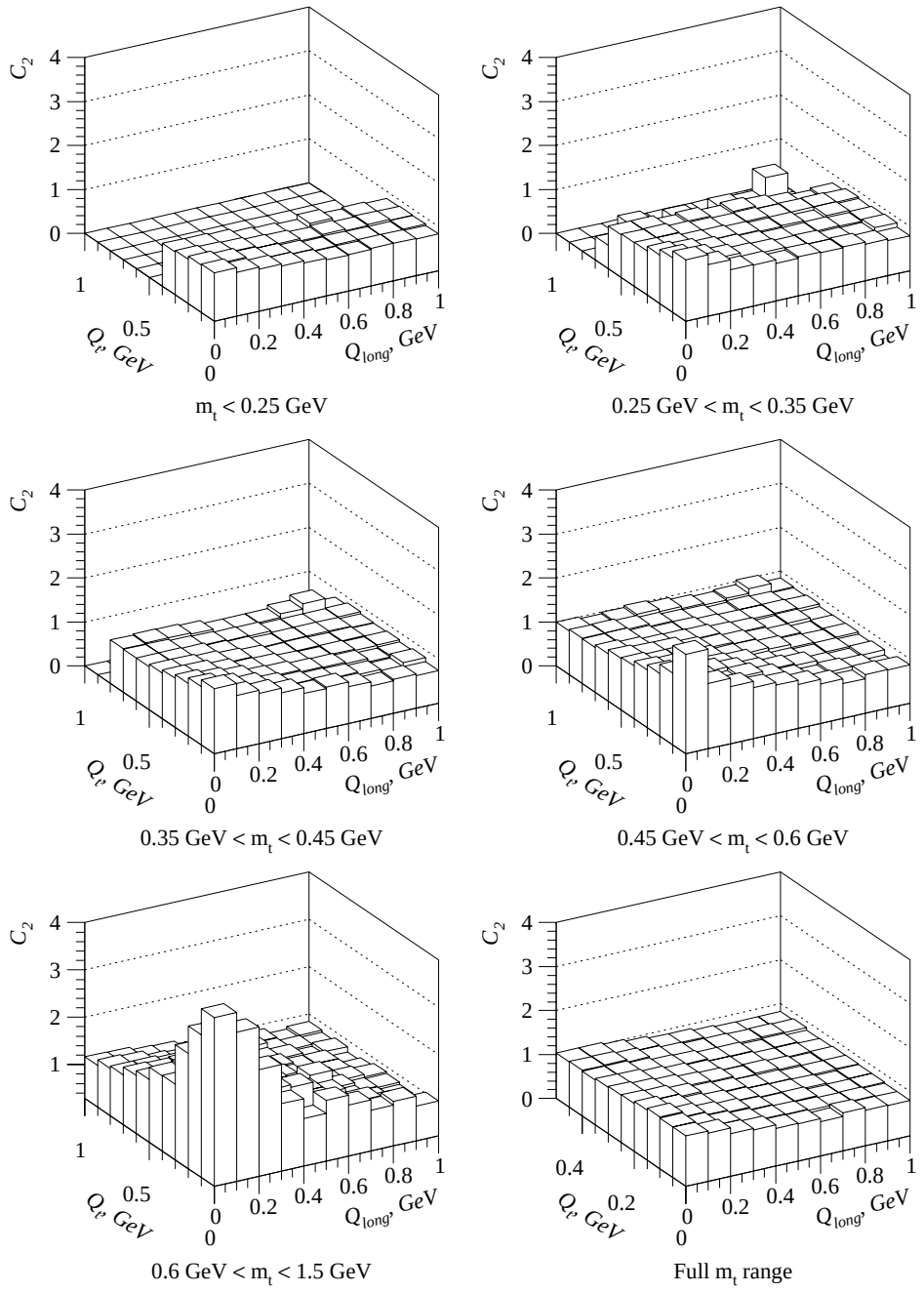

Figure 4.4: *Two-dimensional correlation functions $C_2(Q_t, Q_{long})$ in different m_t intervals.*

Therefore, $R_{t,out}$ gains the additional m_t-dependence due to the boost. This can be tested with the JETSET generator, because it uses the form $C_2 = 1 + \lambda \exp(-R_I^2 Q^2)$ to reproduce the Bose-Einstein enhancement. As shown in Appendix E, dependence of $R_{t,out}$ on m_t is stronger than those of $R_{t,side}$ and R_{long} in JETSET, which is consistent with the discussion above.

Considering the fact that the resonances do have a finite lifetime, thus propagating out of the primary source before decaying into observed pions, one can discuss the possibility that these low momenta (hence, low m_t) pions effectively increase the size of the pion source, reflected in the correlation function. On the other hand, this explanation can not be valid for the JETSET generated events simply because resonances in JETSET do decay without being propagated.

So far, the parameters of the slope, $\delta_{t,out}$, $\delta_{t,side}$ and δ_{long} have not been not discussed. Apparently, they are in general rather small, of an order of ± 0.02, but the assumption that the Bose-Einstein enhancement situates on the top of a three-dimensional non-flat background, even with linear slopes in each dimension, is rather arbitrary. Expression (4.16) suggests that overestimation of δ-parameters results in higher λ values. Moreover, if the background has more complicate shape, it can affect not only the λ parameter, but the radii too, and possibly even their m_t dependence.

Therefore, careful studies of the background are necessary. Partially, existence of the background is due to the presence of uncorrelated particles, while one can not judge *a priory* whether a certain pair is correlated or not. Another contribution comes from long-range correlations. Also considerably high effects appear due to the phase-space limitations.

Attempts to purify the data sample in this analysis included introduction and/or variation of following additional cuts :

- Requirements on impact parameters of each track during the hadronic event selection were tightened to be below 1 cm in the transverse plane and below 5 cm along the beam axis, which removes decay products of some long-living resonances from the sample.

- Correlation function was constructed only of pairs of particles, each having momentum below 5 GeV/c, to avoid the limits of phase space were dynamical correlations are strong.

- Pairs were rejected if their opening angle was smaller than 2° to exclude the possibility of counting tracks, not resolved properly by the detector.

- Additional criterion, connected to the finite detector resolution, was to require Q to be no less than 60 MeV/c. It reduces also the influence of correlated pions from η' decays.

- To move away from the phase-space limits, tracks from both jets were combined into pairs, with the cut on the mean rapidity of the pair $\langle y \rangle > 1$ applied to avoid dynamical correlations.

- To reduce correlations due to the local transverse momentum compensation, pairs were rejected if their opening angle in transverse plane exceeded 120°.

Studies show that these additional selections lead mainly to decrease in slope parameters δ, suggesting that the background becomes more flat. However, the transverse mass dependences of radii parameters does not change significantly, proving that variation of selection criteria gives the estimate of systematic uncertainties, but does not change the overall results.

Variations of the $Q_{t,out}$, $Q_{t,side}$ and Q_{long} ranges used in the fitting procedure were also performed. This study revealed the very high systematic uncertainty of the fit parameters in the region of $0.6\ GeV < m_t < 1.5\ GeV$: about 25% for λ and R_{long}, 40% for $R_{t,side}$ and up to 50% for $R_{t,out}$. Considering also far too big bin width of $0.9\ GeV$ and low statistics in this m_t region, one can conclude that results obtained for $0.6\ GeV < m_t < 1.5\ GeV$ are not very reliable. This can be connected also to the strong influence of hadrons produced in soft gluon jets, which were not eliminated by the two-jet selection procedure. However, preliminary tests with the JETSET generator with gluon emission switched off show rather small sensitivity to the presence or absence of gluon jets for this high m_t region, mainly because of still big statistical uncertainties.

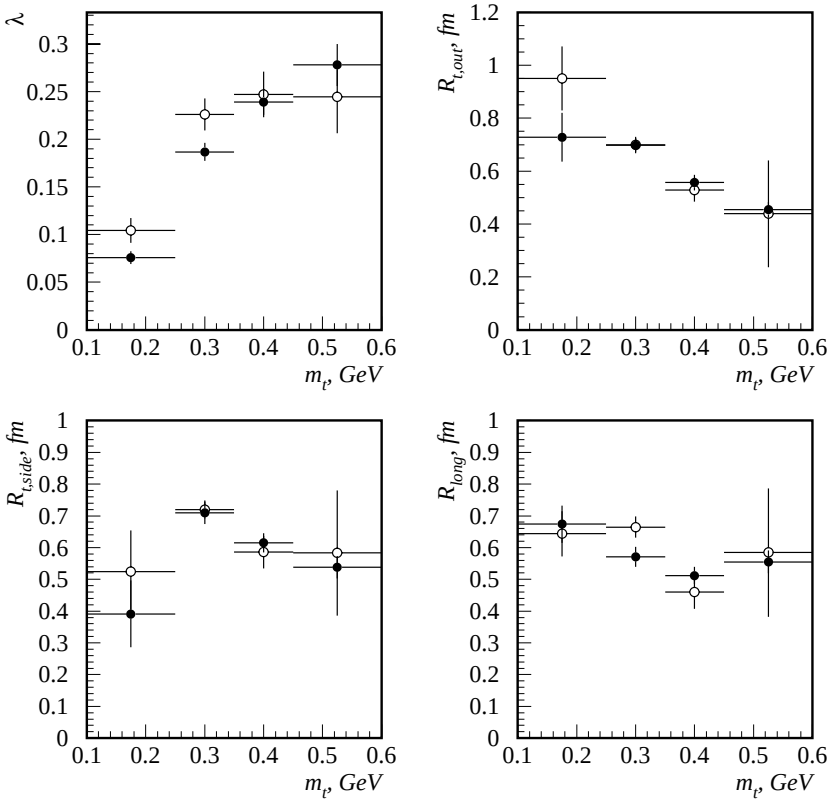

Figure 4.5: *Correlation function parameters as extracted from* JETSET *generated events with (open points) and without (closed points) gluon emission allowed.*

The first m_t interval, namely, $m_t < 0.25\ GeV$ also appears to be of little use, in spite of containing the majority of statistics. As can be seen from Fig. 4.4, with this m_t selection the transverse component of Q does not extend further than $0.4\ /GeV$, which means that

transverse radii parameters can not be properly described by the fit.

As was already mentioned, tests of the influence of soft gluon jets to the m_t dependence of correlation function parameters were made using the JETSET event generator with gluon emission switched on and off (no detector simulation applied; input JETSET parameters are $\lambda = 1$ and $R_I^{-1} = 0.394\ GeV$). While in general m_t dependence of radii and λ parameters in this case are rather smooth, it does not vanish and has behaviour similar to that in data. A comparison of correlation function parameters extracted from JETSET generated events with gluon emission switched on and off is shown in Fig. 4.5. Interval of $0.6\ GeV < m_t < 1.5\ GeV$ is omitted.

These results indicate that gluons do not influence parameters of the correlation function at least in this particular kinematic range, selected with mentioned before criteria. From the position of the string model this could mean that either gluonic kinks of the string do not influence the space-time picture of e^+e^- event within applied kinematical cuts, or that the measured radii parameters are not sensitive to these kinks.

This analysis leads to the conclusion that the Bose-Einstein correlations in electron-positron annihilation are found to behave very much like those in experiments on heavy ion collisions. The radius parameters show the same $\propto 1/\sqrt{m_t}$ dependence, which is well understood in terms of collective hydrodynamical behaviour for the heavy-ions case. Meanwhile, the transverse mass dependence of correlation radii in LCMS for e^+e^- annihilation can not be adequately explained. Apparent existence of similar trend of decreasing radii parameters with increasing transverse mass of the pair both in DELPHI data and JETSET generated events is even more puzzling. Evidently, more studies have to be done in this field in order to find the answers on arisen questions.

Summary

Following the common dialectics law, the development of science is not only powered by revolutionary discoveries, but also has periods of smooth evolution, preparing the ground for future perturbations. The history of the LEP collider is a good illustration of this law : the LEP was designed with aims to discover and study intermediate vector bosons W and Z, but technological progress in antiproton cooling made it possible to discover W and Z already on smaller SPS collider, then proton-antiproton. That made the main task for LEP to become a factory, producing bosons in abundance in order to provide big and clean sample of events for precision tests of various QCD and Standard Model predictions. Nowadays LEP is well-studied and tuned machine equipped with modern detection tools, which allow physicists to study the most complicated processes of nature.

One of the less understood phenomenon is the fragmentation of invisible quarks to observable hadrons. This dissertation is devoted to investigations of hadronization process from different view angles : fragmentation function analysis and two-particle correlations studies. While none of them led to a discovery, some new methods were developed and applied to the analysis.

Method of the transverse and longitudinal fragmentation function proved to be a useful tool for QCD testing. In the case of high statistics, like that available with the LEP, it gives yet another approach to problems like gluon fragmentation function extraction, fragmentation of different quark flavours, strong coupling constant α_s and the weak mixing angle definition, mean charged multiplicity calculation. Results obtained with this method are in a good agreement with other independent measurements, which proves that the present qualitative understanding of the fragmentation process is basically correct. Fragmentation function method also appears as a precision test of QCD, since it is sensitive to high order corrections in α_s.

Multidimensional studies of Bose-Einstein correlations provide a probe of the hadronization process from semi-classical point of view. Analysis of three-dimensional correlation function in different transverse mass intervals gives information about space-time behaviour of the hadronic source. Described in the present thesis first studies of this kind for e^+e^- annihilation revealed the fact that hadrons with low transverse mass m_t are emitted from a bigger source than those with high m_t, analogously to the heavy-ion collisions case. This unexpected result is however approximately reproduced by the JETSET event generator. This suggests that the effect might have a different explanation, which is yet to be found.

In general, the main conclusion is that the data, collected by the DELPHI detector at LEP, provide an enormous material for analysis, which helps to develop our knowledge of nature and its laws.

Acknowledgements

This work would not have been possible to complete without support from many different people in different places. I would like to thank everybody who helped me during these years, giving good advises, generating new ideas, teaching me something new. Here is just a brief list of people whom I would like to express my gratitude.

In Lund:
Göran Jarlskog and Bengt Lörstad for giving the possibility to perform these studies in Lund, sharing the supervisorship; Cecilia Jarlskog, Torbjörn Sjöstrand and Tamás Csörgő (who appears occasionally in Lund) for the very useful discussions and suggestions.

In Dubna:
The DELPHI group within which I started the work, Aleksandre Olshevsky for wise leadership and invaluable assistance, Leonid Tkatchev for attentive supervising, also Nikolay Skachkov for fruitful theoretical support, and all others for many help.

In CERN:
Members of Hadron Calorimeter team lead by Heiner Herr for support and pleasure to work together; *Team 10* members, in particular Alessandro De Angelis, Klaus Hamacher and Amiran Tomaradze for encouraging, interesting discussions and suggestions.

I wish I can thank all those people around the world who invented and developed the *Internet* and the *World Wide Web*, and also those who bothered to set up *WWW*-servers providing preprints, dictionaries, databases and many other extremely useful information on-line. It enormously increases efficiency of the work and speeds it up.

There are dozens of others not mentioned here but whom I always shall remember. Thank you!

Bibliography

[1] S. Myers, "LEP Status and Plans", CERN-SL-95-66-DI (1995). Presented at the 16th Biennial Particle Accelerator Conference - PAC 95, Dallas, TX, USA, 1 - 5 May 1995.

[2] DELPHI Coll., P. Aarnio et al., Nucl. Instr. & Meth. **A 303** (1991) 233.

[3] DELPHI Coll., P. Abreu et al., CERN-PPE/95-194, to be published in Nucl. Instr. & Meth. **A**.

[4] P. Eerola, "Hadron Calorimeter Data Formats", DELPHI Note 89-48 CAL 67 DAS 100 (1989)

[5] R. Lauhakangas, M. Lewandowski, J. Pyyhtia, "Octopus Input/Output Fastbus Module", DELPHI Note 90-24 CAL 73 (1990)

[6] R. Bock et al., "HIGZ Users Guide", nProgram Library Q120, CERN, 1991.

[7] CN/ASD group, "PAW - Physics Analysis Workstation", nProgram Library Q121, CERN, 1995.

[8] R. P. Feynman. *Photon-hadron interaction.* Benjamin, New York, 1972.

[9] Yu .L .Dokshitzer et al. *Basics of Perturbative QCD.* Editions Frontieres, 1991.

[10] G. Altarelli and G. Parisi, Nucl. Phys. **B216** (1977) 298;
V. N. Gribov and L. N. Lipatov, Sov. J. Nucl. Phys. **15** (1972) 78;
Yu. L. Dokshitzer, Sov. Phys. JETP **46** (1977) 641.

[11] I. G. Knowles et al., "QCD Event Generators" HEP-PH 9601212 (1995). Talk given at 2nd General Meeting LEP2 Physics Workshop, Geneva, Switzerland.

[12] R. Odorico, Comp. Phys. Comm. **72** (1992) 238.

[13] G. Marchesini et al., Comp. Phys. Comm. **71** (1992) 465.

[14] B. Andersson et al., Phys. Rep. **97** (1983) 31.

[15] T. Sjöstrand, Comp. Phys. Comm. **28** (1983) 229;
T. Sjöstrand, "PYTHIA 5.6 and JETSET 7.3", CERN-TH.6488/92 (1992).

[16] TASSO Coll., W. Braunschweig et al., Z. Phys. **C47** (1990) 187.

[17] G. Altarelli et al., Nucl. Phys.**B 160** (1979) 301.

[18] G. Altarelli et al., Phys. Rep. **81**, N1 (1982) 1.

[19] EMC Coll., J.J. Aubert et al., Phys.Lett. **B121** (1983) 87;
BCDMS Coll., A. C. Benvenuti et al., Phys. Lett. **B237** (1990) 592;
S. Dasu et al., Phys. Rev. **D49** (1994) 5641.

[20] TASSO Coll., R. Brandelik et al., Phys. Lett. **B114** (1982) 65.

[21] P. Nason, B. R. Webber, Nucl. Phys.**B 421** (1994) 473-517.

[22] P. Nason, B. R. Webber, Phys. Lett. **B 322** (1994) 405.

[23] OPAL Coll., R. Akers et al., Z. Phys. **C68** (1995) 203

[24] ALEPH Coll., D. Buskulic et al., Phys. Lett. **B357** (1995) 487.

[25] DELANA User's guide, DELPHI 89-44 PROG 137;
DELANA Reference manual, DELPHI 89-45 PROG 138, unpublished.

[26] Description of the DELPHI DST content, DELPHI 94-161 PROG 210, unpublished.

[27] PHDST package description, DELPHI 92-118 PROG 189, unpublished.

[28] "DELSIM Reference Manual", DELPHI Note 87-98 PROG 100 (1989), unpublished.

[29] DELPHI Coll., P. Abreu et al., CERN PPE 96-120 (1996), to be submitted to Zeit. Phys. **C**.

[30] DELPHI Coll., P. Abreu et al., Z. Phys. **C 65** (1995) 555.
G. V. Borisov, DELPHI Note 94-125 PROG 208, unpublished.

[31] DELPHI Coll., P. Abreu et al., Phys. Lett. **B377** (1996) 195.

[32] DELPHI Coll., P. Abreu et al., Phys. Lett. **B334** (1994) 435.

[33] DELPHI Coll., P. Abreu et al., Nucl. Phys. **B444** (1994) 3.

[34] E. Schyns, "NEWTAG – π, K, p Tagging for Delphi RICHes", DELPHI Note 96-103 RICH 89 (1996), unpublished.

[35] F. James, M. Roos, Comp. Phys. Comm. **10** (1975) 343.

[36] DELPHI Coll., P. Abreu et al., Phys. Lett. **B277** (1992) 371.

[37] P. J. Rijken and W. L. van Neerven, preprint INLO-PUB-04-96 (hep-ph9604436). To appear in Phys. Rev. Lett.

[38] DELPHI Coll., P. Abreu et al., Phys. Lett. **B311** (1993) 408.

[39] A. de Angelis, "Light Quark Hadrons in Hadronic Z Decays", CERN-PPE/95-135 (1995), proc. of the EPS-HEP Conf., Brussels (1995).

[40] DELPHI Coll., P. Abreu et al., Phys. Lett. **B355** (1995) 415.

[41] B. Lörstad, Int. J. Mod. Phys. **A4** (1989) 2861.

[42] T. Sjöstrand and L. Lönnblad, Phys. Lett. **B351** (1995) 293.

[43] T. Csörgő and S. Pratt, in "Proceedings of the Workshop on Relativistic Heavy Ion Physics", KFKI-1991-28/A, p75.

[44] NA44 Coll., H. Bøggild et al., Phys. Lett. **B349** (1995) 386.

[45] A. N. Makhlin and Yu. M. Sinyukov, Z. Phys. **C39** (1988)39.

[46] T. Csörgő and B. Lörstad, Lund University preprint LUNFD6/(NFFL-7082) 1994, Phys. Rev. C in press

[47] NA44 Coll., H. Beker et al., Phys. Rev. Lett. **74** (1995) 3340.

[48] NA35 Coll., T. Alber et al., Z. Phys. **C66** (1995) 77.

[49] TPC Coll., H. Aihara et al., Phys. Rev. **D31** (1985) 996.

[50] TASSO Coll., M. Althoff et al., Z. Phys. **C30** (1986) 355.

[51] Mark II Coll., I. Juricic et al., Phys. Rev. **D39** (1989) 1.

[52] OPAL Coll., P. D. Acton et al., Phys. Lett. **B267** (1991) 143.

[53] ALEPH Coll., D. Decamp et al., Z. Phys. **C54** (1992) 75.

[54] DELPHI Coll., P. Abreu et al., Phys.Lett. **B286** (1992) 201.

[55] B. Andersson and W. Hoffmann, Phys.Lett. **B169** (1986) 364.

[56] B. Lörstad, "m_t dependence of Boson Interferometry in SPb Reactions at CERN SPS". Talk given at the XXVII International Conference on High Energy Physics, Glasgow, Scotland, 20 - 27 July. Ref. gls0278.

Appendix A

The Performance of the DELPHI Hadron Calorimeter at LEP

The Performance of the Delphi Hadron Calorimeter at LEP

Delphi HAC Collaboration

I.Ajinenko[6], K.Beloous[6], J.Chudoba[5], S.Czellar[3], H.Herr[1], N.Jouravlev[2], N.Khovansky[2], P.Kluit[7], Z. Krumstein[2], K.Kurvinen[3], V.Lapin[6], R.Leitner[5], J .Masik [5] , A.Olchevski[2], J.Ridky[5], Yu.Sedykh[2], P.Sicho[5], O.Smirnova[2], O.Solovianov[6], O.Tchikilev[6], L.Tkatchev[2], Z.Tomsa[5], V.Vrba[5], W.S.Williams[4], A.M.Wetherell[1] and J.Zaslavsky[1]

[1]CERN, CH-1211 Geneva 23, Switzerland
[2]Joint Institute for Nuclear Research, Dubna, Head Post Office, P.O. Box 79, 101 000 Moscow, Russian Federation
[3]Research Institute for High Energy Physics, SEFT, P.O Box 9, FIN-00014 University of Helsinki, Finland
[4]Department of Physics, University of Oxford, Keble Road, Oxford OX1 3RH, UK
[5]FZU, Inst. of Physics of the C.A.S. High Energy Physics Division, Na Slovance 2, CS-180 40, Praha 8, Czech Republic and NC, Nuclear Centre of MFF, Charles University, Areal MFF, V Holesovickach 2, CS-180 00, Praha 8, Czech Republic
[6]Inst. for High Energy Physics, Serpukhov P.O. Box 35, Protvino (Moscow Region), Russian Federation
[7]NIKHEF-H, Postbus 41882, NL-1009 DB Amsterdam, The Netherlands

Abstract

The DELPHI Hadron Calorimeter was conceived more than ten years ago, as an instrument to measure the energy of hadrons and hadronic jets from e^+e^- collisions at the CERN collider LEP. In addition it was expected to provide a certain degree of discrimination between pions and muons. The detector is a rather simple and relatively inexpensive device consisting of around 20,000 limited streamer plastic tubes, with inductive pad read-out, embedded in the iron yoke of the 1.2 T DELPHI magnet. Its depth is at minimum 6.6 nuclear interaction lengths. The electronics necessary for the pad read-out was designed to have an adequate performance for a reasonable cost. This detector has proved over six years of operation to have an entirely satisfactory performance and great reliability; for example less than 1% of the streamer tubes have failed and electronic problems remain at the per mil level. During the past two years an improvement programme has been under way. It has been found possible to use the streamer tubes as strips, hence giving better granularity and particle tracking, by reading out the cathode of individual tubes. The constraints on this were considerable because of the inaccessibility of the detectors in the magnet yoke. However a cheap and feasible solution has been found. The cathode read-out leads to an improved energy resolution, better μ identification, a better π/μ separation and to possibilities of neutral particle separation. The simultaneous anode read-out of several planes of the endcaps of the detector will provide a fast trigger in the forward/backward direction which is an important improvement for LEP200. On the barrel the system will provide a cosmic trigger which is very useful for calibration as counting rates at LEP200 will be very low.

I. INTRODUCTION

The use of plastic limited streamer detectors has become popular in recent years due to their modest cost and good performance. This paper describes an application in elementary particle physics at the CERN collider LEP in the detector DELPHI [1] and the development of the large system over a number of years.

A general view of the DELPHI detector at LEP is shown in Fig.1. The Hadron Calorimeter (HAC) is situated in the return yoke of the superconducting magnet and is constructed of 2 endcaps (Forward Hadron Calorimeter), each consisting of 12 sectors, and the barrel composed of 24 modules. The hadron calorimeter covers nearly the full solid angle between 11° and 169° polar angle and completely azimuthally. Nearly 20,000 plastic tubes, working in the limited streamer mode [2] compose the detector. Overall, the length of tubes varies between 34 cm and 4.1 m depending upon their position.

Operation began with the start up of LEP in 1989 and over 6 years of operation only 180 tubes have definitely failed. The system is very stable and the operating voltage could be increased over 3 years, from 3.7 kV to 4 kV with a gas mixture of Ar: Isobutane: CO_2 of 10:30:60%. With smooth and relatively trouble free operation it was decided to exploit the substantial signals, first used simply for calorimetric purposes, in other ways, namely to provide some spatial tracking information and for fast triggering purposes. The following sections describes the 3 roles of the signal read-out.

II. THE PAD READ-OUT

All streamer tubes are glued on copper coated epoxy read-out boards and covered on top with an aluminium foil to have a constant capacity on both sides. The whole "sandwich" is packed in a mylar foil to avoid any contact with the iron yoke of the magnet.

The boards are scratched to create pads which cover always the same angle in $\Delta\Theta$ (2.96°) and $\Delta\phi$ (3.75°). The average dimensions of a pad is 20 x 30 cm. The boards are installed in the 20 slots of each of the 24 barrel modules and in

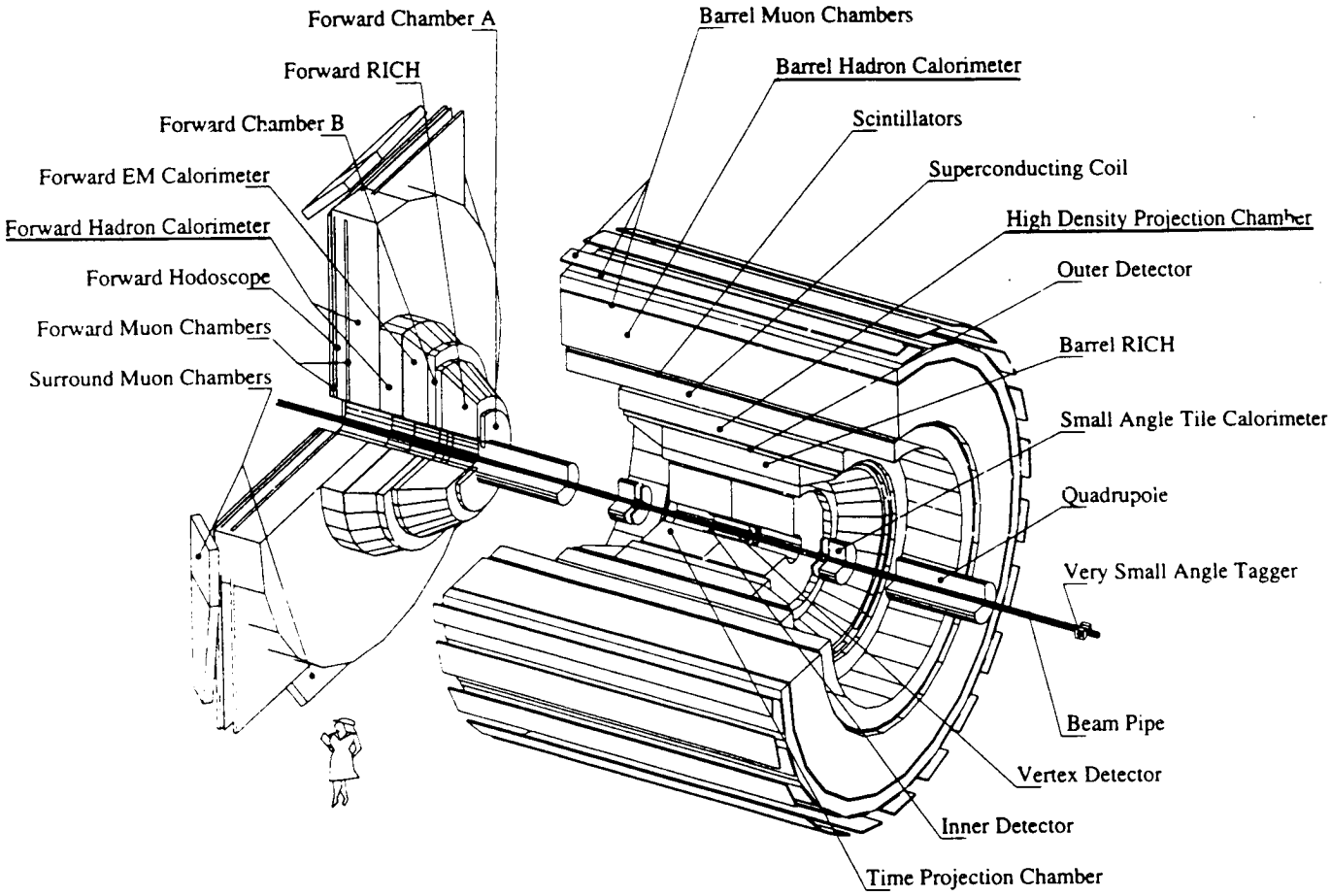

Fig. 1: The DELPHI detector

the 19 slots of each endcap sector. Five pads in the radial direction are connected electrically to form a unit called a "tower". In total there are 20,000 towers. The tower signals are amplified by charge sensitive amplifiers and the multiplexed output signals are digitized by 8 bit fast analog digital converters. The event data from the digital outputs of the front end electronics are transferred via 96 data cables to the Fastbus data acquisition system. During data taking the system has an efficiency of 98%. On average we have 50 noisy channels out of 20,000. 150 channels are disconnected because of faults.

Muons produced in $Z \rightarrow \mu^+\mu^-$ decays have been used for calibration. They have only 2% contamination from $\tau^+\tau^-$ channel and give a clean sample of penetrating particles.

Hadronic showers were used to set the energy scale. Calibration coefficients can be determined for each channel using muons, and from the azimutal symmetry of the total energy deposited in a sample of hadronic Z decays. The tower information is reconstructed as clusters. Fig. 2 shows the energy deposited in the HAC by muons from Z decay, and Fig. 3 shows the total energy deposited by hadronic Z decays (ignoring neutral showers). The calibration for hadronic showers has been checked using pions from single-prong τ decays which are required not to interact in the HPC.

In the barrel region ($52^o < \theta < 128^o$) the energy is then reconstructed with a resolution

$$\sigma(E)/E = 1.12/\sqrt{E/GeV}$$

Fig. 4 illustrates the energy resolution of the hadron calorimeter in two momentum intervals for charged particles depositing energy. It shows the ratio of the energy deposited in both the electromagnetic calorimeter HPC (High density Projection Chamber, Fig. 1) and in the HAC to the momentum of the charged particle. Identified electrons and muons were excluded from the plot.

The read-out system is very stable as can be seen from Fig. 5 which shows the uncorrected hadronic energy deposited in HAC during the 95 data taking.

In view of LEP200, it was felt desirable to improve the HAC both for calorimetry and muon identification by equipping the device with strips giving better granularity and even a certain degree of tracking. This could be achieved by the use of the streamer tubes themselves as 8 cm wide strips. The detectors are totally inaccessible in the magnet yoke but it was found that a signal pick off from the accessible cathodes was possible.

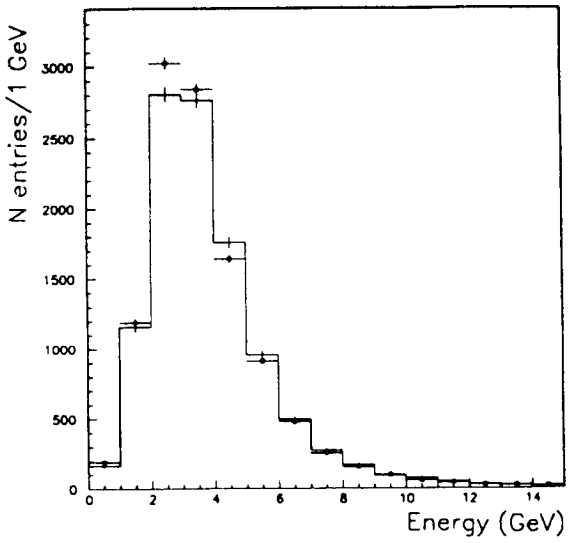

Fig. 2: Energy in HAC deposited by μ identified in the μ chambers (Fig. 1). Data (from the 1994 run) are shown by the points and simulation by the histogram

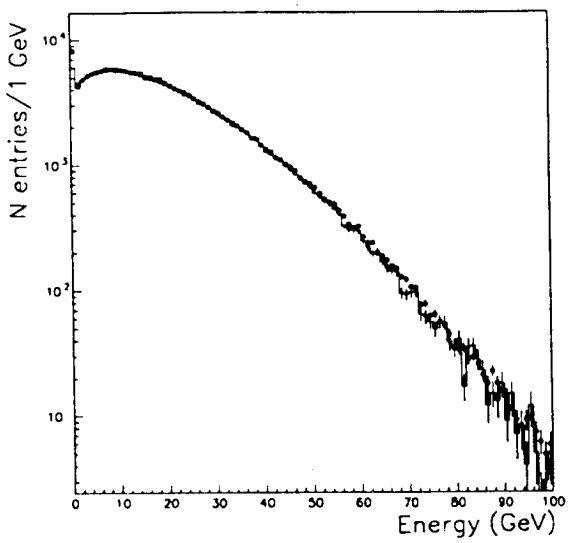

Fig. 3: Total energy deposited in the HAC by hadronic Z decays. Data (from the 1994 run) are shown by the points and simulation by the histogram

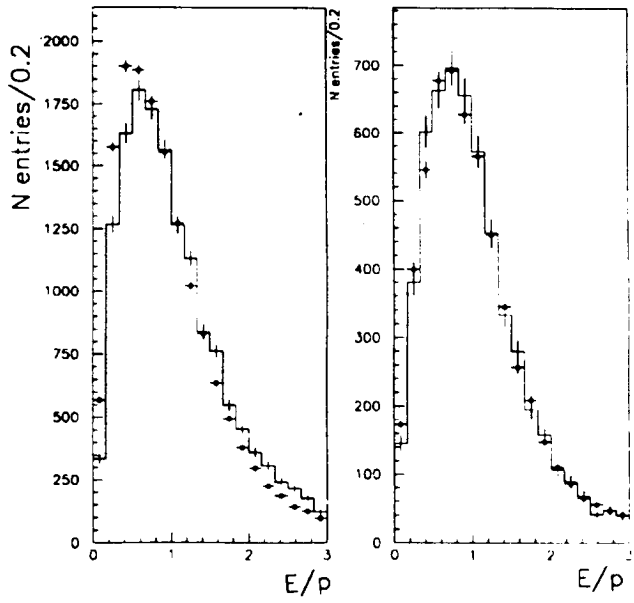

Fig 4: E/P ratio charged tracks with P<6 GeV (a) and P> 6 GeV (b) in Z decays. Here E is the full energy deposited and P the momentum of charged track.Data are shown by the points and simulation by the histogram

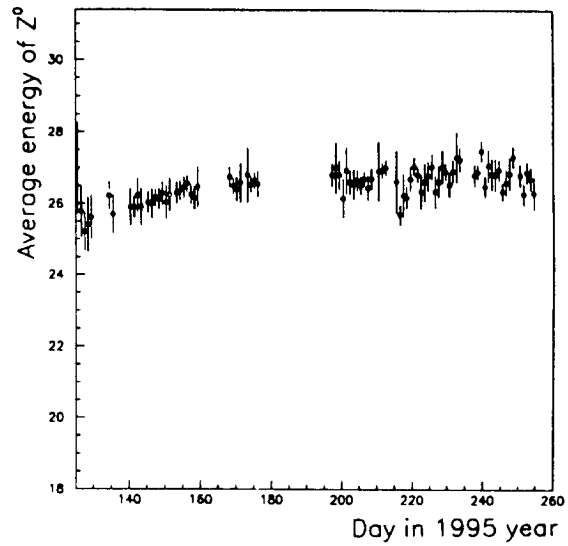

Fig. 5: Mean energy deposited in HAC by one Z vs. day in 1995

III. THE CATHODE READ-OUT

To improve the muon identification and the resolution within hadronic showers it is important to get a finer granularity. As the anode of the streamer tubes was not directly accessible, the problem could be solved by a resistive read-out of the cathodes of the individual limited streamer tubes, which are considered in this case as 8 cm wide strips. This improves the resolution by a factor 3 in ϕ and a factor 5 in the radial direction.

Due to the high resistivity (about 150 kΩ) of the cathode and to large variations around this average resistivity, the shape and the amplitude of the pulse depend very much on the position of the streamer. The amplitude is of the order of a few mV. As a consequence we use this system only to extract a 'yes/no' information. During the last four months of data taking the system was running reliably and delivered high quality data. More details about the electronics and the data acquisition system are given in ref. 3.

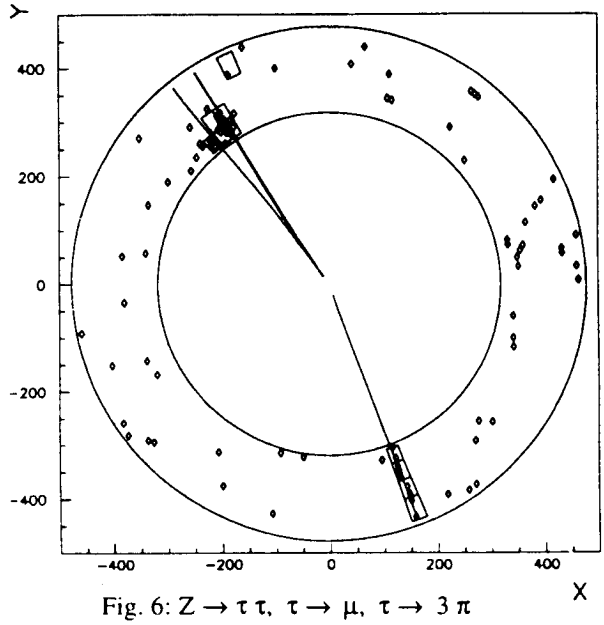

Fig. 6: $Z \rightarrow \tau\tau$, $\tau \rightarrow \mu$, $\tau \rightarrow 3\pi$

The software of the cathode read-out (CRO) for the barrel is now fully implemented into the complete chain of production and analysis. At the reconstruction level procedures of clustering and noise reduction were successfully tested. The extrapolation of tracks through the HAC was improved. The software for CRO analysis was developed and tested on $Z \rightarrow \mu^+\mu^-$ and $Z \rightarrow \tau^+\tau^-$.

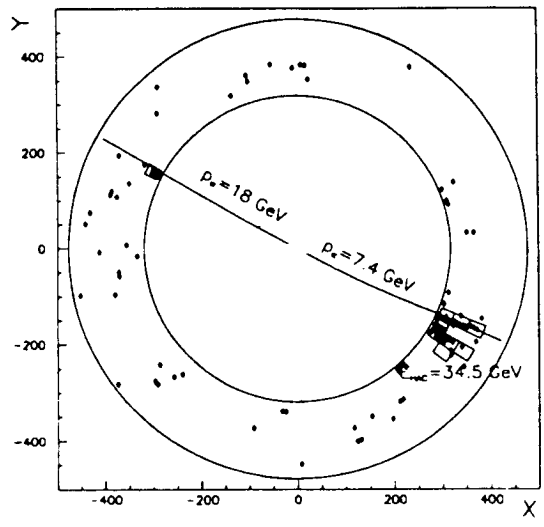

Fig. 7: K_L^0 candidate

The increased granularity of the calorimeter allows to see the cluster structure in much greater detail. Fig. 6 shows a $\tau\tau$ decay of Z^0 leading to π's and a μ. Only those tracks are shown which can be associated to an energy deposition in the pad read-out. In the picture one can clearly distinguish the narrow track of the muon in the lower part of the figure and the more scattered tracks of the pions in the upper part. The picture gives also an idea of the noise level of the cathode read-out. Fig. 7 shows a $\tau\tau$ decay. The big unassociated cluster may belong to a K_L^0 with an energy of about 27 GeV. It is close to the cluster corresponding to the π of 7.4 GeV momentum. The efficiency of the CRO electronics can be estimated from Fig. 8 which displays, for muons from $Z \rightarrow \mu\mu$, the dependence on the polar angle of the mean number of fired tubes along the muon track. For 100% electronics efficiency the Monte-Carlo simulation estimates this number to be 17.5. The maximum value of the efficiency is about 80% and decreases as the distance between the point where the particle crosses the tube and the read-out point increases. This is clearly shown in Fig. 8 where $\theta = 90^o$ corresponds to the maximum value of that distance.

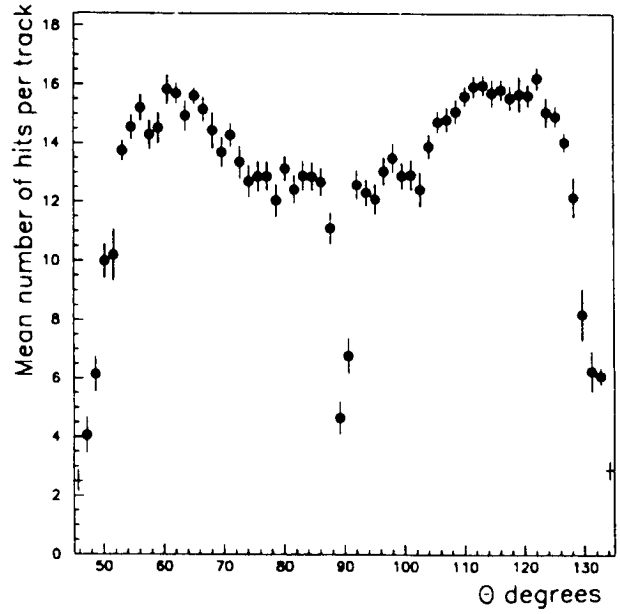

Fig. 8: Mean number of hits per muon track

The dip at 90^o is caused by the inefficiency of the tubes due to their endpieces although the tubes are staggered and overlapping. The decrease of efficiency at the edges of the distribution is due to particles escaping from the part of HAC which is instrumented up to now.

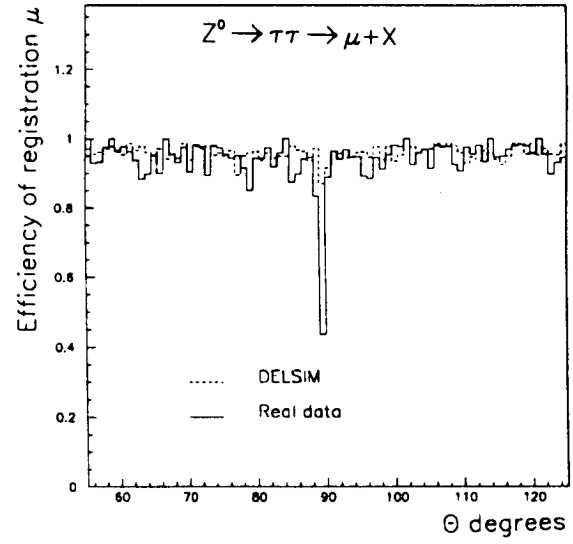

Fig. 9: Efficiency of CRO in Theta

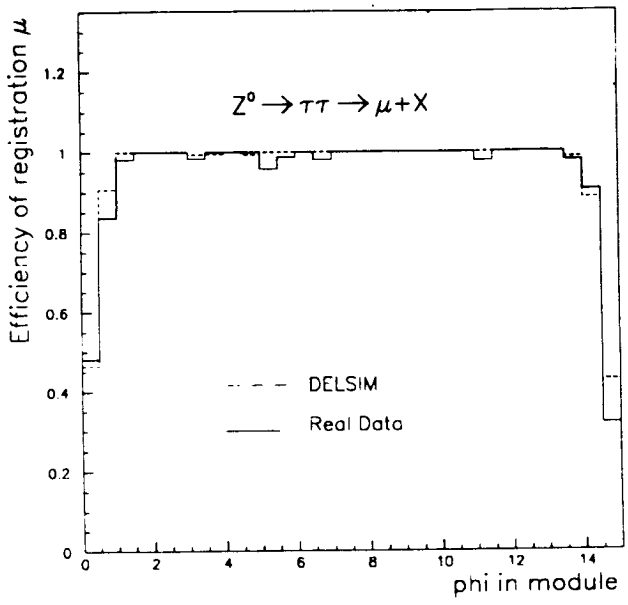

Fig. 10: Efficiency of CRO in Phi

The value of electronics efficiency is sufficient to keep the muon identification efficiency above 95% in the whole barrel, excluding the region close to $\theta = 90°$, already mentioned above (see Fig. 9). Muons with momentum > 2 GeV and with the signal in HAC > 1 GeV were considered as detected by CRO if five or more tubes were hit along the track path. One can see in Fig. 10 that inefficiency is mainly due to tracks which are going between modules or close to their border. This gives a reasonable chance to identify even soft muons which are stopped before reaching the muon chambers.

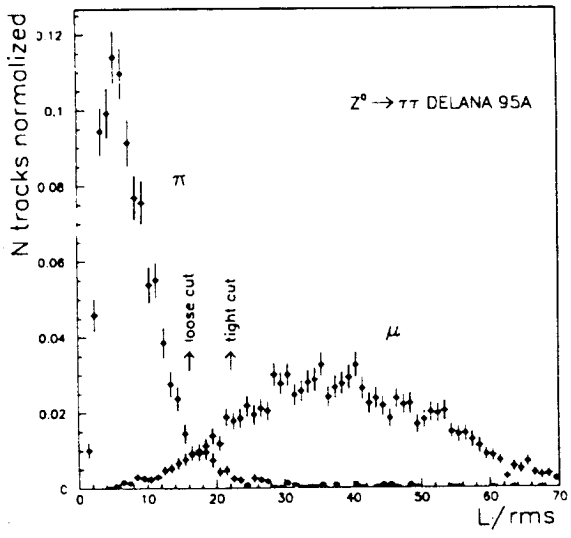

Fig. 11: π/μ separation in data

Fig. 11 and 12 illustrate the possibility of μ/π separation in data and in Monte Carlo. These figures show the distribution of the variable L/rms (L is the length and rms the width of the cluster) for μ and π identified in $Z \rightarrow \tau\tau$ decays. Applying a tight cut (marked on Fig. 11) gives a 85% efficiency for μ identification, with a 97% purity. Fig. 13 shows the correlation between pad and tube read-out. At low energies the behaviour is linear. However, at higher energies there is some "saturation" effect from the cathode read-out. This can be explained by the fact that the cathode read-out provides only a "yes/no" information from one tube independent of the number of particles passing the same tube. Since at higher energies the multiplicity also is higher, the probability that several particles are registered by the same tube increases.

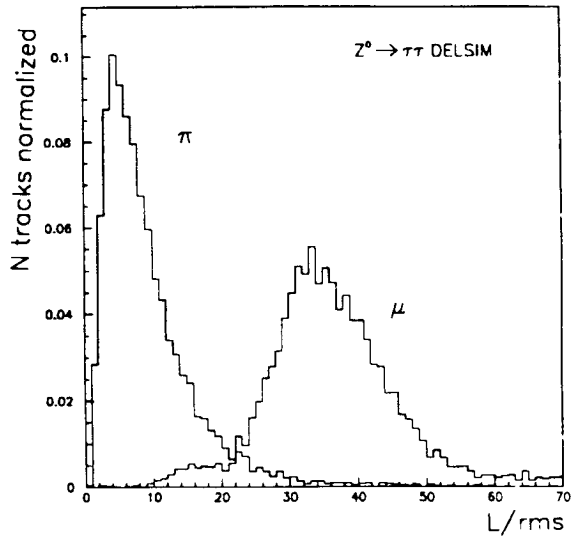

Fig. 12: μ/π separation in Monte-Carlo

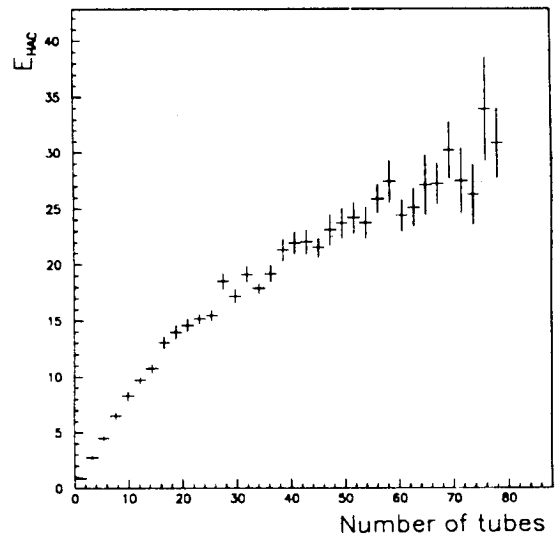

Fig. 13: Relation between Pad and Cathode read-out

IV. THE ANODE READ-OUT

For technical reasons it is not possible to read-out the anode of the individual streamer tubes. However, there is the possibility to pick up from the high voltage distribution of an individual plane a very fast signal which has a rise time of about 20 nsec and an amplitude around 2 mV. Fig. 14 shows

the principle. Combining several planes in an "or" provides a very fast trigger in the forward/backward direction which is very important for the LEP200 physics and a fast trigger for cosmics in the barrel region. Information on the bunch structure in LEP is also available (Fig. 15). This system is under test and will be put fully into operation for the start-up of LEP200 in 1996.

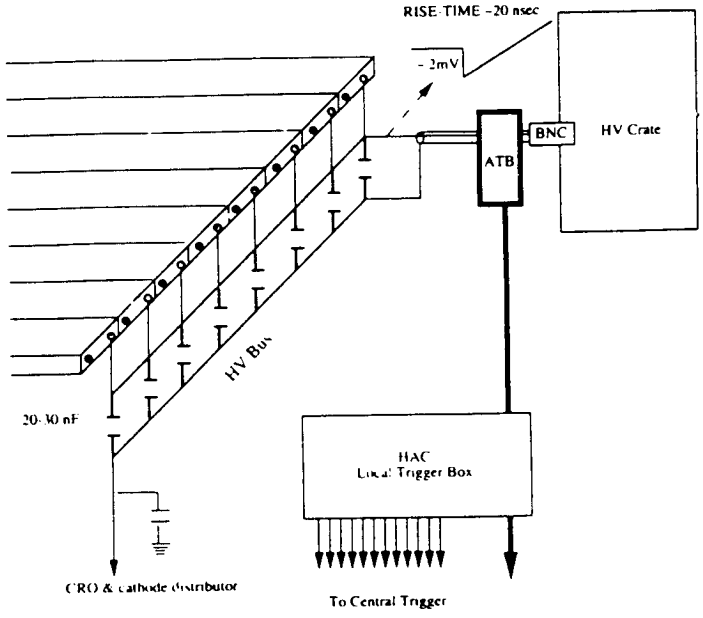

Fig. 14: Schematics of anode read-out

V. CONCLUSION

This paper has aimed to demonstrate the possibilities of improving a large detector based on plastic limited streamer tubes which was first put into operation in 1989. In spite of access problems to the hadron calorimeter in situ (Fig. 1) the possibility to provide strip information, for particle tracking, and fast signals for triggering has been proven, at a very reasonable cost in money and manpower.

Overall the hadron calorimetry will be improved as well as the hadron-lepton separation. The detection of short lived particles, both charged and neutral has become manageable.

It should be emphasised that the solutions described were imposed by the constraints on the operating detector but they may be valid in a wider context.

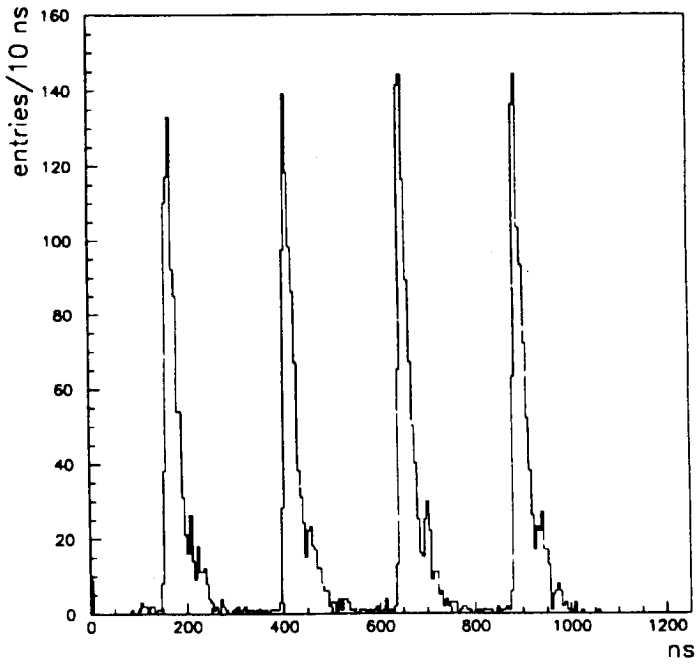

Fig. 15: Bunch structure in LEP seen by anode read-out

VI. ACKNOWLEDGEMENT

We are grateful to J.M. Maugain and R. Seiler for their interest and support. The Prague team has been supported by grant projects GA CR 202/96/0450 and GA AV CR A1010521.

REFERENCES

[1] DELPHI Collaboration, "The DELPHI detector at LEP", *Nucl. Instr.. Meth.* A303 (1991)233

[2] E. Iarocci, "Plastic Streamer tubes and their applications in high energy physics", *Nucl. Instr.. Meth.* 217 (1983)30

[3] I. Ajinenko et al., "The cathode read-out of the DELPHI Hadron Calorimeter", IEEE Trans. on Nucl. Science NS-42 (1995) 485.

Appendix B

The Cathode Read-out of the DELPHI Hadron Calorimeter

THE CATHODE READ-OUT OF THE DELPHI HADRON CALORIMETER

DELPHI Collaboration

I. Ajinenko[6], J. Chudoba[5], S. Czellar[3], V. Falaleev[6], H. Herr[1], N. Khovansky[2], P. Kluit[7], Z. Krumstein[2], K. Kurvinen[3], I. Lapin[6], R. Leitner[5], J. Masik [5] , V. Nikolaenko[6] A. Olchevski[2], J. Ridky[5], Yu. Sedykh[2], P. Sicho[5], O. Smirnova[2], O. Solovianov[6], O. Tchikilev[6], L. Tkatchev[2], Z. Tomsa[5], V. Vrba[5], W.S. Williams[4], A.M. Wetherell[1] and J. Zaslavsky[1]

[1]CERN, CH-1211 Geneva 23, Switzerland
[2]Joint Institute for Nuclear Research, Dubna, Head Post Office, P.O. Box 79, 101 000 Moscow, Russian Federation
[3]Research Institute for High Energy Physics, SEFT, P.O Box 9, FIN-00014 University of Helsinki, Finland
[4]Department of Physics, University of Oxford, Keble Road, Oxford OX1 3RH, UK
[5]FZU, Inst. of Physics of the C.A.S. High Energy Physics Division, Na Slovance 2, CS-180 40, Praha 8, Czech Republic and NC, Nuclear Centre of MFF, Charles University, Areal MFF, V Holesovickach 2, CS-180 00, Praha 8, Czech Republic
[6]Inst. for High Energy Physics, Serpukhov P.O. Box 35, Protvino (Moscow Region), Russian Federation
[7]NIKHEF-H, Postbus 41882, NL-1009 DB Amsterdam, The Netherlands

Abstract

To improve the identification and separation of leptons in the Hadron Calorimeter of DELPHI, one of the four LEP experiments at CERN, the possibility of a direct read-out of the cathodes of the 20,000 limited streamer tubes was studied and successfully tested on a small scale. A larger scale test started in June 1994. This new system which is independent of the present pad read-out provides a "yes/no" information. The combination of both read-out systems makes it possible to use the Hadron Calorimeter as a track detector. The result of these tests show that the cathode read-out provides a better π/μ separation, and improved detection of neutral long lived particles, enhanced discrimination of two showers and a more precise hadron energy measurement. It was decided to equip the whole detector with the new read-out, starting during the 94/95 shutdown.

I. INTRODUCTION

A general view of the DELPHI detector at LEP [1] is shown in Fig. 1. The Hadron Calorimeter forms an integral part of the structure and detection possibility of the whole system. Several studies [2,3] have shown the importance of a higher granularity of the DELPHI Hadron Calorimeter (HAC) for an improvement in the identification and separation of leptons and hadrons. Detailed studies have shown that due to practical limitations the best solution is to read-out the cathode signals of the 20,000 individual streamer tubes. Some measurements with cosmics by the Dubna group at CERN [4] and the Helsinki [5] group have shown the feasibility of this scheme. A detailed test during the end of the 1993 run on one endcap sector of the DELPHI detector and a larger scale test on 4+4 back-to-back barrel modules during the 94 run have proved that this scheme works in the DELPHI environment and provides data with a high efficiency.

II. THE PRESENT READ-OUT OF HAC

Nearly 20,000 Plastic Streamer Tubes (PST) [6] working in the limited streamer mode [7] are glued on 1872 read-out boards. On the individual boards there are a maximum of 64 pads all of which cover the same angle in $\Delta\varphi$ (3.75°) and $\Delta\theta$ (2.96°) seen from the collision point. The assembly of a board and the PST's is called a plane. Five planes are electrically connected in parallel and called a layer. Each PST has a width of 8 cm. In the barrel part of the detector they have a length around 3.5 m while in the endcap the length varies between 34 cm and 4 m.

There are two possibilities to increase the granularity:

- Reading out the individual planes
- Reading out the signals of the individual streamer tubes ("Strips")

The increase of the granularity by reading out the individual planes rather than the layers needs a major modification in cabling and a complete replacement of the present front end electronics. The new electronics would have to be five times more sensitive and have five times more channels, representing a big investment. The use of the individual streamer tubes as "strips" provides a 'yes/no' information with a much higher granularity than the individual plane read-out for a modest investment without interfering with

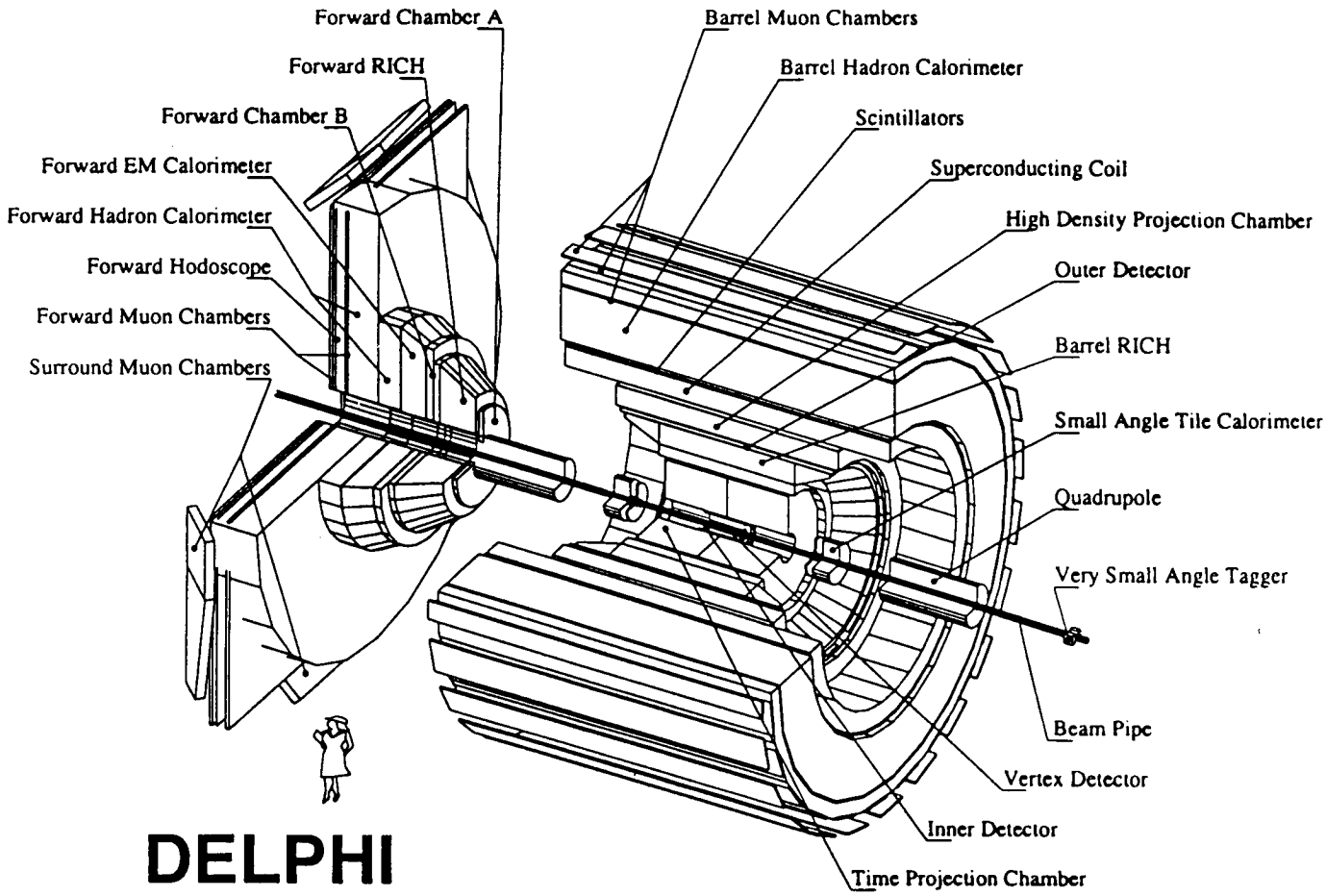

Fig. 1: The DELPHI detector

the present read-out. As a consequence we studied the feasibility of this solution and tested it in the DELPHI Experiment. A first test was done during the end of the 93 run on one endcap sector because of the easier access. During the 93/94 shutdown we prepared a setup in the barrel for 4+4 back-to-back modules. During the 94 run the Cathode Read-out was further developed and data have been taken.

III. PHYSICS APPLICATIONS

Under the assumption that a 'yes/no' signal is available we consider the following cases:

A. The separation of pions and muons

The existing HAC read-out provides a spatial resolution of the order of 20 by 20 by 25 cm^3, and there are four layers presently available (only three layers around 45 degrees). The tube read-out will provide information of hits in the 20 planes of the barrel and for technical reasons only in the twelve most outer planes of the 19 endcap planes. The size of a tube in the φ direction is 8 cm, which corresponds to an angle of 1.4° at the inner radius of the Calorimeter and 1.0° at the outer side.

The existing muon tagging procedure imposes a cut at 3 GeV. At the low momentum end of this range the multiple scattering gives an r.m.s. deviation of about 6 cm at the level of the muon chambers (see Fig. 1). Matching a track segment or hit from the muon chambers to a track from other detectors within that uncertainty will allow some contamination in a muon sample from hadrons that do not interact or have a secondary particle that goes beyond a normal absorption length. The probability that a hadron is accepted as a muon is of the order of 0.7% above 3 GeV with "tight" cuts for the Barrel Muon Chambers (MUB) (see Fig. 1). The principal limitation comes from the probability that a pion with a momentum in this range does not suffer any inelastic collision. This probability is of the order of 0.2%. The preliminary MC studies show that the pion contamination of muons in the energy range 3-4 GeV can be reduced with the help of information from tube read-out by 30-40%.

The possibility of muon identification below 3 GeV (down to less than about 2 GeV) is discussed in part 4A.

B. *Electrons/photons* *which reach the HAC in the "cracks" of HPC (see Fig. 1) or in the region between 36 and 40 degrees.*

A high-energy electromagnetic shower is well defined in the HAC. All energy is deposited in the 1st layer. The shower typically covers 3 towers and there is a strong energy deposition in the central tower. The probability that a fast electron (photon) reaches the HAC is of the order of a few percent. Presently this information is used for identification in the e^+e^- channel.

The information from the tube read-out can facilitate the recognition of the electromagnetic shower. More detailed studies of such signals, based on MC simulation and also on the real data, are needed and are in course of preparation.

IV. SIMULATION OF HAC CATHODE READ-OUT PERFORMANCE

The read-out of each individual streamer tube of HAC will increase both longitudinal (five times) and lateral (three times) segmentation of the calorimeter response. To test the feasibility of tube read-out we have chosen to check muon identification. The muons in Z^0 decays are encountered in μ^+ μ^- channel, τ decays and in $Z^0 \rightarrow q\bar{q}$ where they may indicate the flavour of the quarks (muons are present in 47% of $b\bar{b}$ events and in 14% of $c\bar{c}$ events). Our full DELSIM simulations of 1000 $Z^0 \rightarrow b\bar{b}$ decays as well as simulations of individual pions and muons showed essential improvement of HAC performance for muon identification as described in the following.

Muon identification

A. *Soft muons*

The existing muon tagging uses the muon chambers and is efficient only for muons with energies above 3 GeV. The study of the distribution of the stopping plane of the HAC barrel streamer tubes for muons from $Z^0 \rightarrow b\bar{b}$ decay shows that about 50% of muons stop before the inner muon chambers. Muons stopped in the 1st to 6th planes were not analyzed because of hadron showers background. To tag muons stopped in the region from the 7th plane to the inner muon chambers we applied a two step tagging procedure:

1. We assumed as muon candidate all straight tracks well isolated (without neighbour hits) above the 5th plane.
2. The momentum of charged tracks associated with muon candidates was compared with the range inside the HAC in order to further reduce the pion background. Extending the resulting efficiency to tag muons stopped inside HAC and the purity of the obtained sample for different energies of the muons to all hadronic decays ($Z^0 \rightarrow b\bar{b}$ is only 22% of all hadronic Z^0 decays) we expect 80% efficiency and approximately 50% purity for muon tagging in the region 1-2 GeV.

B. *Hard muons* *(detected also by the muon chambers)*

A similar analysis as for soft muons results in a very high purity of the muon sample (>90%) in $Z^0 \rightarrow b\bar{b}$ events. Moreover the detailed muon tracking by 20 planes of 8 cm wide streamer tubes predicts $R\varphi$ coordinate in barrel muon chambers with the precision of 16 mm independent of muon energy. The precision of muon extrapolation without cathode read-out is limited by multiple scattering and for 3 GeV muons is about 60 mm.

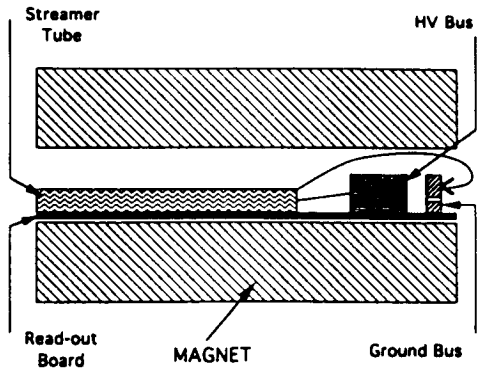

Fig. 2: Access to the cathode of the streamer tube

V. THE PRINCIPLE OF THE CATHODE READ-OUT (CRO)

An access to the anode of individual tubes is technically very difficult. However, to disconnect dead tubes we have rather easy access to the connection of the cathode to the ground (Fig. 2). A resistive coupling allows the read-out of the pulse from the cathode. Due to the high resistivity of the cathode, this pulse is relatively long and has an amplitude of a few mV. Its shape depends on the distance between the position of the streamer and the end of the tube (Fig. 3). As a consequence it was clear from the beginning that we can get only a 'yes/no' information.

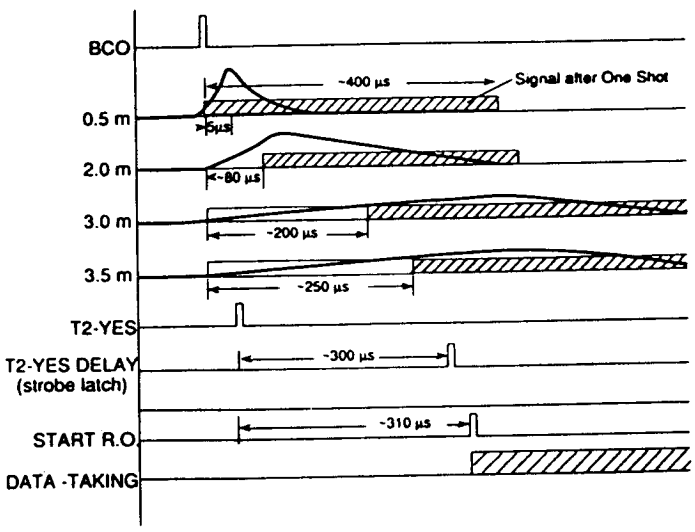

Fig. 3: Timing structure of HAC cathode signals

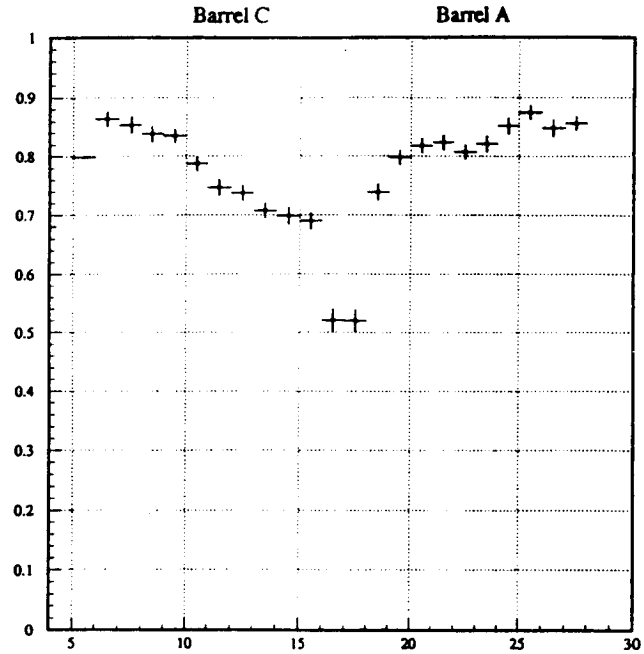

Fig. 7: Efficiency in dependence of θ

dependence of θ which means along the PST's. The drop in the center of the barrel can be explained by dead space due to the installation of the read-out boards and the tubes. The increase of the efficiency in the direction of the outer part of the barrel is caused by the increase of the ionisation due to a more and more inclined angle between tube and particle. In Fig. 8 the difference in azimuth angle between the HAC track and the incident muon direction is shown. The r.m.s. of the distribution is about 0.5° compared to 3.65° for the pad read-out. Similar results are obtained for muons from τ decays.

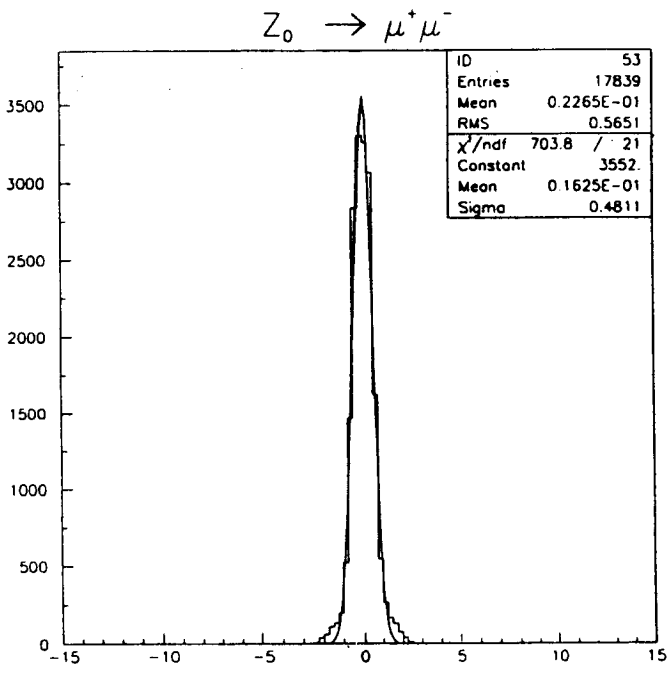

Fig. 8: Resolution of cathode read-out in φ direction

A further possibility is the detection and separation of neutral hadron showers. Due to the improved granularity neutral particles giving a shower in the hadron calorimeter can be clearly separated from showers from close by charged particles. Fig. 9 shows an event where a τ decays to K_L^0 and a charged pion. The K_L^0 interacted in the HPC and gave a shower in HAC that punches through to the barrel muon chambers. This shower can be separated from the shower of the nearby charged pion using the high granularity of the cathode read-out. The normal analysis of the existing HAC pad read-out associated all the hadron energy (41 GeV) with the pion (5 GeV/c). Thus the cathode read-out will allow the detection of long-living neutral hadrons and a better assignment of HAC energy to particular tracks.

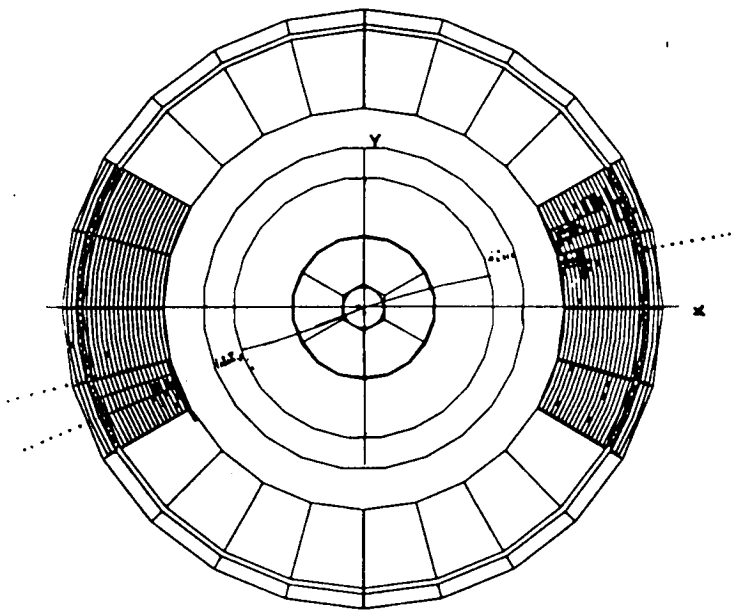

Fig. 9: Example of a $\tau^+\tau^-$ event. On the right side a charged track and a (K_L^0) are detected (■ cathode RO, □ Pad RO)

These results show that the cathode read-out will allow a better analysis of events. In particular :

1. A better pion-muon separation and more efficient and pure muon identification;
2. an improved detection of neutral long-lived hadrons (K_L^0) and neutrons and better two shower separation;
3. a more precise hadron energy measurement.

These new features are not only important for running at the Z^0 peak but also for the search for new particles and the suppression of backgrounds at LEP200.

A big advantage of the proposed scheme is that there is no interference with the present pad read-out system which stays untouched.

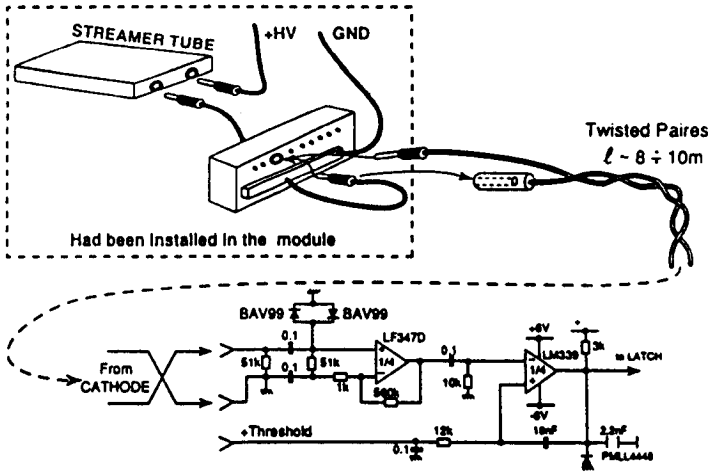

Fig. 4: Electronics for the read-out of one tube

VI. ELECTRONICS, DAS AND FIRST BEAM TESTS

The principle of the electronics is shown in Fig. 4 and 5. One front-end crate can read out the tubes of four modules. The information is sent to a Logical Control Unit which suppresses the read-out of empty channels to keep the dead-time as small as possible. As the cathode and the pad read-out are related to the same detector we will use the same data acquisition system (Octopuses, HFB). The raw data from the cathode and the pads are written in separate banks.

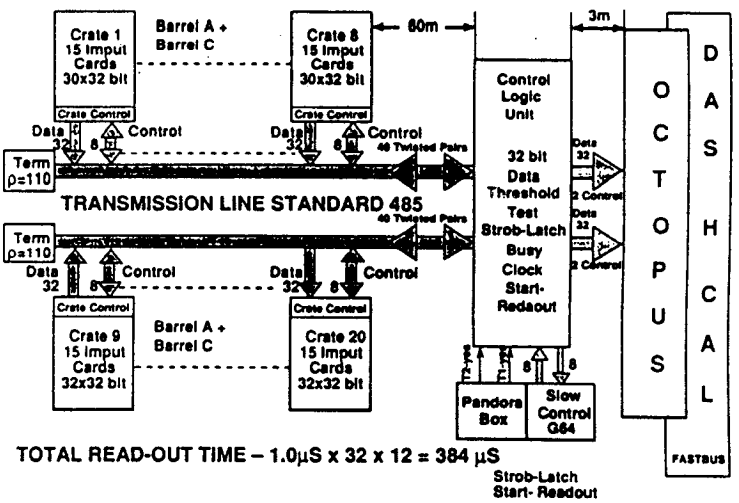

Fig. 5: Structure of the data transmission

The biggest uncertainty was the noise situation in the pit. As the initial measurements were very promising we equipped one endcap module with a prototype of the electronics. Because of the tube configuration the interpretation of the data is more difficult than in the barrel. But the endcaps were chosen because of the easier access and the possibility to disconnect the CRO electronics in the case that it would have created noise on the pad read-out and disturbed data taking. This is not possible for the barrel.

Because of the length of the read-out pulse we checked several settings of the timing to be sure to get the information from the whole length of the 4 m long streamer tubes. Data taking with the most efficient setting was done in the last week of the 1993 run with low statistics. The results were very encouraging and during the 93/94 shutdown 4+4 back-to-back barrel modules have been cabled for reading out the cathode signal.

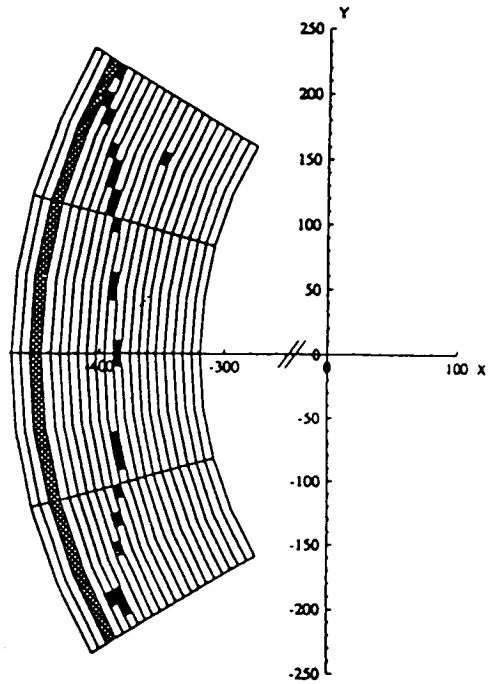

Fig.6: Cosmics event seen by the new cathode read-out (data)

Some inefficiency problems occurred at the beginning for signals from the end of the 3.5 m long tubes. Drastic noise reduction by better grounding and modifications in the read-out electronics improved the efficiency. A demonstration of the possibilities of the new system is given in Fig. 6 showing a cosmic ray event.

VII. PERFORMANCE

The performance of the cathode read-out has been studied using $Z^0 \rightarrow \mu^+ \mu^-$ and $Z^0 \rightarrow \tau^+\tau^-$ events.

On the average a muon gives 14 hits in the 20 layers. No hits are observed for 5% of the muons due to the dead zones between HAC modules. Fig. 8 shows the efficiency in

VIII. SUMMARY

The encouraging results obtained in a very short time with a limited cathode read-out system demonstrates the interest and utility in equipping the whole detector in this way. It was therefore decided to install the barrel read-out during the 94/95 shutdown and start to equip the endcaps as soon as the barrel system has been finished.

REFERENCES

[1] DELPHI Collaboration, "The DELPHI detector at LEP", *Nucl. Instr. Meth. A303 (1991)233*

[2] M. Dam, private communication (DELPHI Forum)

[3] P. Kluit, private communication (DELPHI Week in Strasbourg, 1994)

[4] Dubna variant of the HCAL streamer tubes cathode read-out (unpublished)

[5] K. Kurvinen, "Study of streamer tube cathode signals", Helsinki (unpublished)

[6] E. Iarocci, "Plastic streamer tubes and their applications in high energy physics", *NIM 217(1983) 30*

[7] G. Battistoni *et al*, "Influence of gas mixture and cathode material on limited streamer operation", *NIM 217(1983) 433*

Appendix C

On the determination of the longitudinal component of the fragmentation function of the process $e^+e^- \to h + X$ from DELPHI data

DELPHI Collaboration

DELPHI 95-11 PHYS 472
30 January, 1995

On the determination of the longitudinal component of the fragmentation function of the process $e^+e^- \longrightarrow h + X$ from DELPHI data

N.B.Skachkov, O.G.Smirnova, L.G.Tkatchev

Abstract

DELPHI data are analysed to obtain information on the behavior of longitudinal σ_L and transversal σ_T components of the cross section of inclusive hadron (h) production process $e^+e^- \longrightarrow h + X$. Similarly to the deep inelastic scattering, this provides an important test of the QCD predictions. The DELPHI result on the value of $A = \frac{\sigma_T - \sigma_L}{\sigma_T + \sigma_L}$ is found to be in a good agreement with the s-dependence extrapolation of the TASSO data.

1 Introduction

Study of the inclusive hadron production process $e^+e^- \longrightarrow h + X$ gives a possibility to test the QCD predictions on scaling violation effects in the fragmentation functions of this process $\overline{D}^h_{g(g)}(z, Q^2)$. This function describes the transition of quarks (q) and gluons (g), produced in e^+e^--annihilation, to the final state hadrons h. In the framework of QCD the fragmentation functions do obey the Altarelli-Parisi evolution equations analogous to those used for describing the structure functions of deep-inelastc scattering (DIS). QCD-analysis of the scaling violation effects in the fragmentation function, performed on the basis of these equations, allows one to extract the value of Λ and $\alpha_s(Q^2)$ [1] like in the DIS case.

An important information on the effects of scaling violation and on the shape of quark and gluon distributions comes from the region of small value of relative energy x. In this region, the effects caused by the spin degrees of freedom of the intermediate vector boson and the spin structure of quark current are involved. In the angular dependence of the cross section one can separate the contribution of the longitudinal structure function, that appears to give a nonzero contribution in a region of small x.

In the case of DIS an attention was paid to the problem of the behavior of the ratio of longitudinal σ_L and transversal σ_T cross sections connected to the corresponding structure functions ratio :

$$R(x, Q^2) = \frac{\sigma_L}{\sigma_T} = \frac{F_2(x, Q^2) - 2xF_1(x, Q^2)}{2F_1(x, Q^2)} = \frac{F_L(x, Q^2)}{F_T(x, Q^2)} \qquad (1)$$

This ratio has been measured by a number of collaborations. The data have shown that the value of $R(x, Q^2)$ decreases rapidly with increasing x. Interest in this problem stems from the fact that in contrast with all other structure functions $F_i(x, Q^2)$, $i = 1, 2, 3$ the longitudinal one $F_L(x, Q^2)$ becomes nonzero in the framework of QCD only after inclusion of α_s corrections, being thus strongly connected with the structure of perturbation theory.

As it has been shown by the TASSO collaboration [2] , the longitudinal combination of the structure functions describing the inclusive annihilation (IA) process $e^+e^- \longrightarrow h + X$ appears to be different from zero only at values of $x \leq 0.2$ ($x \stackrel{IA}{\equiv} Z \equiv 2pq/Q^2$).

In this note, we present the study of a longitudinal component of the

fragmentation function of inclusive annihilation, based on the analysis of the DELPHI data, collected during the 1992-93 running period.

The next section contains the discussion of selection criteria of the data used in our analysis. The third section presents the obtained results.

2 Selection Criteria

We have used the data collected by the DELPHI detector [3] at the center of mass energies around $\sqrt{s} = 91.2\ GeV$ ($86.2 \leq \sqrt{s} \leq 94.2\ GeV$). The trigger conditions and features of the tracking apparatus for the registration of charged multihadronic events can be found in [4].

For the analysis only charged particle tracks measured in the Time Projection Chamber (TPC) were used. The following standard [4] cuts were applied :

1. Impact parameter below $5\,cm$ in the transverse plane and below $10\,cm$ along the beam axis.
2. Particle momentum between 0.1 GeV/c and 50 GeV/c.
3. Measured track length above $50\,cm$.
4. Polar angle with respect to the beam axis between 25° and 155°.

Hadronic events were then selected by requiring that

1. Each of the forward and backward hemispheres contained a total charge energy larger than 3 GeV (assuming π mass for the particles).
2. The total energy of charged particles seen in both hemispheres together exceeded 15 GeV.
3. At least 5 charged particles are detected with momenta above $0.4\,GeV/c$.
4. The polar angle θ of the sphericity axis is between $40° < \theta < 140°$ (so that the events are well contained inside the TPC).

A total of about one million events were selected.

Data used for the analysis were divided into eight bins in the x_p variable, as it is shown in Tab.1. The cross sections are corrected for the detector

acceptance and resolution, for our kinematical cuts and for the initial state radiation. The correction factors values

$$C(x_p) = \left(\frac{1}{N}\frac{dn}{dx_p}\right)_{true} / \left(\frac{1}{N}\frac{dn}{dx_p}\right)_{reconstructed} \tag{2}$$

for every bin of x_p are shown in Fig.1 as a function of $\cos\theta$, where θ is the angle between the momentum of the produced inclusive charged hadron h and the axis of the e^- beam. The results shown in Fig.1 were obtained by using events generated with the JETSET 7.4 Lund Monte Carlo program and by simulating the DELPHI detector using the DELSIM package.

3 Separation of the Longitudinal Component of the Fragmentation Function

It is known that in the framework of the naive parton model with spin 1/2 quarks, the longitudinal component of the fragmentation function of the IA process $e^+e^- \longrightarrow h + X$ is equal to zero

$$\overline{F}^h_{0L}(x) = 0 \tag{3}$$

analogously to the case of the longitudinal structure function in DIS (see, for example, the review [5]). This component $\overline{F}^h_{0L}(x)$ is nonzero only in the framework of QCD where it is proportional to α_s [6, 7].

The function $\overline{F}^h_L(z, Q^2) \sim \alpha_s(Q^2)$ and is connected by definition with the scaling violation effects that are the main subject for the study with the QCD perturbation theory.

The cross section of the IA process in the case of the one-photon exchange, i.e. $e^+e^- \longrightarrow \gamma^* \longrightarrow h + X$, is given by the formula[1] ($x_p = p^h/p_{beam}$; $\nu = (E/m)\sqrt{s}$; $\beta = p^h/E^h \approx 1$)

$$\frac{d^2\sigma}{dx_p d\cos\theta} = \frac{\pi\alpha^2}{s} x_p (m\overline{W}_1 + \frac{1}{4} x_p \nu \overline{W}_2 \sin^2\theta) \tag{4}$$

[1] We follow the notation of [2], the results of which will be compared with ours in what follows.

where $Q^2 = s = (2E_{beam})^2$ and the structure functions $m\ \overline{W}_1 = \overline{F}_1$; $\nu\ \overline{W}_2 = \overline{F}_2$ are connected with the transverse and longitudinal structure functions through the relations :

$$\overline{F}_T(x,Q^2) = 2\overline{F}_1(x,Q^2) \tag{5}$$

$$\overline{F}_L(x,Q^2) = 2\overline{F}_1(x,Q^2) + x\overline{F}_2(x,Q^2) \tag{6}$$

Formula (4) is modified after the inclusion of the Z-boson exchange diagram. The parity violating effects that come from the quark electroweak current leads to the appearance of the $\overline{F}_3(x,Q^2)$ structure function and of the dependence on $\cos\theta$. Neglecting, at a first approximation, these rather small effects (proportional to $\varepsilon_W = 1 - \sin^2\theta_W$), one can see that the structure of the formula for the cross section near the Z-peak, defined by the square of the Z-boson exchange diagram, does not differ from that of (4).

Following [2] it is convenient to represent formula (1) in the following form :

$$\frac{d^2\sigma}{dx_p d\cos\theta} \sim 1 + A\cos^2\theta \tag{7}$$

where

$$A = \frac{\sigma_T - \sigma_L}{\sigma_T + \sigma_L} \tag{8}$$

σ_T and σ_L are the contributions to the cross section from transverse and longitudinal photons.

In order to study the behaviour of A at different x_p, one has to perform a fit to the function

$$f(\cos\theta) = p_1 \cdot (1 + p_2\cos^2\theta)$$

on the $\frac{d\sigma}{d\cos\theta}$ distributions in each of the chosen eight x_p intervals. Here p_1 and p_2 are free parameters and $p_2 \equiv A$.

The choice of x_p intervals was based on the necessity to have enough statistics in each of them. The statistics in the last four intervals ($x_p > 0.2$) is low, especially in the last one ($x_p > 0.5$) and the present DELPHI statistics does not allow us to split it more.

Since the value of A we are interested with is the fit parameter, it has both the parameter error and the systematic error. Parameter error is proportional to the uncertainty in the data and reflects the statistical error.

Systematic error on the A value is caused by certain analysis conditions, which stem from the detector features. We considered two main sources of these errors. The first one is connected to the tracking system features : the acceptance of the TPC allows us to measure tracks in the range of polar angles of $-0.9 < \cos\theta < 0.9$, but investigating the behaviour of the correction factor (see Fig.1), which is linear mainly in the region of $-0.7 < \cos\theta < 0.7$, one can conclude that it is reasonable to bound our acceptance to $|\cos\theta| < 0.7$. To study the systematics, caused by such a bounding, we performed the same data analysis changing the acceptanse from $|\cos\theta| < 0.35$ up to $|\cos\theta| < 0.9$, considering the average deviation of the A value as a systematic error.

The second source of systematics also could be seen from the correction factor behaviour (Fig.1) : there is an obvious nonlinearity in the region around $\cos\theta = 0$. This caused by existence of a small dead region in the DELPHI detector. Excluding from the fit points belonging to this region ($\theta = 90^\circ \pm 3^\circ$) we obtained a deviation of A which is considered as another contribution to the systematic error. This study showed also a significant decrease in the χ^2 of the fit (especially in well statistically defined intervals on x_p) after excluding points belonging to $\cos\theta \approx 0$ region from the fit.

Changes in the number of points in the fit procedure obviously affects the statistics. To separate the statistical contribution from above mentioned deviations of A value, we performed the same analysis for Monte Carlo generated distributions on the same statistics. Obtained deviations of A_{MC} were subtracted in quadrature from those of data in order to get the overall systematic error. The study of this error in a statistically well defined x_p intervals shows that after the subtraction of the statistical component it is clear that systematics does not depend on x_p and allows us to assign a common error for all intervals. Different approaches to its calculation (either for each interval separately or using mean values) give us the same result of $\sigma_{syst}^{fit} = 3\%$. The study of the other systematics caused by the detector features and data analysis was performed in [8] and showed $\sigma_{syst} = 3\%$.

The results of these fits are shown in Tab.1, Fig.2 and Fig.3 together with the TASSO data at lower energies (the horizontal bars show the size of x_p bins). From Fig.3 we see that the DELPHI data on A follow well the tendency of the $W = \sqrt{s}(= \sqrt{Q^2})$ - dependence of the same quantity, seen from the TASSO data. At the same time, the DELPHI results approach the value of 1 even at smaller values of x_p. That agrees with the QCD prediction for $\sigma_L \sim F_L \sim \alpha_s(Q^2) \sim \ln^{-1}(Q^2)$ to decrease with the increase of $W^2 = s = Q^2$.

In Fig.4 the value of A is plotted as a function of the particle momentum p. The universal behavior of $A(p)$ can be seen in the energy interval from 14 to 91 GeV. It means that the low energy part of the QCD jets is the same and unsensitive to the initial quark energy.

The same smooth continuation of the s-dependence tendency of the TASSO data is seen in Fig.5 (see the DELPHI data in Tab.1), where we have added new DELPHI data points for the ratio

$$\frac{-\overline{F}_2}{\overline{F}_1} = \frac{-\nu\overline{W}_2}{m\overline{W}_1} = \frac{4}{x}\frac{A}{1+A} \tag{9}$$

to the data at lower energies.

Using the A value one can calculate some other ratios of particular importance. In Fig.6 and in Tab.2 x_p-dependencies of the σ_L/σ_T, $\sigma_L/(\sigma_T+\sigma_L)$ and $\sigma_T/(\sigma_T+\sigma_L)$ values are shown. The ratio σ_L/σ_T must behave as a function

$$\Phi(x_p) \sim x_p^{\alpha}(1-x_p^{\beta})$$

which allows us to fit the distribution of A by the function $(1-\Phi(x_p))/(1+\Phi(x_p))$. The result of this fit is shown in Fig.2.

4 Summary

From the results of the analysis of the DELPHI data we can conclude that the data collected at the M_Z-peak support the tendency of the s-dependence of the fragmentation functions of the inclusive annihilation process measured by TASSO at lower energies. We can also conclude that the DELPHI statistics allows to perform a good separation of the longitudinal component of the fragmentation function $\overline{F}_L(x,Q^2)$.

The same analysis was done on the preliminary DELPHI 1993 data and 1992 data together. The results are shown in Tab.1 and are obviously of the same kind.

5 Acknowledgements

We are grateful to W. de Boer and A. Olshevski for useful discussions and suggestions.

References

[1] E. P. Velicheva, S. P. Kurlovich, N. B. Skachkov : JINR Rapid Comm. No.1[47]-91,p.5, JINR, Dubna, 1991.

[2] TASSO Collab., R. Brandelik et al.,Phys.Lett.**B**114(1982)65, TASSO Collab., W.Braunschweig et al., Z.Phys.,**c**47(1990)187.

[3] DELPHI Collab., P. Aarnio et al.,Nucl.Inst.Methods **A**303(1991)233.

[4] DELPHI Collab.,P. Aarnio et al..Phys.Lett.**B**240(1990)271.

[5] A. Buras, Rev.Mod.Phys. 52(1980)199.

[6] G. Altarelli et al.. Nucl.Phys.**B**160(1979)301.

[7] G. Altarelli et al.. Phys.Rep. 81, N1(1982)1.

[8] DELPHI Collab.,P. Abreu et al.. Phys.Lett.**B**311(1993)408.

[9] S. D. Drell, D. J. Levy, T.-M. Yan, Phys.Rev.**D1**(1970)1617.

x_p	1992 data A	1992 data $-\overline{F}_2/\overline{F}_1$	1992 + 1993 data A	1992 + 1993 data $-\overline{F}_2/\overline{F}_1$
$0.02-0.03$	0.491 ± 0.014	52.7 ± 2.2	0.507 ± 0.010	53.8 ± 1.6
$0.03-0.05$	0.678 ± 0.013	40.4 ± 1.3	0.670 ± 0.009	40.1 ± 0.9
$0.05-0.10$	0.811 ± 0.013	23.9 ± 0.7	0.808 ± 0.009	23.8 ± 0.5
$0.10-0.20$	0.963 ± 0.017	13.1 ± 0.5	0.953 ± 0.012	13.0 ± 0.3
$0.20-0.30$	1.036 ± 0.033	8.1 ± 0.5	1.034 ± 0.023	8.1 ± 0.4
$0.30-0.40$	1.001 ± 0.052	5.7 ± 0.6	1.011 ± 0.037	5.7 ± 0.4
$0.40-0.50$	0.929 ± 0.076	4.3 ± 0.7	0.969 ± 0.055	4.4 ± 0.5
$0.50-1.00$	0.949 ± 0.084	2.6 ± 0.4	0.913 ± 0.060	2.5 ± 0.3

Table 1: Values of $A = \frac{\sigma_T - \sigma_L}{\sigma_T + \sigma_L}$ and the ratio $-\overline{F}_2/\overline{F}_1$ calculated from the DELPHI data on $\frac{d^2\sigma}{dx_p d\cos\theta}$

x_p	σ_L/σ_T	$\sigma_L/(\sigma_T+\sigma_L)$	$\sigma_T/(\sigma_T+\sigma_L)$
$0.02-0.03$	0.342 ± 0.014	0.255 ± 0.007	0.745 ± 0.007
$0.03-0.05$	0.192 ± 0.013	0.161 ± 0.007	0.839 ± 0.007
$0.05-0.10$	0.104 ± 0.013	0.094 ± 0.007	0.906 ± 0.007
$0.10-0.20$	0.019 ± 0.017	0.018 ± 0.009	0.982 ± 0.009
$0.20-0.30$	-0.018 ± 0.033	-0.018 ± 0.016	1.018 ± 0.016
$0.30-0.40$	-0.001 ± 0.052	-0.001 ± 0.026	1.001 ± 0.026
$0.40-0.50$	0.037 ± 0.076	0.035 ± 0.038	0.965 ± 0.038
$0.50-1.00$	0.026 ± 0.084	0.026 ± 0.042	0.974 ± 0.042

Table 2: Different ratios for σ_L and σ_T

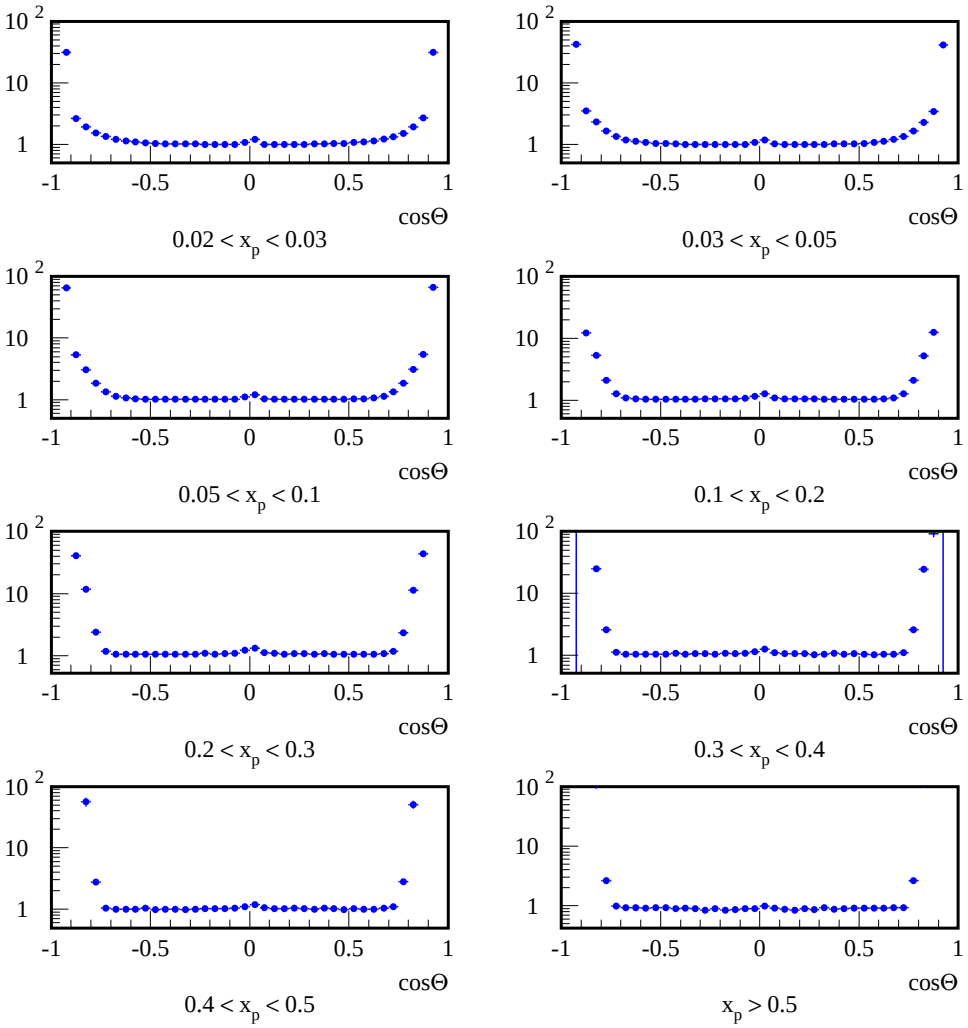

Figure 1: Correction factors.

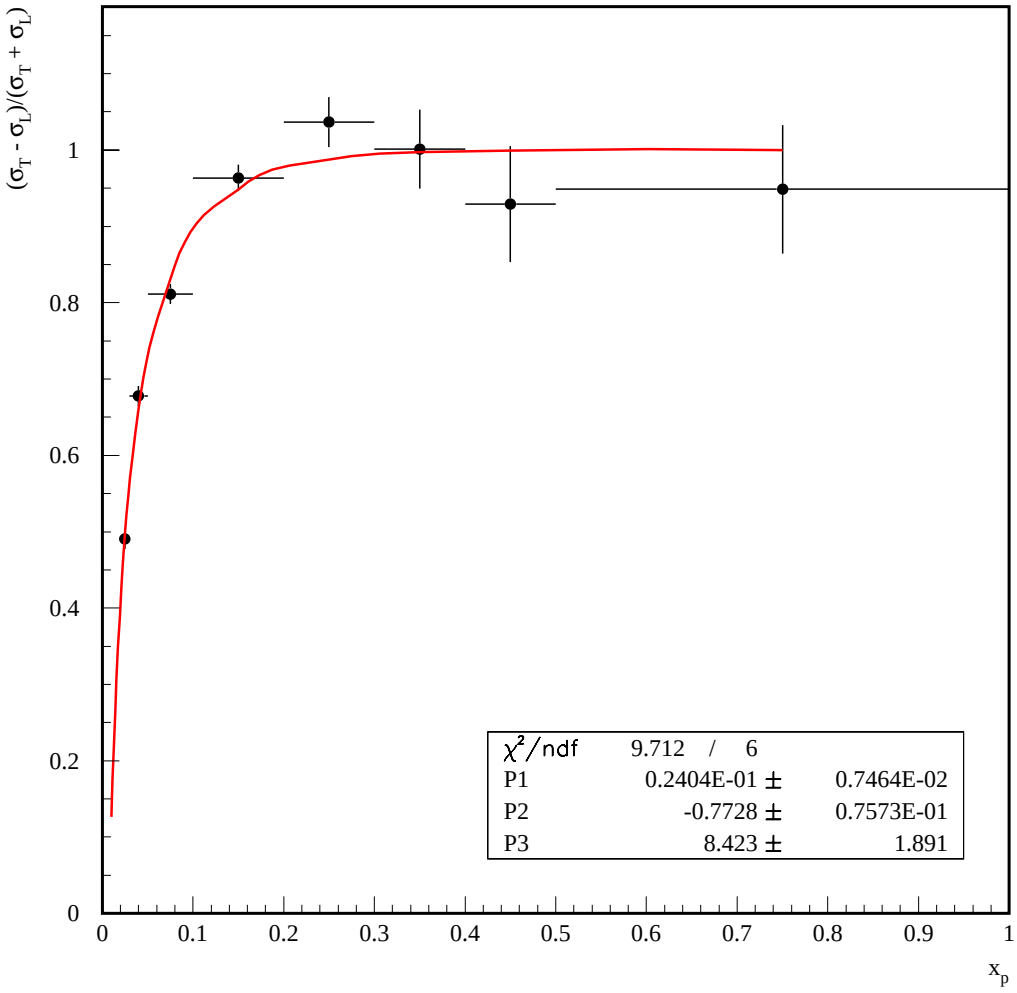

Figure 2: Plot of the $A = \frac{\sigma_T - \sigma_L}{\sigma_T + \sigma_L}$ values calculated in different x_p intervals as in Tab.1. Only statistical errors are shown. The curve is the result of the fit of the $A(x_p)$ dependence to the function $\mathbf{F}(x_p)$=$(1 - \Phi(x_p))/(1 + \Phi(x_p))$, were $\Phi(x_p) = P_1 \cdot x_p^{P_2}(1 - x_p)^{P_3}$

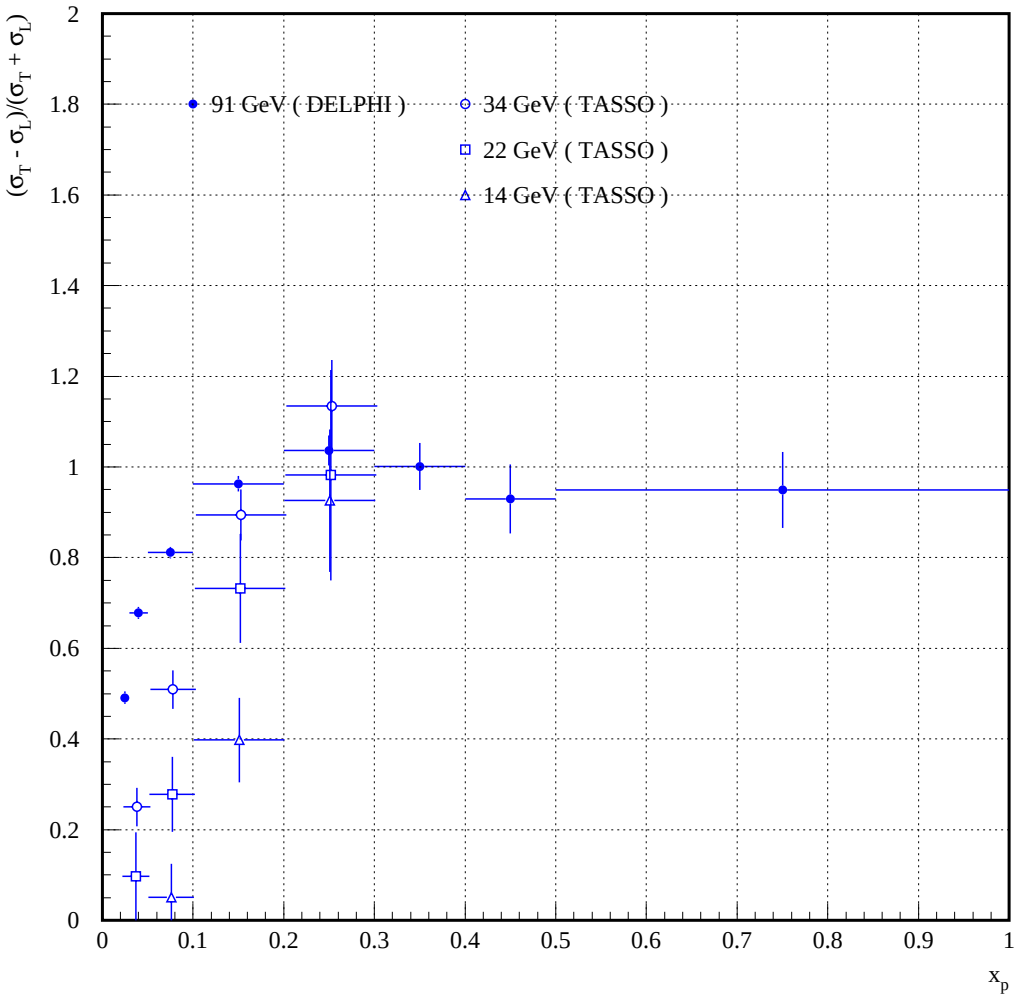

Figure 3: The DELPHI and TASSO results on the $A = \frac{\sigma_T - \sigma_L}{\sigma_T + \sigma_L}$

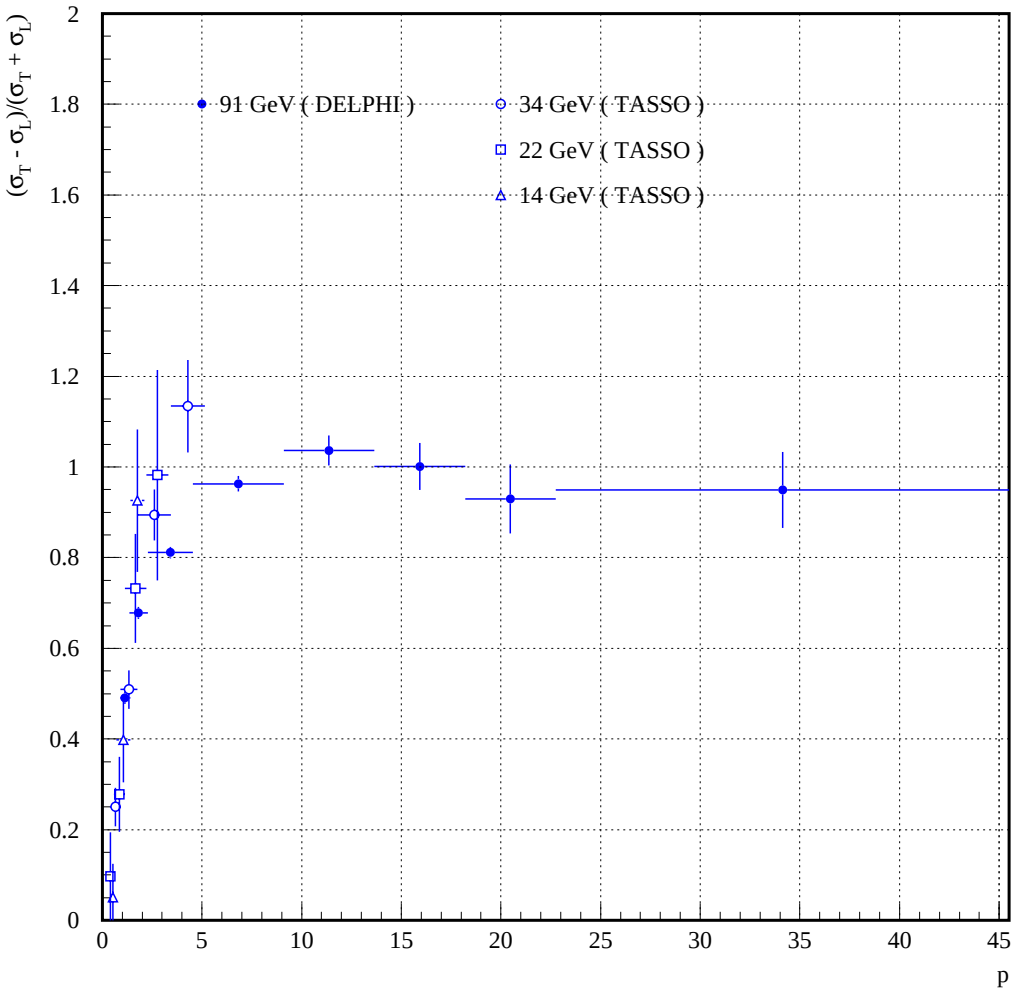

Figure 4: The DELPHI and TASSO results on the $A = \frac{\sigma_T - \sigma_L}{\sigma_T + \sigma_L}$ in p terms

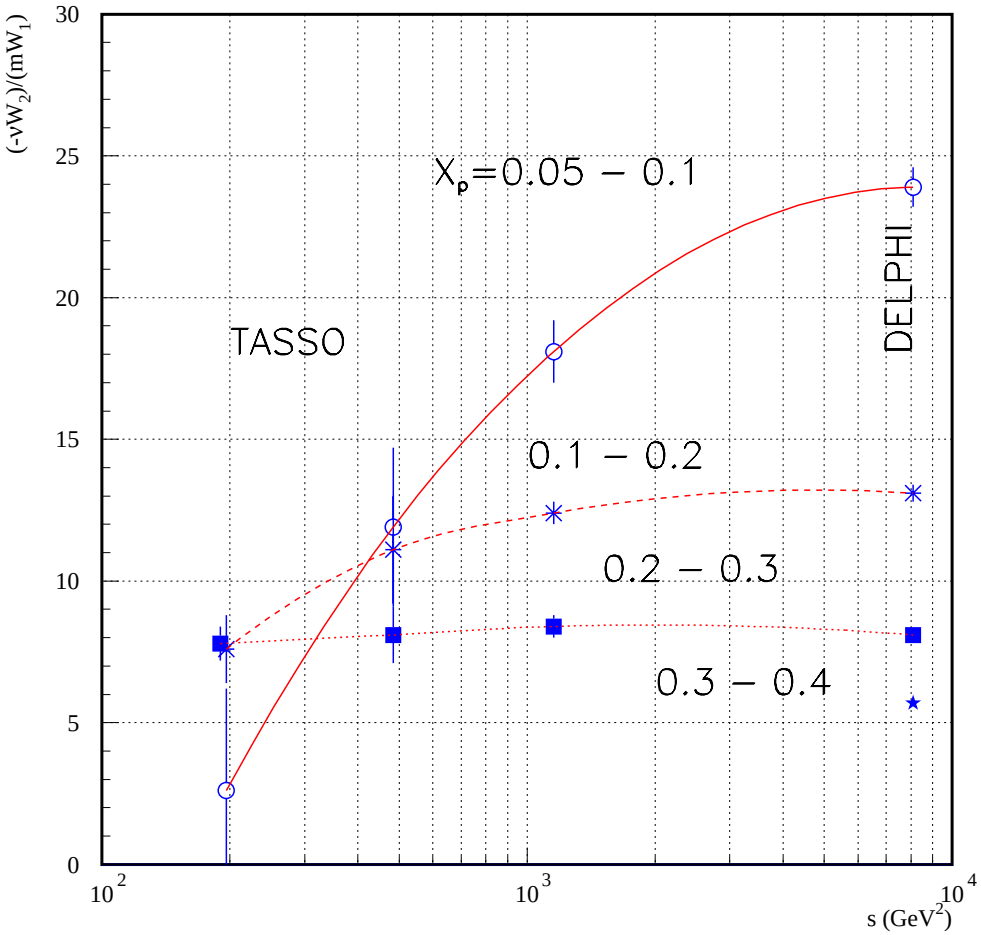

Figure 5: s-dependence of the $\frac{-\overline{F}_2}{\overline{F}_1}$ ratio for the DELPHI and TASSO data

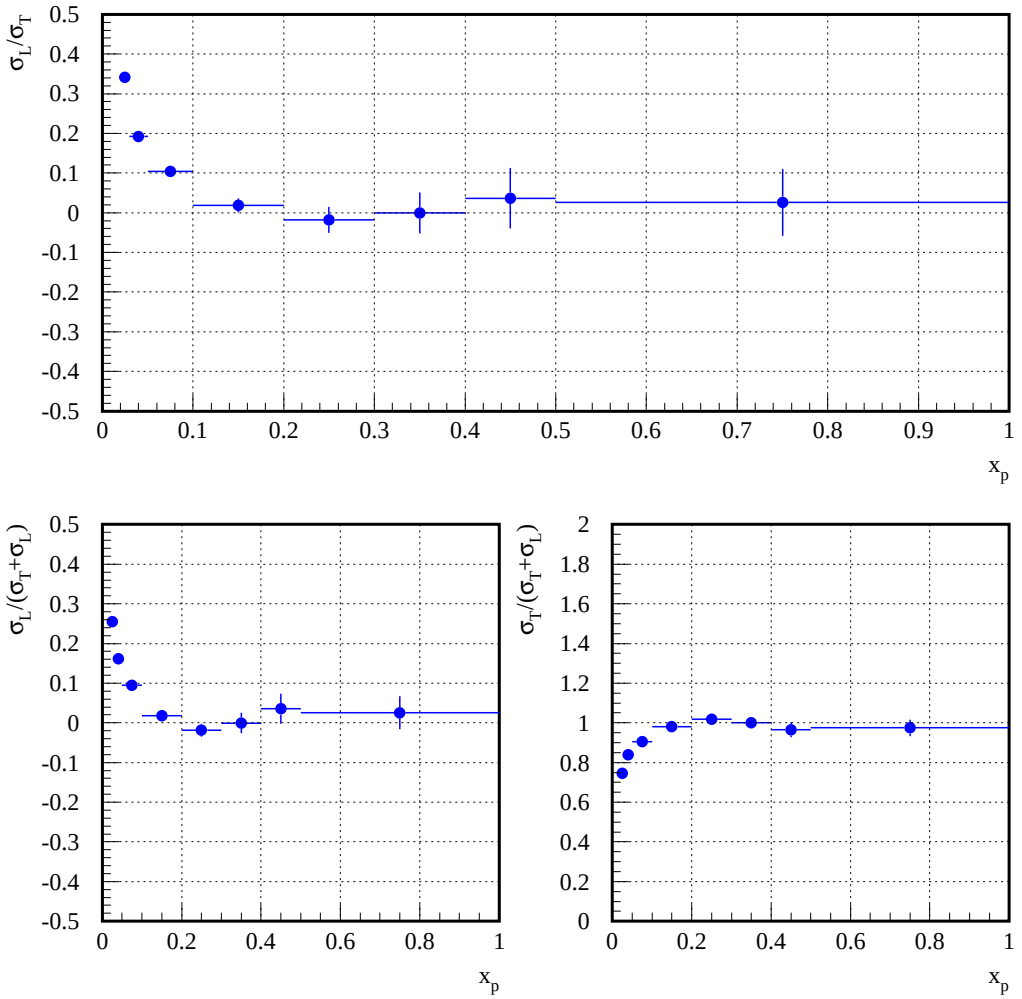

Figure 6: Different ratios for σ_L and σ_T that could be obtained from A values

Appendix D

Measurement of the Quark and Gluon Fragmentation Functions in Z^0 Hadronic Decays

EUROPEAN ORGANIZATION FOR NUCLEAR RESEARCH

CERN–PPE/97–108

8 August 1997

Measurement of the Quark and Gluon Fragmentation Functions in Z^0 Hadronic Decays

DELPHI Collaboration

Abstract

The transverse, longitudinal and asymmetric components of the fragmentation function are measured from the inclusive charged particles produced in e^+e^- collisions at LEP. As in deep inelastic scattering, these data are important for tests of QCD. The transverse σ_T and longitudinal σ_L components of the total hadronic cross section σ_{tot} are evaluated from the measured fragmentation functions. They are found to be $\sigma_T/\sigma_{tot} = 0.949 \pm 0.001(stat.) \pm 0.007(syst.)$ and $\sigma_L/\sigma_{tot} = 0.051 \pm 0.001(stat.) \pm 0.007(syst.)$ respectively. The strong coupling constant is calculated from σ_L/σ_{tot} in next-to-leading order of perturbative QCD, giving

$$\alpha_s(M_Z) = 0.120 \pm 0.002(stat.) \pm 0.013(syst.) \pm 0.007(scale) \ .$$

Including non-perturbative power corrections leads to

$$\alpha_s(M_Z) = 0.101 \pm 0.002(stat.) \pm 0.013(syst.) \pm 0.007(scale) \ .$$

The measured transverse and longitudinal components of the fragmentation function are used to estimate the mean charged multiplicity,

$$\langle n^{ch} \rangle = 21.21 \pm 0.01(stat.) \pm 0.20(syst.)$$

The fragmentation functions and multiplicities in $b\overline{b}$ and light quark events are compared. The measured transverse and longitudinal components of the fragmentation function allow the gluon fragmentation function to be evaluated.

(To be submitted to Zeit. f. Physik C)

P.Abreu[21], W.Adam[49], T.Adye[36], I.Ajinenko[41], G.D.Alekseev[16], R.Alemany[48], P.P.Allport[22], S.Almehed[24], U.Amaldi[9], S.Amato[46], P.Andersson[43], A.Andreazza[9], P.Antilogus[9], W-D.Apel[17], Y.Arnoud[14], B.Åsman[43], J-E.Augustin[25], A.Augustinus[30], P.Baillon[9], P.Bambade[19], F.Barao[21], M.Barbi[46], G.Barbiellini[45], D.Y.Bardin[16], G.Barker[9], A.Baroncelli[39], O.Barring[24], M.J.Bates[36], M.Battaglia[15], M.Baubillier[23], J.Baudot[38], K-H.Becks[51], M.Begalli[6], P.Beilliere[8], Yu.Belokopytov[9,52], K.Beloous[41], A.C.Benvenuti[5], C.Berat[14], M.Berggren[46], D.Bertini[25], D.Bertrand[2], M.Besancon[38], F.Bianchi[44], M.Bigi[44], M.S.Bilenky[16], P.Billoir[23], M-A.Bizouard[19], D.Bloch[10], M.Blume[51], M.Bonesini[27], W.Bonivento[27], M.Boonekamp[38], P.S.L.Booth[22], A.W.Borgland[4], G.Borisov[38,41], C.Bosio[39], O.Botner[47], E.Boudinov[30], B.Bouquet[19], C.Bourdarios[19], T.J.V.Bowcock[22], M.Bozzo[13], P.Branchini[39], K.D.Brand[35], T.Brenke[51], R.A.Brenner[47], R.C.A.Brown[9], P.Bruckman[18], J-M.Brunet[8], L.Bugge[32], T.Buran[32], T.Burgsmueller[51], P.Buschmann[51], S.Cabrera[48], M.Caccia[27], M.Calvi[27], A.J.Camacho Rozas[40], T.Camporesi[9], V.Canale[37], M.Canepa[13], F.Carena[9], L.Carroll[22], C.Caso[13], M.V.Castillo Gimenez[48], A.Cattai[9], F.R.Cavallo[5], V.Chabaud[9], Ph.Charpentier[9], L.Chaussard[25], P.Checchia[35], G.A.Chelkov[16], M.Chen[2], R.Chierici[44], P.Chliapnikov[41], P.Chochula[7], V.Chorowicz[25], J.Chudoba[29], V.Cindro[42], P.Collins[9], M.Colomer[48], R.Contri[13], E.Cortina[48], G.Cosme[19], F.Cossutti[45], J-H.Cowell[22], H.B.Crawley[1], D.Crennell[36], G.Crosetti[13], J.Cuevas Maestro[33], S.Czellar[15], J.Dahm[51], B.Dalmagne[19], G.Damgaard[28], P.D.Dauncey[36], M.Davenport[9], W.Da Silva[23], A.Deghorain[2], G.Della Ricca[45], P.Delpierre[26], N.Demaria[34], A.De Angelis[9], W.De Boer[17], S.De Brabandere[2], C.De Clercq[2], C.De La Vaissiere[23], B.De Lotto[45], A.De Min[35], L.De Paula[46], H.Dijkstra[9], L.Di Ciaccio[37], A.Di Diodato[37], A.Djannati[8], J.Dolbeau[8], K.Doroba[50], M.Dracos[10], J.Drees[51], K.-A.Drees[51], M.Dris[31], J-D.Durand[25,9], D.Edsall[1], R.Ehret[17], G.Eigen[4], T.Ekelof[47], G.Ekspong[43], M.Elsing[9], J-P.Engel[10], B.Erzen[42], E.Falk[24], G.Fanourakis[11], D.Fassouliotis[45], M.Feindt[9], P.Ferrari[27], A.Ferrer[48], S.Fichet[23], T.A.Filippas[31], A.Firestone[1], P.-A.Fischer[10], H.Foeth[9], E.Fokitis[31], F.Fontanelli[13], F.Formenti[9], B.Franek[36], A.G.Frodesen[4], R.Fruhwirth[49], F.Fulda-Quenzer[19], J.Fuster[48], A.Galloni[22], D.Gamba[44], M.Gandelman[46], C.Garcia[48], J.Garcia[40], C.Gaspar[9], U.Gasparini[35], Ph.Gavillet[9], E.N.Gazis[31], D.Gele[10], J-P.Gerber[10], L.Gerdyukov[41], R.Gokieli[50], B.Golob[42], P.Goncalves[21], G.Gopal[36], L.Gorn[1], M.Gorski[50], Yu.Gouz[44,52], V.Gracco[13], E.Graziani[39], C.Green[22], A.Grefrath[51], P.Gris[38], G.Grosdidier[19], K.Grzelak[50], S.Gumenyuk[41], M.Gunther[47], J.Guy[36], F.Hahn[9], S.Hahn[51], Z.Hajduk[18], A.Hallgren[47], K.Hamacher[51], F.J.Harris[34], V.Hedberg[24], R.Henriques[21], J.J.Hernandez[48], P.Herquet[2], H.Herr[9], T.L.Hessing[34], J.-M.Heuser[51], E.Higon[48], S-O.Holmgren[43], P.J.Holt[34], D.Holthuizen[30], S.Hoorelbeke[2], M.Houlden[22], J.Hrubec[49], K.Huet[2], K.Hultqvist[43], J.N.Jackson[22], R.Jacobsson[43], P.Jalocha[9], R.Janik[7], Ch.Jarlskog[24], G.Jarlskog[24], P.Jarry[38], B.Jean-Marie[19], E.K.Johansson[43], L.Jonsson[24], P.Jonsson[24], C.Joram[9], P.Juillot[10], M.Kaiser[17], F.Kapusta[23], K.Karafasoulis[11], E.Karvelas[11], S.Katsanevas[25], E.C.Katsoufis[31], R.Keranen[4], Yu.Khokhlov[41], B.A.Khomenko[16], N.N.Khovanski[16], B.King[22], N.J.Kjaer[30], O.Klapp[51], H.Klein[9], P.Kluit[30], D.Knoblauch[17], P.Kokkinias[11], M.Koratzinos[9], C.Kourkoumelis[3], O.Kouznetsov[16], M.Krammer[49], C.Kreuter[9], I.Kronkvist[24], Z.Krumstein[16], W.Krupinski[18], P.Kubinec[7], W.Kucewicz[18], K.Kurvinen[15], C.Lacasta[9], I.Laktineh[25], J.W.Lamsa[1], L.Lanceri[45], D.W.Lane[1], P.Langefeld[51], J-P.Laugier[38], R.Lauhakangas[15], G.Leder[49], F.Ledroit[14], V.Lefebure[2], C.K.Legan[1], A.Leisos[11], R.Leitner[29], J.Lemonne[2], G.Lenzen[51], V.Lepeltier[19], T.Lesiak[18], M.Lethuillier[38], J.Libby[34], D.Liko[9], A.Lipniacka[43], I.Lippi[35], B.Loerstad[24], J.G.Loken[34], J.M.Lopez[40], D.Loukas[11], P.Lutz[38], L.Lyons[34], J.MacNaughton[49], G.Maehlum[17], J.R.Mahon[6], A.Maio[21], T.G.M.Malmgren[43], V.Malychev[16], F.Mandl[49], J.Marco[40], R.Marco[40], B.Marechal[46], M.Margoni[35], J-C.Marin[9], C.Mariotti[9], A.Markou[11], C.Martinez-Rivero[33], F.Martinez-Vidal[48], S.Marti i Garcia[22], J.Masik[29], F.Matorras[40], C.Matteuzzi[27], G.Matthiae[37], M.Mazzucato[35], M.Mc Cubbin[22], R.Mc Kay[1], R.Mc Nulty[9], G.Mc Pherson[22], J.Medbo[47], C.Meroni[27], S.Meyer[17], W.T.Meyer[1], M.Michelotto[35], E.Migliore[44], L.Mirabito[25], W.A.Mitaroff[49], U.Mjoernmark[24], T.Moa[43], R.Moeller[28], K.Moenig[9], M.R.Monge[13], P.Morettini[13], H.Mueller[17], K.Muenich[51], M.Mulders[30], L.M.Mundim[6], W.J.Murray[36], B.Muryn[14,18], G.Myatt[34], T.Myklebust[32], F.Naraghi[14], F.L.Navarria[5], S.Navas[48], K.Nawrocki[50], P.Negri[27], W.Neumann[51], N.Neumeister[49], R.Nicolaidou[3], B.S.Nielsen[28], M.Nieuwenhuizen[30], V.Nikolaenko[10], M.Nikolenko[10,16], P.Niss[43], A.Nomerotski[35], A.Normand[22], A.Nygren[24], W.Oberschulte-Beckmann[17], V.Obraztsov[41], A.G.Olshevski[16], A.Onofre[21], R.Orava[15], G.Orazi[10], S.Ortuno[48], K.Osterberg[15], A.Ouraou[38], P.Paganini[19], M.Paganoni[9,27], S.Paiano[5], R.Pain[23], H.Palka[18], Th.D.Papadopoulou[31], K.Papageorgiou[11], L.Pape[9], C.Parkes[34], F.Parodi[13], U.Parzefall[22], A.Passeri[39], M.Pegoraro[35], L.Peralta[21], H.Pernegger[49], M.Pernicka[49], A.Perrotta[5], C.Petridou[45], A.Petrolini[13], M.Petrovyck[41], H.T.Phillips[36], G.Piana[13], F.Pierre[38], M.Pimenta[21], E.Piotto[35], T.Podobnik[34], O.Podobrin[9], M.E.Pol[6], G.Polok[18], P.Poropat[45], V.Pozdniakov[16], P.Privitera[37], N.Pukhaeva[16], A.Pullia[27], D.Radojicic[34], S.Ragazzi[27], H.Rahmani[31], P.N.Ratoff[20], A.L.Read[32], M.Reale[51], P.Rebecchi[9], N.G.Redaelli[27], M.Regler[49], D.Reid[9], R.Reinhardt[51], P.B.Renton[34], L.K.Resvanis[3], F.Richard[19], J.Ridky[12], G.Rinaudo[44], O.Rohne[32], A.Romero[44], P.Ronchese[35], L.Roos[23], E.I.Rosenberg[1], P.Rosinsky[7], P.Roudeau[19], T.Rovelli[5], V.Ruhlmann-Kleider[38], A.Ruiz[40], H.Saarikko[15], Y.Sacquin[38], A.Sadovsky[16], G.Sajot[14], J.Salt[48], M.Sannino[13], H.Schneider[17], U.Schwickerath[17], M.A.E.Schyns[51], G.Sciolla[44], F.Scuri[45], P.Seager[20], Y.Sedykh[16], A.M.Segar[34], A.Seitz[17], R.Sekulin[36], L.Serbelloni[37], R.C.Shellard[6], A.Sheridan[22], P.Siegrist[9,38], R.Silvestre[38], F.Simonetto[35], A.N.Sisakian[16], T.B.Skaali[32], N.Skatchkov[16], G.Smadja[25], N.Smirnov[41], O.Smirnova[24], G.R.Smith[36], A.Sokolov[41], O.Solovianov[41], R.Sosnowski[50], D.Souza-Santos[6], T.Spassov[21], E.Spiriti[39], P.Sponholz[51], S.Squarcia[13], D.Stampfer[9], C.Stanescu[39], S.Stanic[42], S.Stapnes[32], I.Stavitski[35], K.Stevenson[34], A.Stocchi[19], R.Strub[10], B.Stugu[4], M.Szczekowski[50], M.Szeptycka[50], T.Tabarelli[27], J.P.Tavernet[23], O.Tchikilev[41], F.Tegenfeldt[47], F.Terranova[27], J.Thomas[34], A.Tilquin[26],

J.Timmermans[30], L.G.Tkatchev[16], T.Todorov[10], S.Todorova[10], D.Z.Toet[30], A.Tomaradze[2], B.Tome[21], A.Tonazzo[27], L.Tortora[39], G.Transtromer[24], D.Treille[9], G.Tristram[8], A.Trombini[19], C.Troncon[27], A.Tsirou[9], M-L.Turluer[38], I.A.Tyapkin[16], M.Tyndel[36], S.Tzamarias[11], B.Ueberschaer[51], O.Ullaland[9], V.Uvarov[41], G.Valenti[5], E.Vallazza[45], G.W.Van Apeldoorn[30], P.Van Dam[30], W.K.Van Doninck[2], J.Van Eldik[30], A.Van Lysebetten[2], N.Vassilopoulos[34], G.Vegni[27], L.Ventura[35], W.Venus[36], F.Verbeure[2], M.Verlato[35], L.S.Vertogradov[16], D.Vilanova[38], P.Vincent[25], L.Vitale[45], E.Vlasov[41], A.S.Vodopyanov[16], V.Vrba[12], H.Wahlen[51], C.Walck[43], C.Weiser[17], A.M.Wetherell[9], D.Wicke[51], J.H.Wickens[2], M.Wielers[17], G.R.Wilkinson[9], W.S.C.Williams[34], M.Winter[10], T.Wlodek[19], J.Yi[1], K.Yip[34], O.Yushchenko[41], F.Zach[25], A.Zaitsev[41], A.Zalewska[9], P.Zalewski[50], D.Zavrtanik[42], E.Zevgolatakos[11], N.I.Zimin[16], G.C.Zucchelli[43], G.Zumerle[35]

[1] Department of Physics and Astronomy, Iowa State University, Ames IA 50011-3160, USA
[2] Physics Department, Univ. Instelling Antwerpen, Universiteitsplein 1, B-2610 Wilrijk, Belgium
and IIHE, ULB-VUB, Pleinlaan 2, B-1050 Brussels, Belgium
and Faculté des Sciences, Univ. de l'Etat Mons, Av. Maistriau 19, B-7000 Mons, Belgium
[3] Physics Laboratory, University of Athens, Solonos Str. 104, GR-10680 Athens, Greece
[4] Department of Physics, University of Bergen, Allégaten 55, N-5007 Bergen, Norway
[5] Dipartimento di Fisica, Università di Bologna and INFN, Via Irnerio 46, I-40126 Bologna, Italy
[6] Centro Brasileiro de Pesquisas Físicas, rua Xavier Sigaud 150, RJ-22290 Rio de Janeiro, Brazil
and Depto. de Física, Pont. Univ. Católica, C.P. 38071 RJ-22453 Rio de Janeiro, Brazil
and Inst. de Física, Univ. Estadual do Rio de Janeiro, rua São Francisco Xavier 524, Rio de Janeiro, Brazil
[7] Comenius University, Faculty of Mathematics and Physics, Mlynska Dolina, SK-84215 Bratislava, Slovakia
[8] Collège de France, Lab. de Physique Corpusculaire, IN2P3-CNRS, F-75231 Paris Cedex 05, France
[9] CERN, CH-1211 Geneva 23, Switzerland
[10] Institut de Recherches Subatomiques, IN2P3 - CNRS/ULP - BP20, F-67037 Strasbourg Cedex, France
[11] Institute of Nuclear Physics, N.C.S.R. Demokritos, P.O. Box 60228, GR-15310 Athens, Greece
[12] FZU, Inst. of Physics of the C.A.S. High Energy Physics Division, Na Slovance 2, 180 40, Praha 8, Czech Republic
[13] Dipartimento di Fisica, Università di Genova and INFN, Via Dodecaneso 33, I-16146 Genova, Italy
[14] Institut des Sciences Nucléaires, IN2P3-CNRS, Université de Grenoble 1, F-38026 Grenoble Cedex, France
[15] Helsinki Institute of Physics, HIP, P.O. Box 9, FIN-00014 Helsinki, Finland
[16] Joint Institute for Nuclear Research, Dubna, Head Post Office, P.O. Box 79, 101 000 Moscow, Russian Federation
[17] Institut für Experimentelle Kernphysik, Universität Karlsruhe, Postfach 6980, D-76128 Karlsruhe, Germany
[18] Institute of Nuclear Physics and University of Mining and Metalurgy, Ul. Kawiory 26a, PL-30055 Krakow, Poland
[19] Université de Paris-Sud, Lab. de l'Accélérateur Linéaire, IN2P3-CNRS, Bât. 200, F-91405 Orsay Cedex, France
[20] School of Physics and Chemistry, University of Lancaster, Lancaster LA1 4YB, UK
[21] LIP, IST, FCUL - Av. Elias Garcia, 14-1°, P-1000 Lisboa Codex, Portugal
[22] Department of Physics, University of Liverpool, P.O. Box 147, Liverpool L69 3BX, UK
[23] LPNHE, IN2P3-CNRS, Universités Paris VI et VII, Tour 33 (RdC), 4 place Jussieu, F-75252 Paris Cedex 05, France
[24] Department of Physics, University of Lund, Sölvegatan 14, S-22363 Lund, Sweden
[25] Université Claude Bernard de Lyon, IPNL, IN2P3-CNRS, F-69622 Villeurbanne Cedex, France
[26] Univ. d'Aix - Marseille II - CPP, IN2P3-CNRS, F-13288 Marseille Cedex 09, France
[27] Dipartimento di Fisica, Università di Milano and INFN, Via Celoria 16, I-20133 Milan, Italy
[28] Niels Bohr Institute, Blegdamsvej 17, DK-2100 Copenhagen 0, Denmark
[29] NC, Nuclear Centre of MFF, Charles University, Areal MFF, V Holesovickach 2, 180 00, Praha 8, Czech Republic
[30] NIKHEF, Postbus 41882, NL-1009 DB Amsterdam, The Netherlands
[31] National Technical University, Physics Department, Zografou Campus, GR-15773 Athens, Greece
[32] Physics Department, University of Oslo, Blindern, N-1000 Oslo 3, Norway
[33] Dpto. Fisica, Univ. Oviedo, Avda. Calvo Sotelo, S/N-33007 Oviedo, Spain, (CICYT-AEN96-1681)
[34] Department of Physics, University of Oxford, Keble Road, Oxford OX1 3RH, UK
[35] Dipartimento di Fisica, Università di Padova and INFN, Via Marzolo 8, I-35131 Padua, Italy
[36] Rutherford Appleton Laboratory, Chilton, Didcot OX11 OQX, UK
[37] Dipartimento di Fisica, Università di Roma II and INFN, Tor Vergata, I-00173 Rome, Italy
[38] CEA, DAPNIA/Service de Physique des Particules, CE-Saclay, F-91191 Gif-sur-Yvette Cedex, France
[39] Istituto Superiore di Sanità, Ist. Naz. di Fisica Nucl. (INFN), Viale Regina Elena 299, I-00161 Rome, Italy
[40] Instituto de Fisica de Cantabria (CSIC-UC), Avda. los Castros, S/N-39006 Santander, Spain, (CICYT-AEN96-1681)
[41] Inst. for High Energy Physics, Serpukov P.O. Box 35, Protvino, (Moscow Region), Russian Federation
[42] J. Stefan Institute, Jamova 39, SI-1000 Ljubljana, Slovenia and Department of Astroparticle Physics, School of Environmental Sciences, Kostanjeviska 16a, Nova Gorica, SI-5000 Slovenia,
and Department of Physics, University of Ljubljana, SI-1000 Ljubljana, Slovenia
[43] Fysikum, Stockholm University, Box 6730, S-113 85 Stockholm, Sweden
[44] Dipartimento di Fisica Sperimentale, Università di Torino and INFN, Via P. Giuria 1, I-10125 Turin, Italy
[45] Dipartimento di Fisica, Università di Trieste and INFN, Via A. Valerio 2, I-34127 Trieste, Italy
and Istituto di Fisica, Università di Udine, I-33100 Udine, Italy
[46] Univ. Federal do Rio de Janeiro, C.P. 68528 Cidade Univ., Ilha do Fundão BR-21945-970 Rio de Janeiro, Brazil
[47] Department of Radiation Sciences, University of Uppsala, P.O. Box 535, S-751 21 Uppsala, Sweden
[48] IFIC, Valencia-CSIC, and D.F.A.M.N., U. de Valencia, Avda. Dr. Moliner 50, E-46100 Burjassot (Valencia), Spain
[49] Institut für Hochenergiephysik, Österr. Akad. d. Wissensch., Nikolsdorfergasse 18, A-1050 Vienna, Austria
[50] Inst. Nuclear Studies and University of Warsaw, Ul. Hoza 69, PL-00681 Warsaw, Poland
[51] Fachbereich Physik, University of Wuppertal, Postfach 100 127, D-42097 Wuppertal, Germany
[52] On leave of absence from IHEP Serpukhov

1 Introduction

The study of the inclusive hadron production process $e^+e^- \to h + X$ provides a test of the QCD predictions on scaling violation effects in the fragmentation functions. These functions, $D^h_{q(g)}(x_p)$, where $x_p = 2p_h/Q$ with p_h and Q the hadron momentum and e^+e^- centre-of-mass energy respectively, describe the transition of the produced quarks (q) and gluons (g) to the final state hadrons (h). In the framework of QCD, the fragmentation functions obey DGLAP [1] evolution equations analogous to those used for describing the structure functions of deep-inelastic scattering. QCD analysis of the scaling violation effects in the fragmentation functions, performed on the basis of these equations, allows the value of α_s to be extracted [2–5], as in the structure function analysis of the process of deep-inelastic scattering.

A number of experiments [6] have studied the behaviour of the ratio of the longitudinal and transverse structure functions, F_L and F_T, in deep-inelastic scattering :

$$R(x) = \frac{F_L(x)}{F_T(x)} = \frac{F_2(x) - 2xF_1(x)}{2F_1(x)} \,, \tag{1}$$

where x is the Bjorken variable, which can be replaced by x_p in electron-positron annihilation. These experiments have shown that the value of $R(x)$ decreases rapidly with increasing x.

In contrast with all other structure functions $F_i(x),\ i = 1, 2, 3$, the longitudinal component F_L vanishes in the parton model and is non-zero only in the framework of QCD, where it is proportional to α_s [7–9], thus being strongly connected with the structure of perturbative QCD.

In analogy with the structure functions, the corresponding inclusive cross-section components in e^+e^- annihilation are also important for perturbation theory. Particularly interesting are the second moments of the fragmentation functions, which can be calculated up to corrections suppressed by some power of Λ/Q, where Λ is the QCD scale parameter.

Important information for studies of the scaling violation effects and on the shapes of the quark and gluon distributions comes from the region of small x_p. In this region, the effects caused by the contribution of the longitudinal component of the fragmentation function become very important.

Measurements of the longitudinal component of the fragmentation function, $F_L(x_p)$, in inclusive charged hadron production, $e^+e^- \to h + X$, were performed by the TASSO collaboration [10] at centre-of-mass energies of 14 GeV, 22 GeV and 34 GeV. Due to the limited number of events, those results gave only a qualitative description of the behaviour of F_L. It was shown that F_L appears to be different from zero only at values of $x_p \leq 0.2$. Similar results were found by DELPHI on the basis of the preliminary analysis of 1991 data [11], where only the ratio of the longitudinal and transverse components was obtained. Measurements of the F_L and F_T fragmentation functions were also published recently by the OPAL and ALEPH collaborations [12,13].

The study of the different components of the fragmentation function in inclusive charged hadron production is performed here using the 1992-1993 DELPHI data. The present approach allows the transverse, longitudinal and asymmetric components of the quark fragmentation function to be measured and the corresponding components of the cross-section to be extracted. Using the value of the longitudinal cross-section obtained, together with next-to-leading order perturbative QCD calculations, the value of the strong coupling constant is evaluated. Finally, the gluon fragmentation function is estimated in the leading order QCD framework.

In the following, Section 2 describes the procedure of hadronic event selection with the DELPHI detector. Section 3 presents the evaluation method for the fragmentation function components and the results obtained. Section 4 is devoted to the calculation of the strong coupling constant. Studies of systematic effects are presented in Section 5. In Section 6 analysis of fragmentation function components in flavour-tagged events is discussed. Extraction of the gluon fragmentation function from F_T and F_L is described in Section 7.

2 Data selection

Data collected by the DELPHI detector in 1992-1993 at centre-of-mass energies around $\sqrt{s} = 91.2$ GeV ($86.2 \leq \sqrt{s} \leq 94.2$ GeV) were used. The detector and its performance are described in detail in [14,15].

Only charged particles in hadronic events were used. In the barrel region they were measured by a set of cylindrical tracking detectors in the solenoidal magnetic field of 1.2 T. The main tracking device was the Time Projection Chamber (TPC), which was cylindrical with a length of 3 m, an inner radius of 30 cm and an outer radius of 122 cm. Up to 16 space points were used for charged particle reconstruction. The space precision was about $\sigma_{R\varphi} = 250\,\mu$m and $\sigma_z = 880\,\mu$m [†].

Additional $R\varphi$ measurements were provided by the Outer Detector (OD) and the Inner Detector (ID). The OD was a cylindrical detector composed of drift tubes and situated at radii between 197 cm and 206 cm; its precision in $R\varphi$ was about $\pm 110\,\mu$m. The ID was a cylindrical drift chamber having an inner radius of 12 cm and an outer radius of 28 cm; its precision in $R\varphi$ was $\pm 90\,\mu$m.

In order to tag $Z^0 \to b\overline{b}$ events, the micro-vertex detector (VD) was used. It was located between the beam pipe and the ID and consisted of three concentric layers of silicon micro-strip detectors. The precision in $R\varphi$ was about $\pm 8\,\mu$m.

In the forward direction (θ between 11° and 33° and between 147° and 169°) charged particles were measured by a set of planar drift chambers, FCA and FCB.

The momentum resolution of the tracking system in the barrel region was

$$\sigma(1/p) = 0.57 \times 10^{-3} (\mathrm{GeV}/c)^{-1}$$

and in the forward region

$$\sigma(1/p) = 1.31 \times 10^{-3} (\mathrm{GeV}/c)^{-1} \ .$$

Each charged particle was required to pass the following selection criteria :

1. particle momentum between 0.1 GeV/c and 50 GeV/c;
2. measured track length above 50 cm;
3. polar angle between 11° and 169°;
4. impact parameter with respect to the beam crossing point below 5 cm in the transverse plane and below 10 cm along the beam axis.

Hadronic events were then selected by requiring :

1. at least 5 charged particles detected with momenta above 0.2 GeV/c;
2. total energy of all charged particles detected above 15 GeV (assuming the $\pi^{\pm}$ mass for the particles);

[†] The DELPHI coordinate system has the z axis aligned along the electron beam direction, the $R\varphi$-plane is perpendicular to it, and θ is the angle between the momentum of the particle and the axis of the e^- beam.

3. polar angle of the sphericity axis between 26° and 154°;
4. total energy of charged particles in each of the forward and backward hemispheres with respect to the sphericity axis above 3 GeV;
5. missing momentum below 20 GeV/c.

In total, 1,055,932 hadronic events were selected.

Only two variables, the fractional momentum x_p and $\cos\theta$ of each charged particle, were used for the analysis. In each x_p and $\cos\theta$ bin, the value of

$$f(x_p, \cos\theta) \equiv \frac{1}{N}\frac{n}{\Delta x_p \Delta \cos\theta} \tag{2}$$

was obtained, where N is the total number of hadronic events and n is the number of particles in a bin of width Δx_p by $\Delta\cos\theta$. The number and widths of the x_p intervals were chosen in order to provide a reasonable number of entries in each. Thus the full range $0 < x_p < 1$ was split into 22 intervals (see Table 1). For the $\cos\theta$ variable, 40 equidistant intervals in the range $-1 < \cos\theta < 1$ were used.

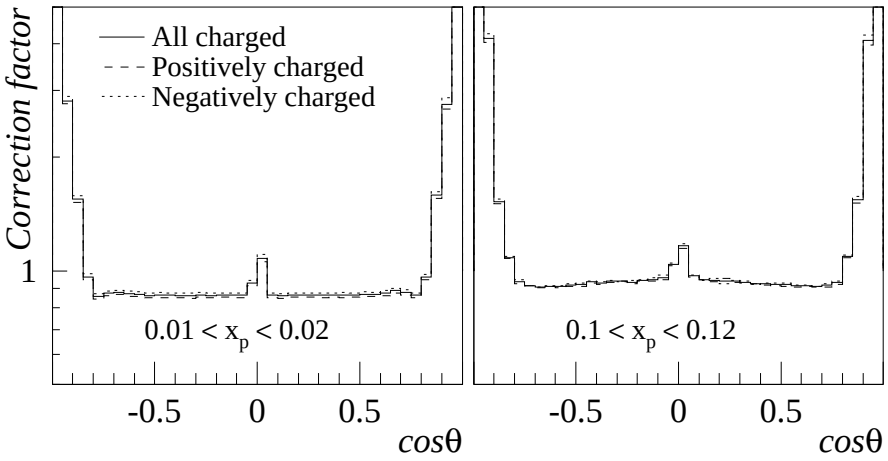

Figure 1: Correction factors for the polar angle distribution of charged particles in two different x_p intervals.

These normalized distributions were corrected for the detector acceptance and efficiency, for the kinematical cuts, and for the initial state radiation. The correction factor values

$$C(x_p, \cos\theta) = \frac{f(x_p, \cos\theta)_{true}}{f(x_p, \cos\theta)_{reconstructed}} \tag{3}$$

are shown in Fig. 1 as a function of $\cos\theta$ for two different bins of x_p. The values of $C(x_p, \cos\theta)$ were obtained by analysing events generated with the JETSET 7.3 PS program [16] with parameters taken from the DELPHI tuning [17]. Here $f(x_p, \cos\theta)_{true}$ is the distribution obtained from the final state hadrons in generated events, and $f(x_p, \cos\theta)_{reconstructed}$ represents the same distribution after full simulation of the response of the DELPHI detector [15] and application of the charged particle reconstruction and analysis procedures in the same way as for the real data. For the analysis of the charge asymmetric fragmentation function (see below), the distributions of positive and negative charged particles were obtained separately by using respective correction factors.

3 Components of the fragmentation function

The double-differential total cross-section for producing a charged hadron h in the process $e^+e^- \to h + X$ via the s-channel exchange of a virtual photon or Z^0 follows from the standard tensor analysis [8,18] :

$$\frac{d^2\sigma^h}{dx_p\, d\cos\theta} = \frac{3}{8}(1+\cos^2\theta)\frac{d\sigma_T^h}{dx_p} + \frac{3}{4}\sin^2\theta\frac{d\sigma_L^h}{dx_p} + \frac{3}{4}\cos\theta\frac{d\sigma_A^h}{dx_p} \ , \tag{4}$$

where $d\sigma_T^h/dx_p$, $d\sigma_L^h/dx_p$ and $d\sigma_A^h/dx_p$ are the transverse, longitudinal and asymmetric components of the differential cross-section, respectively.

In the present analysis, all kinds of charged hadrons have been taken into account. Therefore the overall charged hadron differential cross-sections $d\sigma_T^{ch}/dx_p$, $d\sigma_L^{ch}/dx_p$ and $d\sigma_A^{ch}/dx_p$ were measured :

$$\frac{d\sigma_P^{ch}}{dx_p} = \sum_h \frac{d\sigma_P^h}{dx_p} \ , \tag{5}$$

where the subscript P stands for T, L or A.

With the available number of events, it is possible to measure these components separately by weighting the double-differential total cross-sections :

$$\frac{d\sigma_P^{ch}}{dx_p} = \int_{-v}^{+v} W_P(\cos\theta, v)\left[\frac{d^2\sigma^{ch}}{dx_p\, d\cos\theta}\right] d\cos\theta \tag{6}$$

with appropriate weighting functions W_P ($P = T, L, T+L$, or A) [18] :

$$\begin{aligned} W_T(\cos\theta, v) &= [5\cos^2\theta(3-v^2) - v^2(5-3v^2)]/2v^5 \ , \\ W_L(\cos\theta, v) &= [v^2(5+3v^2) - 5\cos^2\theta(3+v^2)]/4v^5 \ , \\ W_{T+L}(\cos\theta, v) &= W_T(\cos\theta, v) + W_L(\cos\theta, v) \ , \\ W_A(\cos\theta, v) &= 2\cos\theta/v^3 \ , \end{aligned} \tag{7}$$

where the variable v delimits the absolute value of the cosine of the angular range used. In the present analysis, its value was taken as $v = 0.8$ in order to cover the interval where the correction factors are approximately constant (see Fig. 1). The effects of varying this value are taken into account in the systematic uncertainties.

A fitting procedure can also be used for the analysis of the distribution (4), as was done in [10–12]. The results obtained by the two methods are compared below.

Following [18], the transverse, longitudinal and asymmetric fragmentation functions are defined as :

$$F_P(x_p) \equiv \frac{1}{\sigma_{tot}}\frac{d\sigma_P^{ch}}{dx_p} \ , \tag{8}$$

where $P = T, L, A$, and σ_{tot} is the total hadronic cross-section. In the parton model limit ($\alpha_s \to 0$), the longitudinal fragmentation function $F_L(x_p)$ is equal to zero (by analogy with the longitudinal structure function in deep-inelastic scattering) and the transverse fragmentation function $F_T(x_p)$ coincides with the quark fragmentation function.

The asymmetric component, defined as above without reference to the hadron charge, should be zero. But separate analysis of positive and negative charged hadron samples should show a difference in sign between $d\sigma_A^{h^+}/dx_p$ and $d\sigma_A^{h^-}/dx_p$, where the superscripts h^+ and h^- denote the components of the fragmentation function for positively and negatively charged hadrons, respectively. The difference

$$\tilde{F}_A(x_p) = \frac{1}{\sigma_{tot}}\left(\frac{d\sigma_A^{h^+}}{dx_p} - \frac{d\sigma_A^{h^-}}{dx_p}\right) \tag{9}$$

is therefore used, following [18], to define the "charge asymmetric" fragmentation function. Since hadrons with sufficiently high x_p mainly result from the primary quark fragmentation, they carry the information on the primary quark charge. Therefore a non-zero charge asymmetric fragmentation function $\tilde{F}_A$ should be observed in this x_p region, reflecting the forward-backward asymmetry in the primary $e^+e^- \to q\bar{q}$ process.

3.1 Longitudinal and transverse fragmentation functions

The values for F_L and F_T found from this analysis are presented in Table 1 and are shown in Fig. 2, together with those of a similar analysis of JETSET 7.3 PS distributions and the corresponding results of OPAL [12].

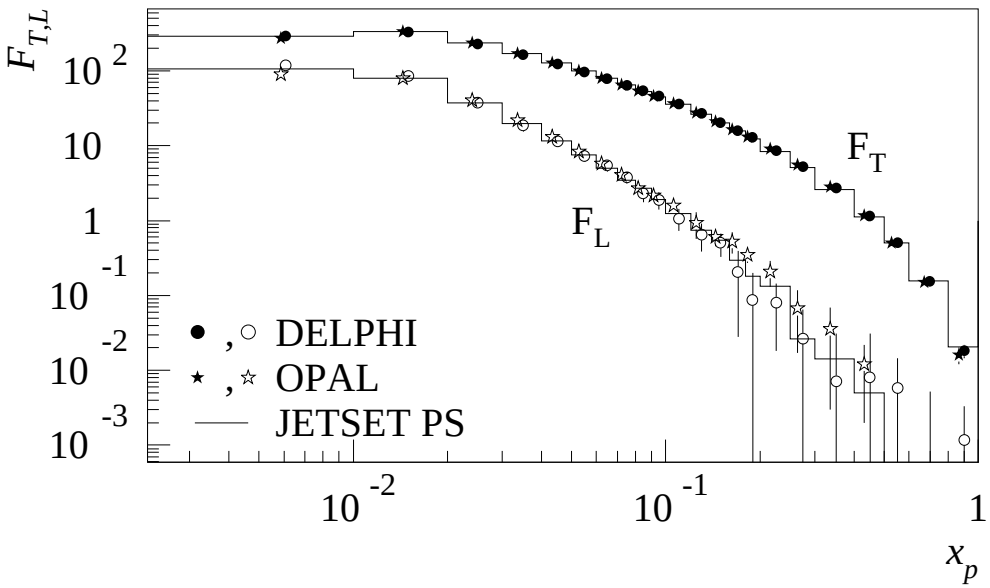

Figure 2: Measured values of F_L and F_T obtained by the weighting method in DELPHI (circles). Also shown are analogous OPAL data (stars, slightly shifted in x_p for clarity) and simulated JETSET PS distributions with the DELPHI tuning (histograms). Data are presented with total (statistical and systematic) errors.

Part of the difference in F_L between the DELPHI and OPAL data in the region $x_p < 0.02$ is due to the use of the x_E variable in OPAL rather than x_p here. Another difference is that OPAL used fits to angular distributions according to formula (4) rather than weighting.

Comparison of JETSET distributions generated with and without DELPHI tuning shows that differences in F_T (as well as in F_L) exist only in the region $x_p < 0.1$, and drop rapidly from 8% at $x_p < 0.01$ to 2% at $0.03 < x_p < 0.05$.

The sum of the transverse and longitudinal fragmentation functions can be evaluated by direct integration of the double-differential cross-section with the weight $(W_T + W_L)$ in the angular range $|\cos\theta| < v$. The result of such an integration, F_{T+L} for $v = 0.8$, is shown in Table 1. The statistical and systematic errors on F_{T+L} are reduced because F_T and F_L are anti-correlated. The ratios of the transverse σ_T^{ch} or longitudinal σ_L^{ch} cross-sections to the total cross-section σ_{tot} are obtained by integrating the corresponding fragmentation function :

$$\frac{\sigma_P^{ch}}{\sigma_{tot}} = \int_0^1 \frac{x_p}{2} F_P(x_p) dx_p \ , \qquad (10)$$

where $P = T, L$. This equation follows from the energy conservation sum rule and leads to the obvious equation $\sigma_T/\sigma_{tot} + \sigma_L/\sigma_{tot} = 1$ for all hadrons. Values of $\sigma_T^{ch}/\sigma_{tot}$ and $\sigma_L^{ch}/\sigma_{tot}$ are shown in the bottom line of Table 1.

The charged particle multiplicity can be obtained by integrating F_{T+L}. This gives

$$\langle n^{ch} \rangle = \int_0^1 F_{T+L} dx_p = 21.21 \pm 0.01(stat.) \pm 0.20(syst.). \tag{11}$$

The systematic uncertainty for $\langle n^{ch} \rangle$ was estimated by analysing the corresponding uncertainties of the fragmentation functions, as presented in Section 5 (see Table 4). The value of $\langle n^{ch} \rangle$ obtained is in good agreement with the average LEP/SLC result 20.99 ± 0.14 [19]. Charged particles with momentum below 0.1 GeV were taken into account through the standard correction factors (3), as were particles produced in secondary interactions. Charged hadrons produced in decays of K_s^0 and Λ are included, as is the usual convention, since the correction procedure considers them as unstable particles. The problem of particle reconstruction inefficiency in the forward regions of the detector was avoided, since the weighting functions W_T and W_L take into account the limited angular range used, effectively performing the extrapolation of the angular distributions to their edges.

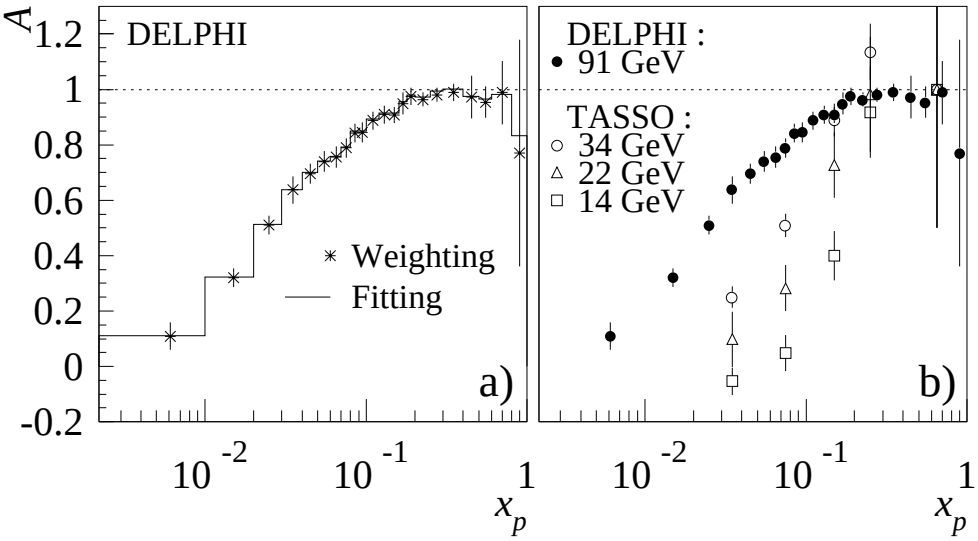

Figure 3: Comparison of $A = (F_T - 2F_L)/(F_T + 2F_L)$ calculated from the DELPHI data by the weighting method with other results : **a)** from DELPHI by applying the fitting method to the same data sample ; **b)** from TASSO at lower centre-of-mass energies. The combined statistical and systematic errors are shown for the DELPHI results.

The values of F_T and F_L have also been used to calculate the ratio $A = (F_T - 2F_L)\,/\,(F_T + 2F_L)$, which is simply connected to the double-differential cross-section (4) in the limit of a negligible asymmetric component :

$$\frac{d^2\sigma^{ch}}{dx_p\, d\cos\theta} \sim 1 + A\cos^2\theta \ . \tag{12}$$

Another way to determine A is by a direct fit of the angular distribution to equation (12), as done previously by TASSO [10] and DELPHI [11]. In Fig. 3a, the values of A obtained by the two methods are plotted as a function of x_p. The fit result generally slightly exceeds that from weighting; but they both behave very similarly, confirming

the theoretical expectation that the longitudinal contribution should be significant in the region of $x_p < 0.2$.

In Fig. 3b, values of A obtained with the weighting method are plotted together with the TASSO results at centre-of-mass energies of 14 GeV, 22 GeV and 34 GeV [10]. The energy dependence of A from TASSO is confirmed by the new precise DELPHI data. The DELPHI results provide a much better description of the A behaviour in the full x_p interval and clearly indicate the region where F_L vanishes, namely $x_p > 0.2$.

Analogously to the ratio (1), measured previously in deep-inelastic scattering experiments [6], the ratio F_L/F_T was calculated. It is plotted in Fig. 4 together with the ratio F_L/F_{T+L} (see values in Table 2). A significant contribution from the longitudinal component is clearly seen in the region $x_p < 0.2$.

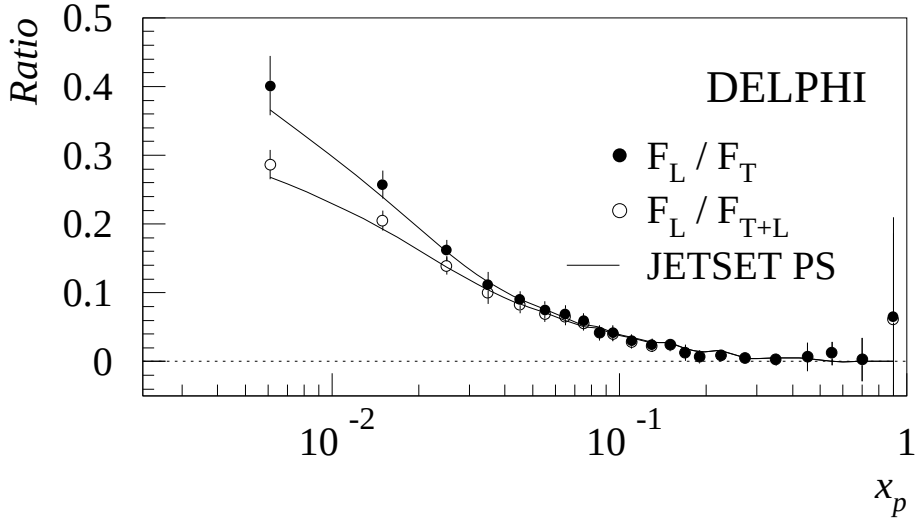

Figure 4: Ratio of the longitudinal to the transverse component of the fragmentation function and of the longitudinal component to the sum of both. Errors are both statistical and systematic.

3.2 Asymmetric fragmentation functions

The asymmetric component of the differential cross-section $F_A \equiv d\sigma_A^{ch}/dx_p$, see Eqs. (4) and (8), appears to be close to zero within errors, as expected, as can be seen from Fig. 5.

The charge asymmetric fragmentation function $\tilde{F}_A$, see Eq. (9), and the ratio $\tilde{F}_A/F_{T+L}$ are shown in Fig. 6. The corresponding JETSET 7.3 PS distributions are seen to agree qualitatively with the data. This charge asymmetric function $\tilde{F}_A$ is proportional to the vector coupling constants v_e and v_q which depend on the weak mixing angle [20]. The default value of $\sin^2\theta_W = 0.232$ was used in the JETSET model. However, studies performed with the JETSET PS model show that the sensitivity of $\tilde{F}_A$ and $\tilde{F}_A/F_{T+L}$ to $\sin^2\theta_W$ is rather weak. Furthermore, the lack of exact theoretical calculations for the dependence of $\tilde{F}_A(x_p)$ on the weak mixing angle in the full x_p interval also prevents extraction of a quantitative result on the value of $\sin^2\theta_W$.

Recently, theoretical leading order (LO), next-to leading order (NLO) and next-to-next-to-leading order (NNLO) QCD predictions of the shape of $\tilde{F}_A(x_p, M_Z)$ have been made [21]. Within the model assumptions used, the charge asymmetric fragmentation

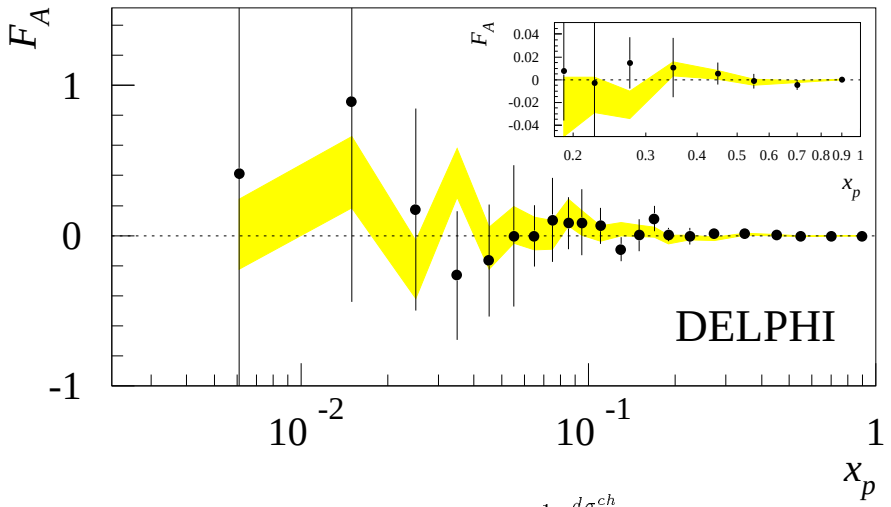

Figure 5: The asymmetric component $F_A \equiv \frac{1}{\sigma_{tot}} \frac{d\sigma_A^{ch}}{dx_p}$ of the fragmentation function for all charged hadrons, defined without reference to their charges. The combined statistical and systematic error is shown for each data point. This error is predominantly statistical for $x_p > 0.06$. The shaded band shows the asymmetric component obtained from the same analysis of the similar amount of JETSET generated events within one standard deviation. The inset shows the high x_p region with an expanded vertical scale.

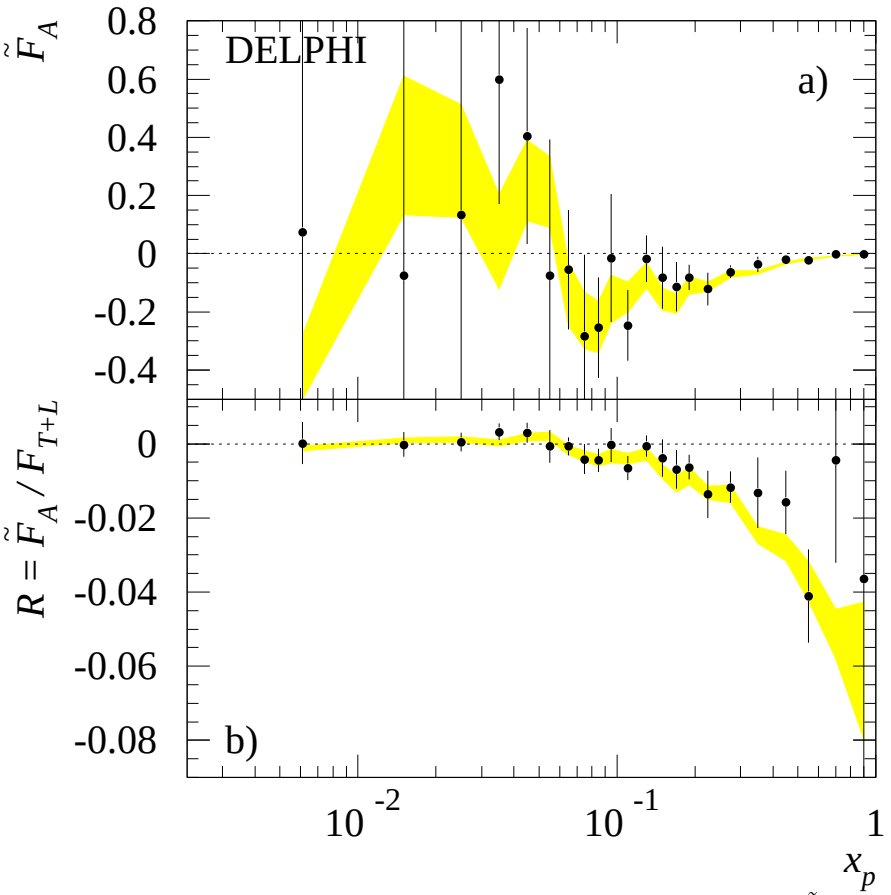

Figure 6: **a)** The 'charge asymmetric' fragmentation function $\tilde{F}_A$ and **b)** the ratio $\tilde{F}_A / F_{T+L}$ extracted from the DELPHI data. The combined statistical and systematic errors are shown. The shaded bands represent the same functions obtained from the analysis of the similar amount of JETSET generated events within one standard deviation.

function is expected to be negative in the whole x_p region; the first and second moments of $\tilde{F}_A$ calculated in the region $0.1 < x_p < 1$ are compared here with DELPHI results :

$$\begin{array}{lccc} & \text{NLO, NNLO} & \text{LO} & \text{DELPHI} \\ \int_{0.1}^{1} \tilde{F}_A dx_p \; = & -0.016 & -0.023 & -0.028 \pm 0.006(stat.+syst.) \\ \int_{0.1}^{1} \tilde{F}_A \frac{x_p}{2} dx_p \; = & -0.0020 & -0.0027 & -0.0036 \pm 0.0008(stat.+syst.) \end{array}$$

The present analysis gives values which are closer to the LO predictions than to the NLO and NNLO ones. The same discrepancy was observed in OPAL data [12] and, as discussed in [21], this can indicate that non-perturbative corrections to $\tilde{F}_A$ are essential.

4 Calculation of α_s

The cross-section components σ_L and σ_T in the inclusive annihilation process are infrared and collinear safe. The order α_s^2 and power corrections to σ_T and σ_L have been calculated recently [22–25]. In principle, this provides a possibility for a new measurement of α_s.

In the next-to-leading order of perturbative QCD, the full (charged plus neutral particles) longitudinal and transverse inclusive cross-sections, σ_L and σ_T, which are connected to the full fragmentation functions F_L and F_T analogously to equation (10), are expressed as [22] :

$$\frac{\sigma_L}{\sigma_{tot}} = 1 - \frac{\sigma_T}{\sigma_{tot}} = \frac{\alpha_s}{\pi} + \frac{\alpha_s^2}{\pi^2}(13.583 - N_f \cdot 1.028) \; , \tag{13}$$

where $N_f = 5$ is the number of active quark flavours.

While Eq. (13) refers to the full charged plus neutral particle cross-sections, in the present analysis only the charged particle cross-sections are measured. To perform the conversion from charged particles to charged plus neutral particles, the ratios of the inclusive charged to the full cross-sections, σ_L^{ch}/σ_L and σ_T^{ch}/σ_T, were studied in the JETSET 7.4 PS and HERWIG 5.9 models. As found previously by OPAL [12], they are approximately equal, with the values of the ratios found being $\sigma_T^{ch}/\sigma_T = 0.6308 \pm 0.0004$ and $\sigma_L^{ch}/\sigma_L = 0.624 \pm 0.005$ in JETSET, and $\sigma_T^{ch}/\sigma_T = 0.6019 \pm 0.0005$ and $\sigma_L^{ch}/\sigma_L = 0.603 \pm 0.007$ in HERWIG.

Assuming this equality gives the following values for the ratios of the full inclusive cross-sections :

$$\begin{aligned} \frac{\sigma_T}{\sigma_{tot}} &= \frac{\sigma_T^{ch}}{\sigma_L^{ch} + \sigma_T^{ch}} = 0.949 \pm 0.001(stat.) \pm 0.007(syst.), \\ \frac{\sigma_L}{\sigma_{tot}} &= \frac{\sigma_L^{ch}}{\sigma_L^{ch} + \sigma_T^{ch}} = 0.051 \pm 0.001(stat.) \pm 0.007(syst.), \end{aligned} \tag{14}$$

where the systematic uncertainties quoted correspond to those on $\sigma_T^{ch}/\sigma_{tot}$ and $\sigma_L^{ch}/\sigma_{tot}$ (see Section 5). Small differences of about 1% between the ratios σ_L^{ch}/σ_L and σ_T^{ch}/σ_T would not lead to significant changes in σ_T/σ_{tot} or σ_L/σ_{tot}.

Substituting the value of σ_L/σ_{tot} into (13) gives the strong interaction coupling constant,

$$\alpha_s^{NLO}(M_Z) = 0.120 \pm 0.002(stat.) \pm 0.013(syst.) \; . \tag{15}$$

In the order α_s^2 calculations [22], the ratios σ_L/σ_{tot} and σ_T/σ_{tot} depend on the mass factorisation scale μ and renormalization scale R. Equation (13) and the value of α_s in (15) correspond to $\mu = R = M_Z$. The dependence of α_s on the factorisation and renormalization scales (assuming $\mu = R$) is shown in Fig. 7. Between $\mu = 2Q$ and $\mu = Q/2$, the value of α_s changes by about 12%. This gives an additional error of ± 0.007.

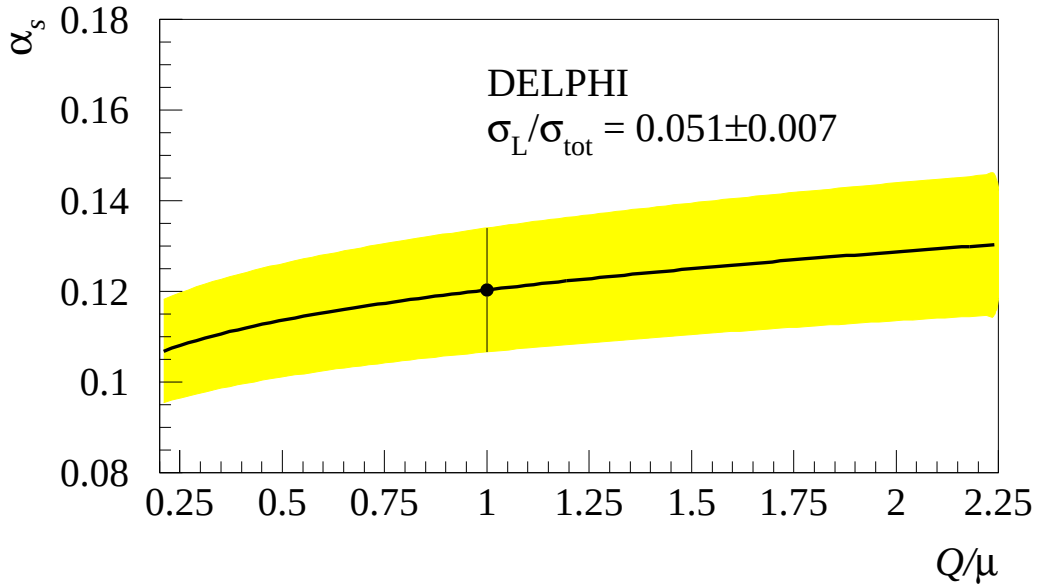

Figure 7: Dependence of the strong coupling constant α_s on the factorisation and renormalization scales ($\mu = R$). The shaded region shows the $\pm 1\sigma$ error band. The point indicates the α_s value obtained in this work for $\mu = Q$.

Non-perturbative corrections to the value of $\delta\sigma_L/\sigma_{tot}$ have also been calculated recently [23,24]. They appear to be comparable with the next-to-leading order contributions. These corrections, which are also known as power corrections, were obtained by different methods, each of which led to a similar $\propto 1/Q$ behaviour. At LEP1 energies, the value of the power corrections calculated in [23] under the assumption of an infrared-regular effective behaviour of α_s was given as $(\delta\sigma_L/\sigma_{tot})^{POW} = 0.010 \pm 0.001$. A similar estimate of the power corrections to the longitudinal and transverse cross-sections was also obtained in [25], based on the assumption of ultraviolet dominance of higher-twist matrix elements. Studies performed with the JETSET 7.4 PS suggest corrections of the same magnitude.

Accounting for this estimate of the non-perturbative power corrections changes the α_s value of (15) to

$$\alpha_s^{NLO+POW}(M_Z) = 0.101 \pm 0.002(stat.) \pm 0.013(syst.) \pm 0.007(scale), \qquad (16)$$

where the scale uncertainty again comes from varying the renormalisation scale in the range $0.5 < Q/\mu < 2$ (see Fig. 7).

5 Studies of systematic effects

Several sources of systematic uncertainties were considered in the estimates quoted above. A study of the systematic deviations of the fragmentation functions caused by

the detector features and selection criteria was described in [5]. Analogous studies are performed here to estimate the systematics on the components of the fragmentation function and other measured variables, like the charged particle multiplicity and the cross-section components. The total systematic errors on F_T and F_L together with the three main contributions are shown as a function of x_p in Table 3. Table 4 shows the systematic error estimates for $\sigma_T^{ch}/\sigma_{tot}$, $\sigma_L^{ch}/\sigma_{tot}$ and $\langle n^{ch} \rangle$.

Firstly, changes of the measured values under variations of the track and event selection criteria described in Section 2 were considered. The most significant changes arose from varying the impact parameter cut, reflecting the influence of short-living mesons and baryons and also of secondary interactions in the detector material, which distort the reconstructed impact parameter distributions and the inclusive spectra. Varying the cut on the polar angle of the event sphericity axis also led to significant changes, since it affected the angular distribution of the hadrons. Varying the cut on the polar angles of the tracks also gave deviations which exceeded the statistical errors. Changing the selection on the minimum particle momentum led to significant deviations in the very first bin, $0 < x_p < 0.01$. Varying other cuts gave less significant changes, not exceeding the corresponding statistical uncertainties.

To study the systematics related to the angular range limitation, the range analysed was varied from $|\cos\theta| < 0.5$ up to $|\cos\theta| < 0.9$, and the average deviation of the resulting values was considered as a systematic uncertainty. Changing the number of points involved in the analysis obviously affects the statistics. To separate out this statistical contribution to the observed deviations, the same analysis was performed on distributions generated by the JETSET 7.3 PS model with a similar number of events. The systematics were estimated by subtracting in quadrature the deviations obtained with the JETSET samples from those obtained with the DELPHI data.

Another source of systematic uncertainty is the angular region around $\cos\theta \approx 0$, where the charged particle reconstruction efficiency is relatively poor (see Fig. 1), due to the effect of the mid-plane of the TPC [14]. To study the influence of this effect, the analysis was repeated with the points between $-0.1 < \cos\theta < 0.1$ replaced by the values of the fitting function (12).

As mentioned above, the weighting and fitting methods gave slightly different results. Studies using generated JETSET PS events showed that the values of F_T from the fitting procedure are systematically higher, and those of F_L systematically lower, than those obtained by weighting. The difference does not exceed the statistical errors for F_T and F_L; it is significant only for $\sigma_L^{ch}/\sigma_{tot}$, where it amounts to 2.5%. The results of the weighting method are closer to those of the JETSET PS generator model than those of the fitting method.

In the determination of the components of the cross-section, proper knowledge of the mean x_p value in each histogram bin plays an important role. To estimate possible uncertainties connected to the association of x_p value with each bin, $\sigma_T^{ch}/\sigma_{tot}$ and $\sigma_L^{ch}/\sigma_{tot}$ were alternatively evaluated as

$$\frac{\sigma_P^{ch}}{\sigma_{tot}} = \frac{1}{\sigma_{tot}} \int_{-v}^{+v} W_P \, d\cos\theta \int_0^1 \frac{x_p}{2} \frac{d^2\sigma^{ch}}{dx_p d\cos\theta} dx_p \ , \tag{17}$$

where $P = T, L$ and integration over dx_p was performed using the actual x_p value for each measured track, instead of histogramming. The cross-sections obtained with this method differed by about 0.2% for transverse and 0.6% for longitudinal components.

Another source of systematics, connected to the mean charged multiplicity, is the fact that the JETSET event generator produces slightly different numbers of K_S^0 and

Λ than are measured experimentally [17]. Studies of the influence of this effect showed that varying the average K^0_S multiplicity by $\pm 5\%$ leads to a change in measured $\langle n^{ch} \rangle$ of ± 0.02. Varying the mean Λ multiplicity did not lead to a significant change in $\langle n^{ch} \rangle$.

Discrepancy between the data collected during 1992 and 1993 data taking periods also contributes to the total systematic uncertainty. However, it exceeds the statistical error only in the region of $x_p < 0.06$.

The quadratic sum of all the above mentioned errors is represented in Tables 3 and 4 as the total systematic uncertainty.

While in perturbation theory the Bjorken x ($x = x_E$) variable is used for fragmentation function calculations, in e^+e^- annihilation it is usually replaced by the x_p variable. Tests using the JETSET generator showed that for F_T and F_L the substitution of x_p with x_E affects only the region $x_p < 0.02$, which is due to mass effects. For cross-sections it causes deviations of approximately 0.3% in the transverse and 2% in the longitudinal component.

6 b and uds enriched event samples

Samples of events originating from quarks of different flavours were selected using the lifetime tag variable P_H [15], defined as the probability for the hypothesis that all the charged particle tracks in a given hemisphere with respect to the thrust axis came from a single primary vertex. Since hadrons containing b quarks have a high charged particle decay multiplicity and a long lifetime ($\approx$ 1.55 ps), and are produced with a high momentum at LEP, this single-vertex probability is small for $Z^0 \to b\overline{b}$ events. The selection was done assuming, according to the simulation, that requiring $P_H < 10^{-3}$ selects $b\overline{b}$ events with purity $\approx 94\%$ and efficiency $\approx 16\%$, and requiring $P_H > 0.3$ selects light quark events with purity $\approx 73\%$ and efficiency $\approx 72\%$. The particles to be analysed were then taken from the opposite hemisphere.

The selected samples consisted of about 42,000 b events and 610,000 uds events. The contamination by heavy flavours in the uds events was estimated to be $\approx$ 11% from bottom and $\approx$ 16% from charm quarks.

As mentioned in Section 2, all experimental distributions have been multiplied by correction factors. These were calculated using (3), with the "true" spectra taken from pure generated b or uds events and the "reconstructed" ones obtained using the DELSIM detector simulation [15] and applying the lifetime tagging procedure to the fully simulated events.

The procedure described in Sect. 3 for separating the longitudinal and transverse components of the fragmentation function was applied to the corrected b and uds event samples. The components of the fragmentation functions for different quark flavours were defined as

$$F_P^q \equiv \frac{1}{\sigma_{tot}^q} \frac{d\sigma_P^q}{dx_p} \,, \tag{18}$$

where $P = T, L$ and $q = uds, b$. The results are shown in Fig. 8 and Table 5.

The charged particle multiplicities in b and uds events were obtained by integrating the fragmentation functions as described in Section 3.1. These too are presented in Table 5, and are in qualitative agreement with the overall multiplicity (11). The charged multiplicity observed in b events is in good agreement with previous DELPHI results [26].

The main difference between the b and uds spectra comes from the transverse component of the cross-section, which is softer for the b quark sample. There is no significant

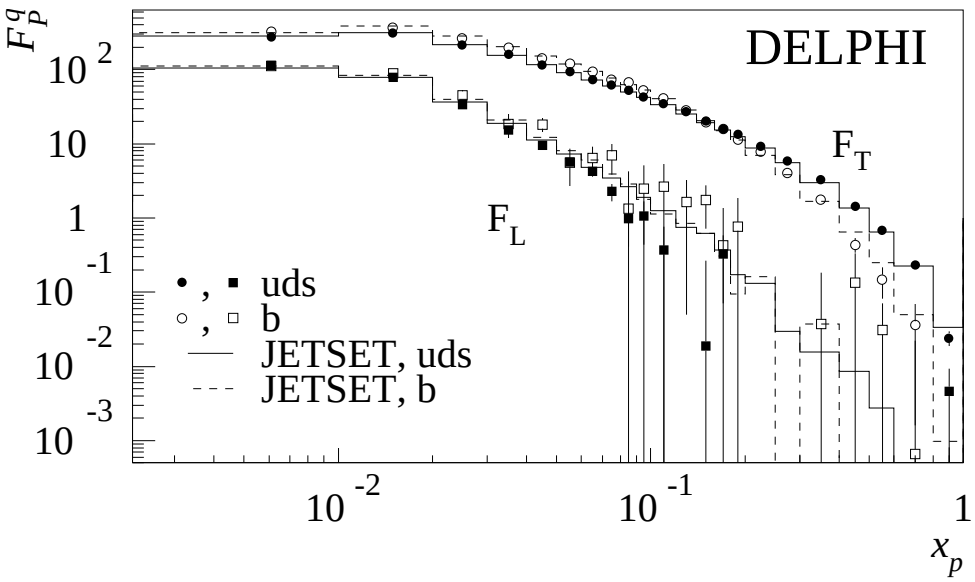

Figure 8: Transverse and longitudinal components of the fragmentation functions of different quark flavours. Errors include both statistical and systematic ones. For b-tagged events, the systematics do not exceed the statistical uncertainties. For light quark events, the systematics dominate mainly in the region $0 < x_p < 0.12$, where they amount to $\pm 1.5\%$ for F_T and about $\pm 10\%$ for F_L.

difference between the longitudinal fragmentation functions F_L^{uds} and F_L^b. The fragmentation function components obtained from the analysis of the JETSET 7.3 PS generated events have the same behaviour as the data.

Studies of systematic uncertainties were performed as described in Section 5. For b-tagged events, the systematics do not exceed the statistical uncertainties. For light quark events, the systematics dominate mainly in the region $0 < x_p < 0.12$, where they amount to $\pm 1.5\%$ for F_T and about $\pm 10\%$ for F_L.

7 Gluon fragmentation function

According to perturbative QCD, the longitudinal component of the fragmentation function is equal to zero in leading order (LO) of α_s [7,27,28], and is given in next-to-leading order by [8,9] :

$$\begin{aligned} F_L(x_p) &= \frac{\alpha_s^{LO}(M_Z)}{2\pi} C_F \int_{x_p}^{1} \frac{F_T(z)}{z} dz \\ &+ \frac{2\alpha_s^{LO}(M_Z)}{\pi} C_F \int_{x_p}^{1} \left(\frac{z}{x_p} - 1 \right) D_g(z) \frac{dz}{z} + \mathcal{O}(\alpha_s^2) \ , \end{aligned} \tag{19}$$

where the colour factor $C_F = 4/3$ and $D_g(z)$ is a function which describes fragmentation of gluons into hadrons, given in leading order. This formula (19) contains the leading order expression for α_s^{LO} :

$$\alpha_s^{LO}(Q) = \frac{4\pi}{\beta_0 \ln(\frac{Q^2}{\Lambda^2_{LO}})} \ , \tag{20}$$

where $\beta_0 = 11 - \frac{2}{3}N_f$, N_f is the number of active quark flavours, Q is the centre-of-mass energy, and $\Lambda_{LO} \equiv \Lambda_{LO}^{(N_f)}$ is the QCD scale parameter. In what follows, α_s is everywhere given for $N_f = 5$. Strictly speaking, expression (19) is not valid in the region where F_L approaches zero, thus it can be used only as an approximation.

Applying the perturbative formula (19) implies knowledge of the α_s^{LO} value consistent with the perturbation analysis. However, experimental results are presented mostly in terms of the next-to-leading order value of α_s only, thus a special analysis should be done to extract the value of α_s^{LO}.

OPAL [12] used for this purpose the approximate ratio $\sigma_L/\sigma_T = \alpha_s^{LO}/\pi$, which can contain higher order and non-perturbative hadronization effects. This method gave a value of $\alpha_s^{LO}(M_Z) = 0.190$ for OPAL data and $\alpha_s^{LO}(M_Z) = 0.171$ for this analysis.

Alternatively, results from deep inelastic scattering experiments at high Q^2 can be used, since perturbation theory is known to be applicable there. To determine the leading order value of $\alpha_s^{LO}(M_Z)$, the QCD scale parameter $\Lambda_{LO}^{(4)}$, found by the BCDMS collaboration [29] was recalculated to $\alpha_s^{LO}(M_Z) = 0.126 \pm 0.006$. A recent analysis of LEP and lower energy e^+e^- annihilation data [30] gave $\alpha_s^{LO}(M_Z) \approx 0.122$.

A third approach is to treat α_s^{LO} as a free parameter of a fit to the measured function F_L using (19) neglecting $\mathcal{O}(\alpha_s^2)$ terms, similar to the ALEPH analysis [13].

The gluon fragmentation function $D_g(x_p)$ can be parameterized by the form [12,13]

$$D_g(x_p) = P_1 \cdot x_p^{P_2}(1 - x_p)^{P_3} e^{-P_4 \ln^2 x_p} \ , \tag{21}$$

where the P_i are free parameters of the fitting procedure. This parametrization is purely phenomenological. The form (21) implies also a strong correlation between the parameters P_i, suggesting that any set of values which describes the D_g may not be unique.

The fit was performed using the measured transverse and longitudinal fragmentation functions F_L and F_T given in Table 1. The x_p interval $0.01 < x_p < 0.6$ was used, in order to stay in the region where F_L is well measured and to avoid the small x_p region, where systematic uncertainties and non-perturbative effects are large.

The strong correlation between the parameters P_i and between the values of α_s^{LO} and P_i, as well as the approximate nature of the fit due to the omission of $\mathcal{O}(\alpha_s^2)$ terms, suggest that special investigation of the uncertainty in D_g is required. To estimate it, the fit was performed in two different conditions, either with a predefined value of $\alpha_s^{LO} = 0.126$ or allowing α_s^{LO} to vary freely. Also, two different data samples were used: a) the F_L and F_T values measured in all hadronic events quoted in Table 1, b) the F_L and F_T values measured in heavy-quark and light-quark tagged events quoted in Table 5 and those measured in the remaining untagged events. The fragmentation functions of the tagged quarks and of the remaining quark mixture were fitted simultaneously, assuming the same shape for the gluon fragmentation function. Parameters evaluated with α_s^{LO} either fixed at the value 0.126 or being a free parameter are shown in Table 6.

The gluon fragmentation function $D_g(x_p)$ corresponding to the parameter values obtained by fitting the F_L and F_T values measured for the natural flavour mix events (see Table 1) with α_s^{LO} free is plotted in Fig. 9 in the x_p interval used in the fit. Similar fits done by the OPAL [12] and ALEPH [13] collaborations are also shown, together with the result of a similar fit to the JETSET PS generated events. In spite of having different sets of parameters in (21) (see Table 6 and references [12,13]), D_g functions obtained by OPAL, ALEPH and DELPHI are in satisfactory agreement. The results obtained also exhibit a low sensitivity to α_s^{LO}, which stems from the strong correlation between α_s^{LO} and D_g and from the semi-empirical nature of the method.

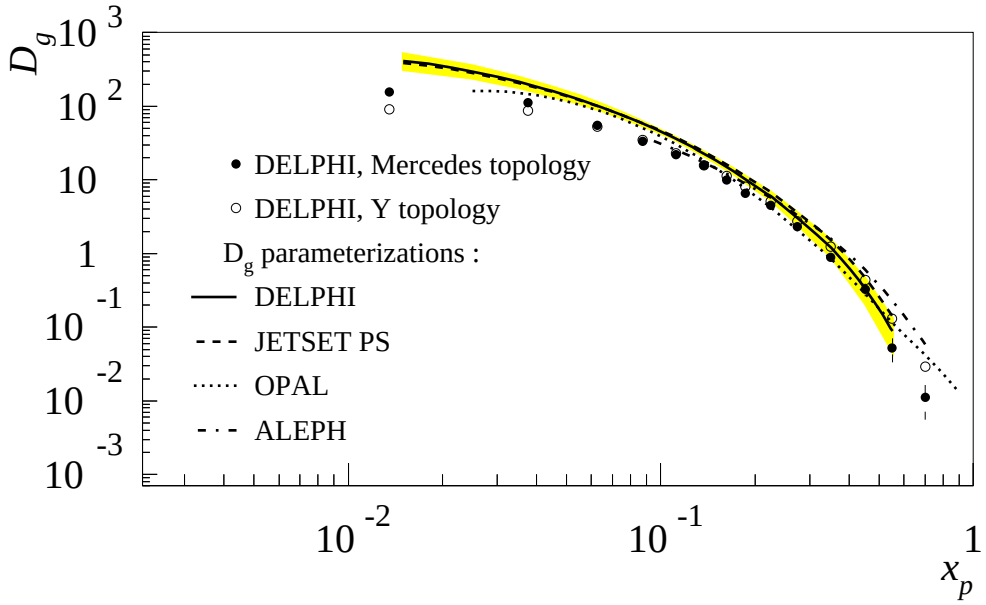

Figure 9: Gluon fragmentation functions $D_g(x_p)$ as obtained from the DELPHI data (full curve, with shaded band showing the uncertainty in D_g) using a fit with the parametrization (21), and by OPAL (dotted curve) and ALEPH (dot-dashed curve) with the same parametrization, compared with a similar fit to distributions generated with the JETSET PS model (dashed curve) and with charged particle spectra from gluon jets in events of different topologies [31] (open and closed circles).

Recently, DELPHI presented measurements of the gluon fragmentation function using a procedure for separating quark and gluon jets in three-jet events [31]. Fig. 9 also compares the gluon fragmentation functions $D_g(x_p)$ with the inclusive particle distributions in gluon jets obtained in this way. The two measurements are complementary. They are in reasonable agreement in the region of $x_p > 0.2$, but there is a systematic difference at small x_p. The method based on fitting F_L and F_T with equation (19) has some limitations, because that equation is valid only in the next-to-leading order of perturbative QCD. However, it is independent of the jet definition and therefore is potentially more reliable in the region of small x_p, where the assignment of particles to jets is arbitrary. In addition, the gluon fragmentation functions obtained with these two methods might have different behaviours due to the effect of Q^2 dependence, because the selected gluon samples have different average energies.

Fig. 10 compares the gluon fragmentation function $D_g(x_p)$ with the transverse fragmentation function $F_T(x_p)$, which can be considered as a quark fragmentation function at large values of x_p, where $F_L(x_p)$ can be neglected. There is a clear indication that the gluon spectrum is softer, as qualitatively predicted by QCD.

8 Summary

Data collected by DELPHI in 1992 and 1993 have been used to measure the inclusive charged hadron cross-section in the full available x_p and polar angle θ intervals. Using the weighting functions method, the transverse F_T, longitudinal F_L and charge asymmetry $\tilde{F}_A$ fragmentation functions were evaluated from the double differential charged hadron cross-section $d^2\sigma^{ch}/dx_p d\cos\theta$. Available statistics of more than one million events allow precise measurement of the longitudinal fragmentation function, which serves as an important

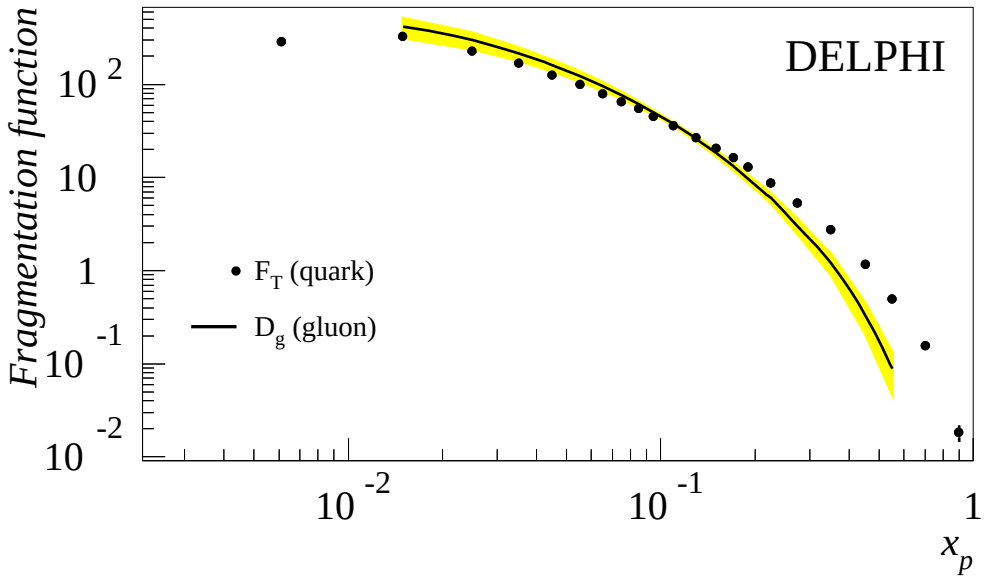

Figure 10: Comparison of the gluon fragmentation function $D_g(x_p)$ with the transverse fragmentation function $F_T(x_p)$ (as in Figure 2). The shaded band shows the range of D_g deviations.

test of QCD. Confirming qualitative theoretical predictions, F_L was found to be non-zero in the region of $x_p < 0.2$ and vanishing at higher x_p.

The transverse σ_T/σ_{tot} and longitudinal σ_L/σ_{tot} fractions of the charged hadron cross-section, defined as the second moments of the corresponding fragmentation functions, were inferred from the data. The value of $\sigma_L/\sigma_{tot} = 0.051 \pm 0.007$ obtained was used to calculate the strong coupling constant $\alpha_s(M_Z)$ to the next-to-leading order of perturbative QCD, giving $\alpha_s^{NLO}(M_Z) = 0.120 \pm 0.013$. Inclusion of non-perturbative power corrections led to the value of $\alpha_s^{NLO+POW}(M_Z) = 0.101 \pm 0.013$.

The measured functions F_T and F_L were used to estimate the mean charged multiplicity, which was found to be $\langle n^{ch} \rangle = 21.21 \pm 0.20$. This value takes into account particle reconstruction inefficiencies in the forward regions of the detector through the weighting functions.

The charge asymmetry fragmentation function $\tilde{F}_A$ is connected to the electroweak theory parameter $\sin^2\theta_W$. Measured data are consistent with the value $\sin^2\theta_W = 0.232$ which was used as an input parameter for JETSET.

Using the lifetime tagging procedure, F_T and F_L were measured from b and uds enriched event samples. Performing simultaneous fit of measured fragmentation functions, the parametrization of the gluon fragmentation function D_g was made. Comparison of D_g to F_T, which is considered as the quark fragmentation function to the leading order of QCD, confirms qualitative QCD prediction, that the gluon fragmentation function is softer than the quark one.

9 Acknowledgements

We are greatly indebted to our technical collaborators and to the funding agencies for their support in building and operating the DELPHI detector, and to the members of the CERN-SL Division for the excellent performance of the LEP collider.

References

[1] V. N. Gribov and L. N. Lipatov, Sov. J. Nucl. Phys. **15** (1972) 78;
G. Altarelli, G. Parisi, Nucl. Phys. **B126** (1977) 298;
Yu. L. Dokshitser, Sov. Phys. JETP **46** (1977) 641.

[2] K. Kato, K. Kitani, T. Munehisa, H. Okada and Y. Shimizu, Phys. Rev. Lett. **50** (1983) 389;
K. Kato, T. Munehisa, H. Okada and Y. Shimizu, Prog. Theor. Phys. **70** (1983) 840.

[3] E. P. Velicheva, S. P. Kurlovich, N. B. Skachkov, "New DELPHI Data on Inclusive $e^+e^- \to h + X$ Process and Check of QCD Predictions for Scaling Violations in Fragmentation Functions", Dubna JINR-1(47)-91-5 (1991);
N. B. Skachkov, "On the Determination of α_s from QCD Analysis of the Scaling Violation in the Fragmentation Functions of the Process $e^+e^- \to h + X$ Studied by DELPHI, TASSO, and Other Collaborations", Dubna JINR-E2-95-189 (1995).

[4] DELPHI Coll., P. Abreu et al., Phys. Lett. **B398** (1997) 194.

[5] DELPHI Coll., P. Abreu et al., Phys. Lett. **B311** (1993) 408.

[6] EMC Coll., J.J. Aubert et al., Phys.Lett. **B121** (1983) 87;
BCDMS Coll., A. C. Benvenuti et al., Phys. Lett. **B237** (1990) 592;
E140X Coll., L. H. Tao et al., Z. Phys. **C70** (1996) 387.

[7] A. Buras, Rev. Mod. Phys. **52** (1980) 199.

[8] G. Altarelli et al., Nucl. Phys. **B160** (1979) 301.

[9] G. Altarelli et al., Phys. Rep. **81 N1** (1982) 1.

[10] TASSO Coll., R. Brandelik et al., Phys. Lett. **B114** (1982) 65.

[11] N. B. Skachkov and L. G. Tkatchev, "On the Determination of the Longitudinal Component of the Fragmentation Function of the Process $e^+e^- \to h + X$", DELPHI Note 92-112 PHYS 218, contrib. to ICHEP Conf., Dallas (1992), unpublished.

[12] OPAL Coll., R. Akers et al., Z. Phys. **C68** (1995) 203.

[13] ALEPH Coll., D. Buskulic et al., Phys. Lett. **B357** (1995) 487.

[14] DELPHI Coll., P. Aarnio et al., Nucl. Instr. & Meth. **A 303** (1991) 233.

[15] DELPHI Coll., P. Abreu et al., Nucl. Instr. & Meth. **A378** (1996) 57.

[16] T. Sjöstrand, Comp. Phys. Comm. **28** (1983) 229;
T. Sjöstrand, "PYTHIA 5.6 and JETSET 7.3", CERN-TH.6488/92 (1992).

[17] DELPHI Coll., P. Abreu et al., Z. Phys. **C73** (1996) 11.

[18] P. Nason, B. R. Webber, Nucl. Phys. **B421** (1994) 473.

[19] PDG, R.M. Barnett et al., Phys. Rev. **D54** (1996) 1.

[20] P. Nason, B. R. Webber, Phys. Lett. **B332** (1994) 405.

[21] P. J. Rijken, W. L. van Neerven, Phys. Lett. **B392** (1997) 207.

[22] P. J. Rijken, W. L. van Neerven, Phys. Lett. **B386** (1996) 422.

[23] Yu. L. Dokshitser, B. R. Webber, Phys. Lett. **B352** (1995) 451.

[24] M. Dasgupta, B. R. Webber, Nucl. Phys. **B484** (1997) 247.

[25] M. Beneke, V. M. Braun, L. Magnea, Nucl. Phys. **B497** (1997) 297.

[26] DELPHI Coll., P. Abreu et al., Phys. Lett. **B347** (1995) 447.

[27] G. Curci, W. Furmanski, R. Petronzio, Nucl. Phys. **B175** (1980) 27.

[28] E. G. Floratos, C. Kounnas, R. Lacaze, Nucl. Phys. **B192** (1981) 417.

[29] BCDMS Coll., A .Benvenuti et al., Phys. Lett. **B223** (1989) 490.

[30] J. Binnewies, B. A. Kniehl, G. Kramer, Phys. Rev. **D52** (1995) 4947.

[31] DELPHI Coll., P. Abreu et al., Zeit. Phys. **C70** (1996) 179.

x_p range	$F_T(x_p)$	$F_L(x_p)$	$\tilde{F}_A(x_p)$	$F_{T+L}(x_p)$
$0.00-0.01$	$291.6 \pm 0.9 \pm 13.0$	$117.0 \pm 0.7 \pm 7.5$	$0.07 \pm 0.48 \pm 2.28$	$408.6 \pm 0.4 \pm 8.6$
$0.01-0.02$	$326.9 \pm 0.6 \pm 6.1$	$84.2 \pm 0.4 \pm 5.5$	$-0.08 \pm 0.30 \pm 1.30$	$411.1 \pm 0.3 \pm 3.1$
$0.02-0.03$	$229.4 \pm 0.5 \pm 3.4$	$37.1 \pm 0.4 \pm 3.2$	$0.13 \pm 0.25 \pm 0.62$	$266.4 \pm 0.2 \pm 2.4$
$0.03-0.04$	$167.2 \pm 0.4 \pm 3.8$	$18.5 \pm 0.3 \pm 2.9$	$0.60 \pm 0.21 \pm 0.38$	$185.7 \pm 0.2 \pm 2.2$
$0.04-0.05$	$126.4 \pm 0.4 \pm 1.8$	$11.3 \pm 0.3 \pm 1.6$	$0.41 \pm 0.18 \pm 0.33$	$137.7 \pm 0.1 \pm 1.4$
$0.05-0.06$	$98.4 \pm 0.3 \pm 1.6$	$7.4 \pm 0.2 \pm 1.2$	$-0.08 \pm 0.16 \pm 0.44$	$105.7 \pm 0.1 \pm 1.2$
$0.06-0.07$	$78.7 \pm 0.3 \pm 1.4$	$5.5 \pm 0.2 \pm 0.9$	$-0.05 \pm 0.14 \pm 0.15$	$84.2 \pm 0.1 \pm 1.0$
$0.07-0.08$	$64.5 \pm 0.3 \pm 1.0$	$3.8 \pm 0.2 \pm 0.7$	$-0.28 \pm 0.13 \pm 0.25$	$68.3 \pm 0.1 \pm 0.8$
$0.08-0.09$	$54.4 \pm 0.2 \pm 0.8$	$2.3 \pm 0.2 \pm 0.5$	$-0.25 \pm 0.12 \pm 0.13$	$56.70 \pm 0.10 \pm 0.69$
$0.09-0.10$	$45.6 \pm 0.2 \pm 0.8$	$1.9 \pm 0.2 \pm 0.5$	$-0.02 \pm 0.11 \pm 0.19$	$47.52 \pm 0.09 \pm 0.59$
$0.10-0.12$	$36.2 \pm 0.1 \pm 0.6$	$1.1 \pm 0.1 \pm 0.3$	$-0.25 \pm 0.07 \pm 0.10$	$37.31 \pm 0.06 \pm 0.46$
$0.12-0.14$	$27.1 \pm 0.1 \pm 0.4$	$0.64 \pm 0.08 \pm 0.25$	$-0.02 \pm 0.06 \pm 0.06$	$27.71 \pm 0.05 \pm 0.37$
$0.14-0.16$	$20.6 \pm 0.1 \pm 0.3$	$0.50 \pm 0.07 \pm 0.15$	$-0.08 \pm 0.05 \pm 0.09$	$21.12 \pm 0.04 \pm 0.26$
$0.16-0.18$	$16.27 \pm 0.09 \pm 0.28$	$0.21 \pm 0.07 \pm 0.17$	$-0.11 \pm 0.05 \pm 0.07$	$16.38 \pm 0.04 \pm 0.23$
$0.18-0.20$	$12.88 \pm 0.08 \pm 0.20$	$0.09 \pm 0.06 \pm 0.10$	$-0.08 \pm 0.04 \pm 0.02$	$12.97 \pm 0.03 \pm 0.17$
$0.20-0.25$	$8.79 \pm 0.04 \pm 0.13$	$0.08 \pm 0.03 \pm 0.05$	$-0.12 \pm 0.02 \pm 0.05$	$8.87 \pm 0.02 \pm 0.11$
$0.25-0.30$	$5.29 \pm 0.03 \pm 0.08$	$0.03 \pm 0.02 \pm 0.03$	$-0.06 \pm 0.02 \pm 0.02$	$5.31 \pm 0.01 \pm 0.07$
$0.30-0.40$	$2.73 \pm 0.02 \pm 0.07$	$0.007 \pm 0.012 \pm 0.020$	$-0.036 \pm 0.009 \pm 0.025$	$2.734 \pm 0.007 \pm 0.057$
$0.40-0.50$	$1.16 \pm 0.01 \pm 0.04$	$0.008 \pm 0.008 \pm 0.022$	$-0.018 \pm 0.006 \pm 0.008$	$1.167 \pm 0.005 \pm 0.019$
$0.50-0.60$	$0.502 \pm 0.007 \pm 0.010$	$0.006 \pm 0.005 \pm 0.007$	$-0.021 \pm 0.004 \pm 0.005$	$0.508 \pm 0.003 \pm 0.008$
$0.60-0.80$	$0.155 \pm 0.003 \pm 0.007$	$0.0004 \pm 0.0021 \pm 0.0043$	$-0.0007 \pm 0.0015 \pm 0.0040$	$0.155 \pm 0.001 \pm 0.008$
$0.80-1.00$	$0.018 \pm 0.001 \pm 0.003$	$0.0012 \pm 0.0007 \pm 0.0020$	$-0.0007 \pm 0.0005 \pm 0.0017$	$0.0193 \pm 0.0004 \pm 0.0023$
$\sigma_P^{ch}/\sigma_{tot}$	$0.5788 \pm 0.0007 \pm 0.0068$	$0.0309 \pm 0.0005 \pm 0.0042$	—	$0.6097 \pm 0.0003 \pm 0.0066$

Table 1: Transverse $F_T(x_p)$, longitudinal $F_L(x_p)$ and asymmetric $\tilde{F}_A(x_p)$ components of the fragmentation function, and the summed function $F_{T+L}(x_p)$, measured using the weighting method. The $\sigma_P^{ch}/\sigma_{tot}$ $(P = T, L, T+L)$ are the corresponding fractions of the charged particle cross-section. The first error is statistical and the second one is systematic. The function $F_{T+L}(x_p)$ was evaluated from the double-differential cross-section by applying the weight $(W_T + W_L)$ and integrating over the angular range $|\cos\theta| < 0.8$. The smallness of the errors on $F_{T+L}(x_p)$ reflects the anti-correlation between the errors on F_T and F_L.

x_p range	F_L/F_T	F_L/F_{T+L}
$0.00 - 0.01$	$0.401 \pm 0.004 \pm 0.043$	$0.286 \pm 0.002 \pm 0.021$
$0.01 - 0.02$	$0.258 \pm 0.002 \pm 0.021$	$0.205 \pm 0.001 \pm 0.014$
$0.02 - 0.03$	$0.162 \pm 0.002 \pm 0.016$	$0.139 \pm 0.001 \pm 0.013$
$0.03 - 0.04$	$0.111 \pm 0.002 \pm 0.019$	$0.100 \pm 0.002 \pm 0.016$
$0.04 - 0.05$	$0.090 \pm 0.002 \pm 0.013$	$0.082 \pm 0.002 \pm 0.012$
$0.05 - 0.06$	$0.075 \pm 0.003 \pm 0.012$	$0.070 \pm 0.002 \pm 0.011$
$0.06 - 0.07$	$0.069 \pm 0.003 \pm 0.013$	$0.065 \pm 0.002 \pm 0.012$
$0.07 - 0.08$	$0.059 \pm 0.003 \pm 0.011$	$0.056 \pm 0.003 \pm 0.010$
$0.08 - 0.09$	$0.043 \pm 0.003 \pm 0.010$	$0.041 \pm 0.003 \pm 0.010$
$0.09 - 0.10$	$0.042 \pm 0.003 \pm 0.011$	$0.040 \pm 0.003 \pm 0.010$
$0.10 - 0.12$	$0.030 \pm 0.003 \pm 0.009$	$0.029 \pm 0.003 \pm 0.009$
$0.12 - 0.14$	$0.024 \pm 0.003 \pm 0.009$	$0.023 \pm 0.003 \pm 0.009$
$0.14 - 0.16$	$0.024 \pm 0.004 \pm 0.007$	$0.024 \pm 0.004 \pm 0.008$
$0.16 - 0.18$	$0.013 \pm 0.004 \pm 0.011$	$0.013 \pm 0.004 \pm 0.010$
$0.18 - 0.20$	$0.007 \pm 0.005 \pm 0.008$	$0.007 \pm 0.005 \pm 0.008$
$0.20 - 0.25$	$0.009 \pm 0.004 \pm 0.006$	$0.009 \pm 0.004 \pm 0.006$
$0.25 - 0.30$	$0.005 \pm 0.005 \pm 0.005$	$0.005 \pm 0.005 \pm 0.006$
$0.30 - 0.40$	$0.003 \pm 0.004 \pm 0.007$	$0.003 \pm 0.005 \pm 0.007$
$0.40 - 0.50$	$0.007 \pm 0.007 \pm 0.019$	$0.007 \pm 0.007 \pm 0.019$
$0.50 - 0.60$	$0.012 \pm 0.011 \pm 0.014$	$0.012 \pm 0.010 \pm 0.013$
$0.60 - 0.80$	$0.003 \pm 0.014 \pm 0.029$	$0.003 \pm 0.014 \pm 0.028$
$0.80 - 1.00$	$0.065 \pm 0.044 \pm 0.139$	$0.061 \pm 0.039 \pm 0.119$

Table 2: Ratio of the longitudinal to the transverse component of the fragmentation function and to the sum of the longitudinal and transverse components. Statistical and systematic errors are shown. The systematic uncertainties are correlated between x_p bins.

x_p range	Track/event selection		Angular range		Region of $\lvert\cos\theta\rvert \approx 0$		Total	
	ΔF_T	ΔF_L	ΔF_T	ΔF_L	ΔF_T	ΔF_L	ΔF_T	ΔF_L
$0.00 - 0.01$	10	5	8	5	1	1	13	7
$0.01 - 0.02$	3	4	5	3	1	2	5	5
$0.02 - 0.03$	1	2	3	2	1	1	4	3
$0.03 - 0.04$	2	2	3	2	0.7	0.8	4	3
$0.04 - 0.05$	1.0	1	1	0.8	0.6	0.7	2	1
$0.05 - 0.06$	0.8	0.6	1	0.8	0.4	0.4	2	1
$0.06 - 0.07$	0.7	0.4	1	0.7	0.4	0.4	1	0.9
$0.07 - 0.08$	0.5	0.3	0.8	0.5	0.2	0.2	1.0	0.6
$0.08 - 0.09$	0.5	0.2	0.5	0.3	0.2	0.2	0.8	0.5
$0.09 - 0.10$	0.4	0.2	0.5	0.3	0.2	0.2	0.7	0.4
$0.10 - 0.12$	0.4	0.1	0.4	0.2	0.1	0.1	0.5	0.3
$0.12 - 0.14$	0.3	0.1	0.3	0.2	0.08	0.09	0.4	0.2
$0.14 - 0.16$	0.2	0.07	0.1	0.06	0.08	0.09	0.3	0.1
$0.16 - 0.18$	0.2	0.1	0.1	0.09	0.01	0.01	0.3	0.1
$0.18 - 0.20$	0.2	0.07	0.07	0.05	0.03	0.03	0.2	0.08
$0.20 - 0.25$	0.1	0.02	0.05	0.03	0.02	0.02	0.1	0.04
$0.25 - 0.30$	0.07	0.009	0.03	0.01	0.009	0.010	0.08	0.02
$0.30 - 0.40$	0.04	0.008	0.05	0.006	0.008	0.009	0.07	0.02
$0.40 - 0.50$	0.02	0.011	0.03	0.016	0.009	0.010	0.04	0.02
$0.50 - 0.60$	0.006	0.003	0.003	0.003	0.0002	0.0002	0.007	0.005
$0.60 - 0.80$	0.005	0.003	0.004	0.003	0.0004	0.0004	0.007	0.004
$0.80 - 1.00$	0.002	0.001	0.002	0.001	0.0009	0.0011	0.003	0.002

Table 3: Main contributions to the systematic uncertainties on F_T and F_L, arising from variations of the track and event selection criteria, the angular range analysed and the influence of the region of $\lvert\cos\theta\rvert \approx 0$, together with the total systematic errors. Systematic uncertainties are correlated between x_p bins.

Criterion	$\Delta\frac{\sigma_T^{ch}}{\sigma_{tot}}$	$\Delta\frac{\sigma_L^{ch}}{\sigma_{tot}}$	$\Delta\langle n^{ch}\rangle$
Track and event selection	0.005	0.002	0.19
Angular range	0.004	0.003	0.05
Region of $\lvert\cos\theta\rvert \approx 0$	0.002	0.002	0.01
Weighting/fitting	0.001	0.0008	0.05
x_p evaluation method	0.001	0.0002	—
Uncertainty in K_s^0	—	—	0.02
Total	0.007	0.004	0.20

Table 4: Systematic deviations of the components of the charged particle cross-section and of the mean charged particle multiplicity due to variations of the specified criteria.

x_p range	$F_T^b(x_p)$	$F_L^b(x_p)$	$F_T^{uds}(x_p)$	$F_L^{uds}(x_p)$
$0.00-0.01$	$331 \pm 9 \pm 22$	$113 \pm 7 \pm 13$	$280 \pm 2 \pm 10$	$115 \pm 1 \pm 6$
$0.01-0.02$	$369 \pm 6 \pm 12$	$89 \pm 4 \pm 9$	$317 \pm 1 \pm 4$	$79 \pm 1 \pm 4$
$0.02-0.03$	$264 \pm 5 \pm 12$	$45 \pm 4 \pm 7$	$218 \pm 1 \pm 3$	$33.7 \pm 0.9 \pm 2.6$
$0.03-0.04$	$200 \pm 5 \pm 9$	$19 \pm 3 \pm 6$	$158.4 \pm 1.0 \pm 2.6$	$15.4 \pm 0.7 \pm 2.1$
$0.04-0.05$	$141 \pm 4 \pm 4$	$18 \pm 3 \pm 3$	$117.5 \pm 0.9 \pm 1.2$	$9.6 \pm 0.6 \pm 1.0$
$0.05-0.06$	$120 \pm 4 \pm 4$	$6 \pm 2 \pm 2$	$91.8 \pm 0.7 \pm 0.9$	$5.6 \pm 0.5 \pm 0.6$
$0.06-0.07$	$94 \pm 3 \pm 3$	$6 \pm 2 \pm 2$	$73.7 \pm 0.7 \pm 0.7$	$4.3 \pm 0.5 \pm 0.5$
$0.07-0.08$	$74 \pm 3 \pm 3$	$7 \pm 2 \pm 2$	$61.3 \pm 0.6 \pm 0.7$	$2.3 \pm 0.4 \pm 0.4$
$0.08-0.09$	$68 \pm 3 \pm 3$	$1 \pm 2 \pm 2$	$51.6 \pm 0.6 \pm 0.7$	$1.0 \pm 0.4 \pm 0.4$
$0.09-0.10$	$53 \pm 2 \pm 3$	$2 \pm 2 \pm 2$	$43.4 \pm 0.5 \pm 0.5$	$1.1 \pm 0.4 \pm 0.5$
$0.10-0.12$	$40 \pm 2 \pm 3$	$3 \pm 1 \pm 2$	$35.0 \pm 0.3 \pm 0.5$	$0.4 \pm 0.2 \pm 0.3$
$0.12-0.14$	$28 \pm 1 \pm 2$	$1.6 \pm 0.9 \pm 1.3$	$26.9 \pm 0.3 \pm 0.5$	$-0.3 \pm 0.2 \pm 0.3$
$0.14-0.16$	$19 \pm 1 \pm 1$	$1.7 \pm 0.7 \pm 0.7$	$20.5 \pm 0.3 \pm 0.4$	$0.02 \pm 0.19 \pm 0.16$
$0.16-0.18$	$15.9 \pm 1.0 \pm 1.1$	$0.4 \pm 0.7 \pm 0.7$	$15.9 \pm 0.2 \pm 0.3$	$0.32 \pm 0.17 \pm 0.19$
$0.18-0.20$	$11.2 \pm 0.8 \pm 1.1$	$0.8 \pm 0.6 \pm 0.9$	$13.7 \pm 0.2 \pm 0.3$	$-0.46 \pm 0.15 \pm 0.36$
$0.20-0.25$	$7.8 \pm 0.4 \pm 0.6$	$-0.2 \pm 0.3 \pm 0.2$	$9.4 \pm 0.1 \pm 0.2$	$-0.16 \pm 0.08 \pm 0.13$
$0.25-0.30$	$4.0 \pm 0.3 \pm 0.3$	$-0.03 \pm 0.20 \pm 0.11$	$5.92 \pm 0.09 \pm 0.10$	$-0.12 \pm 0.07 \pm 0.14$
$0.30-0.40$	$1.8 \pm 0.1 \pm 0.2$	$0.04 \pm 0.10 \pm 0.11$	$3.22 \pm 0.05 \pm 0.06$	$-0.10 \pm 0.03 \pm 0.11$
$0.40-0.50$	$0.44 \pm 0.07 \pm 0.07$	$0.13 \pm 0.05 \pm 0.19$	$1.42 \pm 0.03 \pm 0.06$	$-0.01 \pm 0.02 \pm 0.02$
$0.50-0.60$	$0.15 \pm 0.05 \pm 0.05$	$0.03 \pm 0.03 \pm 0.02$	$0.68 \pm 0.02 \pm 0.03$	$-0.02 \pm 0.02 \pm 0.02$
$0.60-0.80$	$0.04 \pm 0.02 \pm 0.03$	$0.001 \pm 0.012 \pm 0.018$	$0.24 \pm 0.01 \pm 0.01$	$-0.01 \pm 0.01 \pm 0.04$
$0.80-1.00$	$0.0002 \pm 0.0004 \pm 0.0004$	$-0.0001 \pm 0.0003 \pm 0.0001$	$0.024 \pm 0.004 \pm 0.004$	$0.005 \pm 0.003 \pm 0.004$
$\langle n^{ch} \rangle$	$23.47 \pm 0.07 \pm 0.36$		$20.35 \pm 0.01 \pm 0.19$	

Table 5: Transverse and longitudinal components of the fragmentation function for Z^0 decays into either $b\bar{b}$ or light quark-antiquark pairs The first error is statistical and the second one is systematic. The charged particle multiplicities are calculated by integrating the corresponding F_{T+L} distributions.

	Natural flavour mix		Flavour-tagged events	
	$\alpha_s^{LO} = 0.126,\ fixed$	$\alpha_s^{LO} = 0.131 \pm 0.066$	$\alpha_s^{LO} = 0.126,\ fixed$	$\alpha_s^{LO} = 0.133 \pm 0.032$
P_1	0.47 ± 0.07	0.46 ± 0.26	0.47 ± 0.05	0.46 ± 0.15
P_2	-2.90 ± 0.02	-2.85 ± 0.03	-2.84 ± 0.01	-2.84 ± 0.01
P_3	5 ± 1	4 ± 1	3.3 ± 0.5	3.5 ± 0.5
P_4	0.29 ± 0.01	0.30 ± 0.01	0.29 ± 0.01	0.30 ± 0.01
χ^2/ndf	$10/15 = 0.7$	$11/14 = 0.8$	$132/53 = 2.5$	$132/52 = 2.5$

Table 6: Parameters for the gluon fragmentation function (21) obtained from fits with α_s^{LO} either fixed at the value of 0.126 or treated as a free parameter. The *'Natural flavour mix'* columns correspond to the fit to the natural flavour mix data given in Table 1. The *'Flavour-tagged events'* columns correspond to the simultaneous fit to the b- and uds-tagged data given in Table 5 and the remaining untagged events.

Appendix E

Transverse Mass Dependence of Bose-Einstein Correlation Radii in e^+e^- Annihilation at the LEP Energies

TRANSVERSE MASS DEPENDENCE OF BOSE-EINSTEIN CORRELATION RADII IN e^+e^- ANNIHILATION AT THE LEP ENERGIES

B. LÖRSTAD, O.G. SMIRNOVA
Department of Physics, Elementary Particle Physics,
Box 118, 2221 00 Lund, Sweden

The study of the directional dependence of two-particle correlations in the hadronic decays of the Z boson is performed using the data collected by the DELPHI experiment. Investigation of the dependence of correlation radii on the transverse mass reveals a behaviour similar to that in heavy ions collisions, namely, an approximate $1/\sqrt{m_t}$ dependence. Comparison to a simple Monte Carlo model shows a similar tendency.

1 Introduction

Recent interest in profound studies of the Bose-Einstein correlations in Z^0 hadronic decays in e^+e^- annihilation arose mainly in connection to the predictions that the W mass measured in hadronic W^+W^- events can have a shift of about 100 MeV due to the Bose-Einstein effects [1]. Being separated in space and time by distances much smaller than typical source radii, the W^+ and W^- source regions overlap, which means that the Bose-Einstein effects on the hadronization stage can couple identical bosons from W^+ and W^-.

So far, only phenomenological models are used to describe the hadronization process and Bose-Einstein effects in particular. Studies of the identical-boson correlations in e^+e^- annihilation processes at LEP energies up to now were concentrated on the shape of the correlation function in terms of the invariant four-momentum difference of particles Q,[2–4] while at lower energies several collaborations studied Bose-Einstein correlations using two-dimensional distributions in components of Q [5].

High-energy heavy-ion collision experiments developed precision methods for the boson interferometry studies [6–7] to obtain information on the space-time development of the particle emitting source. Analysis performed for the three components of the momentum difference of two identical bosons shows a transverse mass dependence of the correlation radii,[7,8] which is described by hydrodynamical models of the particle source expansion.

Here, a similar analysis of the Z^0 hadronic decays is presented. Two-particle correlations are studied as a function of three components of the four-momentum difference in different transverse mass m_t intervals. Results are compared to those obtained from the analysis of JETSET [9] generated events.

2 Data selection

Data collected by the DELPHI detector [10] in 1991-1994 at centre-of-mass energies around $\sqrt{s} = 91.2$ GeV ($86.2 \leq \sqrt{s} \leq 94.2$ GeV) are used.

Only charged particles in hadronic events are involved in the analysis. In the barrel region they are measured by a set of cylindrical tracking detectors in the solenoidal magnetic field of 1.2 T. The main tracking device was the Time Projection Chamber (TPC). Additional $R\varphi$ measurements are provided by the Outer Detector (OD) and the Inner Detector (ID). In the forward direction (θ between 11° and 33° and between 147° and 169°) charged particles are measured by a set of planar drift chambers FCA and FCB.

Tracks were taken into account if their impact parameter was below 5 cm in the transverse plane and below 10 cm along the beam axis, measured track length was above 50 cm, momentum between 0.1 GeV/c and 50 GeV/c and polar angle between 11° and 169°.

Hadronic events were then selected by requiring that they contain at least 5 charged particles with momentum above 0.2 GeV/c, the total energy of all charged particles exceeded 15 GeV (assuming the $\pi^{\pm}$ mass for particles), having at least 3 GeV in each hemisphere with respect to the sphericity axis, the latter with a polar angle between 26° and 154°. The momentum imbalance was restricted to 20 GeV/c.

Only two-jet events were selected for this analysis. The selection was done using the LUCLUS [9] clustering algorithm (with parameter $d_{join} = 2.7$), requiring also the thrust value to be more than 0.95 and the jet opening angle to be at least 175°. A total of about 670,000 events satisfied those criteria.

For reason of comparison, the same analysis was performed using DELPHI tuned [11] JETSET PS generated events (Bose-Einstein effects included) with the DELSIM [12] detector simulation.

3 Analysis and results

The correlation function of two identical bosons is defined as

$$C(p_1, p_2) = \frac{P(p_1, p_2)}{P(p_1)P(p_2)} \ , \tag{1}$$

where p_1 and p_2 are four-momenta of two particles, $P(p_1, p_2)$ is the two-particle probability density , while $P(p_1)$ and $P(p_2)$ represent single-particle probability densities. In the hypothetical case of absence of two-particle correlations, the product $P(p_1)P(p_2)$ is equivalent to $P(p_1, p_2)$. Therefore it is convenient to use

as the denominator in (1) an artificially created Bose-Einstein correlation-free two-particle distribution.

Measuring the four-momentum differences $Q = \sqrt{-(p_1 - p_2)^2}$, one can rewrite Eq. (1) in the form

$$C(Q) = \frac{N^{\pm\pm}(Q)}{N^{\pm\pm}_{mix}(Q)} \ , \tag{2}$$

where $N^{\pm\pm}(Q)$ is the number of like-charge particles with four-momentum difference Q, and $N^{\pm\pm}_{mix}(Q)$ is the same quantity built from a sample of non-correlated particles. Such a sample was constructed by picking particles randomly from different events. Since this procedure of mixing particles violates energy-momentum conservation and affects the normalization, the correlation function (2) is corrected with the help of JETSET generated events without Bose-Einstein effects included. Thus the two-particle correlation function used in this analysis is defined as

$$C(Q) = \frac{[N^{\pm\pm}(Q)/N^{\pm\pm}_{mix}(Q)]_{data}}{[N^{\pm\pm}(Q)/N^{\pm\pm}_{mix}(Q)]_{\textsc{Jetset}}} \ . \tag{3}$$

The analysis is done in the Longitudinal Centre-of-Mass System (LCMS) of the pair. This is the system in which the sum of the two particles momenta is perpendicular to the jet axis. The momentum difference of the particle pair Q is resolved into Q_{long}, parallel to the jet axis, $Q_{t,out}$, collinear with the pair momentum sum, and complementary $Q_{t,side}$, perpendicular to Q_{long} and $Q_{t,out}$. A schematic picture of LCMS is shown in Fig. 1 in projection into the (Q_{long},$Q_{t,out}$) plane. In this system, projections of the total momentum of the pair onto the "longitudinal" and "side" directions are equal to zero. The difference in emission time of the particles couples to the energy difference between the particles only in the $Q_{t,out}$ direction [13].

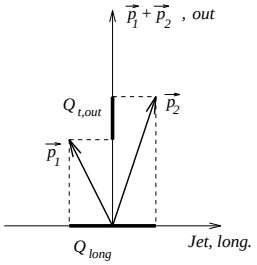

Figure 1: LCMS projection on the (Q_{long},$Q_{t,out}$) plane.

An example for the behaviour of the correlation function (3) and its components, $C(Q_{t,out})$, $C(Q_{t,side})$ and $C(Q_{long})$ is shown on Fig. 2. Results obtained from the DELPHI data are compared to those from JETSET+DELSIM simulated events. While both transverse components of the total correlation function are in good agreement, the longitudinal component shows slightly different behaviour in data and JETSET.

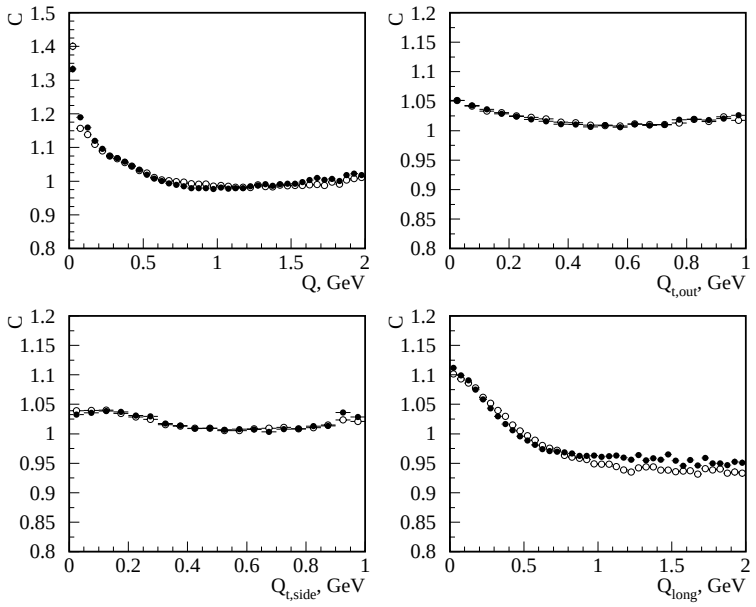

Figure 2: Correlation functions $C(Q)$, $C(Q_{t,out})$, $C(Q_{t,side})$ and $C(Q_{long})$ obtained from the DELPHI data (closed circles) and JETSET+DELSIM simulated events (open circles).

If three projections of Q are known, it is possible to construct a three-dimensional correlation function $C \equiv C(Q_{t,out}, Q_{t,side}, Q_{long})$. Using the common assumption about a Gaussian shape of the correlation function in all three dimensions, it is convenient to parametrize this three-dimensional function as

$$\begin{aligned} C &= N\left[1+\lambda\exp(-R^2_{t,out}Q^2_{t,out} - R^2_{t,side}Q^2_{t,side} - R^2_{long}Q^2_{long})\right] \\ &\times \left(1+\delta_{t,side}Q_{t,side} + \delta_{t,out}Q_{t,out} + \delta_{long}Q_{long}\right) . \end{aligned} \quad (4)$$

By fitting the correlation function by Eq. (4) one can extract the correlation radii, $R_{t,out}$, $R_{t,side}$ and R_{long}.

Studies of Bose-Einstein effects in heavy-ion collisions at CERN SPS by the experiments NA44 [7] and NA35/NA49 [8] revealed that the extracted radii parameters show an approximate $1/\sqrt{m_t}$ dependence, where m_t is the average transverse mass of two particles. This behaviour is consistent with hydrodynamical models describing the pion source evolution in high-energy heavy-ion collisions.[14–20] Thus it is of particular interest to investigate the dependence of the interferometric parameters $R_{t,out}$, $R_{t,side}$ and R_{long} on the transverse mass m_t in electron-positron annihilation.

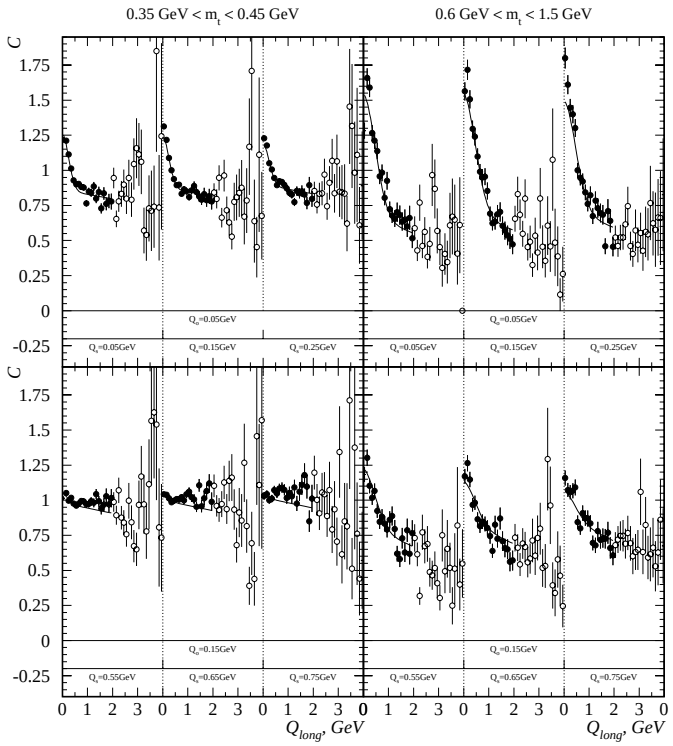

Figure 3: One-dimensional representation of the fit of the correlation function $C(Q_{t,out}, Q_{t,side}, Q_{long})$ by the formula (4). Only closed circles participated in the fit.

The available DELPHI statistics allows us to split all the data into five m_t intervals (see Tab. 1). In each of them a fit by the function (4) was performed. An example of the one-dimensional representation of this fit is shown in Fig. 3. The fit was done in the region of $Q_{t,out} < 1\ GeV$, $Q_{t,side} < 1\ GeV$ and $Q_{long} < 2\ GeV$ (closed circles in Fig. 3), which is statistically well populated.

Results of the fit are listed in Tab. 1 and are shown in Fig. 4. It is clearly seen that the correlation radii decrease with increasing m_t. This decrease is approximately proportional to $1/\sqrt{m_t}$. Low values of the λ parameter at small m_t can be explained by the presence of resonance decays products in this region. At high m_t their contribution vanishes, thus raising λ.

Table 1: Parameters of the fit of the correlation function $C(Q_{t,out}, Q_{t,side}, Q_{long})$ by the formula (4) for $Q_{t,out} < 1GeV$, $Q_{t,side} < 1GeV$ and $Q_{long} < 2GeV$.

$\langle m_t \rangle$ (GeV)	χ^2/ndf	λ	$R_{t,out}$ (fm)	$R_{t,side}$ (fm)	R_{long} (fm)
0.19	834/330	0.187±0.005	1.08±0.04	0.55±0.02	0.83±0.04
0.30	1713/757	0.357±0.006	0.71±0.01	0.526±0.010	0.70±0.01
0.38	3172/1272	0.482±0.009	0.498±0.010	0.487±0.008	0.567±0.010
0.52	4880/1927	0.68±0.01	0.343±0.006	0.451±0.006	0.431±0.006
0.81	3354/1992	1.27±0.03	0.272±0.004	0.366±0.006	0.288±0.004

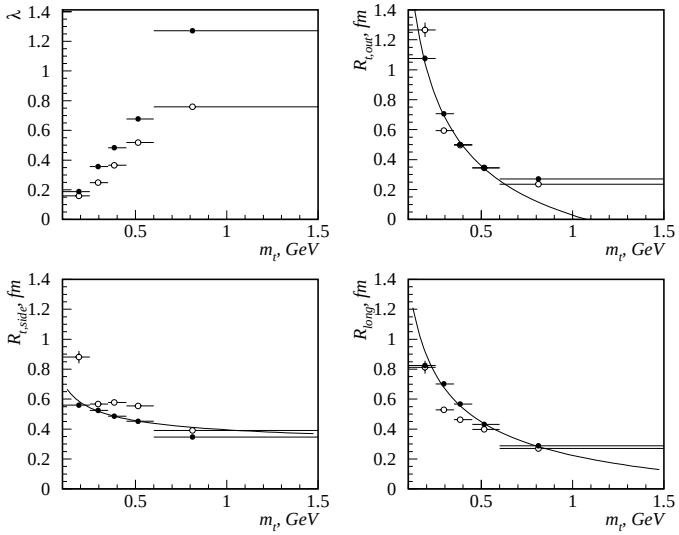

Figure 4: Transverse mass dependence of parameters of the fit of the correlation function $C(Q_{t,out}, Q_{t,side}, Q_{long})$ by the formula (4). Closed circles represent the DELPHI data, while open circles – JETSET+DELSIM simulation. Points are placed at the mean m_t values in bins indicated with horizontal bars. Curves show the $R \propto 1/\sqrt{m_t}$ fit to the data.

4 Conclusion

Analysis of the dimensional- and m_t-dependence of the Bose-Einstein effects using the 1991–1994 DELPHI data showed strong dependence of all the components of the correlation radius on m_t. Similar dependence is observed in simulated JETSET events, although in general JETSET fails to give a fair description of the observed effect. Growth of the λ parameter is readily explained by the vanishing of resonance decay contribution with increasing m_t. A popular explanation of the observed m_t dependence of radii in the data is that it is also due to resonance decays : resonances do propagate out of the primary pion source, and pions produced in their decays do have comparatively low momenta. Therefore the effective size of the source increases at low m_t values. This explanation can not possibly be valid for JETSET generated events, since the resonance propagation is not included in this generator. Therefore, further investigations of the effect have to be done.

References

1. T. Sjöstrand and L. Lönnblad, *Phys. Lett.* B **351**, 293 (1995).
2. DELPHI Coll., P. Abreu et al., *Phys. Lett.* B **286**, 201 (1992).
3. OPAL Coll., P .D. Acton et al., *Phys. Lett.* B **267**, 143 (1991).
4. ALEPH Coll., D. Decamp et al., *Z. Phys.* C **54**, 75 (1992).
5. TASSO Coll., M. Althoff et al., *Z. Phys.* C **30**, 35 (1986);
   Mark II Coll., I. Juricic et al., *Phys. Rev.* D **39**, 1 (1989).
6. NA44 Coll., H. Bøggild et al., *Phys. Lett.* B **349**, 386 (1995).
7. NA44 Coll., H. Beker et al., *Phys. Rev. Lett.* **74**, 3340 (1995).
8. NA35 Coll., T. Alber et al., *Z. Phys.* C **66**, 77 (1995).
9. T. Sjöstrand, *Comp. Phys. Comm.* **28**, 229 (1983);
   T. Sjöstrand, PYTHIA *5.6 and* JETSET *7.3*, CERN-TH.6488/92 (1992).
10. DELPHI Coll., P. Aarnio et al., *Nucl. Instrum. Methods* A **303**, 233 (1991);
    DELPHI Coll., P. Abreu et al., *Nucl. Instrum. Methods* A **378**, 57 (1996).
11. K.Hamacher and M.Weierstall, *Tuning and Test of Fragmentation Models based on Identified Particles and Precision Event Shape Data*, DELPHI Note 95-80 PHYS 515, contrib. eps0548 to to EPS-HEP Conf., Brussels (1995), unpublished.
12. *DELSIM Reference Manual*, DELPHI Note 87-98 PROG 100 (1989), unpublished.

13. T. Csörgő and S. Pratt, in "Proceedings of the Workshop on Relativistic Heavy Ion Physics", KFKI-1991-28/A, p75.
14. S. Pratt, T. Csörgő and J. Zimányi, *Phys. Rev.* C **42**, 2646 (1990).
15. A. N. Makhlin and Yu. M. Sinyukov, *Z. Phys.* C **39**, 39 (1988).
16. T. Csörgő and B. Lörstad, *Phys. Rev.* C **54**, 1390 (1996).
17. T. Csörgő, B. Lörstad and J. Zimányi, *Phys. Lett.* B **338**, 134 (1994).
18. S. Chapman, P. Scotto and U. Heinz, *Phys. Rev. Lett.* **74**, 4440 (1995).
19. S. V. Akkelin and Yu. M. Sinyukov, *Phys. Lett.* B **356**, 525 (1995).
20. B. R. Schlei et al., *Phys. Lett.* B **293**, 275 (1992).